UNIVERSITÉ DE GENÈVE
Département de Physique
Nucléaire et Corpusculaire

FACULTÉ DES SCIENCES
Prof. A. Blondel

Measurement of charged Pion and Kaon production cross sections with NA61/SHINE for T2K

THÈSE

présentée à la Faculté des Sciences de l'Université de Genève

pour obtenir le grade de Docteur ès sciences, mention physique

par

Sebastien Murphy

de Vagnas, France

Thèse N° 4416

GENÈVE
Atelier de reproduction ReproMail
2012

CERN-THESIS-2012-093
04/05/2012

UNIVERSITÉ
DE GENÈVE

FACULTÉ DES SCIENCES

Doctorat ès sciences
Mention physique

Thèse de *Monsieur Sébastien MURPHY*

intitulée :

" Measurement of Charged Pion and Kaon Production Cross Sections with NA61/SHINE for T2K "

La Faculté des sciences, sur le préavis de Messieurs A. BLONDEL, professeur ordinaire et directeur de thèse (Département de physique nucléaire et corpusculaire), Alessandro BRAVAR docteur et codirecteur de thèse (Département de physique nucléaire et corpusculaire), D. RAPIN, professeur titulaire (Département de physique nucléaire et corpusculaire), P. SEYBOTH, professeur (Ludwig Maximilian Universität, Max Planck Institut für Physik, Munchen, Deutschland) et A. RUBBIA, professeur (Institute of Particle Physics, Eidgenössische Technische Hochschule, Zürich, Schweiz), autorise l'impression de la présente thèse, sans exprimer d'opinion sur les propositions qui y sont énoncées.

Genève, le 4 mai 2012

Thèse - 4416 -

Le Doyen, **Jean-Marc TRISCONE**

N.B. - La thèse doit porter la déclaration précédente et remplir les conditions énumérées dans les "Informations relatives aux thèses de doctorat à l'Université de Genève".

Overview of the Thesis

T2K, the long baseline neutrino experiment from J-PARC in Tokai to Kamioka (Japan), aims to precisely measure the last unknown neutrino mixing angle, θ_{13}, by the observation of $\nu_\mu \rightarrow \nu_e$ appearance. The goal is also to refine the measurements of $\{\Delta m^2_{23}, \theta_{23}\}$ by studying ν_μ disappearance. Last year T2K published results claiming a strong indication of a nonzero value of θ_{13}. Although not statistically significant enough to claim a discovery, they constitute the first evidence of $\theta_{13} \neq 0$. It is also the first experiment to observe ν_e appearance.

In T2K, the neutrino beam is generated by the J-PARC high intensity 30 GeV (kinetic energy) proton beam interacting in a 90 cm long graphite target to produce π and K mesons, which decay into neutrinos. The resulting neutrino beam is aimed towards a near detector complex, 280 m from the target, and to the Super-Kamiokande (SK) far detector located 295 km away at 2.5 degrees off-axis from the π and K beam. Neutrino oscillations are probed by comparing the neutrino event rates measured in SK to the predictions of a Monte-Carlo simulation based on flux calculations and near detector event rates. The flux calculations are generally based on hadron production models tuned to sparse available data, resulting in systematic uncertanties which are large and difficult to evaluate. In order to provide more precise and reliable estimates, direct measurements with the NA61/SHINE (SHINE $\equiv$ SPS Heavy Ion and Neutrino Experiment) spectrometer at the CERN-SPS were conducted. We collected the first reference set of proton-carbon interactions, with the beam set at the T2K proton beam energy (30 GeV), in the fall of 2007. The particle identification (PID) in NA61/SHINE is based on time-of-flight measurements (tof) and energy loss per unit length in the TPCs (dE/dx). While the tof offers good precision at low momenta, dE/dx is practical only at higher energies or below ~1 GeV/c momentum. Thus by combining both measurements we are able to obtain a high purity particle identification over a very large momentum range. Just before the 2007 run we built a new time-of-flight detector, the ToF-F, in order to extend the PID to the phase-space needed for the T2K measurements. The combined tof-dE/dx PID together with the large acceptance coverage of the detector and its high track reconstruction efficiency has allowed us to make a series of very precise cross-section measurements. We published first results of charged pion cross-sections in early 2011 and positively charged kaon cross-sections in January 2012. As we shall see, the results have been of considerable benefit for T2K.

I was involved in first building the NA61/SHINE ToF-F detector and calibrating it with the data we had collected in 2007. I then took advantage of the newly built detector to extract the relevant particle yields with the combined PID method and compute the charged pion cross-sections. To validate the method, the results were compared with those from two other analyses: one based on the measurements of negatively charged hadrons for which no PID is needed and another based on dE/dx measurements below 1 GeV/c momentum. A year after that, using the combined tof-dE/dx method, I also provided results of positively charged kaon cross-sections and about 6 months later proton cross-sections.

The first chapter of this thesis provides a general introduction to neutrino oscillation and summarizes the status of the main ongoing experiments in the field. T2K is then described in more details, with emphasis on its needs for reference hadron production data. The NA61/SHINE detector is presented in Chapter 3 along with a summary of the tracking and detector simulation. The Chapter after that, covers the construction, calibration and achieved performances of the ToF-F detector. I then give a detailed description of the analysis that lead to the first charged pion and K^+ cross-section measurements in proton-carbon interactions at 31 GeV/c. Charged pions generate most of the low energy neutrinos and positively charged kaons generate the high energy tail of the T2K neutrino beam. The latter also contribute substantially to the intrinsic ν_e background of the T2K beam. As will be demonstrated, the pion results have significantly contributed to reduce the systematic uncertainties of the first T2K ν_e appearance results. The K^+ measurements are also widely expected to benefit the forthcoming results. Knowledge of proton production is also important since protons contribute to the neutrino flux through target re-interactions. The proton spectra obtained with the same $tof\text{-}dE/dx$ method are given as an appendix.

Résumé en francais

T2K est une expérience d'oscillations de neutrinos qui utilise un faisceau intense de ν_μ produit à J-PARC au Japon. Le détecteur lointain est Super-Kamiokande, détecteur Cherenkov à eau de 50 kt situé à 295 km. Le but principal de T2K est la mesure du dernier angle de mélange inconnu à ce jour, θ_{13}, par l'observation de l'apparition de ν_e. T2K a aussi pour but d'augmenter la précision actuelle sur les valeurs de $\{\Delta m^2_{23}, \theta_{23}\}$ en étudiant la disparition de ν_μ. L'année dernière, T2K a publié un résultat indiquant une valeur de θ_{13} différente de zéro. Bien que la statistique ne soit pas encore suffisante pour pouvoir prétendre à une découverte, à ce jour il s'agit de la mesure la plus précise de θ_{13} tout en étant la première qui indique $\theta_{13} \neq 0$. T2K est également la première expérience à avoir observé un signal d'apparition de ν_e.

A T2K, le faisceau de neutrinos d'une énergie moyenne de ~600 MeV est généré par un intense faisceau de protons de 30 GeV qui interagit dans une cible de carbone de 90 cm de long produisant des pions et des kaons qui se désintègrent en neutrinos. Le faisceau de neutrino ainsi créé est pointé en direction d'un complexe de détecteurs proches, situés à 280 m de la cible, et vers le détecteur lointain Super-Kamiokande (SK) situé à 295 km et 2.5° hors-axe par rapport au faisceau de pions et kaons. Les oscillations sont étudiées en comparant le nombre d'événements mesurés à SK avec celui prédit par des simulations Monte-Carlo basées sur des calculs de flux et sur des mesures au détecteur proche. Les calculs de flux proviennent de générateurs hadroniques en général peu fiables ce qui engendre des erreurs systématiques assez conséquentes et difficiles à estimer. Afin d'augmenter la précision sur la prédiction des flux de neutrinos, nous avons directement mesuré la production de hadrons à l'énergie du faisceau de proton de T2K (30 GeV) au SPS du CERN avec le détecteur NA61/SHINE (SHINE $\equiv$ SPS Heavy Ion and Neutrino Experiment). Nous avons effectué une première prise de données d'interactions proton-carbone à 30 GeV en automne 2007, suivie de deux autres en 2009 et 2010. L'identification des particules dans NA61/SHINE repose sur des mesures de temps de vol (tof), ainsi que sur des mesures de perte d'énergie dans les TPCs (dE/dx). Le tof offre une grande précision sur les particules émises à basses energies (p$\lesssim$ 4 GeV/c) alors que la séparation par des mesures de dE/dx n'est possible qu'à des impulsions plus élevées ou en-dessous de ~1 GeV/c. En combinant le tof et le dE/dx, il est de ce fait possible d'obtenir une identification très précise sur une grande plage d'impulsion. Avant de commencer la prise de données de 2007, nous avons contruit un nouveau détecteur à temps de vol, le ToF-F, afin de permettre l'identification des particules dans l'espace de phase requis par T2K. En combinant l'information du nouveau ToF-F avec la grande acceptance et l'excellente efficacité de recontruction du détecteur, nous avons obtenu des mesures de sections efficaces très précises. Les premiers résultats de section efficaces inclusives de production de pions chargés ont été publiés début 2011. Plus récemment, en janvier 2012, nous avons également publié des sections efficaces de production de kaons positivements chargés. Comme il le sera démontré ces résultats ont été de grande importance pour T2K.

Durant ma thèse, j'ai été impliqué dans la construction du ToF-F ainsi que dans sa calibration avec les données de 2007. Ensuite, j'ai analysé ce même ensemble de données, afin d'extraire les sections efficaces de pions chargés en utilisant la méthode combinée $tof + dE/dx$

pour l'identification des particules. Afin de valider la méthode, les résultats ont été comparés avec ceux de deux autres analyses: une basée sur la mesure de hadrons négatifs sans identifciation de particules et une autre basée uniquement sur des mesures de dE/dx en-dessous de 1 GeV/c. Une année plus tard, avec la méthode $tof + dE/dx$ j'ai également extrait des sections efficaces de K^+.

Le premier chapitre de la thèse donne un aperçu sur l'oscillation des neutrinos et résume le statut des principales expériences en cours dans le domaine. L'expérience T2K est ensuite decrite avec plus de précision en mettant particulièrement en avant la nécessité pour T2K d'obtenir des données de production de hadrons. L'expérience NA61/SHINE est présentée dans le chapitre 3, suivi d'une description de la construction de la calibration et de la performance du ToF-F. Une présentation détaillée des analyses pion et kaon est ensuite exposée. Les pions chargés contribuent à la majorité du flux de neutrinos en dessous de $\sim$ 1 GeV tandis que les kaons produisent les neutrinos de plus hautes energies. Les kaons contribuent également de façon significative à la contamination intrinsèque en ν_e du faisceau, qui constitue un bruit de fond irreductible pour les mesures d'apparition. A la fin du manuscrit, l'implémentation des résultats pions de NA61/SHINE dans la simulation du faisceau de T2K est décrite. Cela permettra de comprendre l'impact des mesures NA61/SHINE sur la réduction des erreurs systématiques du premier résultat de T2K.

Acknowledgments

During the 4 years I spent at the university of Geneva I am fortunate to have met and interacted with many people, a lot of whom became close friends. First of all I am very grateful to professor Alain Blondel who gave me the opportunity to join the neutrino group. Thank you Alain for your valuable suggestions, deep knowledge of the subject and also giving me the privilege to attend a large number of conferences. Secondly it was a pleasure to have the opportunity to work with my other supervisor, Alessandro Bravar. All those long hours wrapping scintillator bars in the university lab and time spent in the CERN North Area installing the time-of-flight will certainly be good memories. Thank you for sharing with us your excellent knowledge on detector hardware; I learnt a great deal. Concerning the analysis, your guidance and insight were decisive to keep me moving forward.

It was more than a privilege to have been able to work with Nicolas Abgrall, now a very good friend. The list of thank yous would be far too long to summarize here. I appreciated your generosity, invaluable advice and fruitful discussions on general physics. Most importantly, thanks for all the memorable fun times; there will be more to come I'm sure. Meanwhile I wish you all the best for your post-doc at LBNL.

It was also a pleasure to have worked with Claudia Strabel. We had a lot of great moments; it was very good to have known you.

In addition I am grateful to all the members of the NA61/SHINE collaboration who were responsible for the various data productions and detector calibrations. None of the work presented in this thesis would have been possible without their dedicated efforts.

I would like to express my gratitude to Marek Gazdzicki, Alberto Marchionni, Boris Popov and Peter Seyboth for their suggestions on how to improve my analysis and also valuable help during the publication of both papers. A special thanks is dedicated to Boris for being patient at the beginning and helping with debugging the simulation software and answering to my daily emails.

I am fortunate to have been able to work with my colleagues at University of Geneva many of which are now good friends. Thank you for making the office a pleasant and inspiring place to work. I would also like to express my recognition to the efforts made by the university technicians, especially Eric Perrin the chief mechanic engineer and Pierre Bennet who assembled the electric circuits for the photomultipliers.

Finally I am immensely grateful to my family, friends and especially my wife Aude. Your love and support will always be remembered, they are the foundations of all I have achieved.

Contents

Chapter 1

Introduction

1.1 Historical background

In 1924 Chadwick firmly established that the beta decay spectrum is continuous [1] which was an apparent contradiction to the law of conservation of energy if the process were a two body decay. This led researchers, such as Niels Bohr [2], to challenge beliefs of both energy and angular momentum conservation. To save the principle, Wolfgang Pauli in December 1930 wrote a famous letter [3] postulating that an extremely light particle with no electric charge, which he named the neutron, was also emitted in the decay process. This particle has spin 1/2 and "should be no larger than 0.01 proton mass". Enrico Fermi changed the name to neutrino in 1931, since another heavy neutral particle called neutron had been discovered shortly after Pauli's letter.

With the advent of fission reactors, physicists got new means of producing vast quantities of neutrinos in a controlled environment. In 1945 Bruno Pontecorvo proposed a method to detect free neutrinos [4] from reactors using the inverse β^- process: $\bar{\nu}_e + p \rightarrow e^+ + n$. According to the process, an electron anti-neutrino hitting a ^{37}Cl atom (which is present e.g in cleaning fluid C_2Cl_4) will transform it into ^{37}Ar, which can be stored and then detected through radioactive decay.

Based on Pontecorvo's idea, Clyde Cowan and Frederic Reines published in 1956 [5] the first evidence of the existence of neutrinos by detection of inverse beta decay at the Savannah river nuclear power plant. Reines was awarded the Nobel Prize in 1995 for their discovery, unfortunately by that time Cowan had passed away. The helicity of the neutrino was measured soon after in 1958 by M. Goldhaber [6]. The observations were consistent with the observation of a single helicity state: all neutrinos are left-handed and all anti-neutrinos are right-handed.

The second neutrino, the muon neutrino ν_μ, was detected in 1962 [7], at Brokhaven using neutrinos produced at an accelerator. The experiment showed that a neutrino from a pion decay was always accompanied by a muon and that hence it couldn't be a ν_e. The τ lepton was indirectly discovered by a series of experiments at SLAC, USA, between 1974 and 1977 [8], which suggested the existence of tau neutrinos ν_τ. It was however only in 2000 that the ν_τ was directly observed in the DONUT experiment at Fermilab [9]. A few years earlier LEP at CERN had concluded from the measurement of the Z boson decay width that the number of active neutrinos must be three (see [10]). Additional neutrino eigenstates could in principle exist but they do not have a charged-lepton partner, and consequently, would not couple to the W boson.

They would neither couple to the Z boson since it decays into only three distinct neutrinos. Such hypothetical neutrinos, which do not have any Standard Model weak couplings, are referred to as sterile neutrinos. To this day there is no proof of the existence of sterile neutrinos.

The year the ν_μ was discovered, Maki, Nakagawa and Sakata [11] introduced two crucial ideas: neutrino flavors can mix, and their mixing can cause one type of neutrino to oscillate into the other (called today flavor oscillation). This mixing may occur only if some of the neutrinos are massive. Pontecorvo had previously suggested in 1957 [12] that a neutrino may oscillate into its antiparticle in vacuum if lepton number is not conserved, just like $K^0 - \bar{K}^0$ oscillation proposed by Gell-Mann and Pais in 1955 [13].

In 1964, Davis and his collaborators proposed to measure the neutrino flux arising from nuclear fusion in the sun by using a 400'000 liter tank of cleaning fluid buried deep underground in the Homestake mine in South Dakota. The ν_e's were detected by the radiochemical process proposed by Pontecorvo. Since the first report in 1968 [14], they have reported fluxes significantly smaller than predicted by the standard solar model, a result that stands to this day as a truly remarkable experimental achievement. This apparent discrepancy will be known as the solar neutrino problem. Gribov and Pontecorvo [15] immediately interpreted the deficit as evidence for neutrino oscillations, however, until recent years, all efforts using neutrino beams to experimentally detect neutrino oscillation gave null results.

The conclusive evidence for the presence of neutrino oscillation came from a different direction. In the early 1980's huge underground Cherenkov detectors such as Kamiokande in Japan, were built to discover proton decay, which is a unique signature of Grand Unified Theories of strong and electromagnetic interactions. No proton decay was ever discovered, what was found however was a large deficit of ν_μ compared to ν_e flux for neutrinos produced by cosmic rays interacting in Earth's atmosphere. Finally, Super Kamiokande (the enlarged facility of Kamiokande by 15 times in mass) in 1998 conclusively showed results which are consistent with $\nu_\mu \rightarrow \nu_\tau$ oscillation with a mass difference of about 0.05 eV^2 [16].

The neutrino oscillation hypothesis was finally confirmed at the Sudbury Neutrino Observatory (SNO) in Canada in 2001. Through measurements of neutrino-deuterium scattering, it confirmed the ν_e deficit which Davis had observed 30 years earlier but also showed that the neutrino flux combining all flavors is in excellent agreement with the standard solar model predictions [17].

1.2 Neutrino mass

Dirac neutrinos

In the Standard Model (SM), the mass of fermions is the strength of their Yukawa coupling to the Higgs field:

$$\mathcal{L}_{Yukawa} = \sum_{\alpha,\beta=1}^{3} \bar{u}_L^\alpha m_{\alpha\beta} u_R^\beta + \bar{d}_L^\alpha m_{\alpha\beta} d_R^\beta + \bar{l}_L^\alpha m_{\alpha\beta} l_R^\beta + \text{h.c} \tag{1.1}$$

α, β label the three generations and l, u, d denote the charged lepton, up and down-type quark fields respectively. The L and R subscripts denote the left and right chirality of the fields. The fields present in this expression are those which take part in the weak interaction and are called flavor states. The mass matrices $m_{\alpha\beta}$ are not necessarily diagonal and do not define the physical masses of the fields. It is obvious from Equation 1.1 that the mass of a fermion requires a right handed (RH) and a left handed (LH) component of the field. Neutrinos do not appear in the Lagrangian because they were thought to be massless and thus no RH neutrino field was added in the SM. To define neutrino mass the most straightforward way is then to extend the theory by including a RH neutrino field. The neutrino would hence acquire its mass just like the other fermions and the Yukawa Lagrangian picks up en extra term:

$$\mathcal{L}_{mass} = \bar{\nu}_L^{\alpha} m_{\alpha\beta} \nu_R^{\beta} + \mathrm{h.c} \tag{1.2}$$

where ν denotes the neutrino field and $\alpha, \beta = e, \mu, \tau$ are the three neutrino flavors which couple to the charged lepton flavors in the weak interaction. To define the physical masses of the neutrinos, the mass matrix must be diagonalized. This is done by choosing two unitary matrices $U_{L,R}$ such that:

$$m' = U_L^{\dagger} \cdot m \cdot U_R \tag{1.3}$$

which is equivalent to re-defining the fields as:

$$\begin{aligned} \nu_R'^{i} &= U_R^{\beta i} \nu_R^{\beta} \\ \nu_L'^{i} &= U_L^{\alpha i} \nu_L^{\alpha} \end{aligned} \tag{1.4}$$

for the left and right handed components. The physical masses of the quark fields are of course defined in exactly the same way with two different matrices $V_{L,R}$:

$$\begin{aligned} u_R'^{i} &= V_R^{\beta i} d_R^{\beta} \\ u_L'^{i} &= V_L^{\alpha i} d_L^{\alpha} \end{aligned} \tag{1.5}$$

These matrices are necessarily unitary and it is therefore equally correct to say that the flavor eigenstates are superpositions of the mass eigenstates and vice-versa. With the definition of Equation 1.4, the Lagrangian for neutrino mass can be re-formulated as:

$$\mathcal{L}_{mass} = \bar{\nu}_L'^{i} m'^{i} \nu_R'^{i} + \mathrm{h.c} \tag{1.6}$$

the primed fields are now called mass eigenstates. The mass eigenstates are those which propagate through space and time and the flavor states participate in the gauge interaction. In particular, the coupling of the charged vector current j_c^{μ}, to the $W\pm$ bosons is given by:

$$j_c^{\mu} = \sum_{\alpha} W_{\mu}^{+} \bar{\nu}_L^{\alpha} \gamma^{\mu} l_L^{\alpha} + W_{\mu}^{+} \bar{u}_L^{\alpha} \gamma^{\mu} d_L^{\alpha} + \mathrm{h.c} \tag{1.7}$$

Once the fields are decomposed in the mass basis according to Equations 1.4 and 1.5, the interaction Lagrangian now includes terms of the form:

$$\sum_{i,j} W_{\mu}^{-} \bar{u}_L^{j} \gamma^{\mu} (V_{u_L}^{\dagger} V_{d_L})^{ji} d^{i} \equiv \sum_{\alpha,i} W_{\mu}^{-} \bar{u}_L^{\alpha} \gamma^{\mu} V^{\alpha i} d_L^{i} \tag{1.8}$$

for the quark fields, and:

$$\sum_{i,j} W_\mu^+ \bar{\nu}_L^j \gamma^\mu (U_{\nu_L}^\dagger U_{l_L})^{ji} l^i \equiv \sum_{\alpha,i} W_\mu^- \bar{\nu}_L^\alpha \gamma^\mu U^{\alpha i} l_L^i \tag{1.9}$$

for the lepton fields. We have just re-written the charged current interaction in term of mass eigenstates with the newly defined V and U matrices which link the flavor eigenstates to the mass eigenstates. V and U are called the CKM (Cabibbo-Kobayashi-Maskawa [18]) and PMNS (Pontecorvo-Maki-Nakagawa-Sakata) matrices respectively; they are also referred to as the quark and neutrino mixing matrices. Their presence modifies the charged current in such a way that it now couples up-type quarks and charged leptons to down-type quarks and neutrino mass eigenstates of different families. By convention, the CKM (PMNS) matrix places all the mixing in the down-type quarks (neutrinos), which means that the weak eigenstates for the up-type quarks (charged leptons) are the same as their mass eigenstates. By definition the weak interaction only couples left handed fields, but there is no fundamental reasons for RH neutrinos not to exist. Since Goldhaber's measurements were consistent with a single left-handed helicity state, and since the mass of the neutrino was consistent with zero at that time, only the left-handed neutrino field was necessary to describe the neutrino. The right-handed field ν_R was simply not included in the SM. If they were to exist, RH neutrinos would never be detected since neutrinos only interact through the weak interaction. They are therefore called sterile neutrinos.

Majorana case

In 1937 Ettore Majorana [19] proposed that the neutrino is a self conjugate, except for helicity. The helicity flip is caused by a mass term that violates the lepton number conservation. If $\mathcal{C}$ is the charge conjugation operator and ν^c the charged conjugate of a neutrino field ν defined as (in what follows the case of a single neutrino is considered and flavors are omitted):

$$\nu^c = \mathcal{C}^\dagger \nu \mathcal{C} = \mathcal{C}\bar{\nu}^T \tag{1.10}$$

The Majorana condition is:

$$\nu^c = \nu \tag{1.11}$$

Consequently a Majorana spinor only contains two independent fields and does not distinguish particles from antiparticle. In other words the neutrino is its own antiparticle. Assuming neutrinos are described by a Majorana spinor, one can generate $\bar{\nu}^c\nu$ or $\bar{\nu}\nu^c$ terms in the Lagrangian which are Lorentz scalar and just as viable as the Dirac terms $\bar{\nu}\nu$. By using different combinations of particles and charge conjugate antiparticle state, we can construct the LH Majorana mass term:

$$\mathcal{L}_{ML} = M_L\,(\bar{\nu}_L^c \nu_L + \bar{\nu}_L \nu_L^c) \tag{1.12}$$

and RH Majorana mass terms:

$$\mathcal{L}_{MR} = M_R\,(\bar{\nu}_R^c \nu_R + \bar{\nu}_R \nu_R^c) \tag{1.13}$$

Those can be added to the Dirac mass terms defined in the previous paragraph:

$$m_D(\bar{\nu}_R\nu_L + \bar{\nu}_L\nu_R)$$

To obtain a general mass term:

$$\begin{aligned}\mathcal{L}_{MD} &= m_D\,(\bar{\nu}_R\nu_L + \bar{\nu}_L\nu_R) + M_L\,(\bar{\nu}^c_L\nu_L + \bar{\nu}_L\nu^c_L) + M_R\,(\bar{\nu}^c_R\nu_R + \bar{\nu}_R\nu^c_R) &(1.14)\\ &= (\bar{\nu}^c_L\bar{\nu}_R)\begin{pmatrix} M_L & m_D \\ m_D & M_R\end{pmatrix}\begin{pmatrix}\nu_L \\ \bar{\nu}^c_R\end{pmatrix} &(1.15)\end{aligned}$$

These fields all satisfy the Majorana condition 1.11, so a Lagrangian containing both Dirac and Majorana mass terms infers that all neutrinos are Majorana neutrinos. Similarly to the Dirac case, to transform the flavor eigenstates to the corresponding mass eigenstates this matrix can be diagonalized using unitary operators. The corresponding eigenvalues m_1 and m_2 on its diagonal are [20]:

$$m_{1,2} = \frac{M_L + M_R}{2} \pm \frac{1}{2}\sqrt{(M_R + M_L)^2 + 4m_D^2} \tag{1.16}$$

in the limiting case where M_L=0 and $M_R >> m_D$ the eigenvalues become:

$$m_1 \simeq -\frac{m_D^2}{M_R} \quad \text{and} \quad m2 \simeq M_R \tag{1.17}$$

Since m_D is generated from the Yukawa coupling to the Higgs field, it is expected to be of the order of the charged fermion masses and if the Majorana mass M_R is taken to be large enough, m_1 acquires a mass which is much lower than the other fermions and m_2 a mass which would be many orders of magnitude higher. This model is called the Seesaw mechanism [21] and is very attractive since it provides a natural explanation for the observed light neutrino masses[1] compared to the charged fermions. If one assumes that the Dirac mass m_D is similar to the mass of the top quark, and the mass of the light neutrino m_1 to be approximately 10^{-2} eV, then Equation 1.17 gives a mass for the right handed neutrino of about 10^{15} GeV, which is very close to where the GUT scale is expected to reside. But this mechanism requires the neutrinos to be Majorana particles which at this time we do not know. Evidence for a Majorana neutrino may come from experiments searching for neutrinoless double beta decay such as GERDA [24], EXO [25] or NEMO [26].

1.3 Neutrino oscillation

The basis of neutrino mass eigenstates being different from that of the flavor eigenstates, as defined in Equation 1.4, allows a phenomenon called neutrino oscillation to be observed.

---

[1] The absolute mass of the neutrino is not known. The most stringent upper bounds on the neutrino mass obtained in the Troitzk and Mainz experiments [22] is $m_\nu < 2.2$ eV. KATRIN [23] aims to determine m_ν to the 0.2 eV level.

1.3.1 Two neutrino oscillation in the plane wave approximation

We first consider an example of oscillation with two families of neutrinos ν_e and ν_μ. This assumption is commonly made as it is much simpler and all the principle points can be studied. As we will see later it turns out that this two-flavor scheme offers anyhow a very accurate approximation to the three-flavor oscillations.

The two flavor eigenstates, ν_e and ν_μ are linear superpositions of the two mass eigenstates ν_1 and ν_2 :

$$\begin{pmatrix} |\nu_e\rangle \\ |\nu_\mu\rangle \end{pmatrix} = U \begin{pmatrix} |\nu_1\rangle \\ |\nu_2\rangle \end{pmatrix} \tag{1.18}$$

U is a 2 dimensional rotation matrix between both basis:

$$U = \begin{pmatrix} \cos\theta & \sin\theta \\ -\sin\theta & \cos\theta \end{pmatrix} \tag{1.19}$$

Let's consider an electron neutrino which has just been created through a charged current interaction of an electron on a proton:

$$e^- + p \rightarrow n + \nu_e$$

This newly created electron neutrino state $|\nu_e\rangle$ will propagate as:

$$\Psi(x,t) = e^{-i(\mathcal{H}t - Px)}|\nu_e\rangle \tag{1.20}$$

Where $\mathcal{H}$ is the Hamiltonian and P the momentum operator. In the basis of propagation (i.e the mass eigenstate basis) they are both diagonal:

$$\Psi(x,t) = e^{-i(E_1 t - p_1 x)} \cos\theta \ |\nu_1\ \rangle + e^{-i(E_2 t - p_2 x)} \sin\theta \ |\nu_2\ \rangle$$

The electron neutrino propagates as a linear combination of mass eigenstates. If we want to make an observation after a propagation time t the wave function must be projected on the flavor basis. Say we want to compute the probability to observe a muon neutrino:

$$\begin{aligned} P(\nu_e \rightarrow \nu_\mu) &= |\langle \nu_\mu | \Psi(x,t) \rangle|^2 \\ &= \left| \Big\langle -\sin\theta\ \nu_1\ + \cos\theta\ \nu_2 \Big| (e^{-i(E_1 t - p_1 x)} \cos\theta\ \nu_1\ + e^{-i(E_2 t - p_2 x)} \sin\theta\ \nu_2\ ) \Big\rangle \right|^2 \\ &= 4\sin^2\theta\ \cos^2\theta\ \sin^2 \frac{(E_1 t - p_1 x) - (E_2 t - p_2 x)}{2} \\ &= \sin^2(2\theta)\sin^2\frac{\phi_1 - \phi_2}{2} \end{aligned} \tag{1.21}$$

Which is the most general equation for two flavor neutrino oscillation. It is expressed as a difference in phase factors $\phi_i = E_i t - p_i x$. The phase factors depend on the energy, the time of flight t and the momentum of each mass eigenstate.

This formula can be simplified if we make the approximation that the two propagating states are described by one plane wave with one common propagation time t and one same energy or same momentum. [27, 28] show that the equal energy scenario is a very good approximation. The main argument in the latter being that, within the detector resolution, the energies must be identical for interferences to be observed. With the hypothesis that $E_i = E$ the momenta of both mass eigenstates become:

$$p_i = \sqrt{E^2 - m_i^2} \qquad i = 1, 2 \tag{1.22}$$

The energy of neutrinos we observe are always orders of magnitude higher than the upper bound on the heaviest neutrino mass. Therefore we can make the approximation that neutrinos we observe are always ultra relativistic: $x = ct \equiv L$, and since $m_i \ll E$:

$$\sqrt{E^2 - m_i^2} \simeq E - m_i^2/2E \qquad i = 1, 2 \tag{1.23}$$

With the above assumptions, the phase factors can be simplified:

$$\begin{aligned} \phi_i &= Et - (E - \frac{m_i^2}{2E})x \\ &= E(t - x) + \frac{m_i^2}{2E}x \\ &= \frac{m_i^2}{2E}L \end{aligned} \tag{1.24}$$

And the oscillation probability from Equation 1.21 can now be expressed as a difference in mass squared:

$$P(\nu_e \to \nu_\mu) = \sin^2(2\theta) \sin^2 \frac{\Delta m^2 L}{4E} \tag{1.25}$$

with $\Delta m^2 = m_1^2 - m_2^2$ and E the common energy to all mass eigenstates. The neutrino thus changes it's flavor as it propagates with the period

$$L_{osc} = \frac{4\pi E}{\Delta m^2} \tag{1.26}$$

and with an amplitude given by the mixing angle $\sin^2(2\theta)$.

1.3.2 Discussion on the plane wave approach

There is a lot of discussions whether the plane wave approximation is an accurate description and therefore if one can really state that all the mass eigenstates have one common energy and one average group velocity (see for example [29, 30]). Also, when making the plane wave approximation we lose a lot of interesting information on the conditions required to observe neutrino oscillations. The correct way to treat the oscillation is to consider each state as a wave packet having a definite momentum and energy with their corresponding quantum-mechanical uncertainty. Neutrino oscillation is observed because we detect a coherent superposition of the wave packets. If the detector's resolution were better than the uncertainty on the wave packet's position and momentum each mass eigenstate would be detected and no oscillation pattern would be observed.

The plane wave approach is also valid if the wave packets preserve their coherence over distances which are large with respect to the calculated oscillation length (Equation 1.26). Indeed, the different neutrino mass states will move apart as they travel due to their differing velocities and will cease to be coherent after a certain distance.

However, as long as we don't measure the momentum with infinite precision (i.e of the order of the quantum-mechanical uncertainty) and the coherence length of our wave packets is larger than the oscillation length, the experimental results are correctly predicted by the plane wave approximation. This is the case in most neutrino oscillation experiments and especially in T2K.

1.3.3 Do charged leptons oscillate?

A follow up to this discussion would be that of charged lepton oscillation. The charged current weak interactions are completely symmetric with respect to neutrinos and charged leptons and therefore charged leptons could also be emitted as superpositions of mass states. In such a case we could in theory observe charged lepton oscillation. The reason that we don't resides in the coherence properties of the produced charged lepton wave packet (see discussion in [31, 32]). The oscillation length is indeed inversely proportional to mass squared splittings of each state. For neutrinos the largest mass squared splitting is of the order of 10^{-3} eV^2 whereas for charged letpons even the smallest (between an electron and muon) is around 10^{15} eV^2. With such a large Δm^2, the oscillation length for leptons with a few GeV energy is about 10^{-13} cm.

In conclusion, we do not observe charged lepton oscillation because of their large differences in masses. This is also why quark flavor mixing cannot be observed directly; quarks are bound into mesons from which mass eigenstates are clearly identified. Neutrino oscillation is hence a quantum mechanical consequence of, not only of the existence of nonzero masses, but also of their very small mass splittings.

1.3.4 Three family mixing

As already stated in Section 1.2, the three neutrino mass eigenstates $i = 1, 2, 3$ are related to their flavor eigenstates, $\alpha = e, \mu, \tau$, by the PMNS matrix U:

$$|\nu_\alpha\rangle = \sum_{i=1}^{3} U_{\alpha i} |\nu_i\rangle \tag{1.27}$$

which is now parametrised by three Euler angles. Unlike the two neutrino case, one non vanishing complex phase δ appears also in the parametrization. As in the quark mixing matrix this single complex phase would explain $\mathcal{CP}$ violation in the lepton sector since then $U^* \neq U$ meaning that neutrinos and antineutrinos would have different oscillation probabilities. $\mathcal{CP}$ violation was established in the quark sector in 1964 when Cronin and Fitch showed that the K_L^0 mass eigenstate of the neutral kaon occasionally decayed into only two and not three pions, as would be expected if $\mathcal{CP}$ was conserved [33]. In the weak interaction it was established in 1957 that Parity, $\mathcal{P}$, was violated [34]. While the weak interactions which mediate the decay process violates $\mathcal{C}$ and $\mathcal{P}$ individually, $\mathcal{CP}$ should still be conserved if the weak eigenstates were identical to the mass eigenstates. Since the observation of neutrino oscillation we know this is not the case, and hence a non zero δ, which will be called δ_{CP} from now on, could in principle exist and be responsible for leptonic $\mathcal{CP}$ violation. In the quark sector the observation of $\mathcal{CP}$ violation was proof that the quark interaction and mass eigenstates were different, which further helped understand mixing in the lepton sector.

If the massive neutrinos are Majorana fermions, the neutrino mixing matrix U must be multiplied by another matrix A containing an extra 2 $\mathcal{CP}$ violating phases defined as [35]:

$$A = diag\left(1, e^{i\alpha_1/2}, e^{i\alpha_2/2}\right) \tag{1.28}$$

which is trivial if neutrinos are dirac particle. Since the phases are situated on the diagonal, they do not induce any $\mathcal{CP}$ violation during neutrino oscillation. A is therefore omitted for the following.

U can be written as a product of three rotations, each of which is described by one of the Euler angles:

$$\begin{aligned} U &= \begin{pmatrix} 1 & 0 & 0 \\ 0 & c_{23} & s_{23} \\ 0 & -s_{23} & c_{23} \end{pmatrix} \begin{pmatrix} c_{13} & 0 & s_{23}e^{i\delta} \\ 0 & 1 & 0 \\ -s_{13}e^{i\delta} & 0 & c_{13} \end{pmatrix} \begin{pmatrix} c_{12} & s_{12} & 0 \\ -s_{12} & c_{12} & 0 \\ 0 & -0 & 1 \end{pmatrix} \\ &= \begin{pmatrix} c_{12}c_{13} & s_{12}c_{13} & s_{13}e^{i\delta_{CP}} \\ -s_{12}c_{23} - c_{12}s_{23}s_{13}e^{i\delta_{CP}} & c_{12}c_{23} - s_{12}s_{23}s_{13}e^{i\delta} & s_{23}c_{13} \\ s_{12}s_{23} - c_{12}c_{23}s_{13}e^{i\delta_{CP}} & -c_{12}s_{23} - s_{12}c_{23}s_{13}e^{i\delta} & c_{23}c_{13} \end{pmatrix} \\ &\equiv \begin{pmatrix} U_{e1} & U_{e2} & U_{e3} \\ U_{\mu 1} & U_{\mu 2} & U_{\mu 3} \\ U_{\tau 1} & U_{\tau 2} & U_{\tau 3} \end{pmatrix} \end{aligned} \tag{1.29}$$

with $c_{ij} = \cos\theta_{ij}$ and $s_{ij} = \sin\theta_{ij}$. θ_{ij} correspond to the three Euler angles and are called the neutrino mixing angles. δ_{CP} can be freely multiplied to any of the mixing angles without changing the physical properties of U but it is usually associated with θ_{13} since, until recently, it was the only unknown angle and could have been equal to zero. As we will see when computing the oscillation probabilities the observation of δ_{CP} indeed requires all three angles to be nonzero.

As in the two neutrino case, one can calculate the transition probability in a vacuum between a state $|\nu_\alpha\rangle$ and $|\nu_\beta\rangle$ in the plane wave approximation:

$$P(\nu_\alpha \to \nu_\beta) = \left| \sum_j U^*_{\alpha j} e^{-im_j^2 L/2E} U_{\beta j} \right|^2 \tag{1.30}$$

which is the square of the sum of the amplitudes for the α flavor neutrino to produce a m_j mass state times a propagation factor, times the amplitude for m_j to be associated with a state of flavor β. The transition for which α and β are different is called the appearance probability since we search for the "appearance” of a neutrino with flavor β in an initial sample of ν_α. On the contrary the transition with α and β identical is called disappearance probability. To make the term in Δm^2_{ij} appear one can further expand the relation:

$$P(\nu_\alpha \to \nu_\beta) = \delta_{\alpha\beta} - 4\sum_{i>j}\mathbb{R}(\mathcal{J}_{\alpha\beta ij})\sin^2\frac{\Delta m^2_{ij}L}{4E} + 2\sum_{i>j}\mathbb{I}(\mathcal{J}_{\alpha\beta ij})\sin\frac{\Delta m^2_{ij}L}{4E} \tag{1.31}$$

Where $\mathcal{J}_{\alpha\beta ij} = U^*_{\alpha i}U_{\beta i}U_{\alpha j}U^*_{\beta j}$ are called the Jarlskog terms.

As in the two neutrino oscillation scenario, the transition probabilities depend on the parameter L/E, the mass squared differences Δm^2_{ij} and the mixing angles θ_{ij}. In the three neutrino case there are two independent mass differences, three mixing angles $(\theta_{12}, \theta_{23}, \theta_{13})$ and the extra complex phase δ_{CP}. If we are dealing with anti-neutrinos, the terms of the matrix must be replaced by their complex conjugate. As a consequence, if U is not real ($\delta_{CP} \neq 0$), the neutrino and anti-neutrino oscillation probability differ by having opposite values of the imaginary term. The observation of:

$$P(\nu_\alpha \to \nu_\beta) \neq P(\bar{\nu}_\alpha \to \bar{\nu}_\beta)$$

indicates a non zero δ_{CP} term and hence violation of $\mathcal{CP}$ invariance.

However the transitions are always expected to be conserved under $\mathcal{CPT}$ (where $\mathcal{T}$ is the time reversal operator):

$$P(\nu_\alpha \to \nu_\beta) = P(\bar{\nu}_\beta \to \bar{\nu}_\alpha)$$

1.4 Neutrino cross-sections in the few GeV region

In the Standard Model of the electroweak theory, neutrino interactions can occur both via neutral (NC) and charged (CC) current interaction:

$$\begin{aligned} \text{CC}: &\quad \nu_l + N \to l + X \\ \text{NC}: &\quad \nu_l + N \to \nu_l + X \end{aligned} \tag{1.32}$$

where l denotes the leptonic flavor, N the nucleon, and X stands for the hadronic final state.

Figure 1.1 summarizes our current knowledge on the charged current neutrino-nucleon cross-sections in the few GeV region. For interactions occurring above ~2 GeV, the nucleon is generally broken up and the final hadronic state is composed of many hadrons. This process is called deep inelastic scattering (DIS).

Around the peak energy of the T2K neutrino beam (~ 600 MeV) the dominant interaction is the quasi elastic (QE) process, where the hadronic final state consists in a single nucleon. The QE interactions apply to both NC and CC modes:

$$\begin{aligned} \text{CCQE:} &\quad \nu_l + n \to l + p \\ \text{NCQE:} &\quad \nu_l + n(p) \to \nu_l + n(p) \end{aligned} \tag{1.33}$$

The hit nucleon might be excited into a resonant state. Around 1 GeV, there is a large contribution from the lightest baryonic $\Delta(1232)$ resonance which produces a single pion in the final state:

$$\begin{aligned} \mathrm{CC}\pi^+: &\quad \nu_l + p(n) \rightarrow l + n(p) + \pi^+ \\ \mathrm{NC}\pi^0: &\quad \nu + N \rightarrow \nu + N + \pi^0 + X \end{aligned} \tag{1.34}$$

The neutral current π^0 ($\mathrm{NC}\pi^0$) channel is one of the main background for the T2K ν_e appearance analysis as the decay of the π^0in two electrons may mimic an electron neutrino interacting in the far detector.

As seen in Figure 1.1 our knowledge of neutrino cross-sections in this region suffers from large uncertainties mainly because most of the measurements originate from bubble chamber, spark chamber, and emulsion experiments that collected their data decades ago [36]. Such measurements are generally limited by poor statistics and large neutrino flux uncertainties. One of the goals of the T2K near detector is also to increase the precision on these cross-sections.

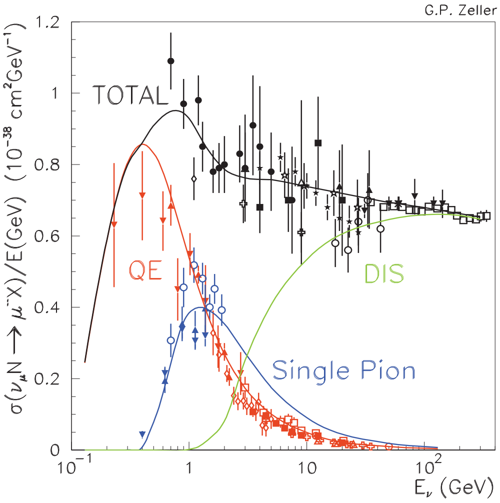

Figure 1.1: Charged current neutrino cross sections divided by energy as a function of neutrino energy. The low energy region is dominated by the quasi-elastic (QE) contribution, the high energy region by the deep inelastic (DIS) contribution. The intermediate range is dominated by the $\mathrm{NC}\pi^0$processes. The cross sections are shown from a variety of collected data [36] along with the prediction from the NUANCE event generator [37]. The figure is from [38].

1.5 Neutrino oscillation in matter

1.5.1 Variable density

When neutrinos travel through matter (e.g in the Sun, Earth, or a supernova), the coherent forward scattering from electrons they encounter along the way can significantly modify their propagation. The different type of neutrinos encounter different potentials: the electron neutrino interacts with electrons via both the neutral and charged currents, whereas ν_μ and ν_τ interact with electrons only via the neutral current. Due to the charged-current interactions, the ν_e

acquires an extra potential energy, V_W, which is defined as [39]:

$$V_W = \pm\sqrt{2}\mathrm{G}_F\mathrm{N}_e$$

where N_e is the local electron density and G_F the Fermi constant. The + sign is for neutrinos and the - sign for anti-neutrinos. This extra term is added to the Hamiltonian $\mathcal{H}$ in the flavor basis for the $\langle\nu_e|\mathcal{H}|\nu_e\rangle$ element of the matrix and as a result, the probability for changing flavors in matter can be rather different than in vacuum. In the two flavor approximation the amplitude and frequency of the oscillation are then governed by a mixing angle θ_M and mass splitting ΔM^2 defined as [40]:

$$\Delta M^2 = \Delta m^2\sqrt{(A-\cos 2\theta)^2+\sin^2 2\theta} \tag{1.35}$$

$$\sin 2\theta_M = \frac{\sin 2\theta}{(A-\cos 2\theta)^2+\sin^2 2\theta} \tag{1.36}$$

with $A = \frac{V_W/2}{\Delta m^2/4E}$. The oscillation probability will significantly differ whether the sign of A agrees or disagrees with the sign of $\cos 2\theta$. This is depicted in Figure 1.2 where the $P_{\nu_e\to\nu_\mu}$ is plotted as a function of L in vacuum and in matter. It is clear that when the two signs agree (disagree) we have $\sin^2 2\theta_M > (<) \sin 2^2\theta$ which means that there is an enhancement (suppression) of the transition amplitude. Optimal enhancement can be obtained when $A = \cos 2\theta$, the so-called resonant condition, in which case $\sin^2 2\theta_M = 1$.

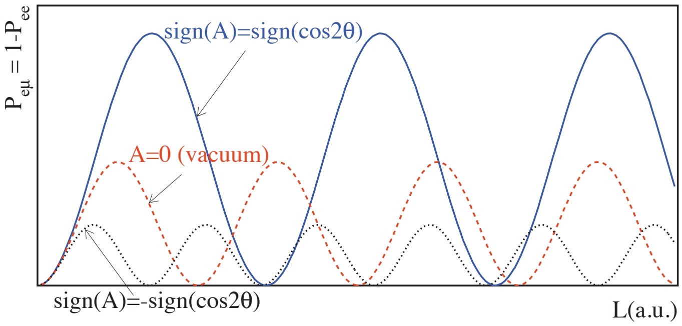

Figure 1.2: $P_{\nu_e\to\nu_\mu}$ as a function of L for fixed values of E, Δm^2, V_W and $\sin^2 2\theta$ in vacuum and in matter, assuming sign(A)=sign($\cos 2\theta$) and sign(A) = -sign($\cos 2\theta$). The figure is from [40].

Since V_W changes sign for antiparticles, one may resolve the sign of Δm^2 by comparing measurements of e.g. $P_{\nu_\mu\to\nu_e}$ with $P_{\bar{\nu}_\mu\to\bar{\nu}_e}$. In other words experimental measurements in which matter effects play a role are sensitive to the sign of Δm^2. Neutrino oscillations in vacuum cannot address this issue. These differences in oscillation probability between neutrino and anti-neutrinos must however not be misinterpreted for a $\mathcal{CP}$ violating signal. As will be mentioned in Section 1.8, the two effects may be untangled by comparing similar experiments with different L/E.

1.5.2 Constant density and MSW effect

If neutrinos are created in a very dense medium and the density drops slowly enough, a propagation eigenstate will remain constant as the neutrino travels, i.e there will be no transition to another mass eigenstate. This is called the adiabatic condition. ν_e's above a few MeV produced in a very dense medium like the sun propagate as pure ν_2 state. For such neutrinos the adiabatic condition is satisfied and the electron neutrino is still in the ν_2 propagation eigenstates as it exits the sun. It will hence travel to the detector without oscillating and the probability to still detect a ν_e on earth will be $P_{\nu_e \rightarrow \nu_e} = |\langle \nu_e | \nu_2 \rangle|^2 = \sin^2 2\theta$. This probability is much lower than the one expected from the probability in a vacuum which would be $1 - (\sin^2 2\theta)/2$. This phenomenon is known as Mikheyev-Smirnov-Wolfenstein (MSW)[41] effect and explains the large deficit of high energy solar electron neutrinos reaching the earth [39, 42]. For low energy solar neutrinos, atmospheric neutrinos and typical baselines of reactor and accelerator neutrinos such as T2K, matter effects are to a large extent negligible. They will play a role for longer baselines (few thousands of km) which are planned for the next generation of neutrino oscillation experiments (see Section 1.8).

1.6 Oscillation probablities in neutrino experiments

The neutrino oscillation experiments which will be described are those aiming at measuring the parameters of the PMNS matrix, namely the mixing angles and the δ_{CP} phase. They also measure the mass squared splittings which govern the frequency of the oscillation. Neutrinos are abundant in nature and come from various sources, the largest neutrino flux we get on earth come from solar or atmospheric neutrinos. The former are electron neutrinos arising from the sun and the latter mainly muon neutrinos created from cascades originating from collisions of cosmic rays with the earth's atmosphere. There also exist two sources of "artificial" neutrinos which have significantly contributed to the measurements: those coming from nuclear power plants (reactor neutrinos) and specifically designed neutrino beams created in accelerator complexes (accelerator neutrinos). In order to gain a full understanding of the whole PMNS matrix different oscillation channels must be explored by various experiments.

1.6.1 Current knowledge of the mixing angles

A 3 neutrino analysis [43] which includes all the data along with the recent T2K and MINOS[2] results on θ_{13} give the current best fit values on the mixing angles:

$$\sin^2 \theta_{12} = 0.306\ (0.265 - 0.364) \tag{1.37}$$

$$\sin^2 \theta_{23} = 0.42\ (0.34 - 0.64) \tag{1.38}$$

$$\sin^2 \theta_{13} = 0.021\ (0.005 - 0.050) \tag{1.39}$$

where the values in parentheses indicate the allowed 3σ range. Note that depending on the experiments the results are also sometimes quoted as $\sin^2(2\theta)$ or as $\tan^2 \theta$. Two of the mixing angles are large ($\theta_{12} \approx 33°$ and $\theta_{23} \approx 45°$), whereas θ_{13} is constrained to be about an order of

---

[2] details of the T2K and MINOS long baseline experiments are given in Section 1.7.1

magnitude smaller. Before 2011 the only available data on θ_{13} were upper bounds which allowed the possibility that $\theta_{13}=0$. Only recently has there been compelling evidence from T2K [44] and MINOS [45] that it is different from 0.

1.6.2 Atmospheric and solar mass splittings

The latest values for the mass squared splittings including all available data [43] are:

$$|\Delta m^2_{21}| = 7.58\ (6.99 - 8.18) \times 10^{-5}\text{eV}^2 \tag{1.40}$$

$$|\Delta m^2_{31}| = 2.35\ (2.06 - 2.67) \times 10^{-3}\text{eV}^2 \tag{1.41}$$

where again the values in parentheses indicate the allowed 3σ range. Since one mass difference largely dominates, 2 mass squared splittings, Δm^2 and ΔM^2, are defined such as $|\Delta m^2| \ll |\Delta M^2|$, with $\Delta m^2 \equiv \Delta m^2_{12}$ and $\Delta M^2 \equiv \Delta m^2_{31} \simeq \Delta m_{32}$. In this situation to a very good approximation we associate the two mass splittings Δm^2 and ΔM^2 with two decoupled two-flavor oscillations. Observations have shown that solar neutrinos oscillate with a "slow" frequency given by $\Delta m^2_,$ whereas atmospheric muon neutrinos oscillate at the faster ΔM^2 scale. For this reason Δm^2 is often called the solar mass difference and ΔM^2 the atmospheric mass splitting. Their associated angles θ_{12} and θ_{23}, which govern the amplitudes of the oscillations, are similarly called solar and atmospheric mixing angles. θ_{13} drives the scale at which the $\nu_\mu \rightarrow \nu_e$ (or $\nu_e \rightarrow \nu_\mu$) processes occur. Since θ_{13} is small, the dominant transition occurring for a muon neutrino would be $\nu_\mu \rightarrow \nu_\tau$ whose amplitude is given by the θ_{23} angle [3].

The frequency of the oscillations also depends on the ratio between the neutrino travel distance L and its energy E (see Equation 1.25). Therefore experiments can be sensitive either to ΔM^2 or Δm^2 by choosing their L/E ratio. For experiments with $L/E \ll \Delta m^2$ the effect on the neutrino oscillation due to Δm^2 can be disregarded and the experiment will be sensitive only to the atmospheric mass squared splitting ΔM^2. Typical L/E values for experiments probing atmospheric oscillations are of the order of 500 km/GeV, these include accelerator or short baseline reactor experiments. Experiments probing the solar oscillations are sensitive to a much larger L/E of around 15 000 km/GeV and generally don't have the resolution to resolve the atmospheric oscillations on top of the dominant solar oscillation.

1.6.3 ν_e disappearance channel

Experiments can search for disappearance of anti-neutrinos from nuclear power plants. If neutrinos travel in a vacuum, the disappearance probability for neutrinos and anti-neutrinos is identical if invariance under $\mathcal{CPT}$ is assumed.

In an experiment searching for ν_e (or $\bar{\nu}_e$) disappearance the probability can be computed from Equation 1.30 taking into account the unitary properties of the PMNS matrix:

$$P(\nu_e \rightarrow \nu_e) = P(\bar{\nu}_e \rightarrow \bar{\nu}_e) =$$
$$1 - 4|U_{e3}|^2|U_{e1}|^2 \sin^2\Delta_{31} - 4|U_{e3}|^2|U_{e2}|^2 \sin^2\Delta_{32} - 4|U_{e2}|^2|U_{e1}|^2 \sin^2\Delta_{21} \tag{1.42}$$

---

[3] explicit proof for $\nu_\mu \rightarrow \nu_\tau$ has not yet been provided and the search is currently ongoing in the OPERA experiment see Section 1.7.1

The kinematic phase factors have been abbreviated and are given by:

$$\Delta_{ij} = \frac{\Delta m^2_{ij} L}{4E} \tag{1.43}$$

Anti-neutrinos emitted from nuclear power plants have fixed energies around 10 MeV. The L/E of the experiment can be varied by selecting the baseline (the distance between the plant and the detector). A reactor experiment with a long baseline will be sensitive to neutrino oscillations at the solar scale while choosing a shorter baseline will allow measurements at the atmospheric L/E.

Atmospheric scale

Reactor experiments with a baseline of a few hundred meters are sensitive to the atmospheric L/E. Examples of such experiments include Chooz [46] or Palo Verde [47] and more recent experiments such as Daya Bay [48], Double Chooz [49] and RENO [50]. The disappearance probability from Equation 1.42 can then be simplified by neglecting the term in Δm^2_{12}:

$$P(\nu_e \to \nu_e) = P(\bar{\nu}_e \to \bar{\nu}_e) = 1 - \sin^2 2\theta_{13} \sin^2\left(\frac{\Delta M^2 L}{4E}\right) + \mathcal{O}(\Delta m^2_{12}) \tag{1.44}$$

Thus the amplitude of the process is proportional to θ_{13}. Therefore short baseline reactor experiments aim at measuring θ_{13} which is currently the angle whose value has the largest uncertainty.

Solar scale

A reactor neutrino experiment such as KamLAND (see Section 1.7.2) has an average baseline of 180 km which makes it sensitive to the solar L/E. Equation 1.42 can be written as:

$$P(\nu_e \to \nu_e) = P(\bar{\nu}_e \to \bar{\nu}_e) = \cos^2\theta_{13}(1 - \sin^2 2\theta_{12}\frac{\Delta m^2 L}{4E}) + \sin^4\theta_{13} \tag{1.45}$$

Therefore the solar parameters (Δm^2_{12}, θ_{12}) can be measured with high precision in such an experiment [4].

1.6.4 ν_μ disappearance channel

From Equation 1.30 the signal for ν_μ disappearance is:

$$P(\nu_\mu \to \nu_\mu) =$$
$$1 \quad - \quad 4|U_{\mu 3}|^2|U_{\mu 1}|^2\sin^2\Delta_{31} \quad - \quad 4|U_{\mu 3}|^2|U_{\mu 2}|^2\sin^2\Delta_{32} \quad - \quad 4|U_{\mu 2}|^2|U_{\mu 1}|^2\sin^2\Delta_{21} \tag{1.46}$$

For accelerator experiments at the atmospheric L/E, such as K2K [51], T2K [52] or MINOS[53], this relation simplifies to:

$$P(\nu_\mu \to \nu_\mu) = 1 - 4|U_{\mu 3}|^2(1 - |U_{\mu 3}|^2)\sin^2\left(\frac{\Delta M^2 L}{4E}\right) + \mathcal{O}(\Delta m^2_{12}) \tag{1.47}$$

---

[4] with $\cos^2\theta_{13} \approx 1$ whose only effect is a small multiplicative reduction of the disappearance probability.

In the limit that $\theta_{13} \to 0$ the amplitude of the oscillation becomes:

$$4|U_{\mu 3}|^2(1-|U_{\mu 3}|^2) = \sin^2 2\theta_{23} \tag{1.48}$$

allowing precise measurements of the atmospheric parameters (ΔM^2 and θ_{23}).

1.6.5 $\nu_\mu \to \nu_e$ appearance channel

Accelerator experiments like T2K, MINOS or NOνA [54] plan to measure θ_{13}, by searching for such a $\nu_\mu \to \nu_e$ transition at the atmospheric L/E. Taking Equation 1.30 with $\alpha \neq \beta$, one can compute the probability for ν_μ to ν_e oscillation in a vacuum [55]:

$$\begin{aligned} P(\nu_\mu \to \nu_e) &= \left|U^*_{\mu 1} e^{-im_1^2 L/2E} U_{e1} + U^*_{\mu 2} e^{-im_2^2 L/2E} U_{e2} + +U^*_{\mu 3} e^{-im_3^2 L/2E} U_{e3}\right|^2 \\ &= \left|2U^*_{\mu 3} U_{e3} \sin\Delta_{31} e^{-i\Delta_{32}} + 2U^*_{\mu 2} U_{e2} \sin\Delta_{21}\right|^2 && (1.49) \\ &\approx \left|\sqrt{P_{atm}} e^{-i\Delta_{32} \pm \delta_{CP}} + \sqrt{P_{sol}}\right|^2 && (1.50) \end{aligned}$$

With $\sqrt{P_{atm}} = \sin\theta_{23} \sin 2\theta_{13} \sin\Delta_{31}$ and $\sqrt{P_{sol}} \approx \cos\theta_{23} \sin 2\theta_{12} \sin\Delta_{21}$.

The sign of δ_{CP} is positive for neutrinos and negative for anti-neutrinos. By expanding the relation we get:

$$P(\nu_\mu \to \nu_e) \approx P_{atm} + 2\sqrt{P_{atm}}\sqrt{P_{sol}} \cos(\Delta_{32} \pm \delta_{CP}) + \mathcal{O}(\Delta m^2_{12}) \tag{1.51}$$

The first term shows that θ_{13} can be measured in this channel providing that θ_{23} is known. The second term which is the interference term cannot be neglected since it is proportional to the atmospheric mass splitting. As can be seen, its sign changes if we are dealing with neutrinos or anti-neutrinos.

Expanding the $\cos\Delta_{32} \pm \delta_{CP}$ term yields one $\mathcal{CP}$ conserving part:

$$2\sqrt{P_{atm}}\sqrt{P_{sol}} \cos\Delta_{32} \cos\delta_{CP} \tag{1.52}$$

and one $\mathcal{CP}$ violating part:

$$\pm 2\sqrt{P_{atm}}\sqrt{P_{sol}} \cos\Delta_{32} \sin\delta_{CP} \tag{1.53}$$

again with a $+$ for neutrinos and a $-$ sign for anti-neutrinos. The observation of $P(\nu_\mu \to \nu_e) \neq P(\bar{\nu}_\mu \to \bar{\nu}_e)$ will therefore indicate a non zero value of δ_{CP}.

The value of the interference term, which appears because we cross neutrino flavors, depends on the value of δ_{CP} and on the sign of $\Delta m^2_{23} \equiv \Delta M^2$. Since both are not yet known, long baseline accelerator experiments searching for θ_{13} quote the results as a function of δ_{CP} and for both signs of ΔM^2. The situation for which ΔM^2 is positive is called normal mass hierarchy and the $\Delta M^2 < 0$ case is called inverted mass hierarchy (see Section 1.7.4). As seen in Equation 1.51 the term proportional to δ_{CP} is proportional to the sine of all three angles, hence the observation of δ_{CP} requires all angles to be nonzero.

1.7 Neutrino oscillation experiments

1.7.1 Measurements of the atmospheric parameters: ΔM^2 and θ_{atm}

Atmospheric neutrinos are neutrinos which are produced in cascades initiated by collisions of cosmic rays with the Earth's atmosphere. The first compelling evidence for atmospheric neutrino oscillation (and for neutrino oscillation in general) was presented by Super-Kamiokande (SK) in 1998 [16]. However there were large systematic errors on ΔM^2 due to the ambiguity on the distance the atmospheric neutrinos travel.

ΔM^2 can be more precisely measured in accelerator experiments where the travel distance is fixed and well known. Accelerator experiments measuring the atmospheric parameters use an artificial beam of muon neutrinos produced from in-flight pion decay. They usually include a near detector designed to study the unoscillated beam spectrum and composition as well as a far detector. Two accelerator experiments have significantly constrained the value of ΔM^2: K2K (KEK to Kamioka) and the MINOS experiment (Main Injector Neutrino Oscillation Search), both by searching for a disappearance of muon neutrino $\nu_\mu \rightarrow \nu_\mu$ from the beam. The baseline (distance between the source of the beam and the far detector) and mean neutrino beam energy are $L = 735$ km, $\langle E_\nu \rangle = 4$ GeV for MINOS and $L = 250$ km, $\langle E_\nu \rangle = 1.3$ GeV for K2K. Results from K2K, MINOS and SK are shown in Figure 1.3 in the $(\Delta M^2 - \sin^2 2\theta_{23})$ space. The most precise measurements in the atmospheric sector are currently given by MINOS and the best two-flavor oscillation fit to its data give the following mixing parameters:

$$\Delta M^2 = (2.43 \pm 0.13) \times 10^{-3} \mathrm{eV}^2 \qquad \sin^2 2\theta_{23} > 0.90 \text{ (90\% C.L.)}$$

More recently MINOS also performed a series of $\bar{\nu}_\mu$ disappearance measurements. Initially (in 2010) MINOS reported indications of differences between the $\bar{\nu}_\mu$ and ν_μ oscillation parameters [56]. Any differences between the measured neutrino and antineutrino oscillation parameters would indicate new physics. However in February 2012 MINOS updated the results with increased statistics and improved systematics which removed the tension previously reported and established consistency between ν_μ and $\bar{\nu}_\mu$ oscillations [57]. The summary of the observed $\bar{\nu}_\mu$ parameters in MINOS are shown in Figure 1.4.

The dominant transition in the atmospheric sector is expected to be $\nu_\mu \rightarrow \nu_\tau$ and OPERA (Oscillation Project with Emulsion-Tracking Apparatus) [58] is currently searching for ν_τ appearance in a ν_μ beam. The experiment uses the CNGS beam (CERN Neutrino to Gran Sasso) which is a ν_μ beam produced at the CERN Super Proton Synchrotron (SPS). OPERA is located 732 km away from the source in the underground Gran-Sasso laboratory in Italy. It is based on photographic emulsion technology and searches for a signature of tau decay which would indicate the presence of a ν_τ in the beam. After two years of running OPERA has observed one candidate ν_τ event in an event sample of 1.89×10^{19} protons on target (p.o.t.) in which 0.54 ± 0.13 ν_τ events are expected. The observation of this possible tau candidate in the decay channel $h^- \pi^0 \nu_\tau$ has a significance of 2.36σ of not being a background fluctuation.

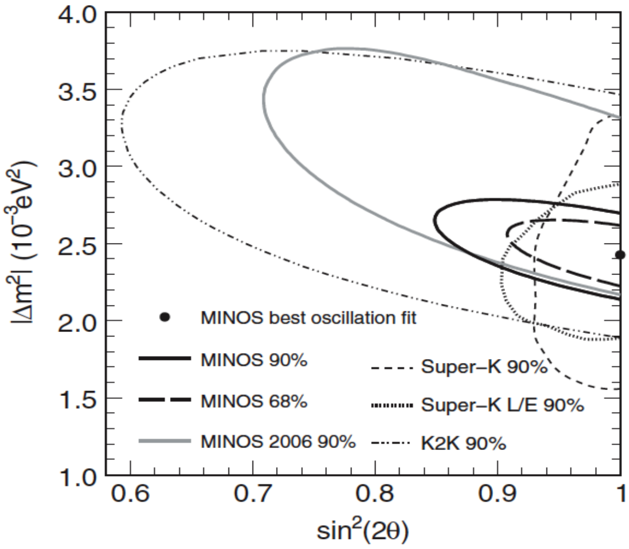

Figure 1.3: Contours of the atmospheric neutrino oscillation parameters for the MINOS [53, 59], K2K [51] and Super K [60] data. The figure is taken from [53]

1.7.2 Measurements of the solar parameters: Δm^2 and θ_{sol}

Solar neutrinos are created via nuclear fusion reactions in the Sun and they contribute to the majority of the neutrino flux we receive on Earth. The neutrino flux from all nuclear fusion processes in the Sun is predicted by the Solar Standard Model (SSM). For years however, solar neutrino experiments observed significantly lower ν_e fluxes than expected from neutrino production calculations. This discrepancy was called the solar neutrino problem which remained unsolved for more than 30 years. In 2001 the SNO experiment proved that the discrepancy was due to neutrino flavour conversion. SNO was an experiment that used 1000 tons of ultra-pure heavy water (D_2O) contained in a spherical acrylic vessel, surrounded by an ultra-pure H_2O shield [17]. Using D_2O as interaction medium instead of ordinary H_2O, as is used in Super-Kamiokande for instance, allowed SNO to be sensitive not only to charged current interactions of the electron neutrino ($\nu_e + d \rightarrow p + p + e^-$) but also to neutral current of all neutrino flavors on the deuterium atom ($\nu_x + d \rightarrow n + p + \nu_x$). Hence SNO was able to determine the electron and non-electron neutrino components of the solar flux. In 2001 the initial SNO result [17] combined with the Super-Kamiokande's high-statistics ν_e elastic scattering result [61] provided direct evidence for oscillation of solar neutrinos. Later, SNO's neutral current measurements further strengthened this conclusion [62].

Under the assumption of $\mathcal{CPT}$ invariance and neglecting the sub-leading atmospheric oscillation, the solar parameters can also be measured by studying the disappearance of $\bar{\nu}_e$'s emitted from nuclear power reactors. The KamLAND experiment (Kamioka Liquid scintillator Anti-Neutrino Detector) in Japan measured the flux from several nuclear power plants in the country and has a flux-weighted average baseline of 180 km. The detector consists in a 1 kton ultra pure liquid scintillator vessel and measures the $\bar{\nu}_e$ flux via the reaction $\bar{\nu}_e + p \rightarrow e^+ + n$. The first KamLAND results with 162 ton.year exposure were reported in December 2002 [63] and showed clear evidence of an event deficit, as expected from neutrino oscillations. KamLAND observed

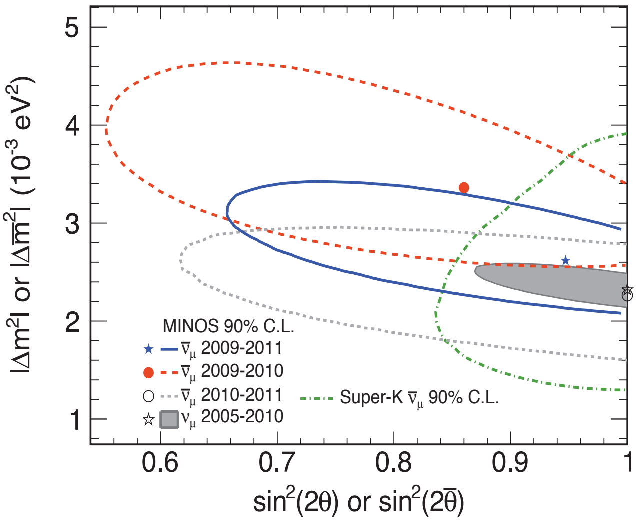

Figure 1.4: Confidence regions for MINOS $\bar{\nu}_\mu$ oscillation parameters for different data taking periods. The regions include statistical and systematic uncertainties. The figure is taken from [57]

not only the distortion of the $\bar{\nu}_e$ spectrum, but also more recently (2008) the periodic feature of the $\bar{\nu}_e$ survival probability expected from neutrino oscillations for the first time (see Figure 1.5).

In 2008 the SNO Collaboration updated a two-neutrino oscillation analysis [64] including all the solar neutrino data (SNO, Super-Kamiokande, chlorine, gallium, and Borexino) plus the KamLAND results. The best fit parameters obtained from this global solar + KamLAND analysis are:

$$\Delta m^2_{12} = 7.59^{+0.19}_{-0.21} \times 10^{-5}\text{eV}^2 \quad \tan^2\theta_{12} = 0.468^{+0.048}_{-0.040} \quad (\theta_{12} = 34.4^{+1.3}_{-1.2}\text{ degrees})$$

Figure 1.6 illustrates the complementarity between the two data sets: the solar neutrino data constrains θ_{12}, and the KamLAND measurements, strongly constrain Δm^2_{12}.

1.7.3 Measurements of θ_{13}

As has been discussed in Section 1.6.3 θ_{13} can be directly measured by short (typically a few hundred meters) baseline reactor experiments studying $\bar{\nu}_e$ disappearance. The Chooz reactor experiment in France was the first to try and measure θ_{13} [46]. Like KamLAND, it is based on liquid scintillator technique to detect the anti-neutrino flux, it has however a much shorter baseline of 1 km (for anti-neutrino energy of a few MeV) which makes it sensitive to the large mass squared splitting ΔM^2 and θ_{13} (see Equation 1.44). At 90% C.L no evidence for $\bar{\nu}_e$ disappearance was found, a result which was furthermore substantiated by the measurements of Palo Verde [47]. Chooz therefore set a 90% C.L. upper limit at $\sin^2 2\theta_{13} < 0.15$.

In accelerator neutrino experiments, θ_{13} can also be measured via the $\nu_\mu \rightarrow \nu_e$ oscillation (see Section 1.6.5). K2K searched for such a signal, but found no evidence of electron neutrino appearance and set a 90% C.L. upper limit at $\sin^2 2\theta_{13} < 0.26$ assuming δ_{CP} =0 [66].

In 2010, the MINOS experiment, which was initially designed to search for ν_μ disappearance,

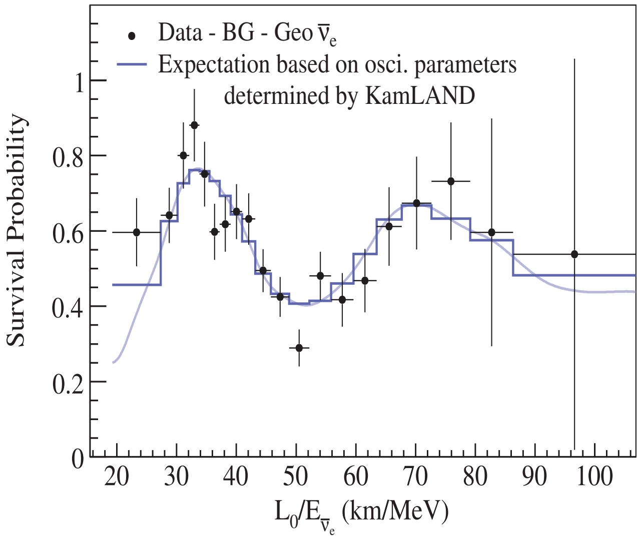

Figure 1.5: Ratio of the $\bar{\nu}_e$ spectrum to the expectation for no oscillation as a function of L_0/E. L_0 is the effective baseline taken as the flux weighted average (L_0=180 km). The curves show the best-fit expectations for $\bar{\nu}_e$ oscillations. The figure is from [65].

reported a new result on the $\nu_\mu \rightarrow \nu_e$ oscillation [67]. They observed 54 ν_e appearance candidate events while the expected number of background events was 49.1±7.0 (stat.) ± 2.7 (sys.). This translates into a 90% C.L. upper limit of $2\sin^2 2\theta_{13}\sin^2\theta_{23} < 0.12$ for $\delta_{CP} = 0$ and the normal mass hierarchy.

More recently (June 2011) T2K observed in data accumulated with 1.43×10^{20} protons on target, six ν_e appearance candidates from an initially pure ν_μ beam were observed in the far detector while 1.5±0.3 (syst.) are expected for θ_{13} =0. This indicates a non zero value for θ_{13} with a 2.45 σ significance [44]. The observations are consistent with $0.03 < \sin^2 2\theta_{13} < 0.28$ at 90% C.L for δ_{CP} =0 and normal mass hierarchy. T2K, which will be described at length in the next chapter, is the first experiment to set an interval for θ_{13} rather than just an upper bound. The low background level makes the T2K results particularly important and robust. The NA61/SHINE charged pion production measurements which are described in this thesis were crucial in reducing the systematics for the T2K analysis.

With an improved analysis and an increased exposure, MINOS also reported in August 2011 a best fit of $2\sin^2 2\theta_{13}\sin^2\theta_{23} = 0.041^{+0.071}_{-0.031}$ from the observation of 62 ν_e events with an estimated background of 49 events, thus disfavoring θ_{13} =0 at 89% Confidence Level [45]. The results from T2K and MINOS are shown in Figure 1.7

Following these new results a global 3 neutrino analysis performed on all the available data provides an update on all the neutrino oscillation parameters and most importantly a better than 3σ evidence for nonzero θ_{13} [43]. The results of the global analysis are shown in Figure 1.8, in terms of allowed ranges for each of the oscillation parameters. The vertical scale represents the number of standard deviations from the best fit point. The estimates of $\sin^2 2\theta_{13}$ and $\sin^2 2\theta_{12}$ are affected by reactor flux systematics; predictions on reactor fluxes were improved in May 2011 including the latest information from nuclear databases [68]. The dashed lines on the figure

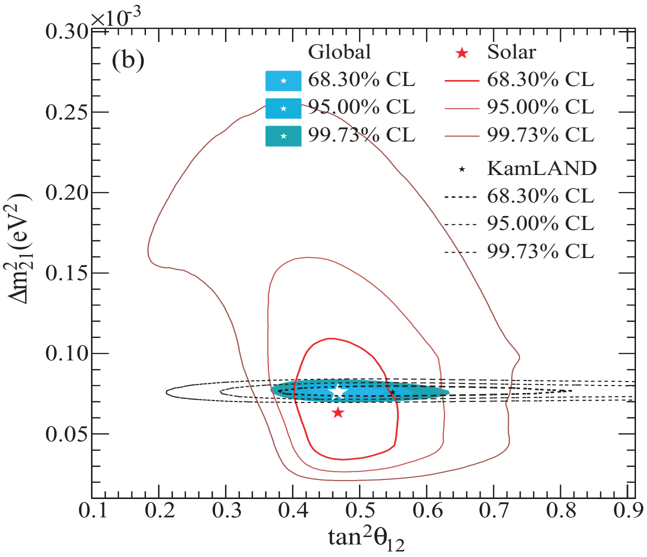

Figure 1.6: Solar and KamLAND oscillation parameter analysis. The solar data include SNO,SAGE, Homestake, Gallex, GNO, Borexino and SK data. The figure is taken from:[64].

refer to the analysis with the new reactor fluxes. So far however, there are no constraints of any significance on δ_{CP} nor is the mass hierarchy known.

1.7.4 Mass hierarchy

Figure 1.9 summarizes what is currently known about the flavor content of the three known neutrino mass eigenstates. The probability of having a neutrino with flavour α in the i-th mass eigenstate is given by the absolute square of the terms of the PMNS matrix $|U_{\alpha i}|^2$. Therefore, from Equation 1.29 we understand that the probability of finding ν_μ (ν_τ) in the 3rd mass eigenstate is $\cos^2\theta_{13}\sin^2\theta_{23} \approx \sin^2\theta_{23}$ ($\cos^2\theta_{13}\cos^2\theta_{23} \approx \cos^2\theta_{23}$) since θ_{13} is very small [69]. Similarly, the ν_e content of the 3rd mass eigenstate is just $\sin^2\theta_{13}$. The muon and tau components of the first and second mass eigenstates are given by the squared amplitudes $|U_{\mu 1}|^2$,$|U_{\mu 2}|^2$,$|U_{\tau 1}|^2$ and $|U_{\tau 2}|^2$ which depend on the value of δ_{CP}.

The sign of Δm^2_{12} is known to be positive (ν_2 is heavier than ν_1), however the sign of ΔM^2 remains unknown. This leads to two possible scenarios:

- either $m_1 < m_2 < m_3$ which is called the normal mass hierarchy
- or $m_3 < m_2 < m_1$ which is the inverted mass hierarchy.

This ambiguity is also reflected in Figure 1.9. As was stressed in Section 1.5, matter effect may lead us to determine the sign of the atmospheric mass splitting and solve the hierarchy problem.

1.8 Summary and future prospects

Besides T2K, the long-baseline accelerator experiment NOνA [54] as well as the reactor experiments Daya Bay [48], Double CHOOZ and RENO, are the upcoming generation of experiments

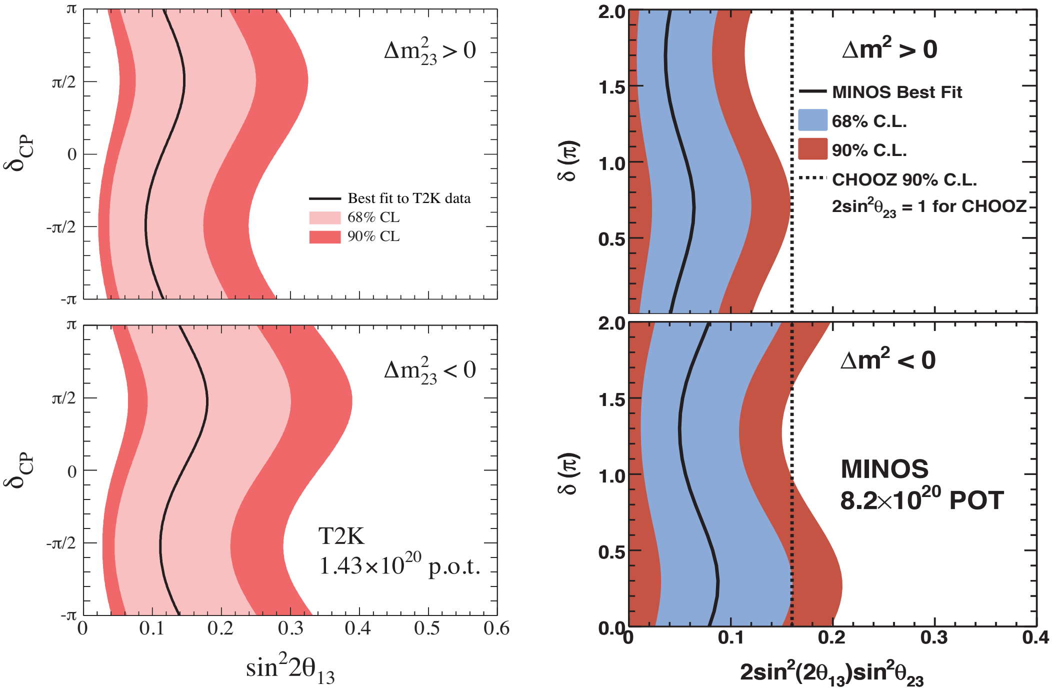

Figure 1.7: Results from the T2K [left] and MINOS [right] ν_e appearance analysis. T2K reports its results as a function of $\sin^2 2\theta_{13}$ and MINOS as a function of $2\sin^2 2\theta_{13}\sin^2\theta_{23}$. The 68% and 90% C.L. allowed intervals are shown as a function of δ_{CP}, for normal (top) and inverted (bottom) mass hierarchy. The best fit values are shown with solid black lines. The CHOOZ limit computed with $\sin^2\theta_{23} = 1$, $\Delta m^2_{32} = 2.43 \times 10^{-3}\text{eV}^2$ is also superimposed on the MINOS results. The figures are taken from:[44] and [45].

searching the value of θ_{13}. These experiments have either recently started or will soon start taking data. The NOνA experiment in the US will start data taking in 2013 with a baseline of 810 km. Since it operates at a higher energy, NOνA will have the capability to study oscillations of both neutrinos and antineutrinos. The fact that T2K and MINOS indicate not only a nonzero, but a potentially large value of θ_{13} is exciting news for all of these experiments as there is now a good chance they will be able to measure the value of this mixing angle with some precision, rather than just setting a limit on it.

The precise measurement of θ_{13}, δ_{CP} and the mass hierarchy, will be pursued in a next generation of neutrino experiments such as super-beams, beta beams or neutrino factories. However, the ability of those experiments to measure these unknown parameters is limited by degeneracies [70]. Indeed any appearance probability $P_{\nu_\alpha \to \nu_\beta}$ has multiple solutions in the $(\theta_{13}, \delta_{CP}, \theta_{23}, \pm\Delta M^2)$ parameter space and determining a single solution would require a combination of several measurements in different oscillation channels. Therefore not one but a combination of next generation experiments may be needed to get a complete picture of the neutrino oscillation parameters. These third generation neutrino beams are likely to be produced at existing accelerator facilities such as CERN, Fermilab or J-PARC. In any case new large far detectors such as megaton water Cherenkov [71], Liquid Argon TPCs [72] or scintillator based detectors [73] should be constructed and be placed in new, or existing, underground labs.

Super-beams consists of an upgrade of the conventional ν_μ beams (created from π decay)

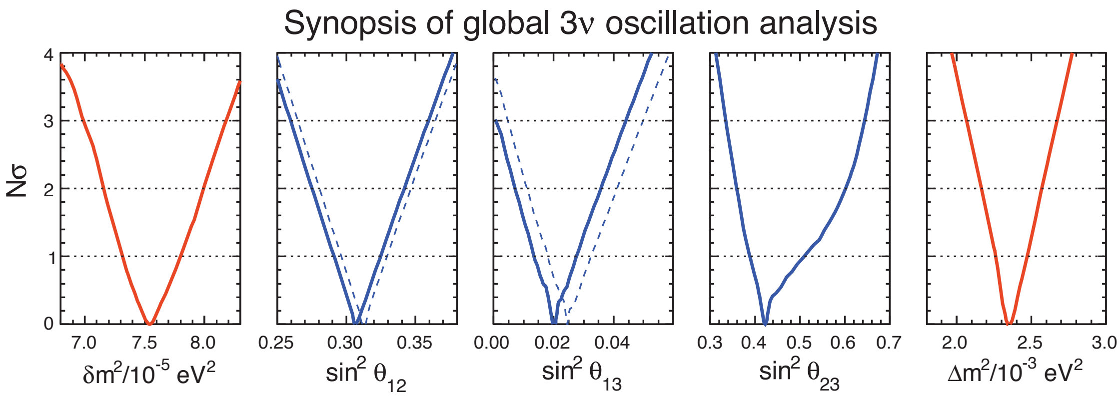

Figure 1.8: Bounds on the mass-mixing oscillation parameters, in terms of standard deviations from the best fit. Solid (dashed) lines refer to the case with old (new) reactor neutrino fluxes. Note the $> 3\sigma$ evidence for $\theta_{13} > 0$.

into high intensity beams to probe the small $\nu_\mu \rightarrow \nu_e$ signal with higher statistics. Super-beams would hence require new, high-power, proton accelerators delivering more intense proton beams on target (typically 2-5 MW). The main challenge resides in delivering those high intensity proton beams. For instance T2K could be upgraded, as already mentioned in the initial letter of intent, by increasing the power of the J-PARC accelerator from 0.75 MW to 4MW and building a megaton water Cherenkov detector, Hyper-Kamiokande [71], to be placed at the same distance as the current T2K far detector, Super-Kamiokande. Another multi-MW proton beam, proposed for construction at Fermilab is also under study [74]. Project X, as it is called, would provide the high intensity neutrino beam for the LBNE (Long Baseline Neutrino Experiment) project which has a proposed baseline of 1300 km between Fermilab and the Deep Underground Science and Engineering Laboratory (DUSEL) in Lead, South Dakota [75]. The main drawback of super-beams however is that, as in conventional beams, there remains intrinsic ν_e contamination in the beam and therefore such a beam might not be the best choice if θ_{13} is found to be small (i.e close to the current lower 3 σ band $\sim 10^{-3}$).

Another high performance beam for neutrino oscillation study is the beta-beam. A beta-beam is produced from boosted light radioactive isotopes and therefore is a pure ν_e or $\bar{\nu}_e$ beam depending on whether the decay is β^+ or β^-. This has the big advantage compared to super-beams that it produces a very pure neutrino beam, with well measured cross sections from β decay. The neutrino oscillation discovery potential in a beta-beam facility is mainly based on the so called golden channel, which is the $\nu_e \rightarrow \nu_\mu$ oscillation. A low-energy beta-beam (sub-GeV range) could be obtained with the present CERN SPS. At this range of energy the baseline from CERN to the existing Modane laboratory in the Frejus tunnel (L =130 km) would match the first atmospheric oscillation peak [76].

The most complete, but also the most challenging, facility would be the Neutrino Factory [77]. It consists of an intense high-energy neutrino source derived from the decay of a stored muon beam. The decay of muons would therefore produce an intense beam of ν_μ ($\bar{\nu}_\mu$) and $\bar{\nu}_e$ (ν_e). The main advantage being that it has access to almost all channels of neutrino flavour transition. The golden channel appears to be particularly attractive [78] since it can be studied simply by looking at the muon charge in the far detector: when running with μ^+ the neutrinos produced

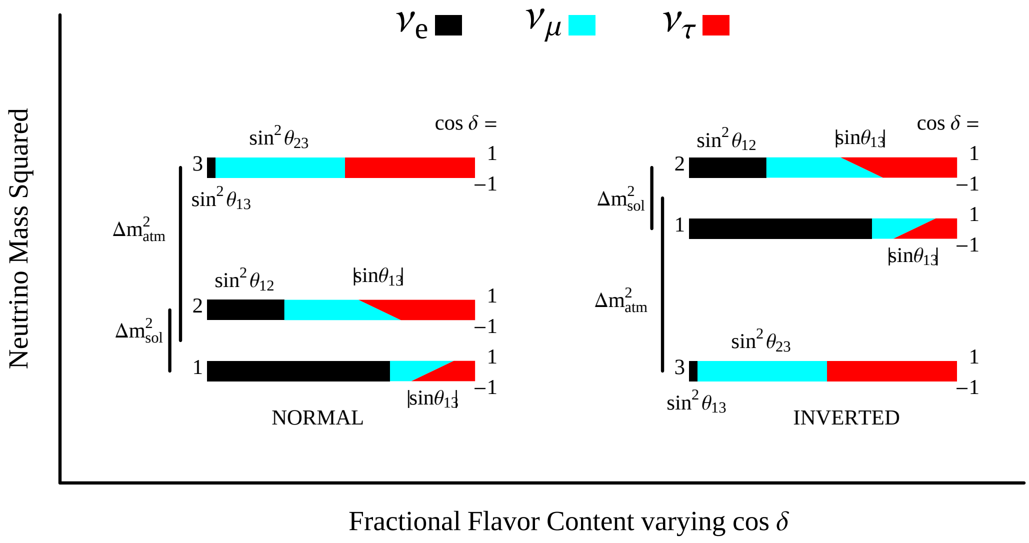

Figure 1.9: Probability of finding the α-flavor in the i-th mass eigenstate depending on the value of the $\mathcal{CP}$ violating phase. The bottom of the bars is for the minimum allowed value of $\cos\delta_{CP} = -1$ and the top of the bars is for the maximum value of $\cos\delta_{CP} = 1$. The other mixing parameters are fixed at $\sin^2\theta_{12} = 0.3$, $\sin^2\theta_{13} = 0.30$, $\sin^2\theta_{12} = 0.03$ and $\sin^2\theta_{23} = 0.50$. The figure is from [69].

in the decay ring are ν_e and $\bar{\nu_\mu}$. In the absence of oscillation, the neutrino interacting in the far detector should generate e$^-$ and μ^+. A detected "wrong sign" muon, indicates clear signal for the $\nu_e \rightarrow \nu_\mu$ oscillation. The study of the golden channel would therefore require a magnetised detector in order to identify the muon's charge. However, in a beta-beam which consists in a pure beam of either ν_e or $\bar{\nu}_e$ no charge identification is needed. Another unique feature of the neutrino factory is it's ability to study the $\nu_e \rightarrow \nu_\tau$ oscillation (silver channel) since, unlike the beta beam, it can provide ν_e's above the tau creation threshold. The signal from the silver channel can be tagged looking for wrong sign muons in coincidence with a τ-decay vertex [79]. Therefore, to separate both channels a far detector with muon-charge identification and vertex reconstruction is needed. A MINOS-like detector made of iron and scintillator, called MIND [73], is under study for this purpose. In any case, the combination of results from the silver and golden channels at a neutrino factory will help disentangle a large part of the correlations and solve degeneracies [80, 81].

To be sensitive to matter effects and hence to the mass hierarchy typical baselines of the order of a few 1000 km are needed. By using the same facility but with different baselines, the integrated electron density between the neutrino production and the detectors is different, hence the matter effects for the two neutrino beams are different. One particular interesting baseline is the "magic baseline" which is such that $V_W = \sqrt{2}G_F n_e = 2\pi/L$ equivalent to [76]:

$$L_{magic} \simeq \frac{32726}{\rho[\mathrm{g/cm^3}]} \simeq 7250\mathrm{km} \tag{1.54}$$

At this baseline, a resonance effect similar to Equation 1.5.1 occurs where δ_{CP} is cancelled by matter effects. An experiment operating at L_{magic} can therefore precisely measure θ_{13} and the mass hierarchy as the experiment is completely insensitive to $\mathcal{CP}$ violation. Placing a second detector at a distance where the sensitivity to θ_{13} is large (around 2500-5000 km [76]), would provide a good measurement of δ_{CP} since θ_{13} would already be constrained by the magic baseline. The possibility of placing a detector in the Pyhäsalmi mine in Finland is under study [82]. It would offer a baseline of 2288 km for a neutrino factory, beta-beam or super-beam at CERN. In addition the distance from the existing J-PARC accelerator complex to Pyhšalmi (7090 km) turns out to be very close to the magic baseline.

Chapter 2

T2K and its needs for a hadron production experiment

The T2K (Tokai-to-Kamioka) experiment is a second generation long baseline neutrino oscillation experiment designed to probe the mixing of the muon neutrino with other species [52]. It is the first long baseline neutrino oscillation experiment proposed and approved to look explicitly for the electron neutrino appearance from the muon neutrino, thereby measuring θ_{13}, the last unknown mixing angle in the lepton sector. T2K will also examine the disappearance of muon neutrinos to improve the current knowledge on ΔM^2 and θ_{23}.

An overview of the T2K experiment is shown in Figure 2.1. An intense muon neutrino beam with $\langle E_\nu \rangle = 0.6$ GeV is produced at J-PARC[1] in Tokai, Japan [83]. The neutrino beam is measured by a set of near detectors at the J-PARC site, and is measured again after traveling 295 km by the Super-Kamiokande water Cerenkov detector [84] (SK) in Kamioka. The neutrino beam is produced by a high intensity proton beam of 30 GeV impinging on a carbon target and producing mesons (π and K). The positively charged mesons are focused by electromagnetic horns and decay into neutrinos (ν_μ,ν_e) in a ~100 m long decay tunnel. The experimental strategy of T2K relies on the comparison between the neutrino flux measured at SK and the one predicted at SK. The prediction of the flux at SK relies on the T2K beam Monte Carlo (MC), which is highly dependent on the models used to simulate the primary interactions of the protons and hadronic re-interactions in the carbon target. To achieve higher precision, NA61/SHINE [85, 86, 87, 88] provides the reference pion and kaon production data in order to tune the available MC codes.

This chapter gives an overview of T2K with emphasis on the production of the neutrino beam and the beam MC simulations. Requirements on NA61/SHINE are discussed and examples of previous hadron production measurements are given.

2.1 T2K experimental setup

The neutrino beam line is produced at J-PARC, which was newly constructed at Tokai, Ibaraki prefecture. It consists of three proton accelerators [89]: a linear accelerator (LINAC), a rapid-cycling synchrotron (RCS) and the main ring synchrotron (PS). The designed acceleration energy

---

[1] Japan Proton Accelerator Research Complex

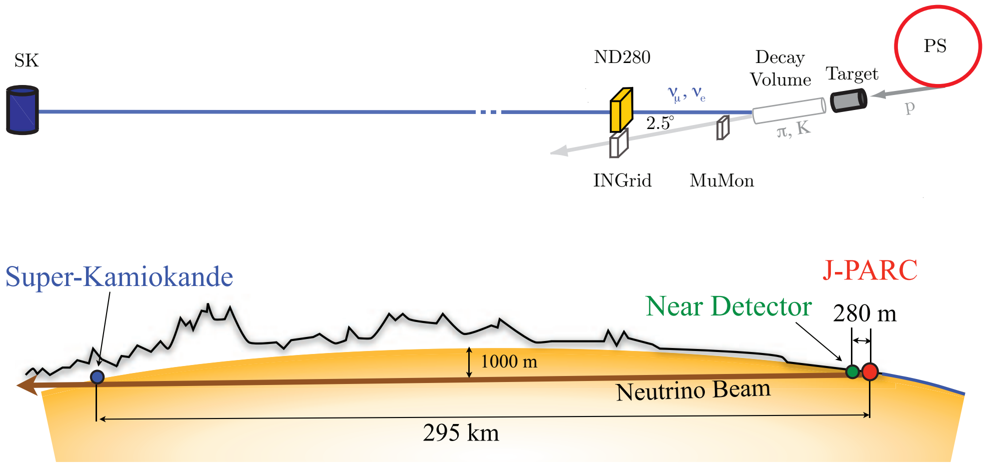

Figure 2.1: Overview of the T2K experiment.

for the LINAC is 400 MeV (180 MeV at present). The protons are then accelerated up to 3 GeV by the RCS and to 30 GeV in the main ring, where they circulate as 8 bunches (six until June 2010). The neutrino beam line is composed of two sequential sections: the primary and secondary beam lines. An overview is shown in Figure 2.2.

In the primary beam line all the proton bunches are extracted within a single turn (fast extraction) yielding an intensity of 3×10^{14} protons per spill with a repetition rate of 0.5 Hz. [52]. The protons are then focused onto a helium cooled cylindrical graphite target. The target which constitutes the begining of the secondary beam line, is 91.4 cm long (1.9 interaction length) and has a diameter of 2.6 cm and a density of 1.803 g/cm^3. About 80% of the incoming protons interact in the target and the secondary positive mesons (mainly pions and kaons) are focused by a set of three electromagnetic horns [90, 91] which operate at a current of 250 kA (the design current being 320 kA). The pions and kaons are collected by the first horn which surrounds the target and foccussed by the second and third horns (see Figure 2.3). They then decay in flight into neutrinos in the decay volume placed just downstream of the horn. The decay volume is a 96 m long steel tunnel filled with Helium gas[2] and surrounded by 6 m thick reinforced concrete shielding. Along the beam axis, 40 plate coils are welded on the 16 mm thick steel wall, to water cool the wall and concrete below 100°C. A 3.15 m thick graphite beam dump is placed at the end of the decay volume and stops all the hadrons, as well as muons below 5 GeV/c. Any muons above 5 GeV/c that pass through the beam dump are monitored by an array of radiation hard sensors called MUMON (Muon Monitor). These measurements give the muon beam position and profile on a spill by spill basis. A full description of the calibration and operation of the MUMON can be found in [92].

---

[2] Helium reduces pion absorption and suppresses tritium production by the beam.

2.1.1 Off-axis beam

The off-axis angle, which is the angle of the neutrino beam with respect to the baseline connecting the proton target to SK is adjustable and set at 2.5 degrees. As shown in Figure 2.2b, the on-axis beam profile is rather broad in energy, while the 2.5° off-axis configuration, despite a loss in intensity, provides a narrow band neutrino beam peaked at 0.6 GeV which maximizes the effect of the neutrino oscillation at 295 km (see Appendix A). Therefore one has a quasi-monochromatic beam at the L/E which coincides with the first minimum in the $P_{\nu_\mu \to \nu_\mu}$ survival probability (see Figure 2.2c). If necessary, the peak neutrino energy can be increased by reducing the off-axis angle to 2.0 degrees. The other advantage of a narrow band beam is the suppression of the high energy tail. This is important in T2K since higher energy neutrinos contribute a large fraction of the background signals in the far detector.

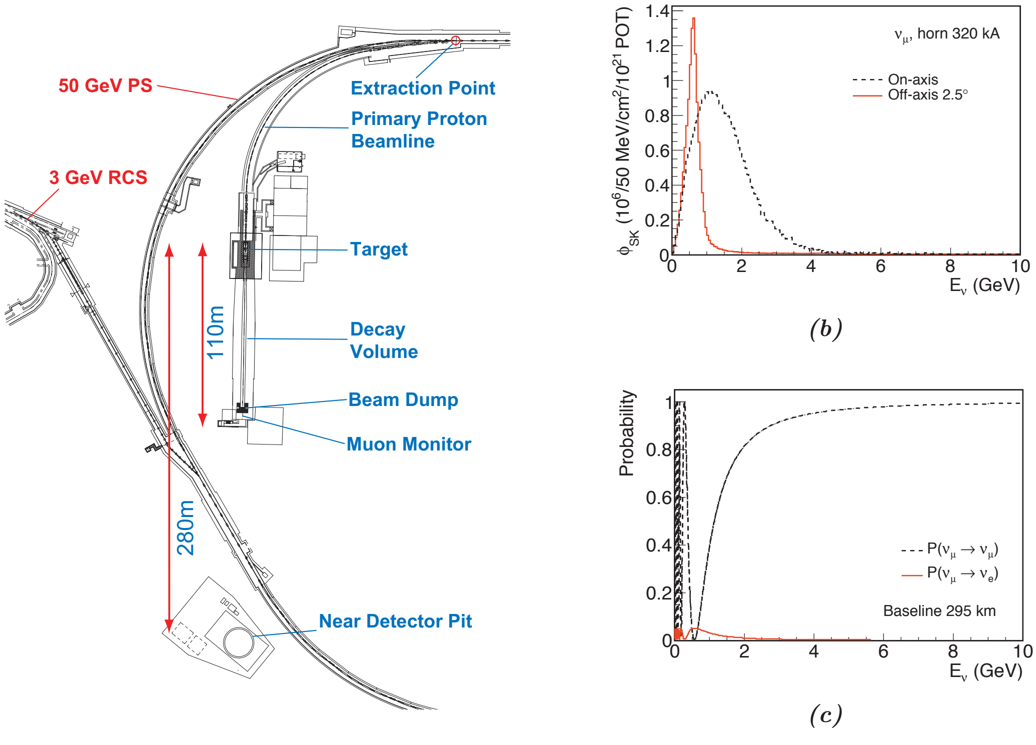

(a)

(b)

(c)

Figure 2.2: Overview of the production of the neutrino beam at JPARC (a). The ν_μ energy spectra at SK in the on-axis and off-axis beam configurations is shown in (b) and the neutrino oscillation probability for a travel length of 295 km as a function of the neutrino energy E_ν is shown in (c). The figures are from [93, 92].

2.1.2 Near detectors

The un-oscillated neutrino beam is measured at 280 m from the production target, by two near detectors (NDs). One detector is placed on the proton beam axis and the other measures the off axis neutrino beam which points to SK. The main purposes of the on-axis detector, INGRID (Interactive Neutrino GRID), is to monitor the neutrino beam direction and intensity while

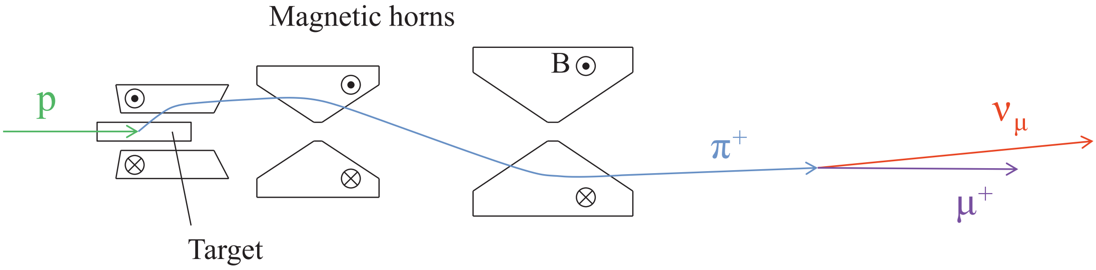

Figure 2.3: Illustration of an example of the pion decay chain producing a muon neutrino. The pion produced in the proton and graphite target interaction is focused by the three magnetic horns, and decays into a muon and a muon neutrino in flight. The figure is from [92].

the off-axis detector (the ND280) aims to measure energy spectrum, contamination of electron neutrinos and neutrino cross-sections in the direction of SK. An overview of the near detector complex is shown in Figure 2.4.

INGRID

INGRID is composed of 14 ($1 \times 1 \times 1$ m^3) identical 7 ton modules arranged in 10 m by 10 m crossed horizontal and vertical arrays centered on the beam. Each module consists of a sandwich structure of 9 iron plates and 11 tracking scintillator planes. The iron plates and scintillators are 6.5 cm and 1 cm thick respectively. Using the number of observed neutrino events in each module, the beam center is measured to a precision better than 10 cm on a day to day basis. This corresponds to 0.4 mrad precision at the near detector pit [52].

ND280

The ND280 consists of several sub-detectors contained within the refurbished UA1/Nomad dipole magnet which provides a magnetic field of approximately 0.2 T. Since the available space inside the magnet is relatively small ($6.5 \times 2.6 \times 2.5$ m^3), careful study was performed to maximise the amount of active elements while providing enough target mass for neutrino interactions.

The detector is a combination of the so called π^0 Detector (P0D) which sits at the upstream end of the magnet and a tracking system consisting of three time projection chambers (TPCs) [94] and two fine grained detectors (FGDs) [95]. All are contained inside a metal frame container, called the “basket” which is surrounded by an electromagnetic calorimeter (ECAL).

The P0D is composed of scintillating bars tracking planes interleaved with lead sheets and water target bags [96]. The primary objective of the P0D is to measure the neutral current process ($\nu_\mu + N \to \nu_\mu + N + \pi^0 + X$) on water which is the main background channel for the ν_e appearance search in SK.

Downstream of the P0D, the three TPCs, together with the two FGDs measure the energy spectrum and flavor content of the neutrino beam by identifying ν_μ and ν_e Quasi Elastic (QE) and non QE (nQE) Charged Current interactions. The TPCs are readout with bulk MicroMegas detectors [97] providing excellent imaging capabilities and a high momentum resolution. The achieved resolution of the specific ionization loss (dE/dx) is about 7.8% for minimum ionizing particles, better than the design requirement of 10%, allowing a very precise particle identification by dE/dx. The FGDs are made of layers of finely segmented scintillating bars. They provide target mass for neutrino interactions as well as tracking of charged particles coming from the interaction vertex.

The P0D, TPCs, and FGDs are all surrounded by a sampling electromagnetic calorimeter whose role is to detect showering particles (e^-, γ) which did not convert in the inner detectors. Finally, all sides of the magnet are instrumented with plastic scintillator plates inserted between gaps of the magnet yoke called the Side Muon Range Detector (SMRD) [98]. The goal of the SMRD is to measure the trajectory of muons which exit the side of the inner detectors and to veto/trigger on cosmic particles.

The data collected with the ND280 is used to characterize the neutrino beam prior to oscillation, in order to provide a reference measurement for the determination the flux at SK and to reduce uncertainties in the overall oscillation measurements. This includes the characterization of un-oscillated ν_μ spectra, and cross section measurements of potential background signals in SK such as ν_μ neutral current π^0 production and general CC QE/nQE processes. The goal is also to measure the ν_e content of the beam which is expected to be approximately 1% of the ν_μ flux and creates a significant non-removable background in the ν_e appearance search.

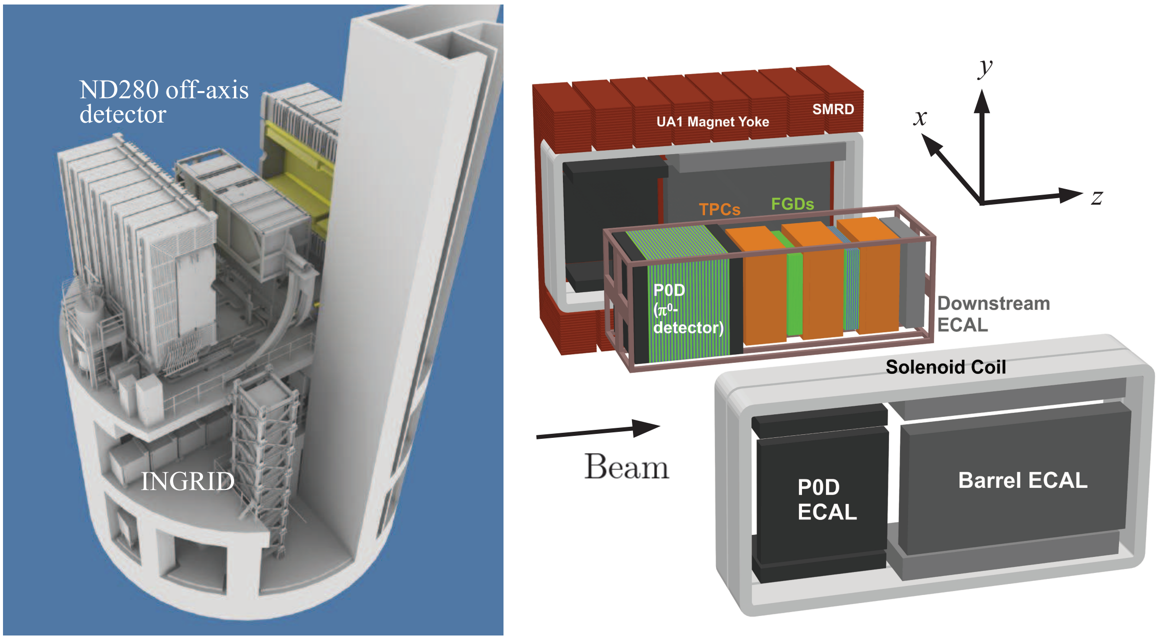

(a) The ND280 detector site ***(b)*** Exploded view of the off-axis detector

Figure 2.4: The ND280 detector complex. (a) indicates the location of the off-axis detector and magnet; the INGRID modules are located on the level below the ND280 detectors. A detailed view of the ND280 off-axis detector is shown in (b) with its main components along the beam direction.

2.1.3 Far detector

The world's largest water Cerenkov detector, Super-Kamiokande (SK), serves as the far detector in the T2K experiment. Super-Kamiokande has been running since 1996 and has produced data for a number of well-known results that include measurements of solar, atmospheric and accelerator neutrinos (see Chapter 1) and world-leading limits on the proton lifetime [99, 100, 101].

The detector is located 295 km west of J-PARC in the Kamioka mine, 1 km deep inside the Mt. Ikenoyama mountain. SK is a cylindrical cavern, 39 m in diameter and 42 m in height, filled with 50 kton of pure water. It is mainly comprised of two segments: the inner and outer detectors which are separated by a cylindrical stainless steel structure. The outer detector serves as an active veto of cosmic ray muons and other backgrounds and is instrumented along its inner walls by 1,885 outward-facing 20 cm photomultiplier tubes (PMTs). The inner detector holds 11,129 inward-facing 50 cm diameter PMTs on its cylindrical wall. A shematic view of the detector geometry is given in Figure 2.5.

Neutrinos are detected by measuring the cone of Cerenkov light emitted by the relativistic charged products of neutrino interactions in water. When the photons reach the PMTs on the detector walls they produce a ring-shaped hit pattern which gives information on the produced particle's vertex, energy and direction. e/μ separation is easily achieved by studying the shape of the Cerenkov rings: the ring is clear and well defined for non-showering minimally ionizing particles such as pions or muons and fuzzy for showering electromagnetic particles (e or γ). The primary strategy to measure the flavor composition of the T2K neutrino beam at Super-Kamiokande, and thereby observe the oscillation of ν_μ to either ν_e or ν_τ , is to count charged current quasi-elastic (CCQE) interactions for muon and electron neutrinos, both of which produce leptons of their respective flavor. An interacting ν_μ will produce a clean μ-like ring whereas the signature of ν_e event will be a fuzzy e-like ring. GPS synchronization between J-PARC and SK is used to identify T2K beam neutrinos from the atmospheric neutrino events and other low energy backgrounds. The beam neutrinos are expected to arrive at SK approximately 1 ms after the proton beam hits the target at J-PARC.

Finally, because of the detector's long-running operation, the behavior of SK is well understood. The calibration of the energy scale is known to the percent level, and the software for modeling events in the detector matches calibration samples to the percent level as well.

2.1.4 T2K data taking period

The construction of the J-PARC accelerator complex began in 2001 and was completed in 2008. At the end of April 2009, the first proton beam was successfully extracted from the Main Ring synchrotron to the target station. At the end of 2009, most of the commissioning tasks were completed and T2K began accumulating the neutrino beam data for physics analysis in January 2010. This first series of the physics runs continued till the end of June, 2010 and defines the Run 1 data taking period. During the summer shutdown, new kicker magnets were installed in order to allow an operation of the beam with the designed number of 8 bunches per spill. The data taking resumed in November 2010 but was stopped dramatically on March 11th 2011, when the country was hit by its most powerful earthquake to date. As we know the earthquake was followed by the tsunami and the events at the Fukushima Nuclear power plant, causing colossal human and material loss in addition to disastrous consequences for the environment. Repair work on the experiment is currently ongoing and data taking is expected to resume soon.

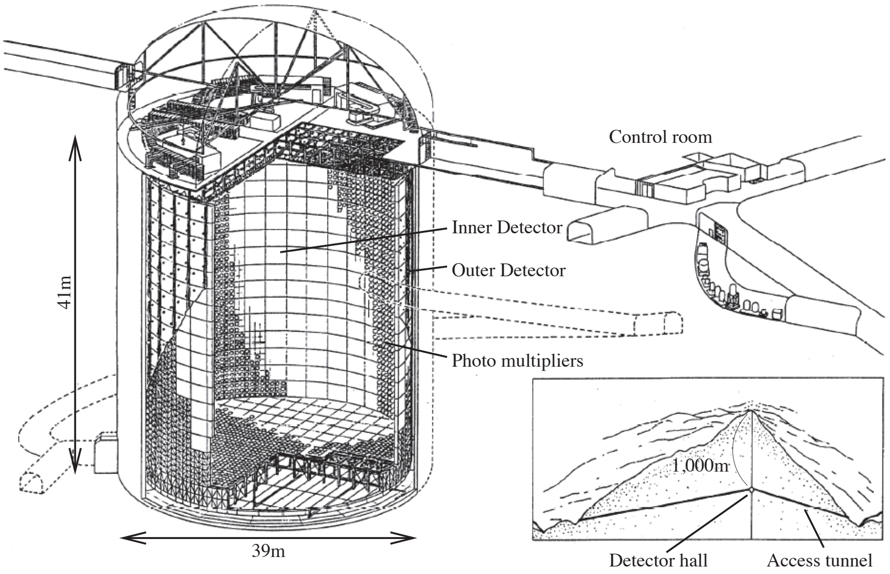

Figure 2.5: A schematic view of the Super-Kamiokande Detector. The figure is from [102].

2.2 Goals and analysis strategy in T2K

By collecting 3.75 MW×10^7 equivalent POT (protons on target), T2K aims at improving the knowledge on the atmospheric parameters by searching for ν_μ disappearance from the beam and measuring θ_{13} by looking for the appearance of electron neutrino signals. From Sections 1.6.4 and 1.6.5, both these neutrino flavor transitions in T2K are approximated by:

$$P(\nu_\mu \to \nu_\mu) = 1 - \sin^2 2\theta_{23} \sin^2 \left(\frac{\Delta M^2 L}{4E}\right) \tag{2.1}$$

$$P(\nu_\mu \to \nu_e) = \sin^2 \theta_{23} \sin^2 2\theta_{13} \sin^2 \left(\frac{\Delta M^2 L}{4E}\right) \tag{2.2}$$

Where the interference terms with the $\mathcal{CP}$ conserving and $\mathcal{CP}$ odd phases are not shown in the latter.

These parameters will be probed by using the measurements of both near (ND280 detector) and far (SK) detectors. As has been seen in Section 1.4, the signals in the region of interest for T2K are dominated by charged-current quasi-elastic reactions (CCQE) ($\nu_l + n \to l + p$, l=μ, e). In both near and far detector, the neutrino energy E_ν can be reconstructed as E_ν^{rec} by measuring the lepton momentum p_l and angle θ_l with respect to the beam direction:

$$E_\nu^{rec} = \frac{2M_n E_l - (M_n^2 + m_l^2 - M_p^2)}{2\,(M_n - E_l + p_l \cos\theta_l)} \tag{2.3}$$

where M_n, M_p and m_l are the mass of the neutron, proton and lepton, respectively. The target nucleon potential is neglected (the nucleon is assumed to be at rest).

For both analyses, the measurements are based on comparing the number of CCQE events observed in SK with the expectation. The expected flux at SK is extrapolated from the measurements at the near detector using the beam Monte Carlo (see Section 2.5).

2.2.1 ν_μ disappearance

One of the goals of T2K is to reach a 1% precision on $\sin^2 2\theta_{23}$ and 3% on ΔM^2 ($\delta(|\Delta M^2|) = 10^{-4}$ eV^2). As demonstrated in Equation 1.50 a precise knowledge of these atmospheric parameters is also important for the measurement of θ_{13}. The main source of backgrounds for the ν_μ disappearance analysis are non quasi elastic (nQE) events. A CCQE interaction is not fully characterized in SK, since the daughter proton is generally produced below its Cerenkov threshold of 1050 MeV/c and only the lepton is reconstructed. Around the T2K beam energy, there is a fairly large contribution from nQE events which include single pion production or deep inelastic scattering (see Figure 1.1). In such interactions the daughter hadrons are generally also produced below the Cerenkov threshold and only the outgoing lepton will be measured, making it impossible to distinguish from a CCQE event. Using Equation 2.3 for a nQE interaction will lead to an under-estimate of the neutrino energy which will consequently introduce distortions in the oscillation spectra. Around 1 GeV, the main nQE background for the ν_μ analysis, is the CC1π interaction, where the pion is produced below the Cerenkov threshold. The ratio of nQE/CCQE events will be measured in the ND280 and extrapolated to SK.

2.2.2 ν_e appearance

The main objective of T2K is the measurement of θ_{13}. The aim is to reach a sensitivity of $\sin^2 2\theta_{13}$=0.006 at 90% C.L. Since θ_{13} is small, the number of ν_e appearance events will be consequently limited. Therefore accurate predictions of background in the ν_e appearance is a key factor in reducing the overall systematic uncertainty. The major background to the ν_e appearance measurement is π^0 production from ν_μ NC interactions (NCπ^0). The resulting e^+, e^- pair will produce two adjacent e-like rings which may be reconstructed as a single ring and mimic a ν_e interaction. This background will be quantified by the P0D in the ND280 detector, by measuring the NCπ^0 cross section on water. Another important source of background is intrinsic beam ν_e contamination of the beam. The ν_e's that contribute to the beam, are mainly produced from kaon and muon decay (see Section 2.4). This background will also be measured at the ND280.

It is important to notice that, in both measurements, most of the background interactions occur for neutrinos having a slightly higher energy than the T2K beam peak energy. This further underlines the importance of the off-axis configuration which reduces the amount of background by providing a narrow beam peaked around 600 MeV.

The goal of the ND280 is to measure the un-oscillated spectra to compare with that of SK, but also to provide the necessary background and cross-sections measurements. Both signal and background however must be accurately extrapolated to SK.

2.3 The beam Monte Carlo simulation: JNUBEAM

In order to predict the neutrino fluxes at ND and SK, a neutrino beam Monte Carlo simulation, called JNUBEAM , has been developed. The simulation code is based on GEANT 3.21 [103] for particle propagation, while in the original release (JNUBEAM 10a) primary and secondary interactions are simulated by the GCALOR model [104]. Since early 2011 and for the published T2K ν_e appearance result FLUKA [105] tuned to the NA61/SHINE measurements is used to simulate the primary interaction. This later version will be discussed in Section 6.5 once the NA61/SHINE analysis has been presented. For the moment, the data presented in this section is taken from the JNUBEAM 10a simulation. The quoted numbers and plots are just for the purpose of general understanding and in that respect the differences between the two releases are marginal. Particles are propagated through the geometry and magnetic fields of the beam line including target, cooling envelope, magnetic horns, decay pipe and beam dump. Protons with a kinetic energy of 30 GeV are injected into the 90 cm long graphite target. The beam profile is assumed to be Gaussian-like and the beam is centered on the target axis with no divergence [106]. The produced secondaries are focused in the horn magnets and are propagated through the beam line geometry until they decay into neutrinos. The neutrino tracks are then extrapolated to ND and SK. A detailed description of JNUBEAM package can be found in [107, 108].

2.4 Composition of the T2K neutrino beam

The main decay channels and branching ratios of the neutrino parent particles are given in Table 2.1. The shape of the ν_μ and ν_e spectra at the near detector estimated with JNUBEAM are shown in Figure 2.6 along with the contributions of the corresponding parent particles. This contribution is also summarized in Table 2.2. In summary, ν_μ's are primarily produced from charged pion decay at the peak neutrino beam energy (0.6 GeV) and two body kaon decay ($\mathrm{K}^\pm_{\mu2}$) at higher energies. The main contributions to the ν_e flux at the peak neutrino energy are from muon decay. Above 2 GeV, however, the quasi totality of the ν_e flux comes from the kaon 3-body decay ($\mathrm{K}^\pm_{e3}$) with a non negligible contribution from K^0_L decay.

Finally the ν_e flux relative to ν_μ in the absence of $\nu_\mu \rightarrow \nu_e$ oscillations is expected to be about 1.1 % integrated over all energies [108].

Channel	B_r[%]
$\pi^\pm \rightarrow \mu^\pm \nu_\mu(\bar{\nu}_\mu)$	99.9877
$\mu^\pm \rightarrow e^\pm \nu_e(\bar{\nu}_e)\bar{\nu}_\mu(\nu_\mu)$	100
$K^\pm \rightarrow \mu^\pm \nu_\mu(\bar{\nu}_\mu)$	63.55
$K^\pm \rightarrow \pi^0 e^\pm \nu_e(\bar{\nu}_e)\ (K^\pm_{e3})$	5.07
$K^0_L \rightarrow \pi^\pm e^\mp \nu_e(\bar{\nu}_e)\ (K^0_{e3})$	40.55
$K^\pm \rightarrow \pi^0 \mu^\pm \nu_\mu(\bar{\nu}_\mu)\ (K^\pm_{\mu3})$	3.35
$K^0_L \rightarrow \pi^\pm \mu^\mp \nu_\mu(\bar{\nu}_\mu)\ (K^0_{\mu3})$	27.04

Table 2.1: Main decay channels and branching ratios of neutrino parents used in JNUBEAM .

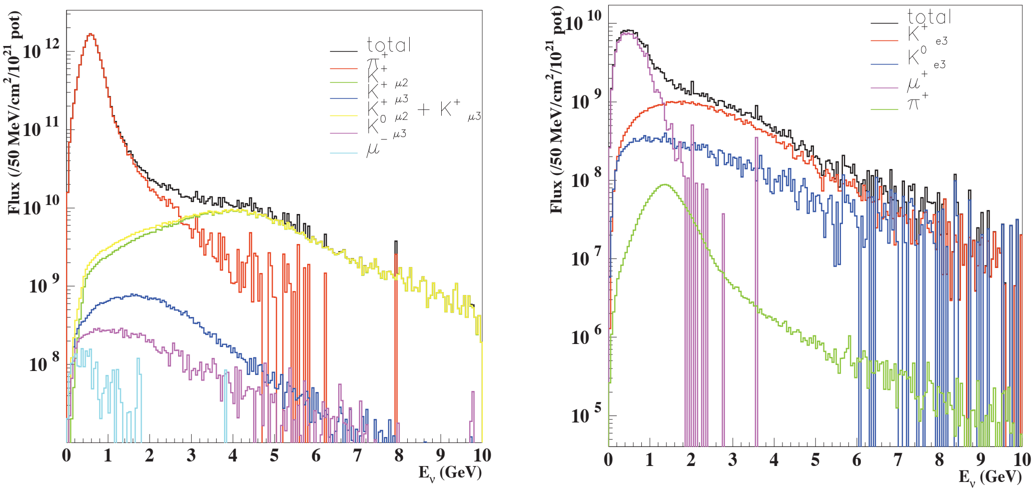

Figure 2.6: Composition of the ν_μ (left) and ν_e (right) energy spectra at the ND280. The figures are from [106].

ν species	**Parent particle**									
	$\pi^\pm$		$K^\pm_{(\mu,e)2}$		$K^\pm_{(\mu,e)3}$		K^0_L		$\mu^\pm$	
	%	$\langle E \rangle$	%	$\langle E \rangle$	%	$\langle E \rangle$	%	$\langle E \rangle$	%	$\langle E \rangle$
ν_μ	95.5	0.69	4.2	4.15	0.2	2.13	0.1	2.10	<0.01	0.80
ν_e	1.0	1.58	-	-	30.7	2.48	11.1	2.52	57.2	0.62

Table 2.2: Contribution to the ν_μ and ν_e flux at the ND280 near detector. The quoted mean energies are in GeV.

2.5 Prediction of the flux at SK

Both ν_μ and ν_e analyses are based on the comparison of the observed flux at SK with predictions with or without oscillations. The predicted flux at SK (Φ^{exp}_{SK}) is extrapolated from the measured energy spectra at the ND280 (Φ_{ND}) with the so called far to near ratio $R_{F/N}$:

$$\Phi^{exp}_{SK}(E_\nu) = R_{F/N}(E_\nu).\Phi_{ND}(E_\nu) \tag{2.4}$$

The far to near ratio (F/N ratio) is obtained by estimating the fluxes at the ND280 and SK with JNUBEAM ($\Phi^{MC}_{SK}(E_\nu)$ and $\Phi^{MC}_{ND}(E_\nu)$ respectively).

If the neutrino source is point-like and isotropic, the F/N ratio is given by the ratio of the square of the distances from the neutrino source (solid angle), and is energy independent. In practice however, as is illustrated in Figure 2.7, since the near detector is close to the source it accepts a larger solid angle and is sensitive to the finite extension of the production region. As a consequence the mean value of the distributions of $\Phi^{MC}_{SK}(E_\nu)$ and $\Phi^{MC}_{ND}(E_\nu)$ are slightly shifted with respect to one another. This leads to a rather complicated F/N ratio which is determined by the geometry of the source and by the momentum distributions of hadrons at production .

This is illustrated in Figure 2.8 and Figure 2.9 where the simulated ν_μ and ν_e fluxes at near and far detector, along with their far to near ratios are plotted. As can be seen the ν_μ flux at the near detector is rather different than that at SK, leading to the strongly energy dependent far to near ratio.

In summary, the far to near ratio, and hence the SK observables, depends on the flux of secondary hadrons produced at the target. Therefore, a detailed knowledge of the hadron production at the T2K target is necessary to correctly predict the neutrino flux.

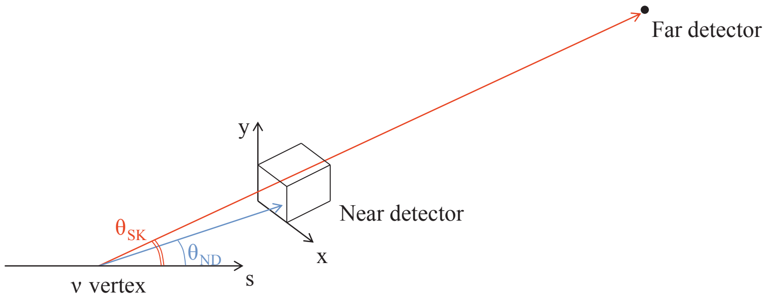

Figure 2.7: Illustration of the near and far detectors showing their acceptance difference from a viewpoint of the J-PARC site. θ_{ND} and θ_{SK} are the directions from a given neutrino vertex to the near and far detectors, respectively, relative to the beam axis s. Since the source is point like for SK, θ_{SK} is always the same independent from the neutrino production vertex position. On the other hand, the value of θ_{ND} depends on the position of the neutrino production vertex.

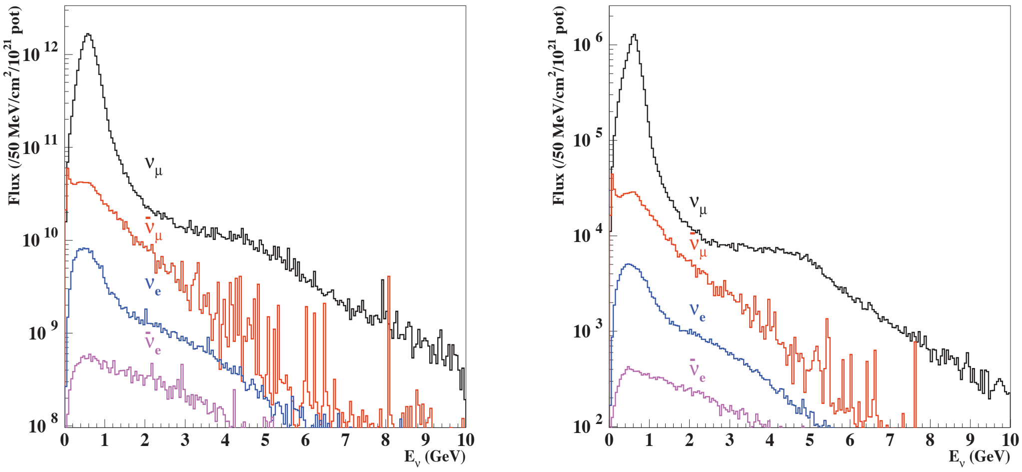

Figure 2.8: Energy spectra for ν_μ (black), $\bar{\nu}_\mu$ (red), ν_e (blue) and $\bar{\nu}_e$ (purple) at the ND280 (left) and at the far detector (right). The flux at the near detector has a slightly higher mean energy due to the larger solid angle subtended by the detector and the finite extension of the production region.

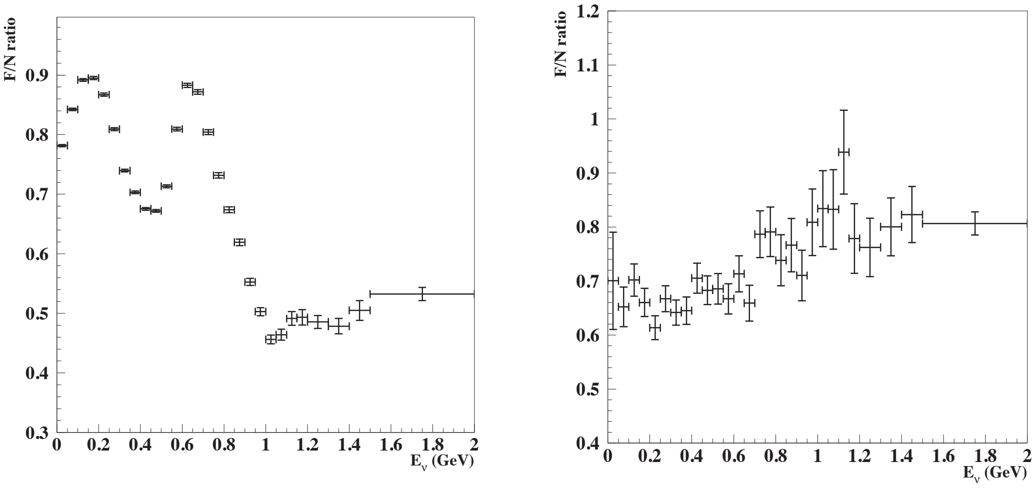

Figure 2.9: Far to near ratio of the ν_μ (left) and ν_e (right) fluxes.

2.6 T2K physics requirements

The expected number of events at SK as a function of the reconstructed neutrino energy, E_ν^{rec} is given by:

$$
\begin{aligned}
N(E_\nu^{rec})_{SK}^{exp} &= \int \left[\Phi_{SK}^{exp} \;.\; r(E_\nu, E_\nu^{rec}) \;.\; P_{osc}(E_\nu) \;.\; \sigma(E_\nu) \;.\; \epsilon_{SK}(E_\nu)\right] \mathrm{d}E_\nu \\
&= \int \left[\Phi_{ND} \;.\; R_{F/N}(E_\nu) \;.\; r(E_\nu, E_\nu^{rec}) \;.\; P_{osc}(E_\nu) \;.\; \sigma(E_\nu) \;.\; \epsilon_{SK}(E_\nu)\right] \mathrm{d}E_\nu
\end{aligned}
\tag{2.5}
$$

Where P_{osc} is the oscillation probability, σ the neutrino cross-section, ϵ_{SK} the detection efficiency and $r(E_\nu, E_\nu^{rec})$ the detector response function representing the probability to observe the true neutrino energy E_ν as E_ν^{rec}. Φ_{SK}^{exp} is the expected flux at SK which is extrapolated from the measured flux in the ND280 (Φ_{ND}) with the corresponding F/N ratio ($R_{F/N}$).

This formula is of course valid for both signal and background expectations in SK. In order for T2K to reach its physics goals, requirements on detector performances, efficiencies and overall systematic uncertainties are rather stringent. The error on the expected number of events at SK can be summarized from the errors on the different terms of Equation 2.5. The energy determination in the near detector should reach a precision as good as the current 2% resolution at SK; the detection efficiency at the ND280, should also reach a comparable level to that of SK (∼1 %); as has already been mentioned, our knowledge of neutrino-nucleon interactions around 1 GeV is limited but is of primary importance for the T2K background predictions. To achieve the T2K goals, the systematic error on the prediction of background events has to be less than 10%, which requires to measure the corresponding cross-sections within ∼5% in the ND280.

Since errors on the F/N ratio influence not only the signal but also the background predictions, it is of primary importance to keep them as low as possible. Sources of errors on the F/N ratio arise from the MC simulation chain (geometry, etc..) and from the model which is used to produce the hadrons in the target. The goal is to reduce the error on the F/N ratio to a negligible level compared to other contributions. It was estimated [87] that both ν_μ and ν_e F/N ratio should be known within 2-3%:

$$\delta\left[R_{F/N}(E_\nu)\right] = 2 - 3\% \tag{2.6}$$

2.7 Need for a hadron production measurement

The T2K neutrino flux predictions depend on the choice of the hadronization model used in JNUBEAM to treat primary and secondary interactions in the target. The systematic uncertainties on the neutrino flux predictions and the F/N ratio that would come from the use of such models, have been estimated by comparing the results from three different model: GHEISHA [103] (default GEANT3 hadronization model), GFLUKA [103] and GCALOR [104]. Figure 2.10, clearly shows that the absolute neutrino fluxes at SK could be different by a factor of up to 2 depending upon the choice of model. Those variations in the fluxes would furthermore influence the F/N ratio. In Figure 2.11 it is demonstrated that the ν_μ F/N ratio varies by more than 3 % as a function of the neutrino energy depending on the model. This uncertainty is unsatisfactory with respect to the required 2-3% error on the F/N ratio. With such large variations in the flux predictions, the objective of 5% on the absolute neutrino cross-section measurements in the near detector, would also be compromised.

Therefore, using the T2K beam line simulation without adequate particle production data to constrain the hadron production model, would not allow T2K to fulfill its physics goals.

There exists no cross-section measurements at the energy of the T2K proton beam. The nearest data of proton on carbon were taken at 12 GeV by the HARP experiment [109] and at 158 GeV by NA49 [110]. Extrapolations to the T2K beam energy are not very reliable, since they would be based on parametrisation of existing data taken at different energies and with different target materials. Therefore the NA61/SHINE experiment provides the reference data by measuring the secondary hadron production in proton carbon interactions at 30 GeV kinetic energy.

2.8 Requirements on the NA61/SHINE measurements

NA61/SHINE is an experiment located in the CERN North Area making use of the SPS beam. An extensive description of the detector is given in the next chapter, in this section I summarize the requirements on the NA61/SHINE measurements from the T2K physics goals.

2.8.1 Target contribution

To fully characterize the T2K flux and to better constrain the F/N ratio, the data is collected in p+C interactions at 30 GeV using two different targets:

- data with a 2 cm thick target to explicitly measure the total proton carbon production cross-section and inclusive production cross-sections of secondary charged hadrons;
- data with the T2K replica target to provide information on hadrons produced in re-interactions in the target.

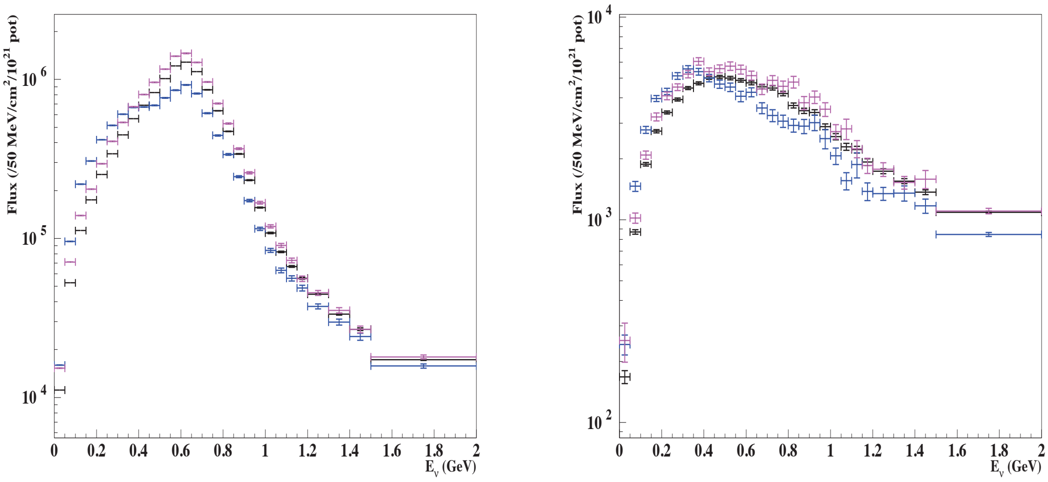

Figure 2.10: ν_μ (left) and ν_e (right) spectra at the far detector. Predictions are shown for different models used for the simulation of both primary and secondary interactions: GCALOR (black), GFLUKA (purple), GHEISHA (blue).

	Thin target	replica target
Material	isotropic graphite	isotropic graphite
Density [g/cm^3]	1.8395	1.831
Dimensions [cm]	$2.5 \times 2.5 \times 2.0$	$\varnothing = 1.6$ length=90
Interaction length	0.04 λ_I	1.9 λ_I

Table 2.3: Specifications of the thin and replica targets

One is referred to as thin target and the other as long target or "T2K replica target", their dimensions and material properties are summarized in Table 2.3. The two measurements are complementary. The thin target data is important for measuring the primary particle production in p+C collisions without distortions due to target re-interactions. The results are used to tune the generator used for the primary interaction in JNUBEAM . Secondary interactions in the target or in the target cooling envelope (e.g: helium pipe, horns, decay tunnel, etc,) will be modeled by JNUBEAM . In addition, the results will also allow to test and improve existing hadron production models in this energy region which is not well constrained by measurements at present.

In the T2K replica target campaign all the hadrons exiting the target are measured. Therefore the long target measurements (unless primary and secondary interaction vertices are reconstructed in the target) cannot provide production cross-sections. These measurements are of primary importance however, since hadrons from target re-interactions account for a large fraction of the neutrino flux. Hadrons which are not produced in the primary interaction are called indirect contributions to the neutrino flux. Figure 2.12 shows that the indirect contributions account for about 42 % of the ν_μ flux at peak energy, including 30% of re-interactions in the

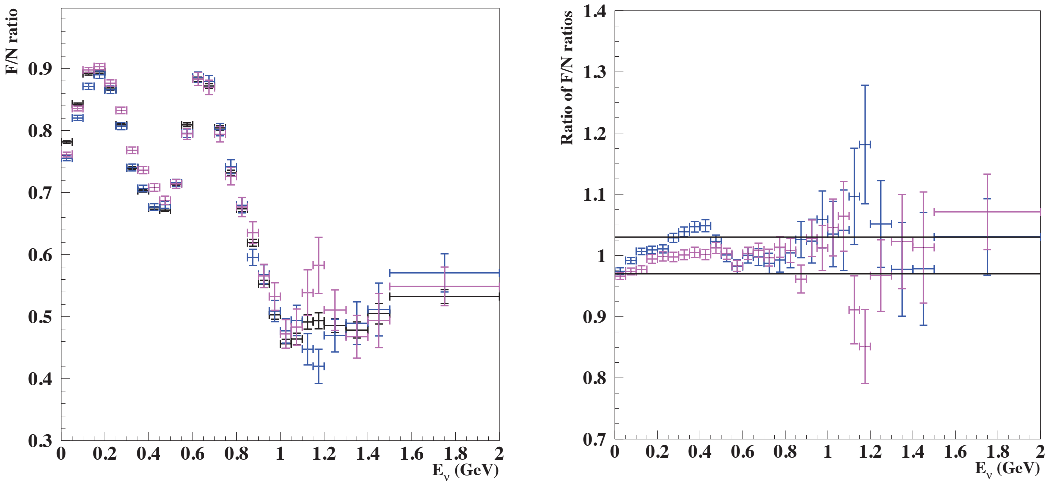

Figure 2.11: Relative fraction of the GHEISHA (blue) and GFLUKA (purple) models with respect to the GCALOR predictions on the ν_μ (left) and ν_e (right) F/N ratio. The horizontal black lines show a ±3 % band.

target [106].

2.8.2 Particle species, phase space and statistics

The main particles which contribute directly or through decay chains to the T2K neutrino beam are $\pi^\pm$, $K^\pm$, K_L^0 (see Figure 2.6). Protons also contribute via re-interactions in the target. The phase space regions of the different particle species at production have been simulated with JNUBEAM by studying the laboratory momentum, p, and polar angle θ distributions of those which contribute to the neutrino flux in the T2K far detector. The corresponding $\{p, \theta\}$ plots are shown for π^+, K^+ and protons in Figure 2.13. Pion and kaon distributions are mainly peaked in the momentum range of $1 < p < 10$ GeV/c and production angle $0 < \theta < 250$ mrad. Protons which contribute are those produced at a much lower angle (< 50 mrad) and high momentum ($10 < p < 31$ GeV/c). The minimal requirement on NA61 is that its geometrical acceptance fully covers those regions.

Statistical estimates were performed by introducing random variations on charged pions belonging to the T2K phase space and studying the amount by which those fluctuations affect the variations on the energy spectrum at the near and far detectors, and on the corresponding far to near ratio. The results show [107] that 5% statistical fluctuations on the yields meet the goals of the 5% precision on the absolute flux and the 2-3% on the F/N ratio. In terms of statistics required for the long target, it was estimated, based on NA61/SHINE 2009 trigger efficiency, that 10 M triggers are sufficient to meet the required goals. The replica target data must be reconstructed in 6 equidistant longitudinal bins because absolute neutrino fluxes and far to near ratio predictions are sensitive to the exit position of the neutrino parent particles on the surface of the target [106]. Since the NA61 detector acceptance is similar for both target configurations, and the longitudinal binning constraint does not apply for the thin target, a factor 6 less triggers would be a rough estimate of the required statistics for the thin target. In total about 6 M thin

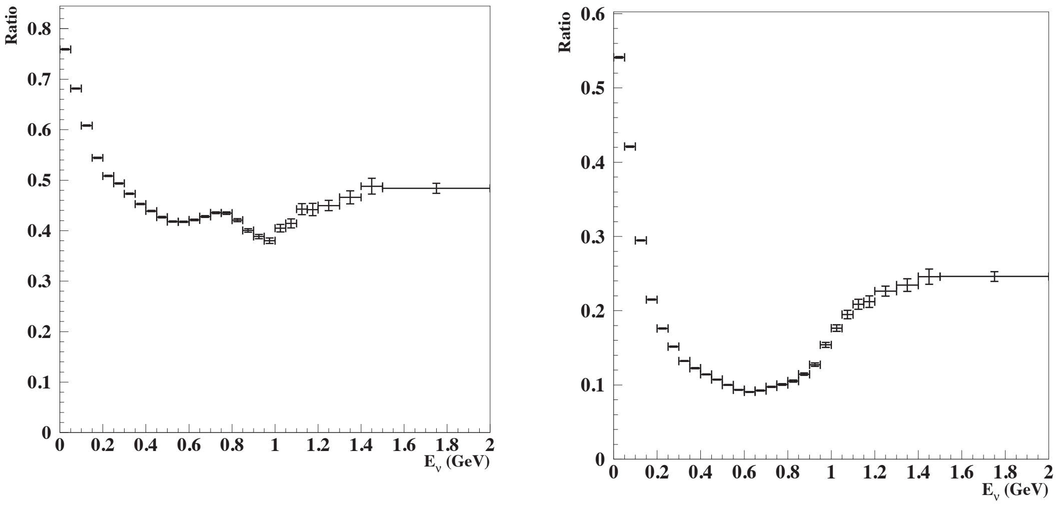

Figure 2.12: Ratio of indirect to total contribution [left] and non-target to total contribution [right] at the far detector for ν_μ. Secondary interactions are responsible for about 41% of the neutrino flux at peak energy, only 10% of which come from non target interaction. The figure is from [106].

target triggers were anyhow collected (see Section 3.4).

2.9 Input from other hadron production experiments

With increased intensities of accelerators, results from the next generation of accelerator neutrino experiments such as T2K, become dominated by systematic uncertainties linked to the unsatisfactory prediction of the neutrino flux. Over the past years, several hadron production experiments have been conducted to provide the needed reference data. These experiments have been conducted over a range of incident proton beam momenta from around 10 GeV/c to 450 GeV/c, using different target materials, mostly beryllium, aluminum, copper and lead [111].

The HARP experiment [112] at CERN-PS was a large acceptance spectrometer to provide such reference hadro-production measurements. Data were taken for various incident beam particle type (protons, charged pions), beam momentum (from 1.5 to 15 GeV/c), nuclear target material (from hydrogen to lead), and nuclear target thickness (from 2% to 100% λ_{int}). The results were subsequently applied to the final analysis of K2K [51], and MiniBooNE [113]. In K2K, the data from 12.9 GeV/c protons interacting on a thin aluminum target ($\lambda_{int} = 5\%$) had a significant impact on the final disappearance analysis . It allowed a reduction of the dominant systematic error associated with the calculation of the far to near ratio from 5.1% to 2.9% and thus an increased K2K sensitivity to the oscillation signal [114]. The double-differential inelastic cross-section for the production of positive pions from proton beryllium interactions at 8.9 GeV/c [113] have also contributed to the MiniBooNE results. In both analyses, the Sanford and Wang parametrization [115] was used to extend the pion differential production cross section across different incident primary beam momenta.

More recently, the MIPP experiment[116] at Fermilab has also been constructed to study particle production in the energy range from 5 to 120 GeV beam energy on various targets including beryllium and carbon. Measurements at 120 GeV/c with the NUMI graphite target are

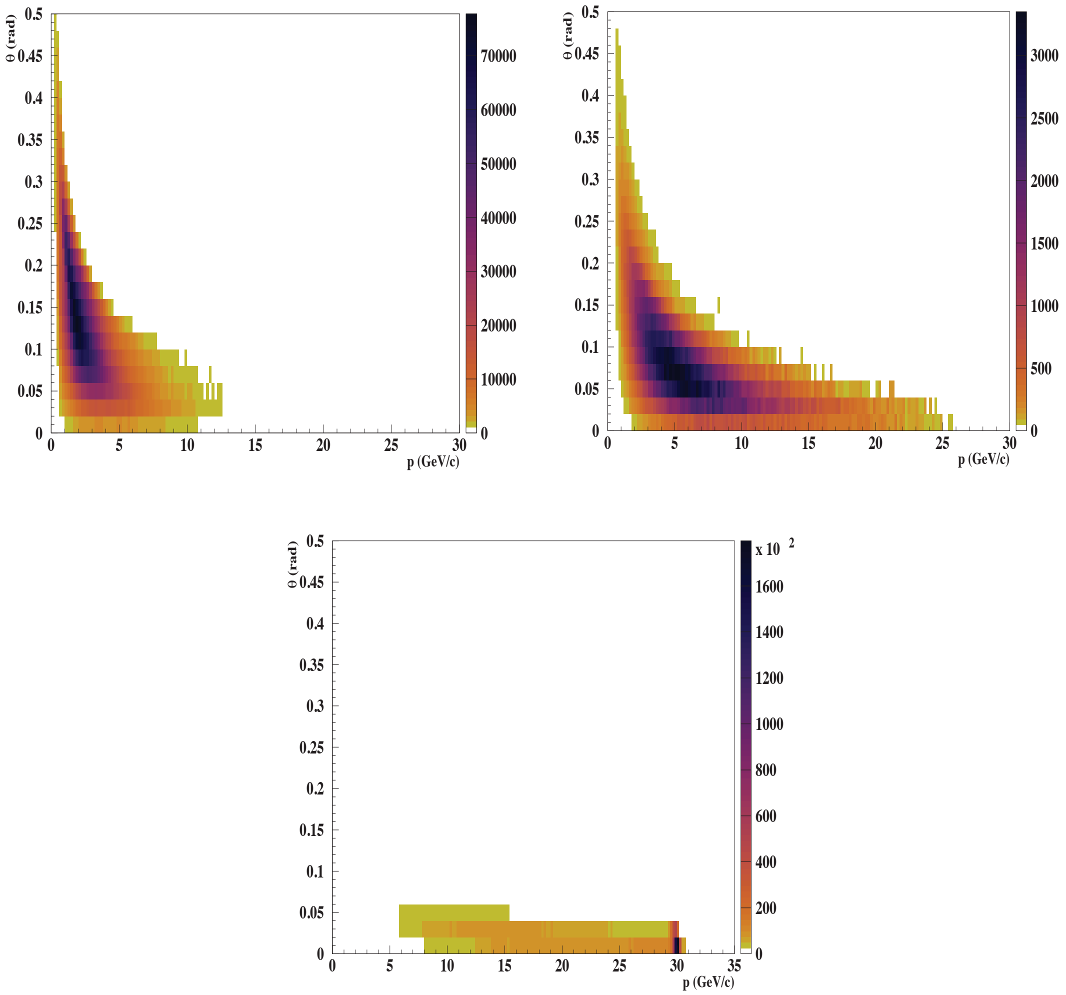

Figure 2.13: $\{p, \theta\}$ distributions of primary particles giving neutrinos in the far detector. The spectra are shown for π^+[top-left] and K^+ [top-right]. Protons which contribute through re-interactions in the target are shown in the bottom plot.

expected to benefit the forthcoming NOνA experiment, also in terms of reduction of systematic errors on the F/N ratio.

The NA61/SHINE experiment, in addition to measuring the proton carbon cross section at 30 GeV for T2K, pursues a program of hadro-production measurements for the cosmic air shower experiments, Pierre Auger [117] (π+C 158 and 358 GeV/c) and KASCADE [118].

2.10 Summary

By providing hadron production reference data, NA61/SHINE aims at constraining the F/N ratio which is at the core of the T2K analysis since it is used to predict the flux of both signal and background at SK. Past measurements have shown that input from hadron-production experiments has helped reduce the systematic errors on the final oscillation results. In NA61/SHINE, these measurements have been performed with both replica and thin targets. Let us stress again that both measurements are necessary. The replica target measurements give an accurate estimate of more than 90% of the neutrino flux in T2K, thus removing almost all model dependencies of hadronic re-interaction in the target, along with their large associated systematic uncertainties. The thin target data provides direct information on the production cross-section and can directly be compared with various event generators used in JNUBEAM . Furthermore by comparing the thin target spectra with those from the long target, the spectra corresponding to the production of secondaries in the target may be obtained and provide useful insight on the production of secondaries in JNUBEAM . A dedicated analysis of the long target data has been performed in [106].

This thesis gives a detailed description of results obtained from data collected in 2007 with the thin target. Charged pion cross-sections have been extracted and published [119] and although the data sample was statistically limited K^+ spectra where also obtained in a more restricted phase-space. These results were also published in [120].

In the next chapter, the NA61/SHINE hadron production experiment is presented along with the improvements that have been implemented to extend the acceptance of the spectrometer in the phase space regions needed for the T2K measurements. A new time-of-flight detector was added for that matter, its construction and calibration is described in Chapter 4. The new time-of-flight detector provided the particle identification to extract the K^+ and π^+cross sections which are described in the two last chapters of this thesis. At the very end of my Ph.D. I also extracted proton cross-sections. As was mentioned previously, the knowledge of proton production is essential since protons contribute to the neutrino flux through target re-interactions. Since the analysis which lead to the proton cross-sections is based on exactly the same methods as for the charged pions and kaon cross-section the details are not discussed. The preliminary results are shown in Appendix H.

Chapter 3

The NA61/SHINE Experiment

The NA61/SHINE experiment is a large acceptance spectrometer at CERN SPS. The physics program mainly consists of three main subjects. In addition to measuring the proton carbon interactions at 31 GeV/c for T2K it collects a variety of data used for the description of cosmic-ray air showers in the KASCADE [118] and Pierre Auger [117] experiment. It also studies hadron production in p+p, p+A, and A+A collisions needed as reference data for a better understanding of nucleus-nucleus reactions. The energy dependence of hadron production properties will also be measured in p+p and p+Pb interactions as well as in nucleus-nucleus collisions, with the aim of identifying the properties of the onset of deconfinement and finding evidence for the critical point of strongly interacting matter. NA61/SHINE inherits its main detector components from the NA49 spectrometer [121] which was developed for the study of hadron production and offered a typical precision on the measured particle yields of about 5-10% [110] (3% for p+p data [122]). To meet the requirements of the new program, the spectrometer has been upgraded with faster readout electronics and additional detectors.

The first section describes the main experimental components as well as the configuration of the beam-line during the T2K data taking period. The particle identification method is then briefly discussed in Section 3.6, this subject will be addressed in more detail in the next chapters. The last section presents the track reconstruction methods and gives an overview of the simulation software.

3.1 Experimental components

The NA61/SHINE experiment is a large acceptance hadron spectrometer in the North Area using the H2 beam-line of the CERN SPS. The schematic layout of the detector is shown in Figure 3.1 together with the overall dimensions. The principal components of the current detector were constructed and used by the NA49 collaboration. The main tracking devices of the spectrometer are 4 large volume Time Projection Chambers (TPCs).

Two of the TPCs, the vertex TPCs (VTPC-1 and VTPC-2 in Figure 3.1), are located in a free gap of 100 cm between the upper and lower coils of the two superconducting dipole magnets. Their maximum combined bending power is 9 Tm. In order to optimize the acceptance of the detector at 31 GeV/c beam momentum, the magnetic field used during the 2007 data taking

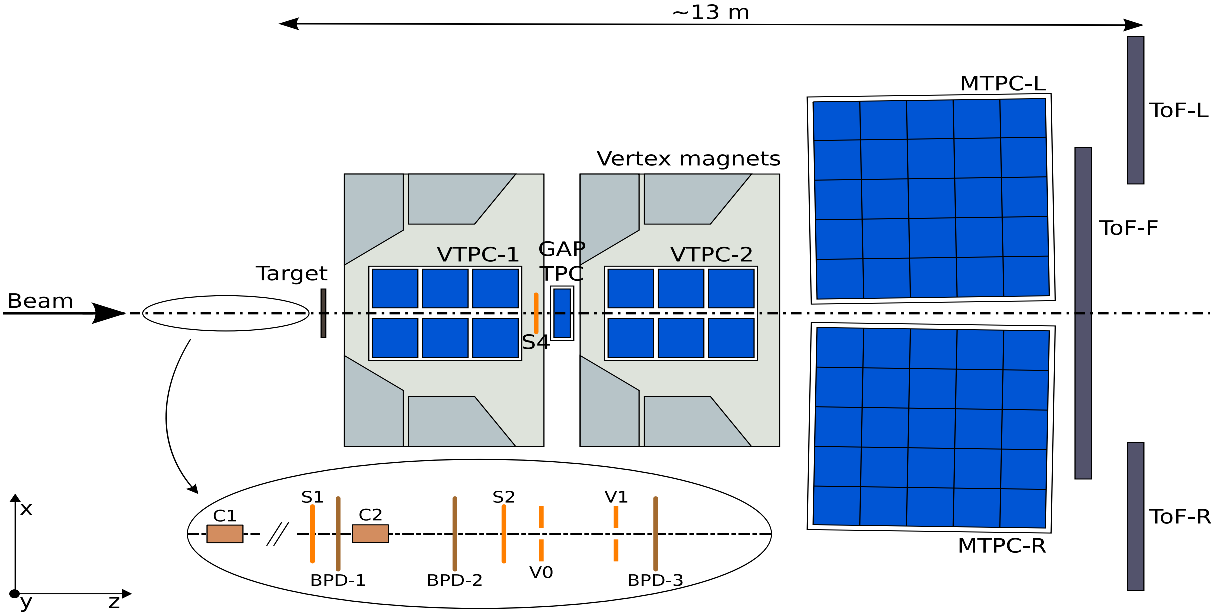

Figure 3.1: The layout of the NA61/SHINE set-up in the 2007 data taking.

period was set to a bending power of 1.14 Tm. Two larger TPCs (MTPC-L and MTPC-R) are positioned downstream of the magnets symmetrically to the beam line. The presented TPC system is extended in the beam region with a small-size chamber, the Gap-TPC (GTPC). The device is placed between VTPC-1 and VTPC-2 such that the beam passes through its sensitive volume. It allows to measure trajectories of high momentum charged particles, which pass through the gap of the VTPCs and MTPCs. For the analysis described in this thesis however the GTPC was not included in the track reconstruction procedure. The TPCs provide particle identification (PID) by measuring the particle's ionization energy loss per unit of length, dE/dx, in the TPC gas. The technical specifications of the TPCs are summarized in Table 3.1.

Energy loss measurements have to be backed up by independent methods in the region of minimum ionization, $\beta\gamma \approx 3$. Three Time-of-Flight (ToF) scintillator detectors are therefore installed behind the MTPC. The ToF-L and ToF-R arrays of scintillator pixels have a time resolution of better than 90 ps [121]. Before the 2007 run we upgraded the experiment with a new forward time-of-flight detector (ToF-F) in order to extend the acceptance. The ToF-F which is discussed in detail in the next chapter consists of 64 scintillator bars with photomultiplier (PMT) readout at both ends resulting in a time resolution of about 115 ps. As demonstrated in Figure 3.2, the geometrical acceptance of the spectrometer including both the TPCs and ToF-F fully covers the relevant phase-space for the T2K data taking. The ToF-F was extended in 2009 by two extra modules on either side to improve the acceptance at lower momentum (cfr also Figure 3.2).

A set of scintillation and Cherenkov counters as well as beam position detectors (BPDs) upstream of the spectrometer provide timing reference, identification and position measurements of the incoming beam particles. Details on this system are presented in Section 3.2. The target under study is installed 80 cm upstream of VTPC-1. As discussed in Section 2.8 to fully address the T2K physics requirements data must be collected with both the thin and replica target, a picture of both targets installed on the NA61/SHINE beam-line is shown in Figure 3.3. The work presented in this thesis was based on the thin target. For a detailed review of the long target analysis refer to [106]. Altogether, proton carbon interactions at 31 GeV/c with both thin and replica target were collected during dedicated periods in 2007, 2009 and 2010. The details of the available data is given in Section 3.4. During the 2008 shutdown, the readout of the TPCs and the data acquisition (DAQ) system was upgraded [123] allowing to reach a maximum event rate of about 70 Hz which corresponds to an increase of a factor of 10 with respect to the original NA49 DAQ system.

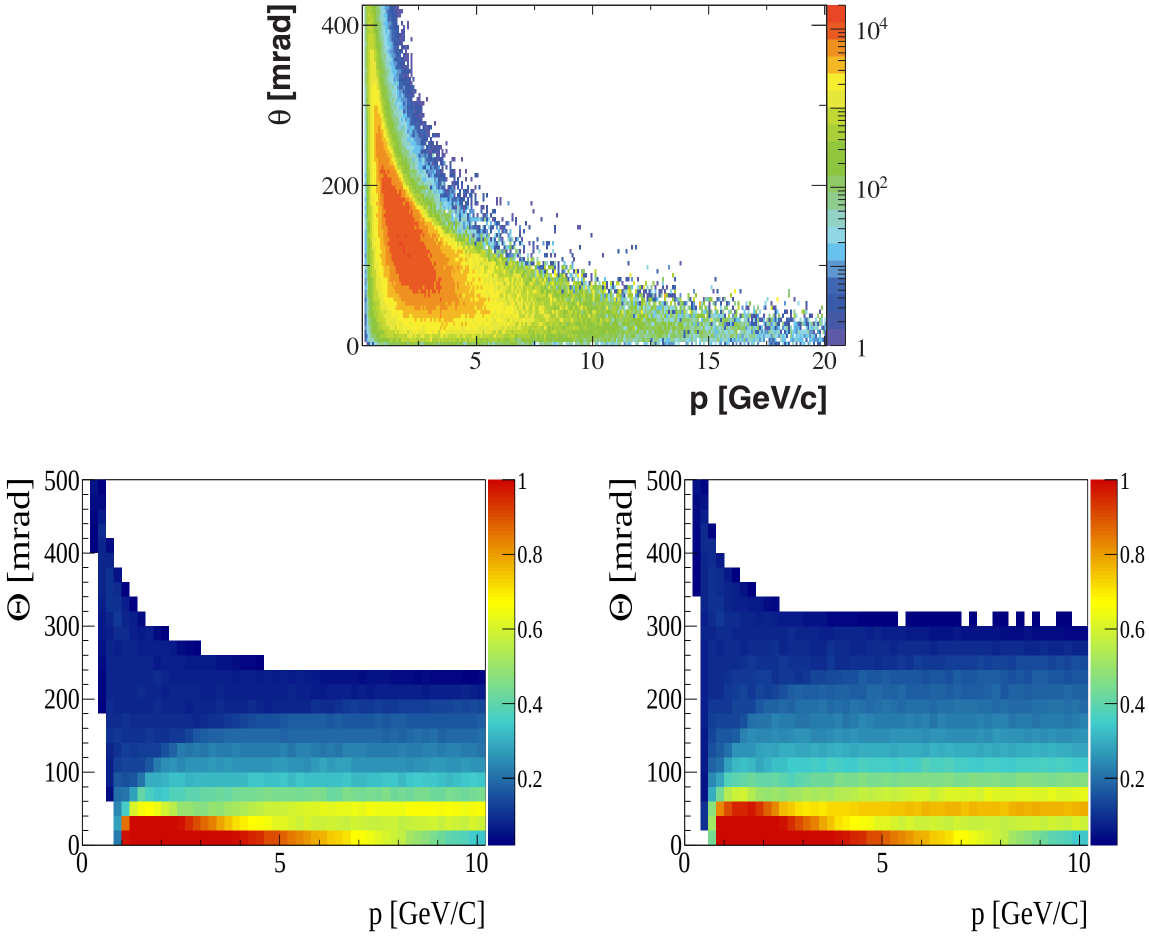

Figure 3.2: Top:$\{p,\ \theta\}$ distribution for positively charged pions weighted by the probability that their decay produces a muon neutrino passing through the SK detector. Bottom: NA61/SHINE ToF-F+TPC acceptance in the 2007 data taking (left) and with the 2009 ToF-F extension (right).

The NA61/SHINE coordinate system is a right-handed Cartesian coordinate system with origin in the middle of VTPC-2. The orientation of the coordinate system is defined by the direction towards the Jura mountains or MTPC-L (x), the drift direction of electrons in the TPCs (y) and the beam axis (z) (cfr Figure 3.1).

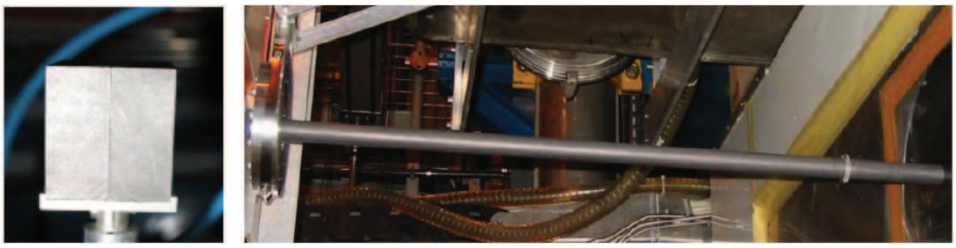

Figure 3.3: Picture of the thin and T2K replica targets.

	VTPC-1/2	GTPC	MTPC-L/R
Volume [m^3]	$2 \times 2 \times 0.98$	$0.38 \times 0.20 \times 0.59$	$3.9 \times 3.9 \times 1.8$
Gas	$Ar/CO_2(90:10)$	Ar/CO_2 (90:10)	Ar/CO_2(95.5:4.5)
Drift voltage [kV]	13	11	19
Drift velocity [cm/μs]	1.4	1.2	2.3
Drift length [mm]	666	666	1117
Number of pads	27648	672	63360
Pad dimensions [mm^2]	$35 \times 16/28$	40×28	$36/55 \times 40$

Table 3.1: Technical parameters of the NA61/SHINE TPCs.

3.2 beam-line setup

A 31 GeV/c secondary hadron beam is produced from 400 GeV protons extracted from the SPS in slow extraction mode. The beam is transported along the H2 beam-line towards the experiment. Collimators in the beam-line are adjusted to get an average beam particle rate of 15 kHz. The setup of beam detectors is illustrated in Figure 3.4. Protons from the secondary hadron beam are identified by two Cherenkov counters, a Nitrogen filled CEDAR [124] and a threshold counter, labeled C1 and C2, respectively. The CEDAR counter, using a 6-fold coincidence, provides positive identification of protons, while the threshold Cherenkov counter, operated at pressure lower than the proton threshold, is used in anti-coincidence in the trigger logic.

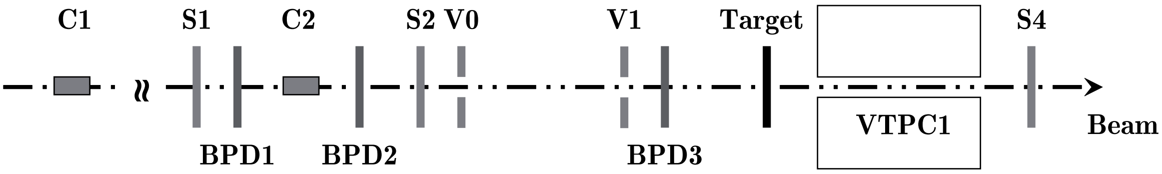

Figure 3.4: The beam-line configuration for the 2007 thin target runs.

The CEDAR absolute pressure was set to 3.3 bar and the one of the threshold Cherenkov counter to 1.65 bar. The fraction of protons in the beam was about 14%. A selection based on signals from Cherenkov counters allowed the identification of beam protons with a purity of about 99%. A consistent value for the purity was found by bending the beam into the TPCs with the full magnetic field and using the dE/dx identification method.

Two scintillation counters, S1 and S2, provide beam definition, together with the two veto counters V0 and V1 with a 1 cm diameter hole, which are collimating the beam on the target. The S1 counter provides also the timing (start time for all counters). Beam protons are then selected by the coincidence $\mathrm{S1} \cdot \mathrm{S2} \cdot \overline{\mathrm{V0}} \cdot \overline{\mathrm{V1}} \cdot \mathrm{C1} \cdot \overline{\mathrm{C2}}$.

The trajectory of individual beam particles is measured by three beam position detectors along the beam-line (BPD-1/2/3 in Fig. 3.4). These counters are small (3×3 cm) proportional chambers with cathode strip readout, providing a resolution of about 200 μm in two orthogonal directions, see [121] for more details. The beam profiles, measured by the three BPDs, are presented in Figure 3.5 for the 2007 short target data. The beam spot measured close to the target, at BPD3, is also shown in Figure 3.6 along with the divergence obtained from measurements of the beam tracks in the three BPDs. Both these figures show that the beam profiles are Gaussian shaped and the protons hitting the target (BPD3) are well confined within the 1 cm diameter of the veto counter's hole.

The beam momentum was measured directly in a dedicated run by bending the incoming beam particles into the TPCs with the full magnetic field. The measured beam momentum distribution is shown in Figure 3.7. The mean value of 30.75 GeV/c agrees with the set value of 30.92 GeV/c within the available precision of setting the beam magnet currents (≈0.5%) in the H2 beam-line.

3.3 Trigger system

The use of a thin target of only 4% of an interaction length requires an interaction trigger. Interactions are selected by anti-coincidence of the incoming beam particles with a small, 2 cm diameter, scintillation counter (S4) placed in the beam-line between the two vertex magnets (Figure 3.4). This interaction trigger is a minimum bias trigger based on the disappearance of the incident proton particle. This definition does not prevent fake triggers where the proton undergoes a large angle coherent elastic scattering on the target nuclei and does not reach S4, nor does it consider interactions where a secondary particle hits S4 preventing from triggering on the event. All these effects must be taken into account when measuring the interaction cross section for the normalization and are explained in [93].

During 2009 data taking an additional larger size veto counter, called V1′, was placed in-between V0 and V1. In 2009 it was possible to register data with several trigger conditions at the same time each of which were pre-scaled by a given factor and recorded simultaneously. They include the trigger on the beam, called T1, defined as $\mathrm{S1} \cdot \mathrm{S2} \cdot \overline{\mathrm{V0}} \cdot \overline{\mathrm{V1}'} \cdot \overline{\mathrm{V1}} \cdot \mathrm{C1} \cdot \overline{\mathrm{C2}}$ and the trigger on interactions, T2 which has the additional $\overline{\mathrm{S4}}$ requirement. Furthermore special triggers, called T3 and T4 were simultaneously recorded. They had different definitions throughout the data taking and were used for systematic beam studies.

Given the large absorption probability of the T2K replica target, there is no need of a ded-

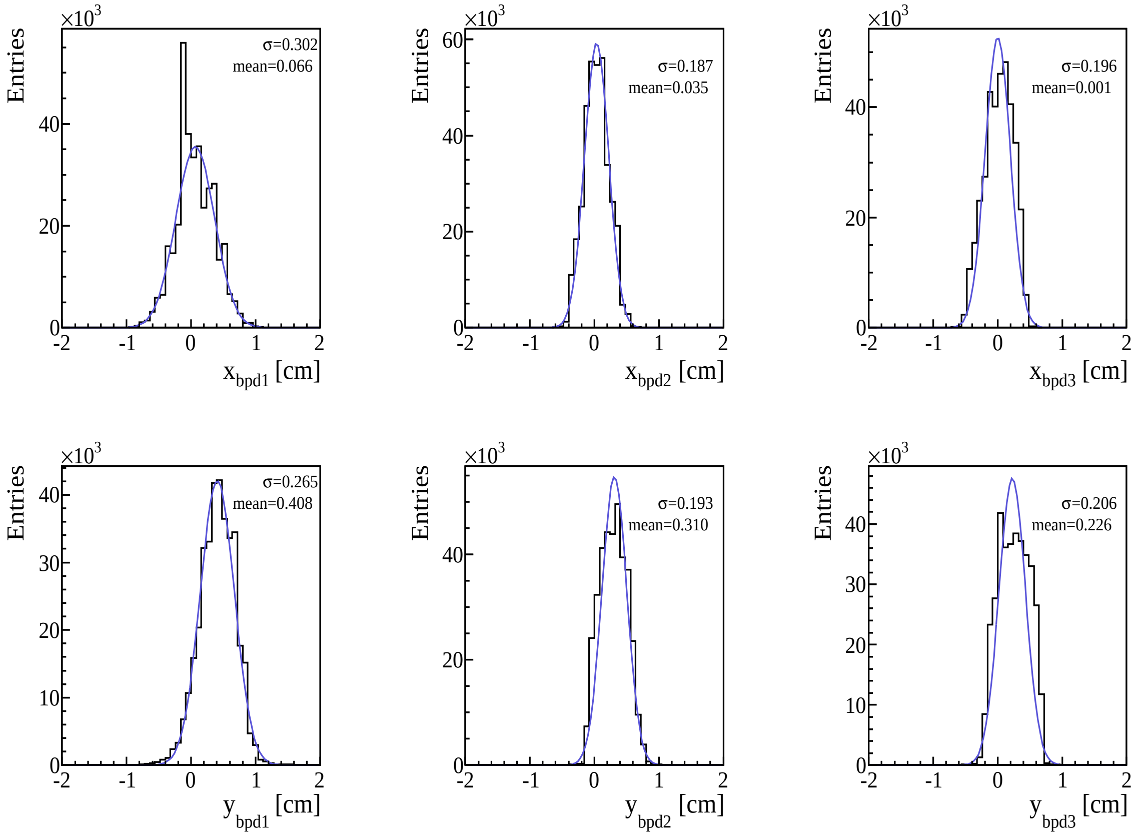

Figure 3.5: x (top) and y (bottom) profiles of the beam measured in the BPDs during the 2007 run

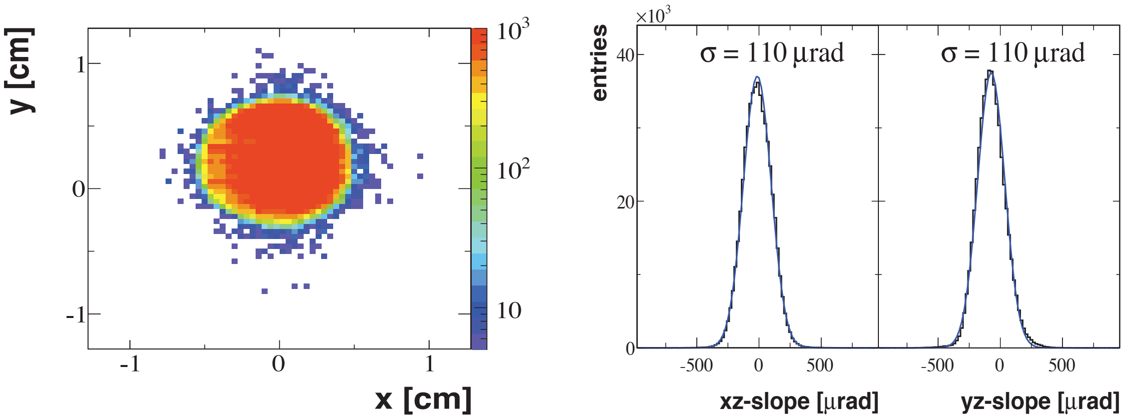

Figure 3.6: *Left:* The beam spot as measured by BPD-3 after the $\overline{\mathrm{V1}}$ cut described in the text. *Right:* The beam divergence in x and y.

icated interaction trigger, therefore all beam triggers are recorded. For the 2009 run an extra trigger counter was added, with the same cross section as the diameter of the T2K target, mounted just upstream of the target. This insured that the selected beam protons go through the target, increasing the trigger efficiency.

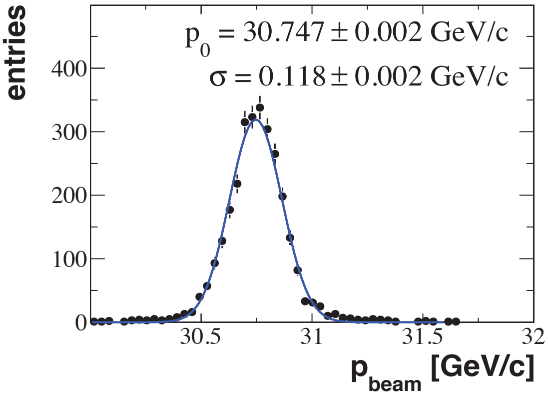

Figure 3.7: Beam momentum distribution measured by the reconstruction of beam particles in the TPCs.

3.4 Data sample collected for T2K

The total available data collected for T2K is summarized in Table 3.2. At the time of writing the 2009 and 2010 replica target data had not been analysed, therefore the quoted numbers are approximate and have not been verified in detail for their quality.

The results presented in this thesis are based on 420k interaction triggers from the 2007 thin target data set and 46 k events recorded with the carbon target removed. The latter is of importance for the evaluation of the cross section normalization (see Chapter 5).

All data further presented in this thesis,unless otherwise noted, relates to the 2007 thin target data sample.

target	$N_{trig} \times 10^3$		
	2007	2009	2010
Thin target	667	5'598	-
Replica target	230	∼4'000	∼10'000
Empty target	46	780	-

Table 3.2: number of registered triggers in 2007,2009 and 2010 for different target configurations. The quoted number of triggers for the 2009 thin target sample corresponds to approximately 4 M interaction triggers (T2).

3.5 Track reconstruction

In the TPCs, when an avalanche from drifting electrons is created on a sense wire, it induces charges on several cathode pads (see Figure 3.8). Several adjacent pads in padrow with induced signal form a cluster. In the reconstruction procedure the space information from pads is used to restore the x coordinate and the time information gives the y coordinate of the 3D cluster. This information will be used for the reconstruction of a particle trajectory. The width of the cluster represents the resolution of the TPC. It depends on a variety of parameters such as relative orientation of track and pads (β in Figure 3.8), distance electrons have to drift, geometry of pads, gas mixture, settings for electronics and so on. The precise prediction of the cluster width would be extremely complicated to calculate and is therefore measured and parametrized (as it is in every experiment) [125]. Since the gas mixture in the TPCs in NA61/SHINE differs from the one used in NA49, a new parametrization of the uncertainties was performed.

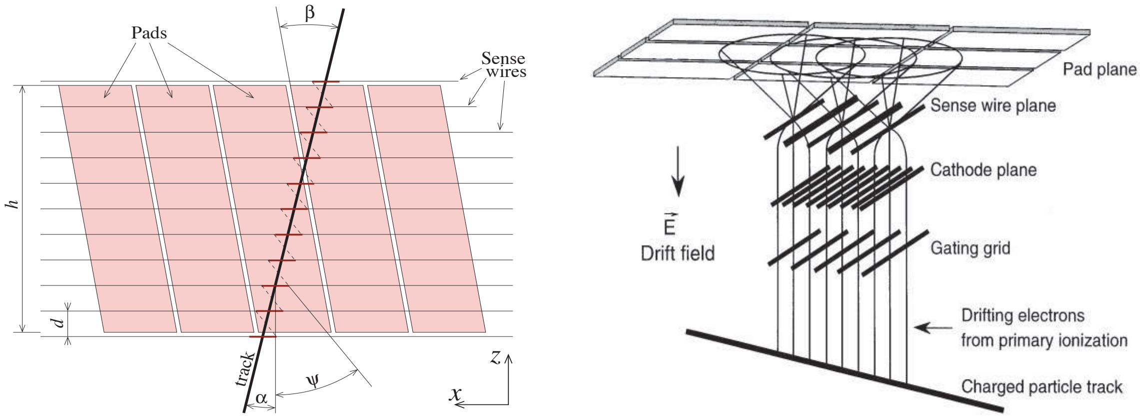

Figure 3.8: Left: Particle track crosses a padrow. Definition of geometrical dimensions and of the angles. Right: Schematic layout of the TPC readout chambers. The drift direction is vertically upwards.

By construction pads are oriented in such a way to be aligned with respect to tracks emitted in the same direction in which they are bent by the magnetic field (i.e $p_x > 0$ for positive charges and $p_x < 0$ for negative charges). However, at the energy we operate for T2K, softer particles dominate and a large fraction of the tracks are emitted in the opposite direction (see Figure 3.9). The sample of tracks for which $p_x/Q > 0$ is called Right Side Tracks (RST) and the one with $p_x/Q < 0$ is referred to as Wrong Side Tracks (WST). A WST can either remain on the same side of the spectrometer (i.e $x < 0$ for a positive particle) or cross the beam axis before hitting the ToF-F. The former sample is very close to the RST topology and the latter is composed of much softer tracks which have a small bending radius. They are called WRST (Wrong-Right-Side-Tracks) and WWST (Wrong-Wrong-Side-Tracks) respectively. The angle β is close to 0 for RST and WRST and the TPC resolution along x is about 300 μm. For WWST the angle β is big and the width of the cluster is generally larger by 10-20% [126].

The first step of the data reconstruction process consists in localizing the charge clusters from the TPC raw data and correcting their position for inhomogeneities in the electric field, as well as $\vec{E} \times \vec{B}$ distortions. The track fragments, called RTrack, are then extrapolated to other detectors and matched to their counterparts to form so called Global RTracks. Reconstructed global RTracks are used for the momentum fit employing the Levenberg-Marquardt algorithm [127]. The fit minimizes the χ^2 based on the deviations of the measured points from the fitted trajectory. Figure 3.10-left shows a distribution of the number of points included in global RTracks. The structure of the TPCs with different number of pad-rows and sectors (VTPC-1, VTPC-2 = 72 (3×24) and MTPC-L/R=90 (5×18)) is clearly visible. A distribution of the

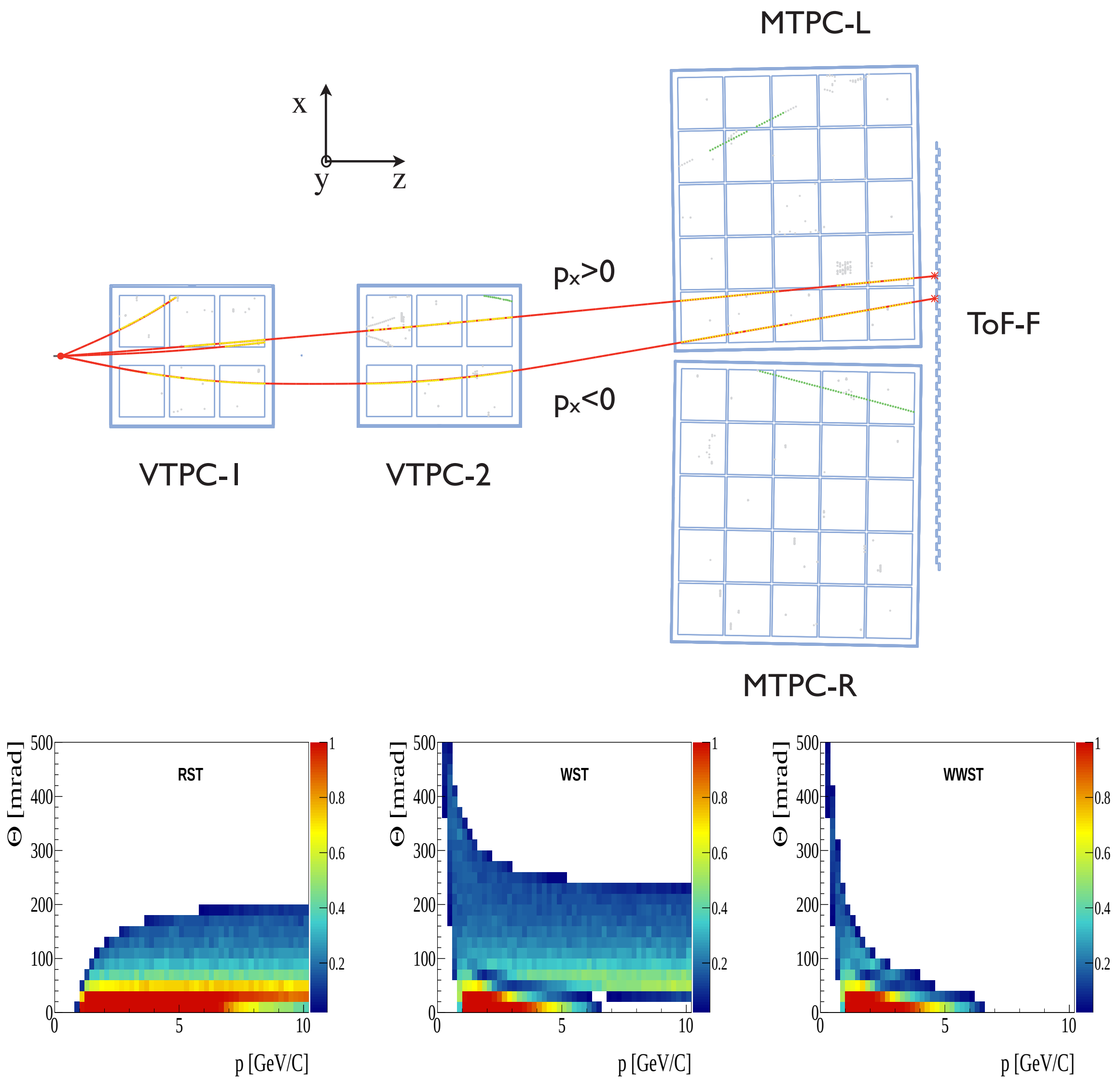

Figure 3.9: Schematic drawing of the experimental apparatus and a reconstructed p+C interaction event. Yellow (green) points indicate TPC clusters (not) associated to reconstructed primary tracks. Stars correspond to hits reconstructed in the ToF-F. Red lines are the fitted particle trajectories. Positive particles emitted with $p_x > 0$ are categorized as Right-Side-Tracks (RST) and those emitted with $p_x < 0$ are called Wrong-Side-Tracks (WST). The two track topologies have distinct acceptances (bottom plots). The subcategory of softer WST which have a smaller bending radius and cross the beam axis before hitting the ToF are called Wrong-Wrong-Side-Tracks (WWST).

number of points N_p as a function of the maximal number of points $N_p(max)$ calculated from the track trajectory is presented in Figure 3.10-right. For most of the tracks, N_p is close to the $N_p(max)$ indicating a high efficiency of the NA61/SHINE TPCs and of the clustering and tracking algorithms.

The statistical uncertainty of the TPC points used for the calculation of χ^2 is estimated from the parametrization of the cluster width. Figure 3.11-left shows the distribution of χ^2/NDF of momentum fits for the reconstructed global RTracks. The mean value is close to 1, indicating that the parametrization accurately describes the cluster width.

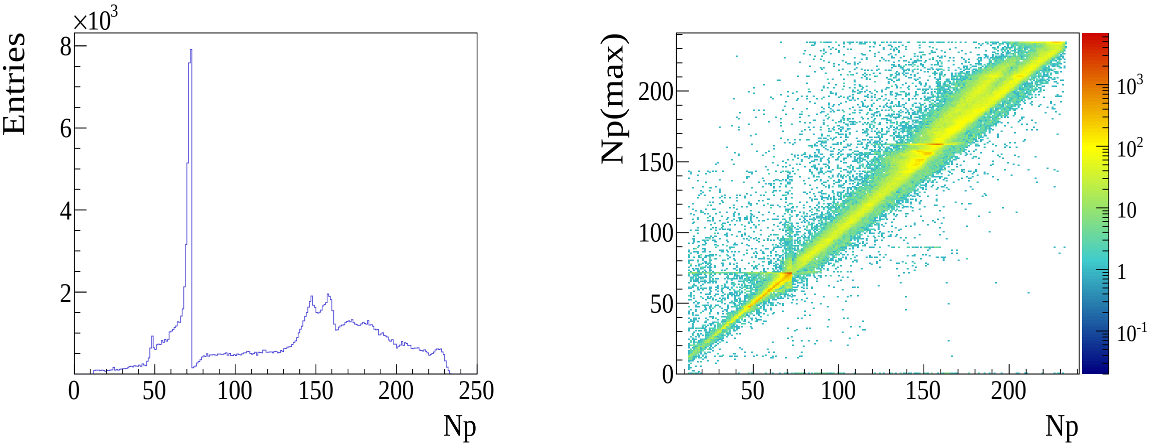

Figure 3.10: Distribution of the number of points (left) and the number of points versus maximal number of points (right) for reconstructed Global RTracks.

The momentum of Global RTracks is given at the first measured point. After reconstruction of the primary interaction point (vertex), the NA61/SHINE reconstruction software assigns the track momentum at the vertex. To do so the Global RTracks are extrapolated in the magnetic field upstream and used to fit the position of the vertex. In the fit procedure the primary interaction point is assumed to be located on the beam particle trajectory measured by the BPD detectors. Thus, only the z-coordinate of the interaction point is fitted. Track momenta are once again determined with the assumption that the tracks stem from the main vertex. Global RTracks for which the fitted momentum is evaluated at the primary vertex are called Tracks. Figure 3.11-right shows a distribution of the differences between momenta measured at the first point and at the vertex. It is centered at 0, indicating that no bias is introduced when the main vertex constraint is added to the fit.

With the obtained information on the particle tracks the last step of the tracking procedure is carried out, which removes split tracks. Split tracks are unmatched track segments which belong to the same particle. For this purpose two different clients were developed. The DOMERGE client which was optimized for the high-multiplicity environment of heavy ion collisions and REFORM which was developed for accurate matching in the lower-multiplicity environment of proton-nucleus or proton-proton collisions. DOMERGE does not have the extra GTPC detector included, and therefore if one wishes to use the GTPC information the REFORM client must be used.

Once tracking is completed the particle's time of flight and energy loss are determined. Finally vertices from non charged parents, so called V0's, are located. Precise identification of V0's, and more specifically the identification of K^0_S, are of importance for T2K, since the K^0_{e3} decay mode of K^0_L accounts for about 10% of the intrinsic ν_e background in the beam (see Section 2.4). Precise study of K^0_S production in proton-carbon interaction at 31 GeV/c have not yet been performed in NA61/SHINE but the plan is to extract such cross sections from the 2009 data set. Results from previous analyses in NA49 suggest a high quality of V0 reconstruction [128, 129].

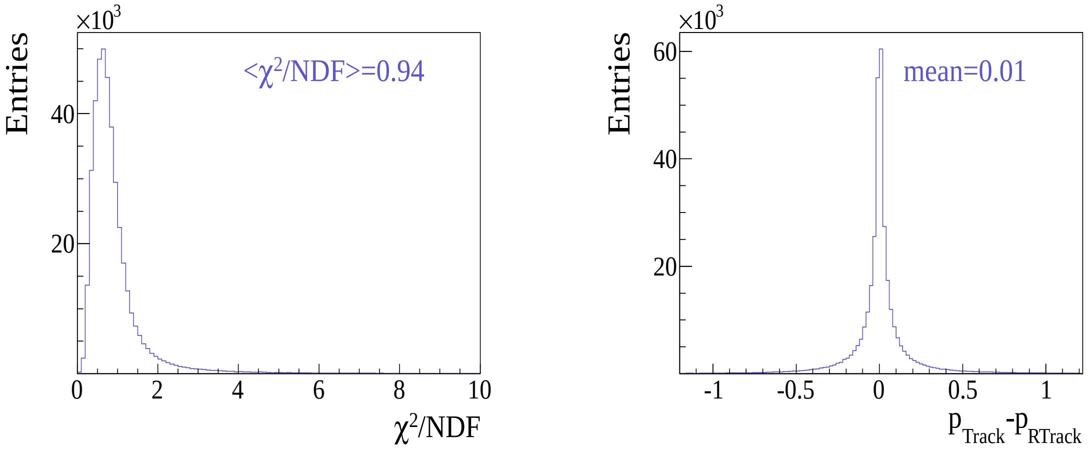

Figure 3.11: Distribution of χ^2/NDF for reconstructed global RTracks (left) and difference between Global RTrack momenta (measured at first point) and Track momenta (measured at vertex) (right).

The whole software reconstruction chain consists of different processes based on the client/server data manager DSPACK [130, 131]. A more technical description of the reconstruction process along with the detail and names of the different software packages which are incorporated is given in [132]. All information from the reconstructed as well as unreconstructed (raw) data is stored on the CERN Advanced STORage (CASTOR) management system [133]. Reconstructed events are stored on Data Summary Tapes (DSTs) where they can be accessed for data processing. The data is analysed with the C++ ROOT analysis framework which has been extended to ROOT61 [134] by adding extra classes specific to NA61.

3.6 Particle identification

The method of particle identification (PID) in NA61, relies on combining the time of flight measurements, tof, from the ToF-F and energy loss measurements from the TPCs (dE/dx) to achieve a high purity particle separation that covers a large momentum range. While the tof allows good particle separation at lower momenta, dE/dx information is needed at higher momenta. The combination of both measurements enables to select particle yields with a very high efficiency over the whole momentum range relevant for the T2K measurements. Here a brief overview is given, this part will be subject to a lot more detail when the analysis techniques are described (Chapters 5 and 6).

tof

The particle's mass squared is obtained by combining the information from the particle's time of flight, tof, measured in the ToF-F with the track length, l, and momentum, p, measured in the TPCs:

$$m^2 = p^2 \left(\frac{c^2 tof^2}{l^2} - 1 \right) \tag{3.1}$$

The uncertainty on the mass measurement is dominated by the time resolution, and therefore the m^2 resolution worsens quadratically with increasing momentum. This can be seen in Figure 3.12 where a plot of the mass squared versus momentum is shown. Pions, protons and kaons are clearly visible. Pions can be separated from protons up to about 8 GeV/c momenta, while kaons are visible in the 1-3 GeV/c range. The ToF-F resolution is around 110 ps. Details on the construction and calibration of the ToF-F are discussed in Chapter 4.

dE/dx

The TPCs allow a measurement of the particle's energy loss per unit length, dE/dx, from the energy deposited by the ionization processes in its active volume. A dedicated calibration procedure is applied to the data to correct the measured cluster charge deposits for various detector effects, e.g., charge absorption along the drift path, effective sample length and variations of gain between the TPC sectors [135]. However, the mean value and width of the distribution of the energy loss samples on the track is always sensitive to the large energy fluctuations of the ionization processes. Therefore the energy loss distribution per unit track length is described by a Landau distribution. To reduce the effect of the long Landau tail, the dE/dx is defined as the mean calculated from the lowest 60% of the TPC cluster charges (troncated mean dE/dx). A scatter plot of the energy loss, i.e. the truncated mean dE/dx value of the track, versus the particle's momentum is shown in Figure 3.12. The function parameterizing the Bethe-Bloch relation [136] is also superimposed.

Combined tof-dE/dx

The PID capabilities of the dE/dx signal in the TPCs are pretty much limited between ∼1 and ∼3 GeV/c where the different particle species overlap. However, beyond this limit (along the relativistic rise region), the energy loss signal can efficiently discriminate between the different particle species. The tof signal shows as well an efficient particle discrimination up to ∼6 GeV/c. By combining the mass squared measurements with the dE/dx information from the TPCs a high purity particle identification is possible over the whole detector's phase space. This is demonstrated in Figure 3.12 where particles between 2 and 3 GeV/c of momentum are sorted corresponding to their dE/dx signal and the mass squared obtained from the ToF-F. At momenta above ∼4 GeV/c the separation of (e,π) from (K,p) is performed essentially by dE/dx, whereas the ToF measurement is needed to distinguish between kaons and protons. Below 4 GeV/c, π, K and proton identification can be performed almost exclusively by the ToF-F while the dE/dx is needed to separate electrons.

3.7 The NA61/SHINE simulation chain

The NA61/SHINE simulation chain inherits from the software developed for the NA49 experiment. The chain is interfaced to GEANT 3.21 [103] for the particle propagation through the detector geometry and material. It uses a model based input (VENUS 4.12 generator [137]) for the primary kinematics. The TPC digitization is performed by a dedicated plug-in during the reconstruction. Monte Carlo (MC) events are produced in the same format as raw data so that both are reconstructed with the same chain. A sketch of the geometry used in the simulation is shown in Figure 3.13.

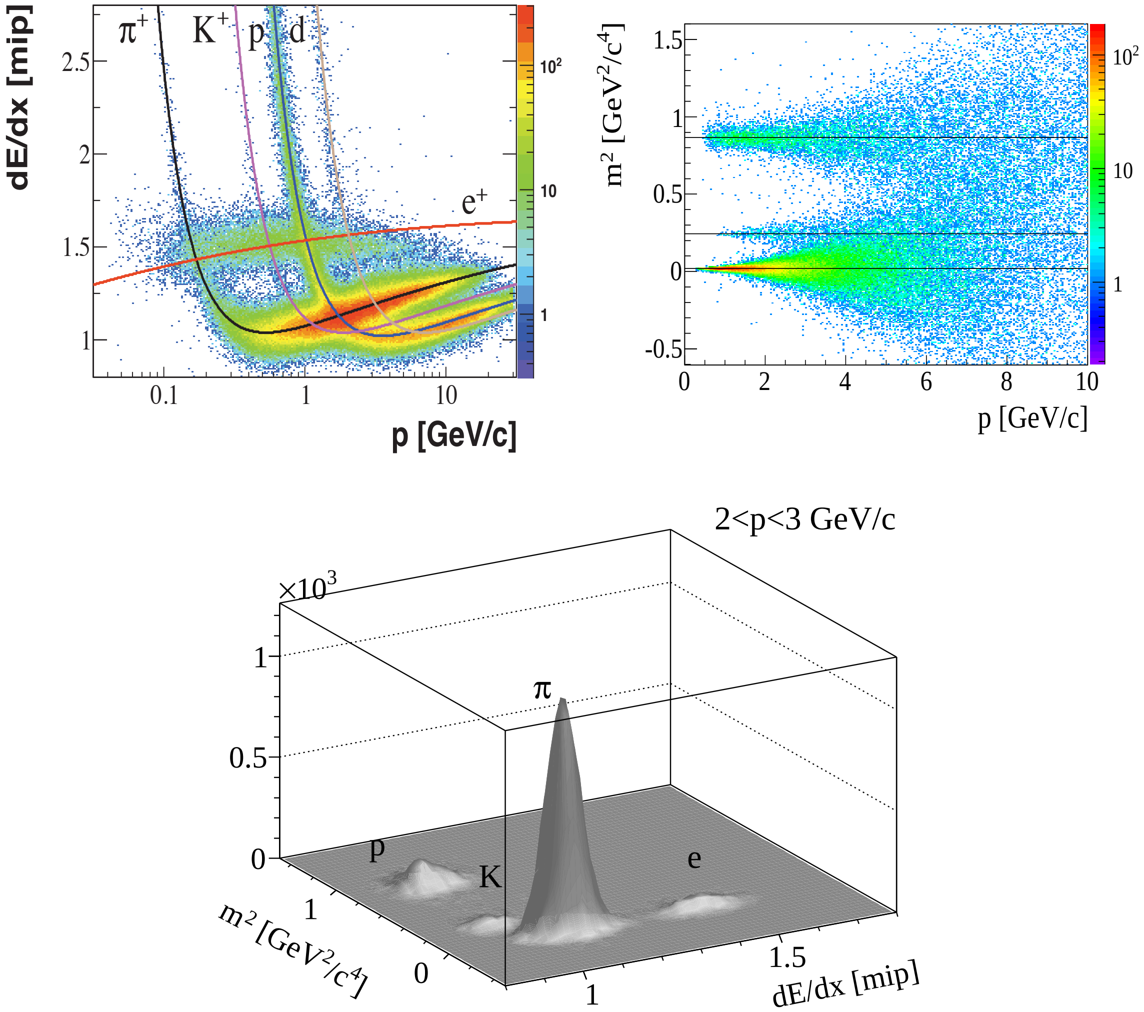

Figure 3.12: [Top-Left]: dE/dx versus log(p) spectra and Bethe-Bloch parameterization superimposed. [Top-Right]: mass squared spectra from the Forward Time of flight, protons kaons and pions are visible. [Bottom]: mass squared versus dE/dx in the momentum range 2-3 GeV/c in which 4 islands corresponding to pions, electrons kaons and protons are clearly defined.

The simulation of the detector response consists of the following steps:

- **Event generation:** VENUS is used by default. Intrinsic generators, like single or multiple pid flat phase space may also be used for specific studies (see for example study of the detector's acceptance in Section 5.2.1).

- **Propagation:** outgoing particles are propagated through the detector material using the GEANT 3.21 package which takes into account the magnetic field as well as relevant physics processes, such as particle interactions and decays.

- **Format conversion:** the `G2DS_NA61` package provides the conversion from zebra output of GEANT to the DSPACK format which is used in the overall framework of the NA61/SHINE software.

- **Digitization:** the digitization of the NA61/SHINE TPCs is performed by a dedicated package (`MTSIM`). Energy loss from GEANT output is converted into ADC spectra and Monte Carlo data are packed in the same format as raw data. This package also applies to the simulated data all distortions which are corrected for in the real data reconstruction: effects of non-uniform electric and magnetic fields in the VTPCs (e.g. $\vec{E} \times \vec{B}$ distortions) and time offsets of the electronic channels are applied to the simulated clusters. As shown in Figure 3.14, during the 2007 data taking some of the TPC mother boards were missing. This was reproduced in the simulation by locally switching off simulated pad rows in the MTPCs. The correct simulation of the number of clusters on track is of significant importance for the analysis and in this respect, a consistent treatment of the missing mother boards is required.

- **Reconstruction:** Monte Carlo data are reconstructed with the chain used to process raw data. The chain calls the same clients (cluster finding, pattern recognition, track merging and fitting, etc.) including correction of distortions applied to the data.

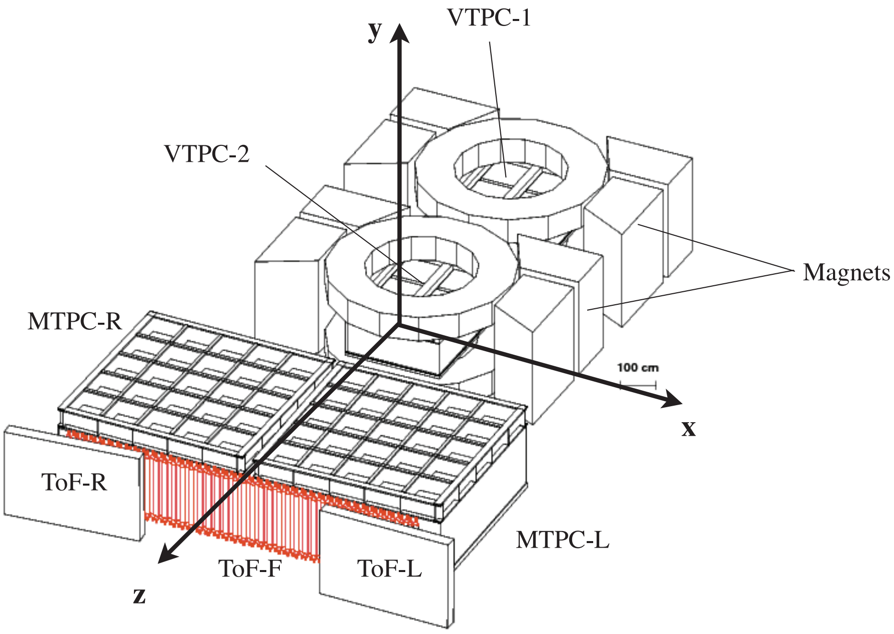

Figure 3.13: Overall simulated geometry of NA61/SHINE with the reference coordinate system. The upper magnet yokes are not displayed to show the vertex TPCs. For each TPC the cover of the readout planes are not displayed to show the structure of the readout sectors.

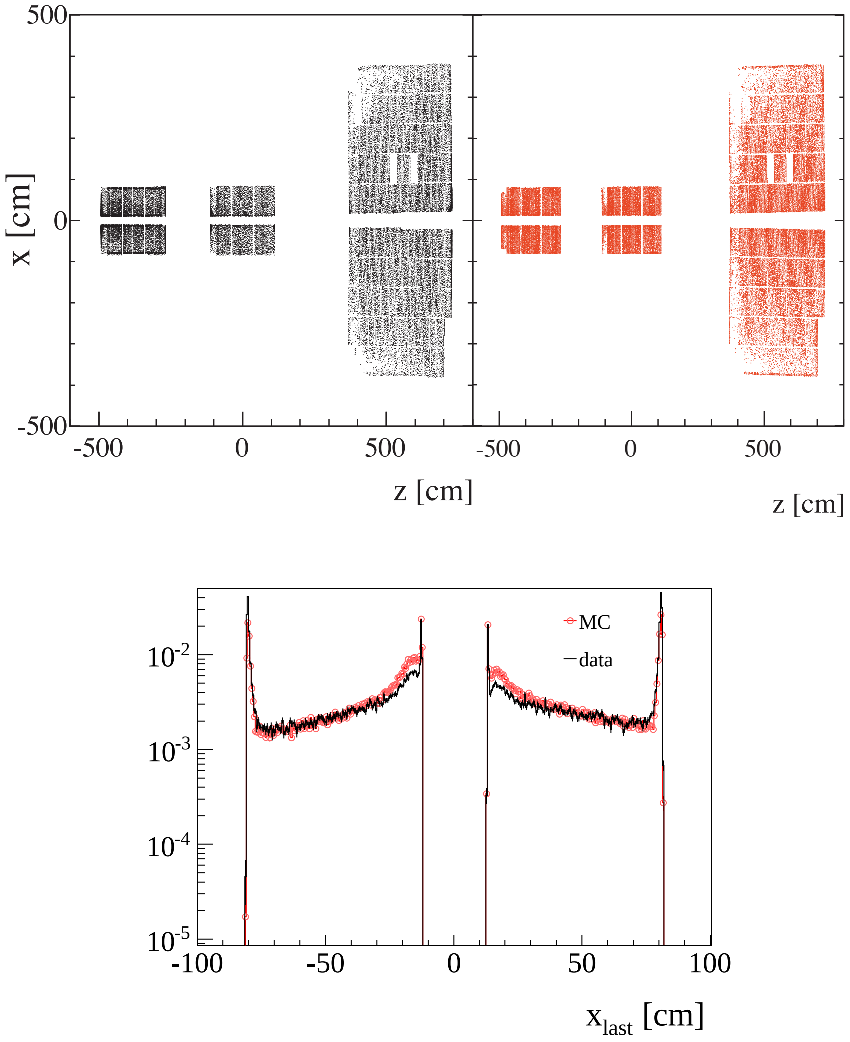

Figure 3.14: **[Top]**: Reconstructed clusters (first and last points) of real (left) and simulated (right) tracks in the TPCs in the x-z projection. Regions without clusters in the MTPCs correspond to missing mother boards in the readout sectors. Those regions are correctly described by the detector simulation.**[Bottom]**projection along the x coordinate of reconstructed last points in VTPC-2 for real (black) and simulated tracks (red).

3.7.1 Flat phase-space Monte Carlo

A flat phase-space Monte Carlo is used to perform precise acceptance studies of the detector geometry with high statistics. The T2K momentum-angle space is divided into bins of 200 MeV/c from 0 to 25 GeV/c and 20 mrad from 0 to 500 mrad respectively. The binning is fine enough so that small variations in the detector geometry are visible in the $\{p, \theta\}$ plane. 10'000 tracks in each of those bins are generated at the vertex with p, θ, ϕ randomly taken from flat distributions (with $0 < \phi < 2\pi$). Since the acceptance may also depend on the vertex coordinates the transverse size of the beam is reproduced by randomly distributing the vertex according to a Gaussian function whose variance is taken from the measured beam spot at BPD3. The z coordinate is exponentially distributed along the target thickness (2.0 cm) with the appropriate interaction length. The tracks are then propagated through the detector and magnetic field with no simulation of physics processes such as decays, secondary interactions etc... The positions of the simulated clusters in the VTPCs are corrected for $\vec{E}\times\vec{B}$ effects by calling the MTSIM package. The acceptance is then defined by requirements on track coordinates, number of simulated TPC points or that the track reaches a sensitive volume (ToF, VTPC, MTPC).

3.8 Data set used for the analysis

In order to meet the requirements of NA61, several improvements and modifications have been brought to the original NA49 reconstruction software. For each software release the raw and simulated data are reprocessed which results in a new production of DSTs. The first production showing sufficient quality to extract physics results is the 07H production, on which the preliminary $\pi^+$and π^-cross-sections released in late 2009 [138] are based. The final results from 2007 which are presented in this thesis, are based on the 07Nbis production for which the files where processed using REFORM with the `v2r2-1a` software release. For this production, only events recorded after run 5581 are processed which corresponds to about two thirds of the total 667'567 triggers collected in 2007 (see Table 3.2). The reason for doing so is that the newly constructed ToF-F detector was in stable operation only after this run. Analysis which do not use the ToF-F, like the h-minus analysis [139] or dE/dx below 800 MeV/c [140], may however employ the entire data-set.

The next chapter gives a summary of the efforts invested in building and calibrating the Forward ToF-F. As will be discussed, adding this new detector was mandatory to meet the T2K physics requirements as it provided the necessary particle identification in the T2K phase-space. The analyses that lead to the final 2007 results are then presented in the last two chapters.

Chapter 4

Construction and calibration of the Forward Time-of-Flight detector

The time-of-flight (ToF) system of NA49 used in NA61/SHINE consisted of two side modules (ToF-L and ToF-R) which were not sufficient to provide full acceptance and adequate particle identification in the phase space region of interest for T2K. A new detector identifying low energy particles exiting the MTPCs in the forward direction had to be added. Before the first data taking period, in summer 2007, we therefore constructed the forward ToF (ToF-F) to be placed in between the two existing ToF-L and ToF-R modules. The ToF-F was later extended in 2009 to increase the acceptance coverage.

The chapter covers the main stages of the construction and calibration of the ToF-F in 2007. Particle identification (PID) performances for the 2007 short and T2K replica target as well as for the 2009 runs are also reported. Similar resolution on the final mass squared spectra are reached for all data-sets.

4.1 The ToF-F coverage according to the T2K physics requirements

The $\{p, \theta\}$ distributions relevant for the hadron production in T2K which have been presented in Figure 2.13, are peaked at low angle and low momenta. The produced pion yield, for instance, is maximal around $1 < p < 4$ GeV/c and $50 < \theta < 250$ mrad. Kaons have a slightly higher momentum distribution ($1 < p < 7$ GeV/c). As is demonstrated in Figure 4.1, the geometrical acceptance of the NA49 ToF detector does not cover entirely the T2K phase-space. Since it has been established in Section 3.6 that PID through tof measurements is mandatory over the entire phase-space and especially at low momentum, an extra ToF detector covering the forward region must be added for the T2K data taking. The increased geometrical acceptance with PID of NA61, thanks to the new ToF-F, is shown in Figure 4.1. With the new ToF-F, NA61/SHINE covers more than 80% of the T2K phase-space.

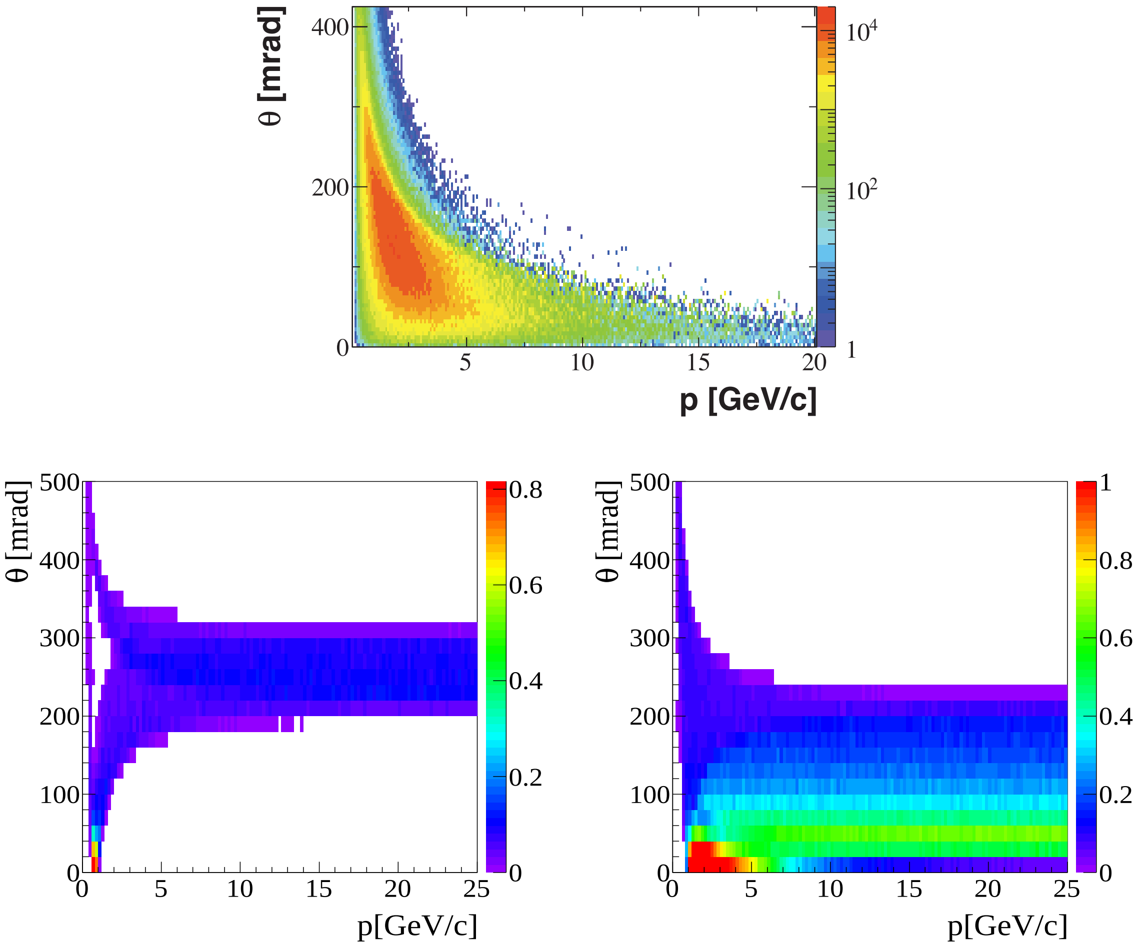

Figure 4.1: **[Top]**: $\{p, \theta\}$ distribution for positively charged pions weighted by the probability that their decay produces a muon neutrino passing through the SK detector. **[Bottom]**: geometrical acceptance of NA49 with only the two side ToFs (left) and NA61/SHINE acceptance with the new ToF-F.

4.2 Experimental Layout

In the 2007 data taking, the ToF-F detector consists of 64 scintillator bars vertically oriented. The bars were tested and mounted by groups of 8 in independent frames (module) out of which half were placed on the left side and half on the right side of the detector in order to match the left/right symmetry. The size of each scintillator is 120×10×2.5 cm^3 and are staggered with 1 cm overlap to prevent un-instrumented area. In 2009 we upgraded and extended the ToF-F by adding an extra two modules on each side yielding a total active area of 720×120 cm^2. Each scintillator bar is read out on both sides with 2″ photo-multipliers (PMT) Fast-Hamamatsu R1828, for presently a total of 160 read-out channels. The scintillators are plastic scintillator (*Bicron BC-408*) with a scintillation rise time of 0.9 ns, a decay time of 2.1 ns and attenuation length of 210 cm [141], their maximal emission wavelength is about 400 nm perfectly matching the PMT spectral response. Fish tail PMMA[1] light guides were glued on both ends for the

---

[1] Poly methyl methacrylate (transparent Plexiglas)

read out. The bars and light-guides were wrapped in aluminium foils to ensure light reflection towards the light-guide and covered with black plastic foils and tape. To ensure proper optical contact between the PMTs and the light-guides, a so called "silicone cookie" is inserted in the interface. It consists of a 3 mm thick silicone cylinder, which matches the diameter of the PMT and light-guide. A few pictures of the construction procedure are shown in Figure 4.2. A top view sketch of the experiment and a zoom around the ToF-F with the corresponding channel mapping is presented in Figure 4.3.

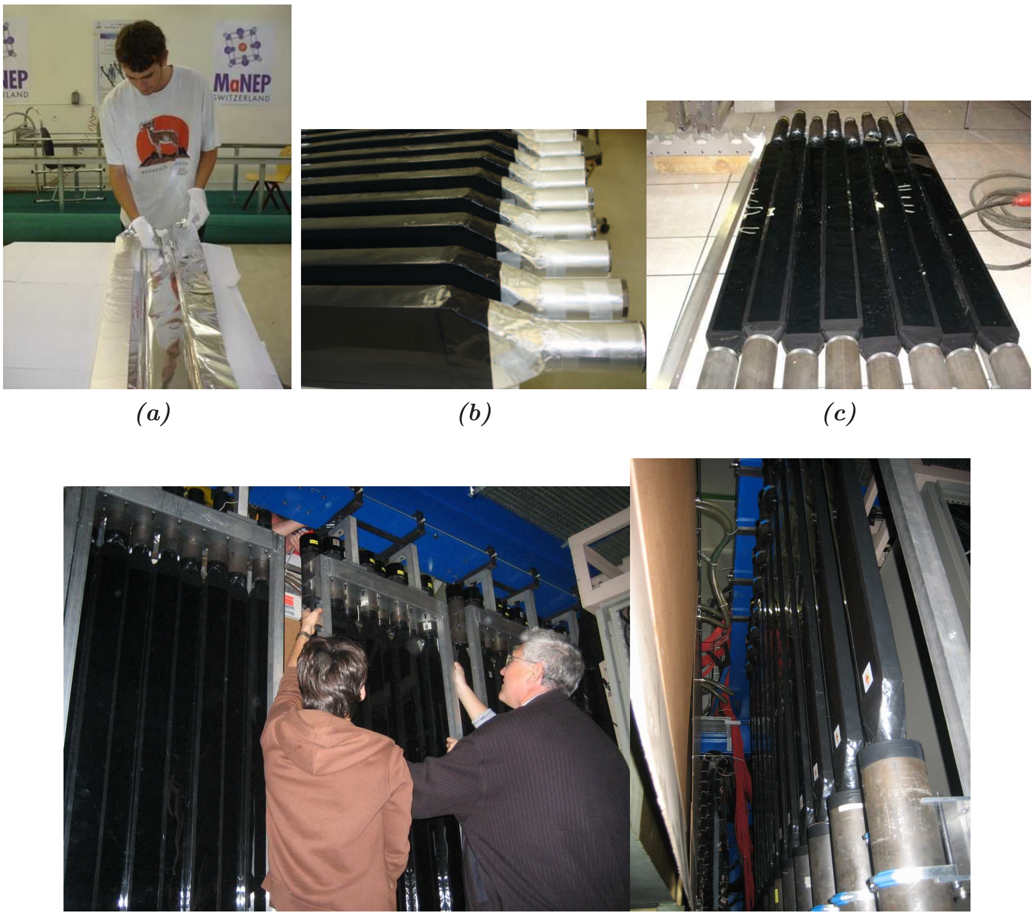
(a) *(b)* *(c)*

(d) *(e)*

Figure 4.2: Pictures showing the different stages of the ToF-F construction. The scintillators are wrapped in aluminium foil (a), covered in black tape (b) and mounted on 10 independent aluminium frames (c). The frames are then carefully hung and aligned behind the MTPCs in the experimental hall(d). Finally the 160 PMTs are connected to the HV and coaxial signal cables (e).

Most of the electronics for the ToF-F were inherited from the two NA49 Grid ToFs [142] which were removed since their acceptance coverage is marginal for the T2K runs.

Each PMT channel is operated near 1700V by LeCroy1461 independent 12-channel high voltage (HV) cards and the analog signals are transported from the ToF to the counting house by 26 m RG58 50Ω coaxial cables. To obtain fast logic signals and not be influenced by the variations in amplitude of the PMT response the cables are passed to Constant Fraction Discriminators (16-channel KFKI CFD5.05 VME module). At the input they include an internal passive divider

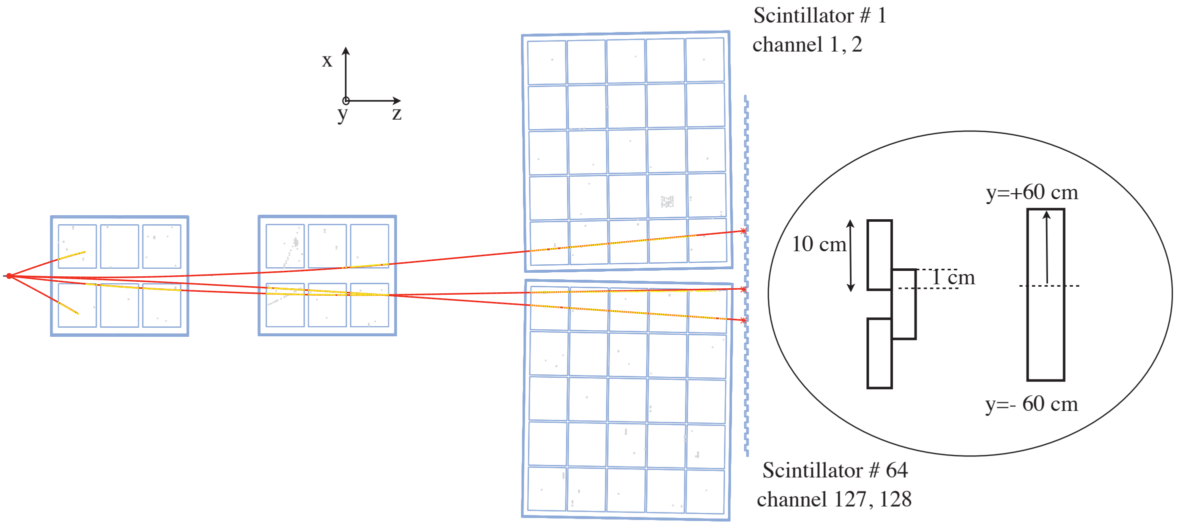

Figure 4.3: Top view of the detector and zoom on the ToF-F. The scintillators are labeled from 1 to 64 with decreasing x. Each bar has a 1cm overlap along x and is read out by two PMT channels at each end. The active area of the ToF-F is centered at 0 on the vertical (y) axis of the NA61/SHINE coordinate system and extends to $y = +60$ and $y = -60$ cm. Scintillator number n is read out by channels number $2n - 1$ and $2n$.

of 1:3 to provide the signals for the integrated charge and time measurements, respectively, and the necessary delay lines at their output. In order to minimize the cross talk of the neighbouring channels an appropriate order is chosen between the PMT outputs and the CFD inputs. The output signals of the CFDs of the PMT-channels serve as "stop" signals for the time of flight measurements. The start signal is provided by a fast beam counter of the central NA61 trigger system. The time measurement is carried out by LeCroy Fastbus Time-to-Digital Converter (TDC) units digitizing the time in 12 bits dynamic range with a sampling time of 25 ps. The analog signals of the PMTs are converted by LeCroy Analog-to-Digital Converter (ADC) units into 12 bits.

4.3 On-line monitoring

Prior to the physics data taking dedicated beam time was attributed to calibrate the ToF-F channel by channel. A lead target was used for this purpose to provide maximal particle multiplicity and a ROOT based on-line monitoring was developed to check the response of each channel on a run by run basis. The amplitude of the PMT signals (in ADC units) and the distributions of measured "stop" times (TDCs) are constantly monitored. As an example a distribution of the ADC and TDC response for one channel is shown in Figure 4.4. The ADC distribution contains the signal, which is located around 1000 ADC counts and a lower amplitude peak, called pedestals, which corresponds to events for which no particles hit the read out scintillator. The pedestals are removed when a signal above the CFD threshold is requested. This is demonstrated in Figure 4.5 where the black curve shows all the recorded amplitudes and the super-imposed red curve has the additional requirement of a stop signal in the corresponding TDC. Both curves should have the same value when the amplitude is above the pedestals, any other pattern indicates a malfunctioning or inefficiency of the CFD for this specific channel and is therefore immediately replaced. The voltage of the PMTs as well as the parameters affecting the operation of the CFDs (threshold and zero crossing) are optimized for every channel by visually inspecting the ADC and TDC distributions. The goal is to keep the peak of the signal around 1000 ADC counts and the thresholds at a slightly lower value not to reduce the overall detection efficiency while keeping it well above the pedestals. Each distribution is fitted with a Landau curve, the returned mean values are checked and the PMT voltages are set accordingly. Figure 4.6 shows the fitted mean values per channel after a calibration run.

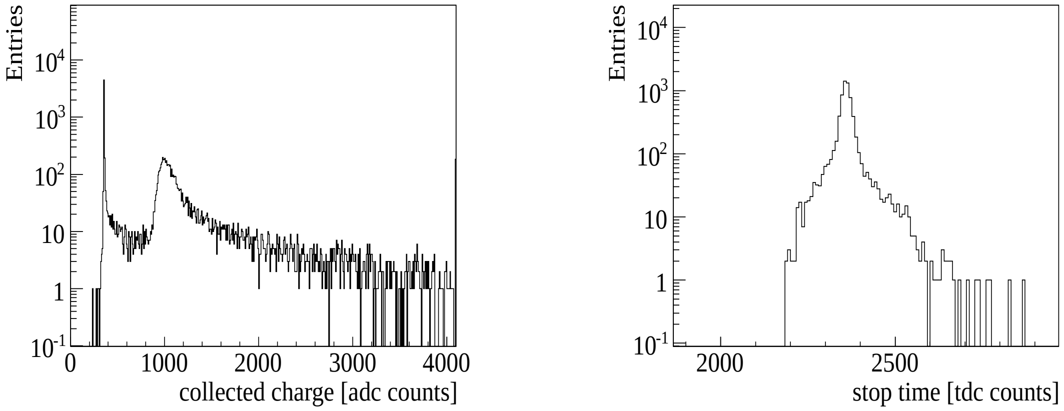

Figure 4.4: ADC (left) and TDC (right) distribution for channel 79 of the ToF-F.

4.4 Geometrical calibration

The geometrical calibration, is done off-line. It consists in attributing a mean x, y coordinate to each scintillator slat. If centered accurately the y coordinate is expected to be close to 0. The x coordinate will be used as the criterion for a track being associated or not to the scintillator, therefore an accurate calibration of this parameter is of primary importance. The scintillator coordinates (called x_s and y_s) are retrieved by extrapolating all the global RTracks from the TPCs with the TrkPar routine. TrkPar uses a Runge-Kutta numerical approach to propagate the tracks through the spectrometer and magnetic field, to a given z coordinate of the ToF. The 3 momentum coordinates at the last cluster of the RTrack, which are input parameters for the extrapolation, are retrieved with a Kalman filter [143]. The precision of the procedure is of the order of 1-2 mm (see Section 5.5). x_s is retrieved by comparing the extrapolated x with the barycenter of the active scintillators (i.e scintillators with at least one attached channel to have a registered stop signal). For that matter, within one event all the track which are susceptible to leave a hit in the ToF-F are extrapolated. At this stage, it is important to apply a certain amount of selection criteria on the primary track sample in order to retain only those which are in the ToF-F geometrical acceptance and which are hence susceptible to hit the expected

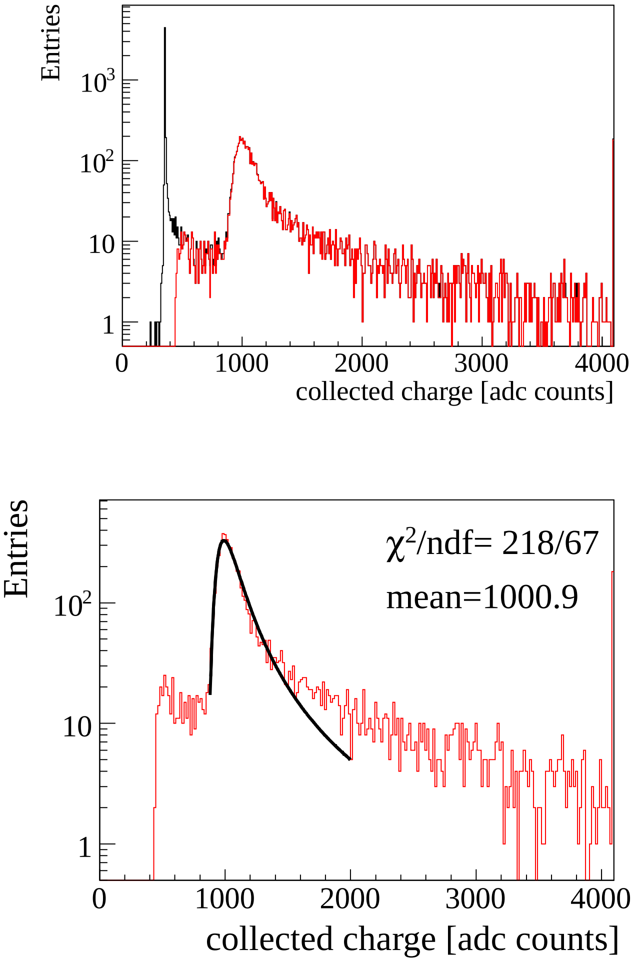

Figure 4.5: Distributions of integrated charge for channel number 79 of the ToF-F. Top: the black curve corresponds to the charge measured for all the events. Pedestals are removed when requesting stop signal in the corresponding TDC (red curve). Bottom: A fit with a Landau distribution is used to retrieve the mean value of the ampliude

slats. Furthermore since the momentum coordinates serve as input for the extrapolation process it is important to select only well-measured tracks in the TPCs. The following track cuts are therefore applied:

1. a minimum of 12 reconstructed points in the two TPCs used for momentum measurement (i.e. VTPC-1 and VTPC-2) is required,
2. the track must leave the primary vertex at an azimuthal angle ϕ within $\pm 20^\circ$ around the horizontal plane. This excludes most of the tracks traversing the detector in the regions where the reconstruction capability is limited by the magnet aperture or by the presence of un-instrumented regions in the VTPC (see Figure 4.7).

Furthermore decays in flight should be avoided since the extrapolated coordinates may differ from the coordinate of the actual hit. Unstable particles can be rejected by considering only

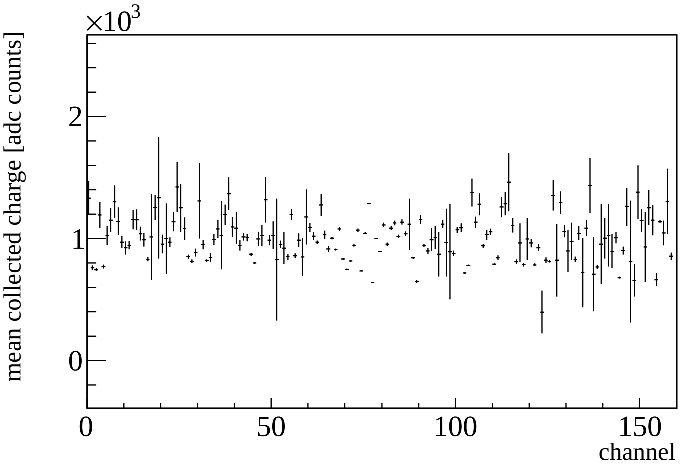

Figure 4.6: Fitted mean ADC as a function of the channel number after adjustment of the PMT voltage

tracks reconstructed until the downstream edge of the MTPCs. This can be achieved by the following cut:

3. the z position of the last reconstructed point should be greater than 680 cm.

A distribution of the extrapolated x (x_{tof}) as a function of the active scintillator number is presented in Figure 4.8. To populate the scintillator bars located in the un-instrumented region along the beam axis (around x=0), the cut on zlast is released and tracks are extrapolated from the downstream end of VTPC-2. The slightly higher smearing in this area is explained by the lower tracking efficiency and momentum resolution of such low angle tracks ($\lesssim$ 20 mrad) which are located on the edge of the detector's acceptance.

To accurately define the mean value of each slat, the projections of the x_{tof} distributions per scintillator are retrieved. An example of two such distributions is presented in Figure 4.9. They are fitted with a sum of two error functions defined as:

$$\mathcal{F}(x, w, \mu, n_1, n_2) = \xi + A\left[\mathrm{erf}\left(\frac{(x+w)-\mu}{n_1}\right) - \mathrm{erf}\left(\frac{(x-w)-\mu}{n_2}\right)\right] \tag{4.1}$$

$$\mathrm{erf}(X) = \frac{2}{\sqrt{\pi}}\int_0^X e^{-t^2}dt \tag{4.2}$$

ξ is the background which may be due to detection inefficiencies or to broken tracks such as large kink decays or secondary interactions where the hit scintillator is different from the expected one. A is the amplitude and w is the parameter defining half of the width of the distributions and should be around 5 cm since the active width of a slat is 10 cm. However detection efficiencies on the side of the scintillators may be somewhat limited due to lower light yields reaching the PMTs, which is the reason for the scintillators to be mounted with a 1 cm overlap . This lower efficiency on the sides of the slat is input in the fit as the two parameters n_1 and n_2, which control the slope of the function on each side. Two different n are also input in the fit, in the eventuality that the distributions are asymmetric. This can be true for the few middle scintillators where

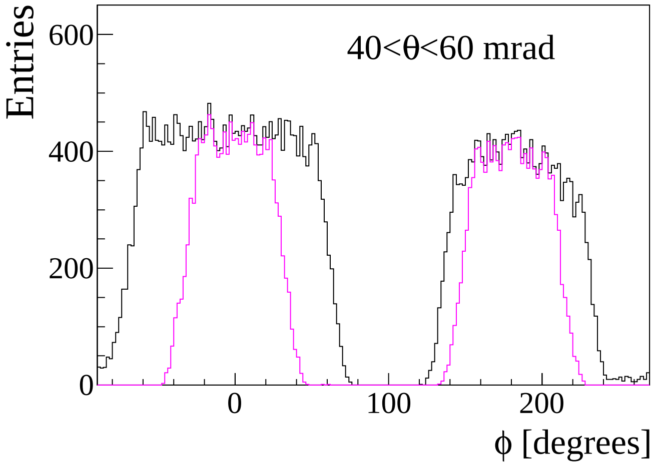

Figure 4.7: Example of an azimuthal angle distribution for positive tracks emitted with $40 < \theta < 60$ mrad polar angle. The black line corresponds to tracks that have a minimum of 12 reconstructed points in the VTPCs, and the magenta line describes those which reach the ToF-F.

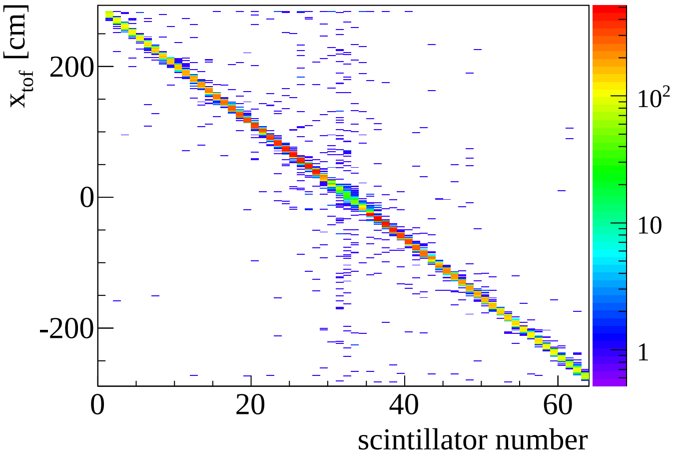

Figure 4.8: Distribution of extrapolated x as a function of the active scintillator number

the NA61/SHINE acceptance is greatly reduced and varies brutally as a function of x_{tof}. For each distribution the mean value μ is retrieved and kept as the reference coordinate to define the barycenter of each slat. The values are all given in Appendix B and as expected they are separated by $\sim$ 9 cm from one another. The track-scintillator association is performed by retrieving the mean x coordinate of the active scintillators (x_s) in the current event. For each of the selected tracks, the minimum difference between x_s and the extrapolated x (x_{tof}) is computed, this quantity defines the ToF-F impact parameter b_x^{tof}:

$$b_x^{tof} = x_s - x_{tof} \tag{4.3}$$

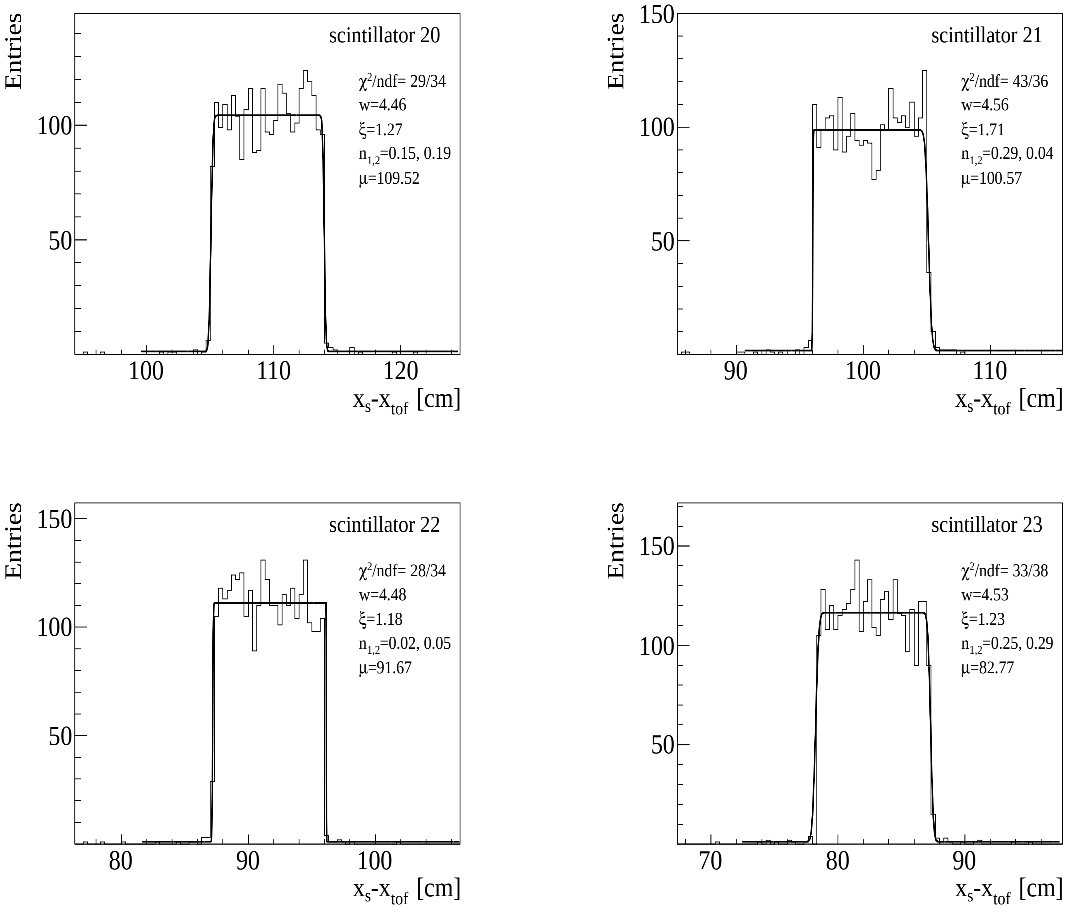

Figure 4.9: Example of extrapolated x distributions to 4 consecutive scintillator slats (number 20 to 23). The fitted central values are taken as the reference x_s for each scintillators

The distribution of the all the b_x^{tof} is shown in Figure 4.10. First observation is that the distribution is centered on 0, which indicates that all the values of x_s are correctly calibrated. Taking the minimum between x_s and x_{tof} as matching criteria removes any possibility of counting twice the tracks that leave two signals by hitting the overlapping regions of two scintillators. The track will only be associated to the slat which has the closest impact parameter. This explains the 4.5 cm width of impact parameter distribution of Figure 4.10-left: the scintillators are 10 cm wide with an overlap of 1 cm on either side, thus the active region of one considered scintillator is 4 cm plus 0.5 cm on either side, above this value the track is counted as belonging to the neighbouring slat. Thus one can say that the effective active region of a given scintillator totals to 9 cm.

A track is defined to be matched to the scintillator or to be *in the tof* if its corresponding b_x^{tof} is contained within a certain value. In principle, all the selected tracks should reach the ToF-F and therefore should be associated to a scintillator. Equivalently all recorded hits should have an associated track. The tracks should thus all be contained within ±4.5 cm of the tof impact parameter as demonstrated in Figure 4.10–left. The estimation of x_{tof} may still however be slightly biased from particles which decayed in the 80 cm gap between the downstream end of the MTPCs and the ToF-F. This accounts for the small tails on either side of the distribution. The tof signal corresponding to those tracks is still nevertheless perfectly valid. To estimate the value of b_x^{tof} defining that a track is *in the tof*, the ratio between the number of selected tracks (those which should, in principle, leave a hit in the ToF-F) and the number of matched tracks are shown as a function of the cut on the ToF impact parameter in Figure 4.10-right. Since the curve stabilizes at the maximum ratio ($\simeq$99%) around 5 cm, it is reasonable to assume a cut of 6 cm which leaves an extra security margin for extrapolation and alignment errors. The ratio of the graph stabilizing at 99% demonstrates that the previous track cuts correctly define the ToF-F geometrical acceptance, and additionally suggests a high scintillator detection efficiency. The latter is evaluated at the analysis level (Section 5.5).

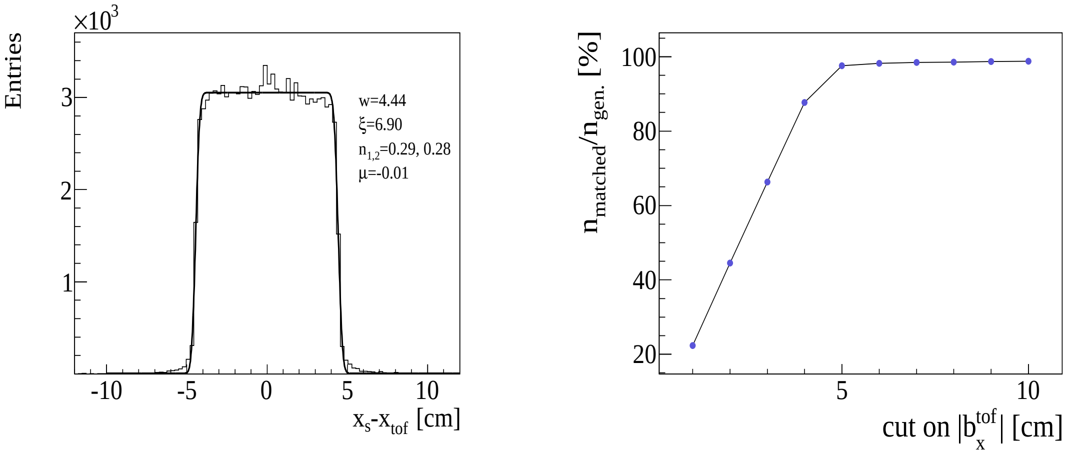

Figure 4.10: left: ToF impact parameter for all scintillators. right: scintillator matching efficiency for different ToF impact parameter cuts (upper limits).

4.5 Time dependent calibration

4.5.1 Procedure

As illustrated in Figure 4.11 the tdc measurements attributed to a track hitting the ToF-F, $t_{stop} - t_{S1}$, is the sum of the proton's time of flight between S1 and the target plane (t_{beam}), the produced particle's time of flight ($tof_{particle}$) and the delay before which the signal triggers the CFDs (t_{cable}). t_{beam} is the time of flight of a 30 GeV/c momentum proton and is constant for each event, t_{S1} is the start signal provided by the S1 counter located on the beam-line. As discussed in Section 4.7, t_{S1} can be corrected for the position of the incident proton hit on the S1 counter. t_{cable}, which is the most important time offset, is specific to each channel as it depends on cable length, PMT gain and CFD response. For each event the particle's tof can be expressed as:

$$\begin{aligned} tof_{particle} &= t_{stop} - t_{S1} - t_{beam} - t_{cable} \qquad (4.4) \\ &= t_{stop} - t_{S1} - t_0 \qquad (4.5) \end{aligned}$$

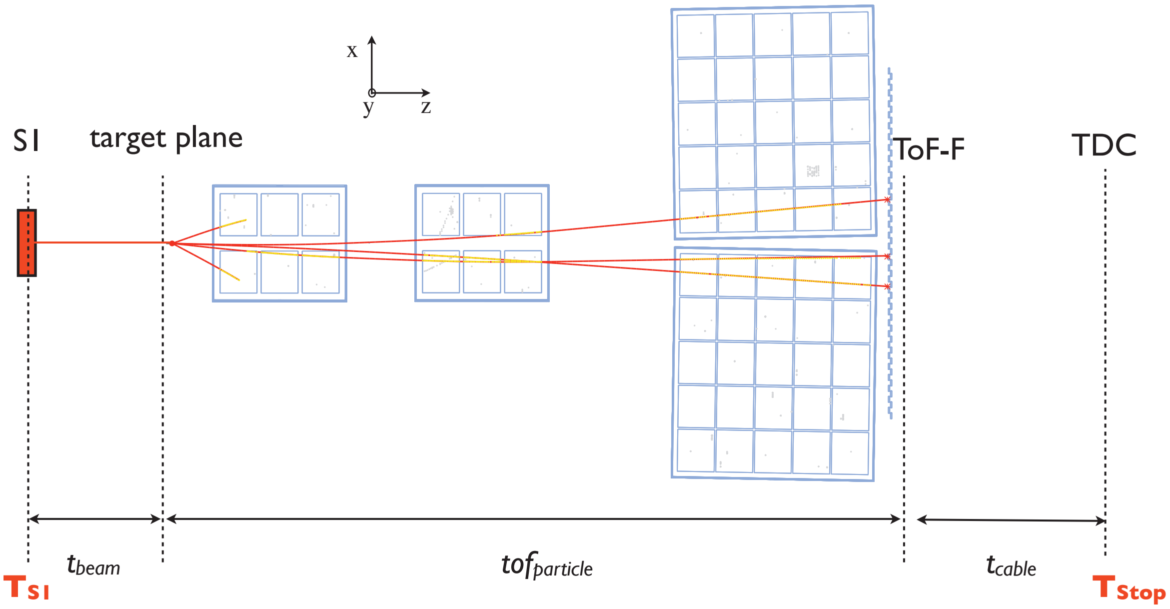

Figure 4.11: Overview of the time dependent calibration.

Hence the true particle's tof is retrieved by correcting t_{stop} by the two quantities t_0 and t_{S1}. The latter varies for each event since it depends on the transverse position of the incident proton. It is typically at the tens of pico-second scale and can be largely neglected (see Section 4.7). t_0 on the other hand is mainly due to the different cable lengths between the PMTs and CFDs and should, in principle, be stable throughout the data taking period. It is of the order of a few tens of nanoseconds.

Particles hitting the vertical scintillator bars will be seen by at least one of the attached PMTs. In most situations the stop signal will be recorded by both of them allowing for the average time $(t_{up} + t_{down})/2$ to be measured, where t_{up} (t_{down}) refers to the TDC value provided by the PMT attached to the top (bottom) of the considered bar. In some rare situations, only one PMT will register the signal. This may happen if one of the channels is inefficient or if the light yield is not high enough to trigger the CFD (e.g particle hit produced far from the PMT). Of course the mean time should be computed whenever available since it provides a better resolution on the tof measurement. Figure 4.12 gives the distribution of the active scintillators which are associated to a track, the green distribution indicates the hits for which the mean time is available and the red histogram those when only t_{up} or t_{down} had to be used. During the 2007 data taking there were two dead channels, which explains why two scintillators are read out by only one PMT, however more than 98% of the hits are seen by the two PMTs. For the small sub-sample of tracks with one PMT read out the tof resolution will be lower, but if this percentage is kept low ($\sim$ a few percent) the effect on the final mass squared distributions and on the particle identification will be negligible. On the contrary leaving a scintillator completely inactive will introduce strong bin to bin variations and high correction factors for the ToF detection efficiency. With these considerations, one can define the stop signal as:

$$t_{stop} = (t_{up} + t_{down})/2 \quad (\sim 98\% \text{ of the hits for the 2007 run}) \tag{4.6}$$

$$t_{stop} = t_{up} \text{ or } \; t_{stop} = t_{down} \quad (\sim 2\% \text{ of the hits for the 2007 run}) \tag{4.7}$$

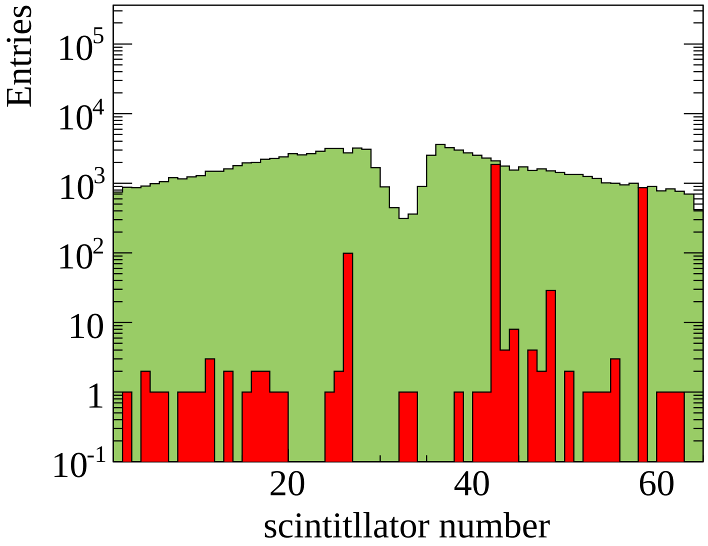

Figure 4.12: Distribution of the hits for which the average time is used (green) and those for which only t_{up} or t_{down} was available. The fraction of single time measurements is about 2% of that of the double time measurement.

The TDC modules have a designed sampling value, dt, of 25 ps. This value was checked by pulsing each channel with a known delay and the linearity of the response was also verified by varying the intensity of the pulses. The measured times are given in Appendix B, the raw TDC of each channel are multiplied by the measured dt to provide a value of t_{stop} in ps.

The pulse height-dependency of the time measurements (time walk) was also checked for each scintillator slat by plotting the distributions of the mean time versus the amplitude of the hit registered in both PMTs separately. As is demonstrated in Figure 4.13 no significant dependency is observed and no time walk correction is needed.

4.5.2 Correction for the transverse hit coordinate

In order to provide a tof measurement for tracks which have a single PMT read out, each PMT channel is calibrated independently. The stop signals registered by only t_{up} or t_{down} are

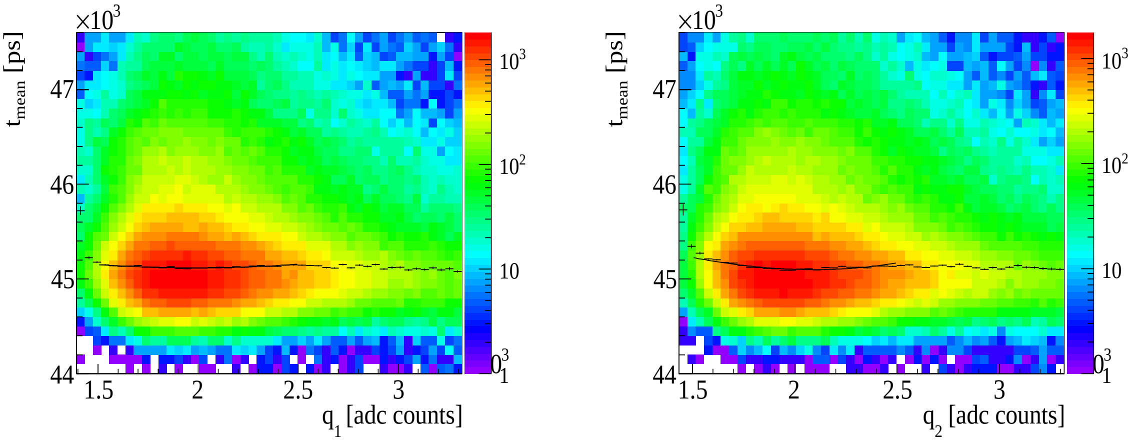

Figure 4.13: Mean time as a function of q1 (left) and q2 (right) for all scintillators. The black markers indicated the mean values of the projections.

dependent on the extrapolated transverse coordinate of the hit (y_{tof}) in the slat:

$$t_{up} = t^0_{up} + (1/v) \times y_{tof} + tof_{particle} \tag{4.8}$$

$$t_{down} = t^0_{down} + (1/v) \times (l_{scint} - y_{tof}) + tof_{particle} \tag{4.9}$$

$$\tag{4.10}$$

Where v is the speed of the light propagation along the bar (see Figure 4.14), $l_{scint} = 120$ cm is the total length of the read out bar and t^0_{up} and t^0_{down} refer to the t_0 offsets of t_{up} or t_{down}. It should be noted at this point that computing the mean time, provides a stop signal independent of y_{tof}:

$$(t_{up} + t_{down})/2 = t^0_{up}/2 + t^0_{down}/2 + tof_{particle} + l_{scint}/v \tag{4.11}$$

$$\equiv t_0 + tof_{particle} \tag{4.12}$$

When only one PMT read out is available however, the resolution is improved by removing from t_{up} and t_{down} the dependency on the transverse hit coordinate. For each slat, a set of measurements (T_{up}, T_{down}) is defined as:

$$T_{up} = t_{up} - (1/v) \times y_{tof} \tag{4.13}$$

$$T_{down} = t_{down} - (1/v) \times (l_{scint} - y_{tof}) \tag{4.14}$$

v is retrieved by measuring the slope of the distributions of t_{up} and t_{down} as a function of y_{tof} for each slat. Figure 4.14 gives an example of such a distribution for scintillator number 35. Distributions are slightly distorted on either side, when the hit is produced at the other end of the attached PMT (-60 cm for t_{up} and +60 cm for t_{down}), those regions are excluded from the linear fit by applying a cut on the transverse position of ±50 cm. The fitted v, which are given in Appendix B, correspond to the speed at which the light propagates through multiple reflections along the bar, the values are generally around $15{\times}10^{-3}$ cm/ps.

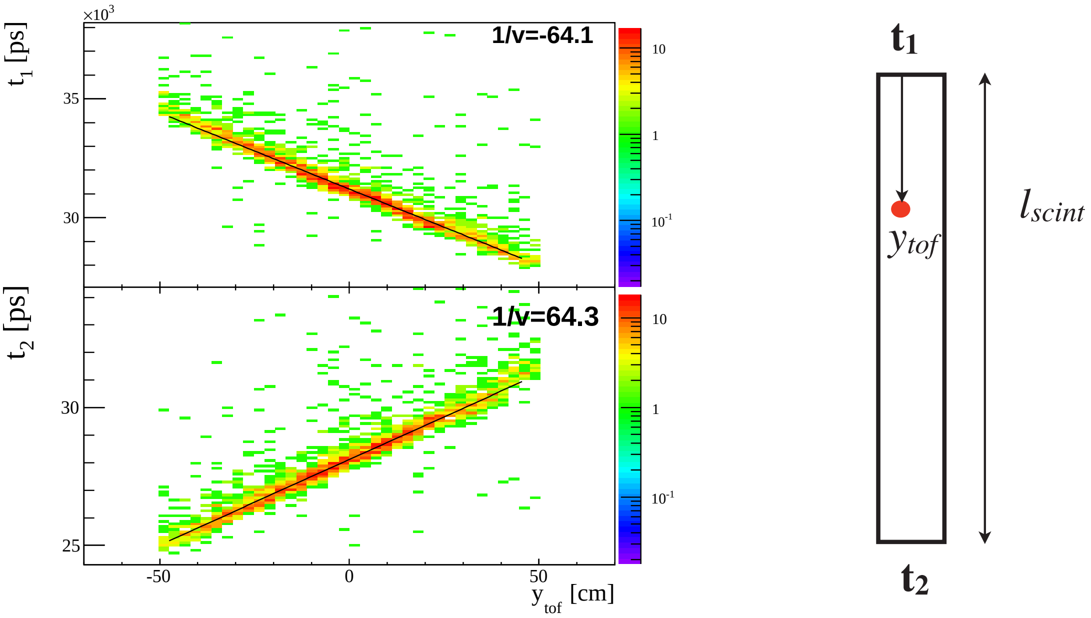

Figure 4.14: t_{up} (top) and t_{down} (bottom) as a function of y_{tof} for scintillator number 35. The corresponding slopes are retrieved to correct for the hit position and improve the time resolution of single PMT measurements.

4.5.3 Global t_0 calibration

The t_0 for each channel is set by assuming all particles are pions and computing the difference between the measured t_{stop} and the pion time of flight. Since precision on the time of flight degrades quadratically with increasing momentum, only tracks which have a momentum below 3 GeV/c are selected. As an example the distribution of $t_{stop} - t_\pi$ is given in Figure 4.15 for channel number 80. Assuming that the time response of the ToF-F is Gaussian-like distributed, the distributions are fitted and the mean gives a first estimate of t_0. This value is sufficient to discriminate pions from protons in the mass squared–dedx plane. t_0 is then refined by selecting only pions and running further iterations of the procedure.

4.5.4 Cut on tdc distributions

The accuracy of the calibration may be checked by plotting the distributions of $T_{up} - T_{down}$ for each scintillator slat. $T_{up} - T_{down}$, unlike the mean time, should give a constant value since the $tof_{particle}$ terms of Equations 4.9 and 4.10 cancel out. The values should be Gaussian-like distributed and centered on 0 once the time offsets are correctly set for each channel. Figure 4.16 is one example of such a distribution for scintillator number 35. As can be noticed however, tails to the distribution appear on either side. Such large time differences occur when at least one

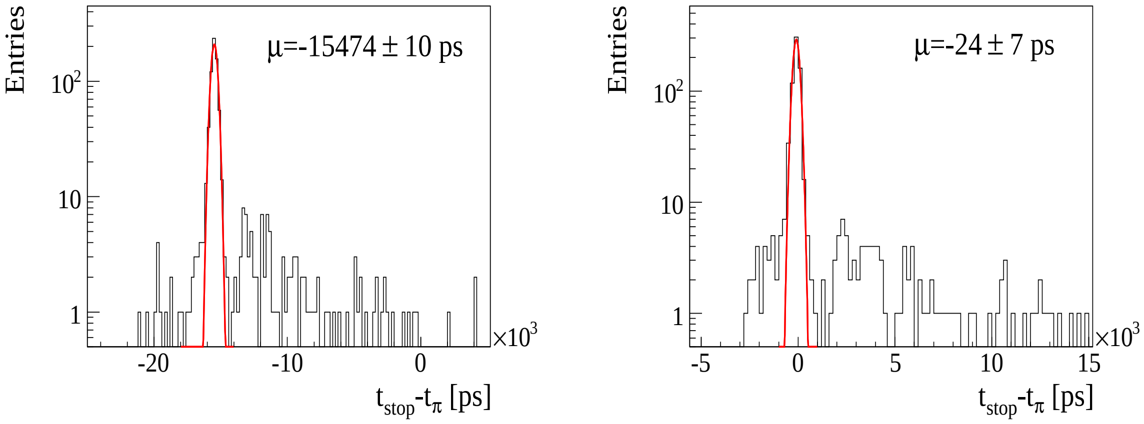

Figure 4.15: $t_{stop} - t_\pi$ for channel number 80 (corresponding to t_{up} of scintillator 40) before (left) and after (right) t_0 calibration. The mean of the fitted pion peak (left plot) corresponds to the t_0 offset for this specific channel. The distribution is then shifted accordingly, several iterations may be needed to get $t_{stop} - t_\pi$ close to 0 (right). Tails to the right of the distributions correspond to the tof of heavier particles such as protons

of the corresponding stop signals is biased. By visually scanning a few events we noticed that this effect is due to pairs of particles that hit the same scintillator slat: one TDC measurement will be from the track under study while the other one from the accompanying track whose signal reached the PMT before the signal of the main track. The bias will lead to an incorrect estimate of the mass-squared and consequently a degradation of the PID due to the presence of non-Gaussian tails which would be difficult to fit. Therefore those hits are removed by applying a $\pm 3\sigma$ cut on the fitted width of each distribution. Note that such a cut cannot be applied if only one PMT read out is available. This cuts removes approximately 2% of the total number of hits.

4.6 Intrinsic ToF resolution

The 64 scintillator bars are mounted in such a way that they overlap by 1 cm on either side as shown in Figure 4.3. The intrinsic ToF-F resolution is obtained by selecting particles that hit the overlapping region and plotting the time difference between the two scintillator signals as shown in Fig. 4.17. The Gaussian fit gives a resolution $\sigma_{tof} = \frac{155}{\sqrt{2}} \approx 110$ ps. The mean value of about 100 ps is also what one would expect since the slats are separated by about 3 cm along z (the slats are 2.5 cm thick and mounted with a $\sim$ 0.5 cm gap between each). Note that the quoted resolution is intrinsic to the ToF-F array and does not take into account additional effects which may contribute to the tof measurement and consequently to the final mass squared spectra (start detector, uncertainties in tracking, length, etc...).

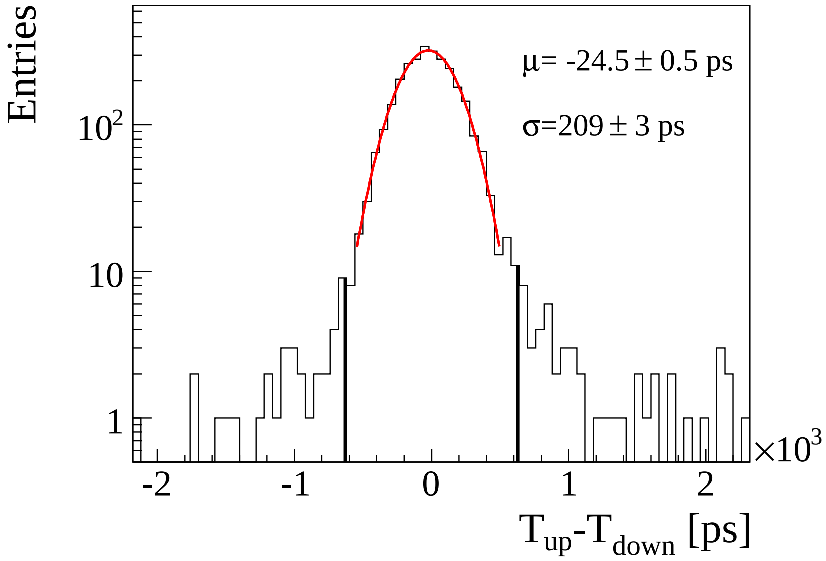

Figure 4.16: Example of a distribution of T_{up}-T_{down} for scintillator number 20. The black lines indicate the $\pm 3\sigma$ cut.

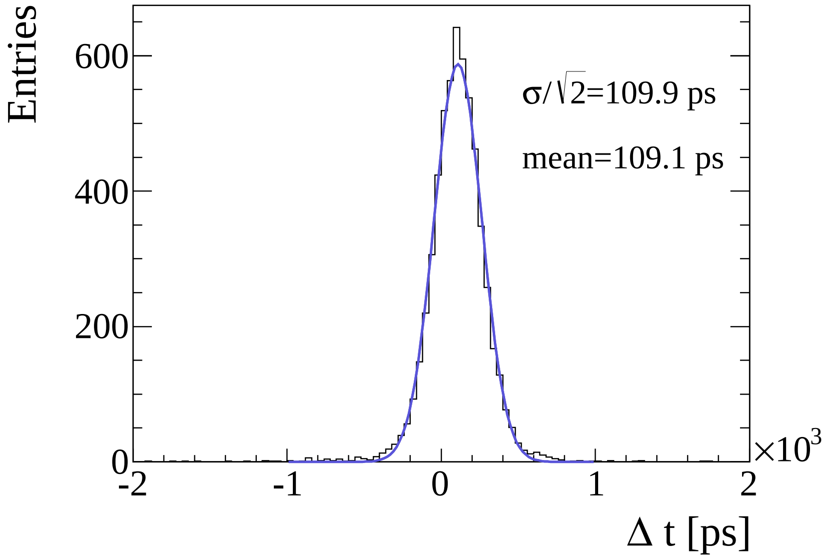

Figure 4.17: Distribution of the difference between a particle's time-of-flight measured independently by the overlapping scintillator bars of the ToF-F detector. The width of the distribution is about 155 ps, indicating a tof resolution of about 110 ps for a single measurement.

4.7 Start counter

The start signal for the time of flight measurement is given by a scintillator counter, called S1, positioned on the beam-line 10 meters upstream of the target. It consists of a square 5×5 cm^2 scintillator counter read out by 4 PMTs as shown in Figure 4.18. t_i ($i = 2, 3, 4$) are the time differences between the $t_{start} \equiv t_1$ signal and the signal from PMT number i; they each provide an independent time and charge measurement of the signal induced by a beam proton interacting in S1. As illustrated in Figure 4.19, the intrinsic resolution of S1 is 70 ps which is obtained by calculating the difference in mean time between two oppositely facing PMTs $((t_1 + t_3)/2 - (t_2 + t_4/2))$.

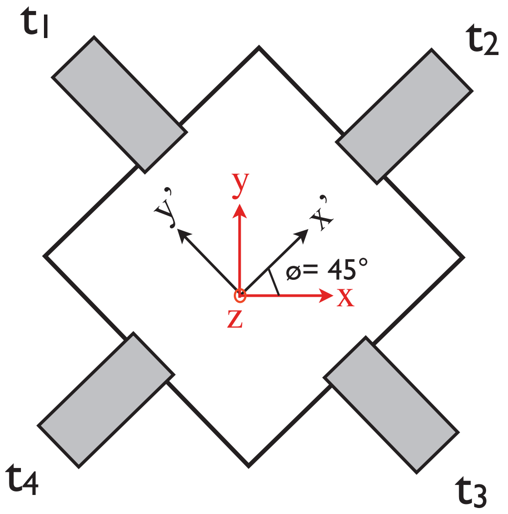

Figure 4.18: Sketch of the S1 start counter. It is rotated by 45 degrees around the z axis with respect to the NA61/SHINE coordinates (in red).

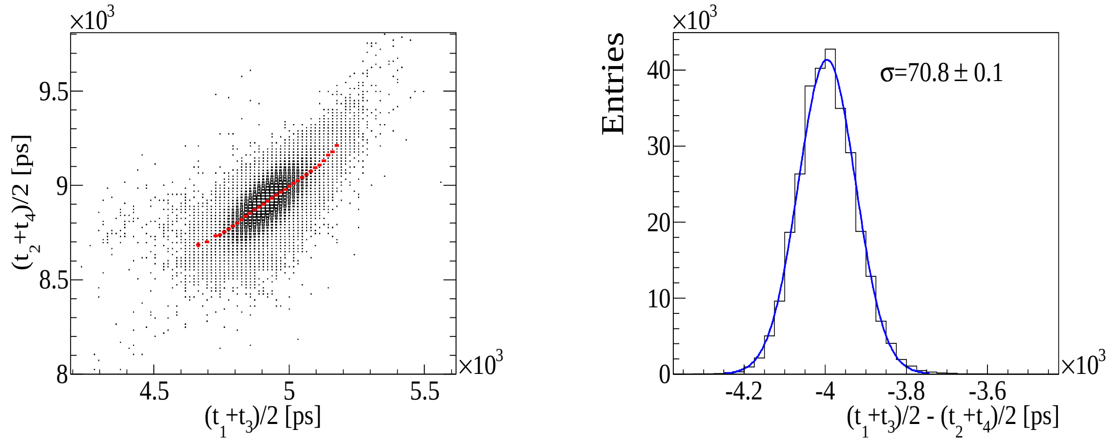

Figure 4.19: Correlation between the two mean times $(t_1 + t_3)/2 - (t_2 + t_4)/2$ from oppositely facing PMTs (left) and difference between the two which provides an estimate of the S1 resolution at ~70 ps.

The 4 PMT read out gives a precise information as to where the incoming proton hit the counter, this information is used on an event by event basis to improve the time of flight measurement. The correction applied to the start measurement t^{cor}_{S1}, for the hit position in S1 is added at each event to the global t_0 offset:

$$t_{S1}^{cor} = \frac{1}{2}\left[\frac{t_1 + t_3}{2} + \frac{t_2 + t_4}{2}\right] \tag{4.15}$$

where t_1 is the start signal and is hence equal to zero. The size of the correction is proportional to the size of the beam spot hitting the S1 counter. It can be estimated by checking for correlations between the spatial coordinates provided by bpd1, placed ∼15 cm downstream of the counter, with $t_1 - t_3$ or $t_2 - t_4$ (see Figure 4.18). Note that for the correlation to appear, the bpd1 coordinates (in red on the figure) must be rotated by 45 degrees to match the S1 local coordinate $(x\prime, y\prime)$. An estimation of the time smearing due to the size of beam in the $y\prime$ and $x\prime$ direction is presented in Figure 4.20. As can be seen for the 2007 short target run the size of beam spot does not allow for any correlations to be observed within the intrinsic resolution of S1. The correction from Equation 4.15 is nevertheless always applied.

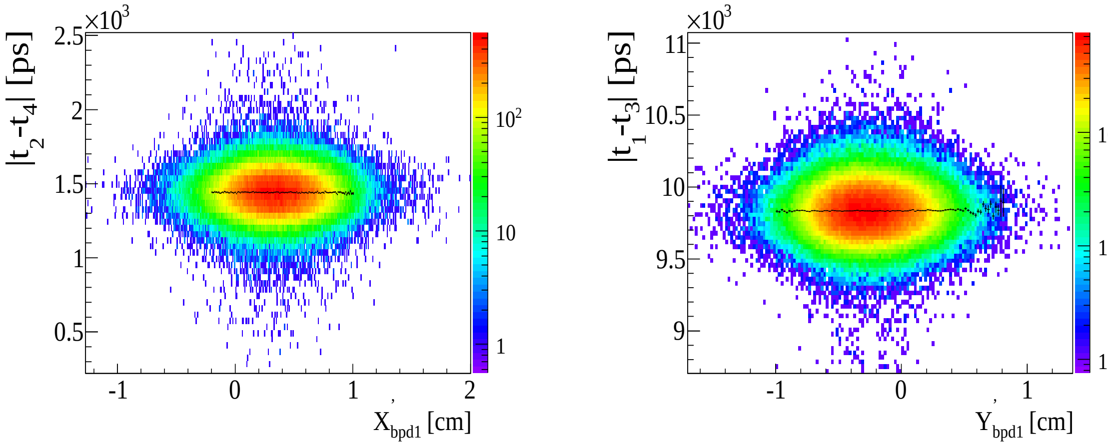

Figure 4.20: Beam spot at S1 for 2007 thin target run. The black markers indicate the mean value of the projections.

4.8 Mass squared spectra

Combining the information from time of flight, track length and momentum the particle's mass squared is computed according to Equation 3.1. The length of a track is retrieved from the TPCs and from the extrapolation process to the ToF. The length is calculated from the nominal z position of the target (-581.4 cm) to the associated z coordinate of the scintillator. The calculated mass squared as a function of momentum is presented in Figure 4.21 for the 2007 thin target and replica target runs. The spectra for the 2009 data taking period where the statistics are about 10 time higher are also shown. The mass squared in three different momentum ranges for the 2007 thin target data are also given in Figure 4.22; pions, kaons and protons are well separated. The top figure shows that at momentum below ∼ 1 GeV pion/electron separation is possible.

As can be noticed from Figure 4.21, similar performances in terms of PID have also been

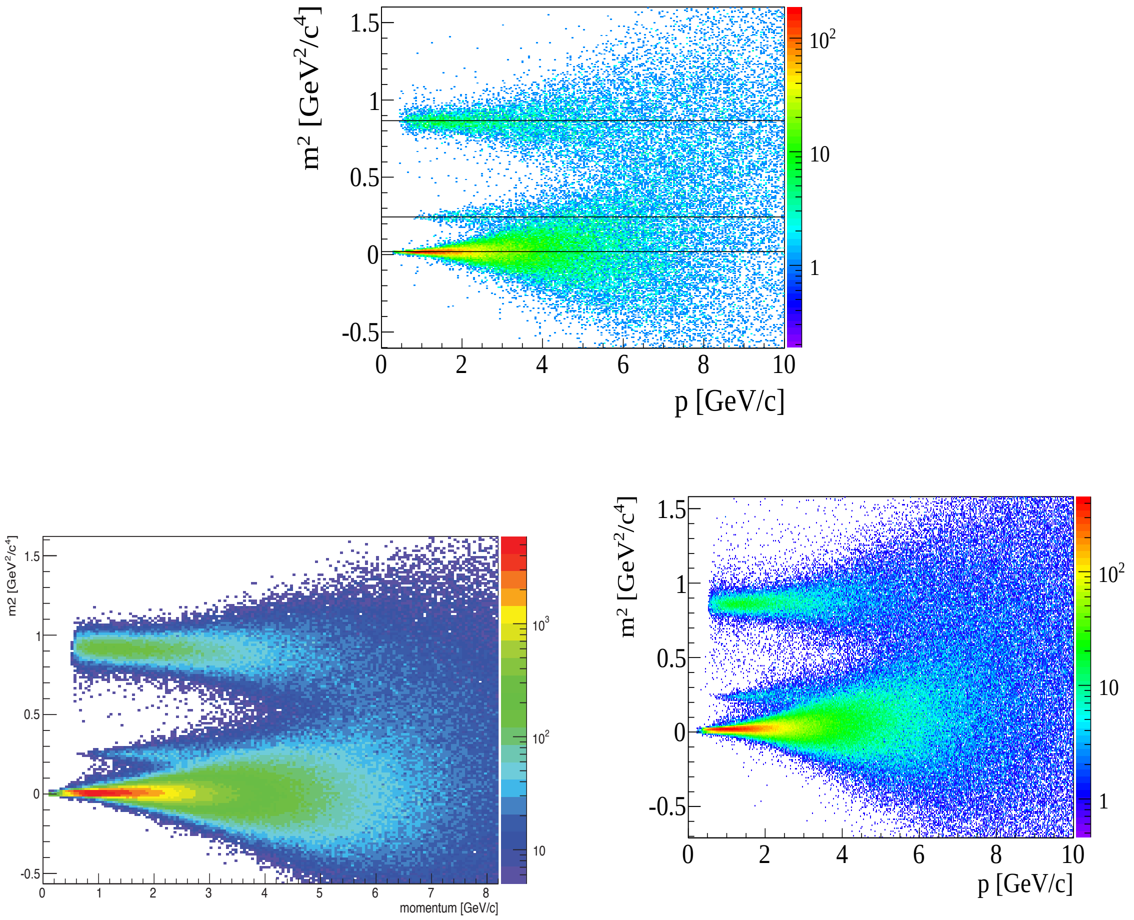

Figure 4.21: mass squared versus momentum for the 2007 thin target run (top), 2009 thin (bottom-left) and replica target runs (bottom-right).

reached with the replica target data. This is furthermore demonstrated in Figure 4.23-left where the fitted sigma of the pion peak are presented for both 2007 thin and replica target data-sets. For the replica target we do not reconstruct the point of interaction and the length is calculated from a plane located at the center of the target. Since the measured time is the difference between the beam proton hitting S1 and the particle hitting the ToF-F (see Figure 4.11), the induced bias is only given by the difference in time of flight between the beam proton ($\beta = 1$) and the produced particle. For a 1 GeV pion ($\beta \simeq 0.99$), the time difference, δt, one gets from extrapolating at the middle of the target is:

$$\delta t = \frac{L_{beam}}{\beta c} \times (\beta_{beam} - \beta_{\pi}) \simeq 15 \text{ ps} \tag{4.16}$$

considering the worst case of L_{beam}= 45 cm for pions produced upstream or downstream of the target. This value is negligible with respect to the resolution on the tof measurement. For a proton produced at 1 GeV/c ($\beta \simeq 0.73$), δt is around 400 ps; as observed in Figure 4.23-right the difference in widths of the proton peaks between long and thin target is more pronounced.

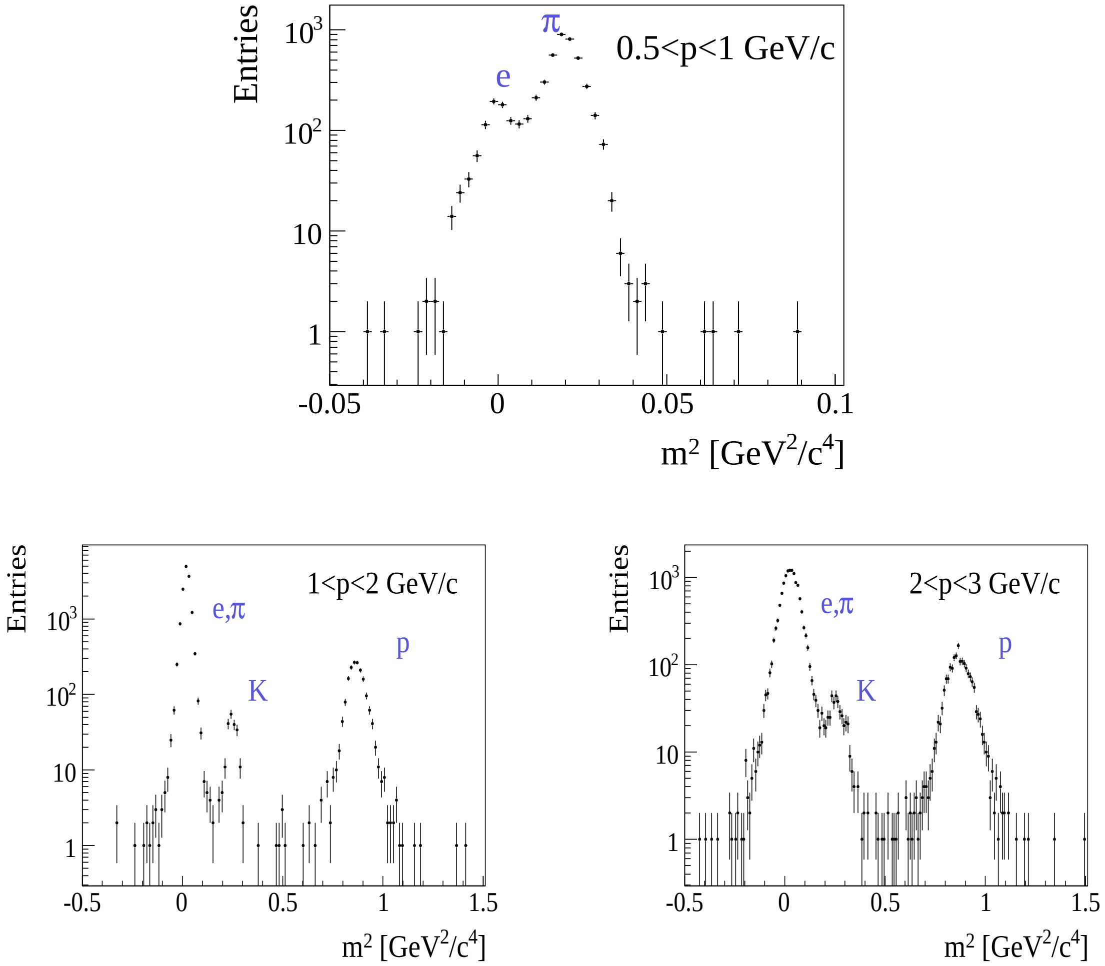

Figure 4.22: mass squared from ToF-F in selected momentum ranges. The accumulations corresponding to pions, kaons and protons are clearly visible. At momentum below 1 GeV/c electrons can also be separated from the pion peak (top figure).

Protons are however well separated from the pion and kaon peaks and thus the corresponding loss in resolution for the replica target is of limited consequence on the purity of the proton samples.

Finally stability of the t_0's over the thin and replica target running periods have been checked. Figure 4.24 gives the fitted mean value of the pion mass as a function of the run during the thin target data taking period. As can be seen no systematic deviation from the expected mass is observed.

4.8.1 Final remarks concerning the ToF-F calibration

The ToF-F was constructed fairly quickly as we had to be ready for the 2007 run. With more time maybe we could have implemented a laser system which would have made the calibration process a lot simpler. Here the only way to calibrate each slat was to use the beam during the

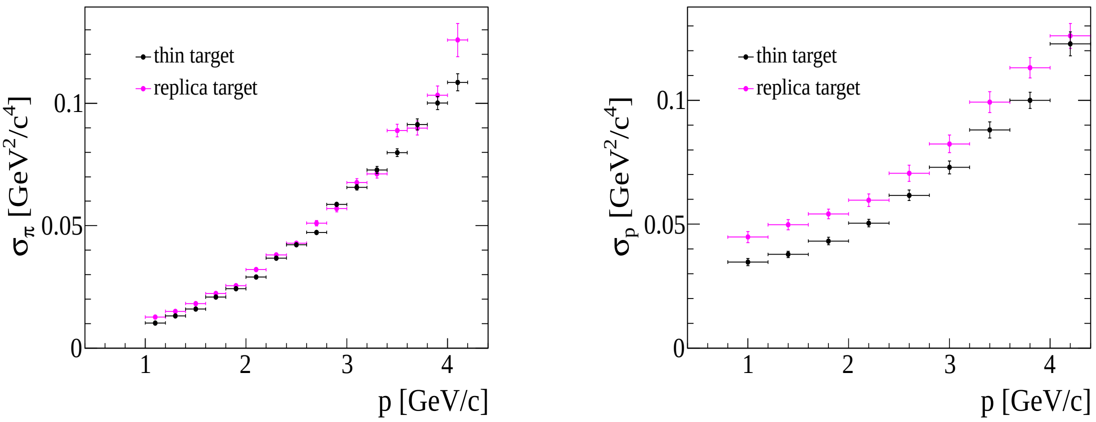

Figure 4.23: Fitted width of the pion (left) and proton (right) peaks as a function of momentum for 2007 short target and replica target runs.

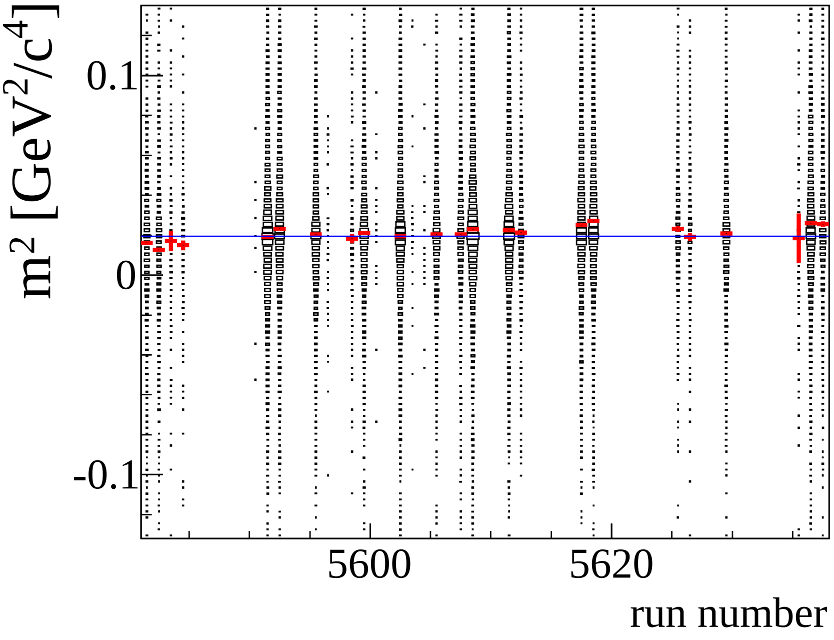

Figure 4.24: Fitted pion mass squared as a function of the 2007 thin target runs. No significant deviation from the expected mass (blue line) is observed indicating the t_0's are constant over this data-taking period.

machine development periods with a lead target to illuminate as much as possible the whole ToF-F wall. Optimal high voltage values for each PMT were set by looking at the ADC spectra once we had enough data in each of the slats. The same was done to calibrate the thresholds of the CFDs. Once the ToF-F was fully calibrated the extrapolation code, along with the time and geometrical calibration values, were included in the reconstruction software via the `ftof_client`. This client is called at the end of the reconstruction chain and returns information such as PMT numbers, ToF-F coordinates, time of flight and mass-squared of the corresponding track that hit the ToF-F. These values are now part of the final information available in the NA61 analysis structures.

Chapter 5

Measurements of K^+ cross-sections with the combined tof-dE/dx particle identification

While charged pions generate most of the low energy muon neutrinos, positively charged kaons generate the high energy tail of the T2K beam, and contribute substantially to the intrinsic ν_e component of the beam (see Section 2.4). Accurate knowledge of kaon multiplicity is therefore crucial to reduce the error on the flux prediction. The kinematic region of interest for this analysis is defined by the spectra of positively charged kaons whose daughter neutrinos pass through the SK detector shown in Figure 5.1. The low statistics available in this pilot data set imposes a rather coarse $\{p, \theta\}$ binning which covers only the most populated region of phase space relevant for T2K. Moreover, the statistics of the 2007 data does not allow for measurements of negatively charged kaons.

5.1 Data binning

The adopted binning scheme is mainly driven by the available statistics and is represented in Figure 5.1. Details can be found in Table 5.2. The highest θ limit is determined by the requirement for the track to be in the geometrical acceptance of the ToF-F detector. Only two angular intervals are defined. The first angular interval extends from 20 to 140 mrad so as to cover most of the T2K relevant θ range and, combined with a 0.8 GeV/c momentum bin width, to have a few thousands of selected tracks per interval (see Table 5.2). Measurements were performed up to 7.2 GeV/c. This choice comes from the fact that in the relativistic rise region (above 4-5 GeV/c) particle identification requires extracting the rapidly decreasing kaon signal from the predominant proton one. With the available statistics of 2007 data the applied procedure turned out to be robust only up to about 7 GeV/c.

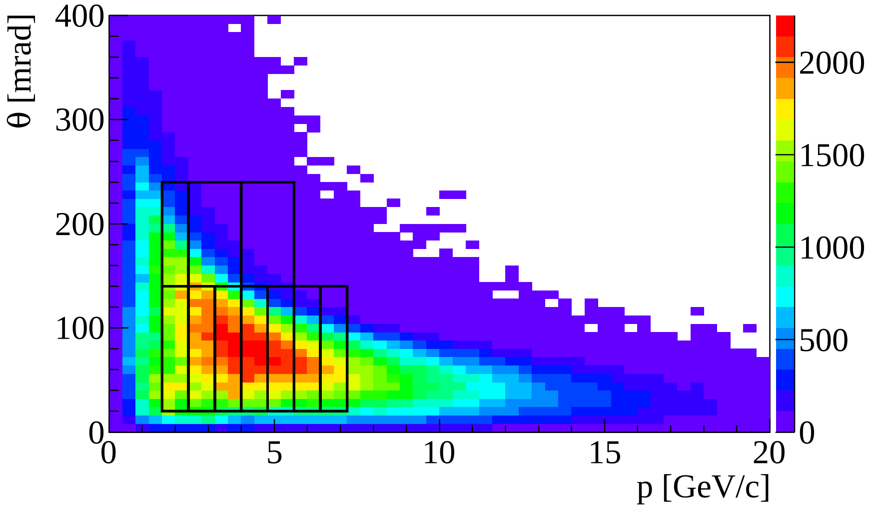

Figure 5.1: The prediction from the T2K beam simulation; the $\{p, \theta\}$ distribution for positively charged kaons weighted by the probability that their decay produces a neutrino passing through the SK detector. The binning used in the present analysis is superimposed; the kinematic range considered is $1.6 < p < 7.2$ GeV/c and $20 < \theta < 240$ mrad.

5.2 Event and track selection

In total this analysis is based on 452'718 reconstructed events collected during the 2007 data taking. To clean up the sample and to reduce the amount of events happening in the material outside of the carbon target, only events for which a beam track is properly reconstructed by the BPDs are kept. For this purpose, a selection based on the BPD coordinates is performed. This cut, called BPD cut(II), ensures that the x and y directions of the beam particle has been measured by all three beam position detectors and additionally that the BPD3 coordinates were taken into account in the BPD-vertex fit. The effect of the cut is illustrated in Figure 5.2. Approximately 20% of the events are removed by this selection.

In addition to the event cut, several criteria were applied to select well-measured positively charged tracks in the TPCs and ensure high reconstruction efficiency as well as to reduce the contamination of secondary tracks:

(i) TRK cut(I): track momentum fit at the interaction vertex should have converged,

(ii) TRK cut(II): a minimum of 12 reconstructed points in the two TPCs used for momentum measurement, VTPC-1 and VTPC-2, is required,

(iii) TRK cut(III): the track must have a dE/dx signal and an associated ToF-F hit

(iv) TRK cut(IV): the distance of closest approach of the fitted track to the interaction point (impact parameter) is required to be smaller than 4 cm in both transverse directions,

(v) TRK cut(V): the track must leave the primary vertex at an azimuthal angle ϕ within ±20° around the horizontal plane, for the first θ interval, and ±10° for the second,

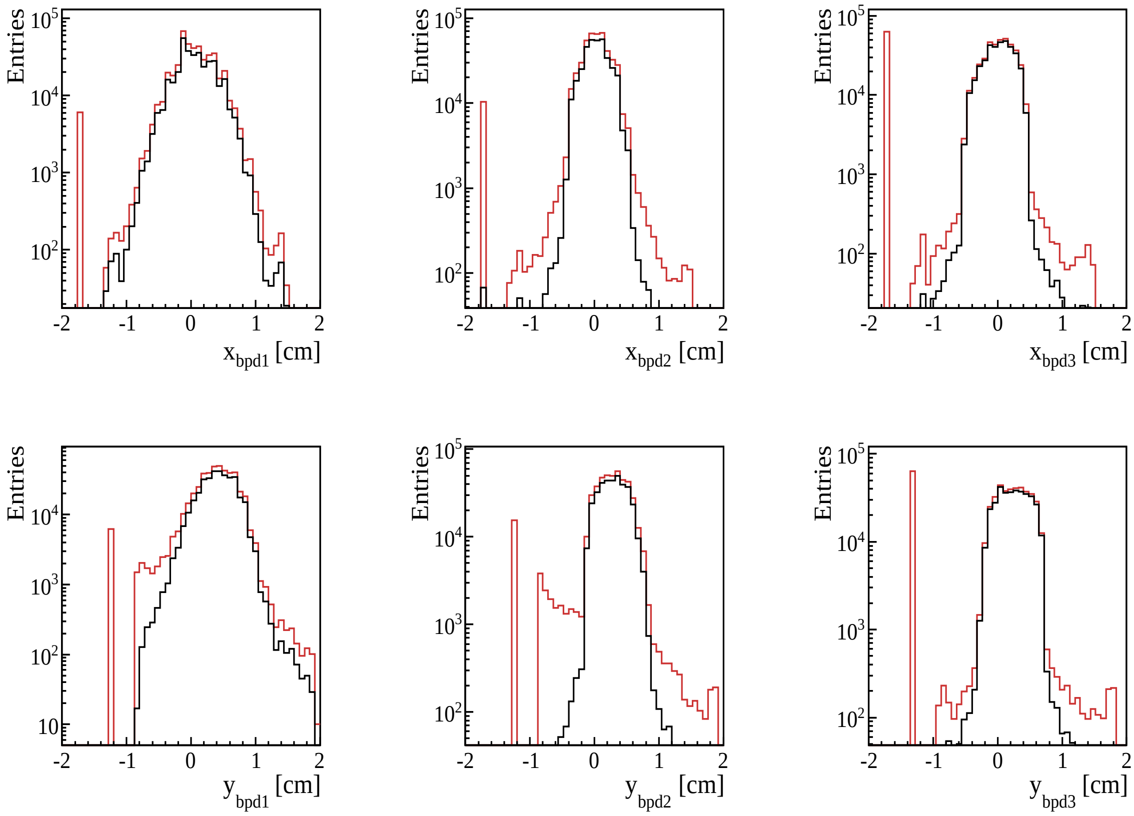

Figure 5.2: Distribution of BPD coordinates before (in red) and after (in black) the event cut.

(vi) TRK cut(VI): The z position of the last reconstructed point, z_{last}, must be greater than 680 cm.

Only tracks which have a momentum determined at the vertex are used in this analysis, TRK cut(I) ensures that the angle and momentum of those tracks, along with their respective errors, are well determined. A minimum number of points in VTPC is required in order to select tracks with a well measured momentum. The full set of cuts furthermore defines the detector's geometrical acceptance by rejecting particles reconstructed at the edges of the VTPCs where non-uniformity of the magnetic field may affect the momentum determination. As is demonstrated in Figure 5.3, the momentum resolution for the selected tracks ($\delta p/p$) is kept around 1%.

Due to the presence of the magnet material and uninstrumented region along the beam axis, the azimuthal acceptance of the NA61/SHINE setup in the $x - y$ projection (transverse to the beam axis) is limited to only the central part of the left and right hemispheres of the phase space (see Figure 5.4). This region is further constrained to smaller angles by requiring that tracks hit the ToF-F. As demonstrated in Figure 5.5 where the distributions of azimuthal angles, ϕ, are plotted for both angular bins considered, tracks emitted close to the central planes at $\phi = 0$ of $\phi = 180$ have maximal geometrical acceptance, and thereby selecting only the flat regions of the distributions ensures that only well measured tracks are present in the final sample. Most importantly, as will be shown in Section 5.4, it prevents from making large Monte Carlo based

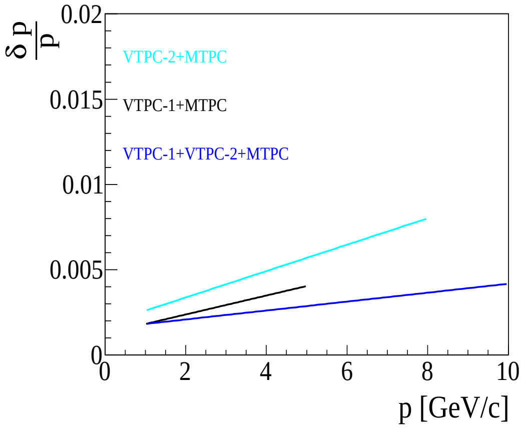

Figure 5.3: Track momentum resolution ($\delta p/p$) as a function of momentum for different track topologies.

acceptance and efficiency corrections. Since the azimuthal acceptance varies with the polar angle an individual wedge in azimuthal angle was adjusted for each particular bin. The asymmetry in the distributions from Figure 5.5 is due to the different track content of each peak: the peak at $\phi = 0°$ is populated by positive right-side-tracks (ratio of p_x momentum component over charge $p_x/Q > 0$, see Section 3.5), while the peak centered around $\phi = 180°$ is populated by positive wrong-side-tracks ($p_x/Q < 0$).

Requiring a reconstructed point at the upstream edge of the MTPC (TRK cut (VI)) assures that no, or very few, decay-in-flight kaons are associated with a ToF-F signal. The purpose of this cut, which is of crucial importance to clean up the final kaon sample, is discussed in Section 5.2.2.

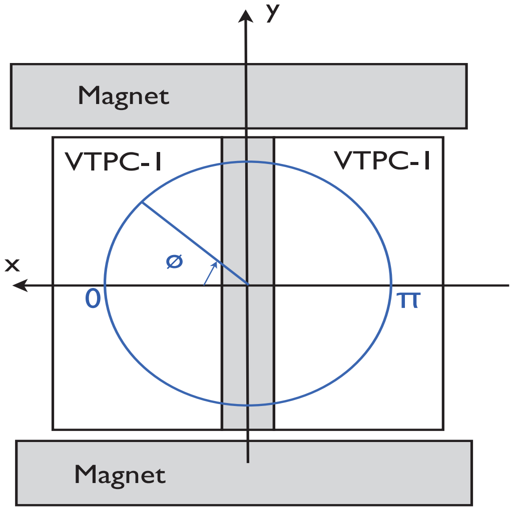

Figure 5.4: Illustration of the NA61/SHINE azimuthal coverage. The azimuthal angle, ϕ, is measured from the horizontal plane starting from the positive x side of the NA61/SHINE reference system. The coverage is limited by the presence of the magnets or uninstrumented TPC regions (shaded areas).

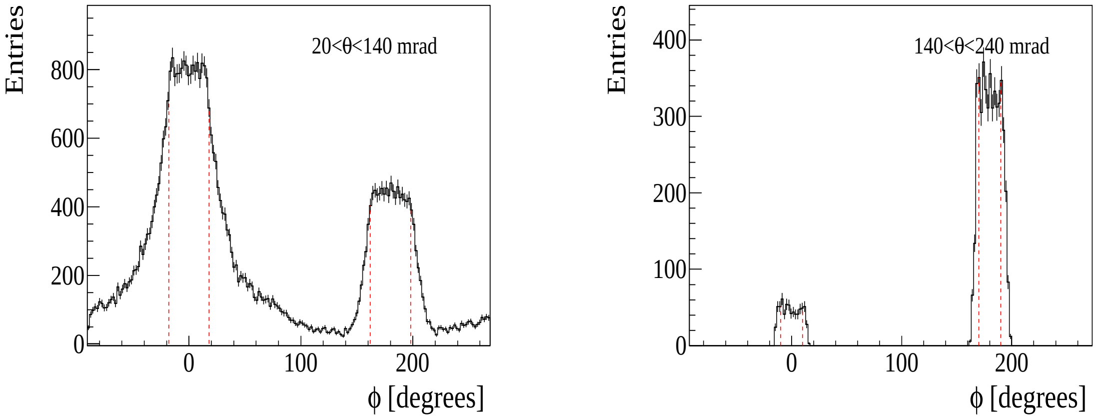

Figure 5.5: Distributions of azimuthal angle for positively charged particles that reach the ToF-F in the first (left) and second (right) angular bin. The dotted red lines indicate the applied cuts.

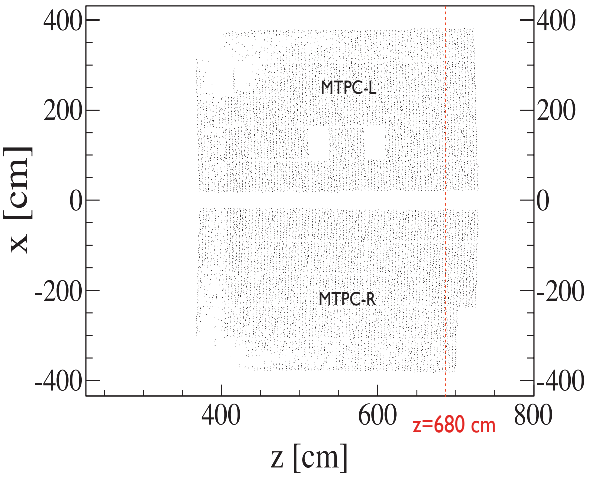

Figure 5.6: Reconstructed points in the MTPCs. Only tracks for which the last point is greater than z=680 cm (red line) are selected.

5.2.1 Geometrical acceptance

The selection on the azimuthal angles, along with the requirements on the number of points and the cut on z_{last} (TRK cut (V), (II) and (VI) respectively) define the detector's geometrical acceptance. A study of the acceptance in the $\{p, \theta\}$ plane is performed by generating a flat phase space Monte Carlo, as defined in Section 3.7. p and θ are randomly distributed in each bin and the azimuthal angle, ϕ, is constrained to be within the selected wedges. The acceptance is then defined by retaining tracks which pass selection criteria II, V and VI and normalizing each bin by the generated sample. Figure 5.7 shows the geometrical acceptance of the detector for both right-side-tracks (RST) and wrong-side-tracks (WST) sub-samples, the considered kinematic range for the analysis along with the binning is super-imposed in black. The selection on the azimuthal wedge are such that a uniform detection efficiency is obtained over a maximal area of the $\{p, \theta\}$ phase space of interest. There are however sharp drops in the acceptance in some areas, in fact for the same $\{p, \theta\}$ bin, the fraction of accepted tracks differs significantly between the two topologies. RST produced at high angle ($\gtrsim$ 200 mrad) are bent out of the ToF-F acceptance while for WST, the lower acceptance at smaller angles ($\lesssim$ 100 mrad) is a consequence of the uninstrumented regions in the TPCs along the beam axis. In order to improve the accuracy of the Monte Carlo correction and to reduce the dependence on the model used for simulation, only one track topology per bin, the one with the highest acceptance, is chosen. This defines an additional track cut:

(vii) TRK cut(VII): only RST are selected in the first angular bin and only WST in the second.

The removed samples are hatched in Figure 5.7. Figure 5.8 shows the WST, RST and final track content in each bin. As can be seen, while the selection of track topologies based on the acceptance does not reduce the available statistics in the second angular bin, it removes approximately one third of the tracks in the first angular interval. It is however preferable to select a small and well under control sample of tracks which do not require any (or, at least, a very small) geometry correction. If we were to keep tracks that require important acceptance corrections, any discrepancies between the data and the simulation would lead to high and difficult to estimate systematical errors. The same argument also justifies the azimuthal cut. The impact of the event and track selection on the initial sample is presented in Table 5.1. Figure 5.9 shows the final statistics in each bin which is available for particle identification.

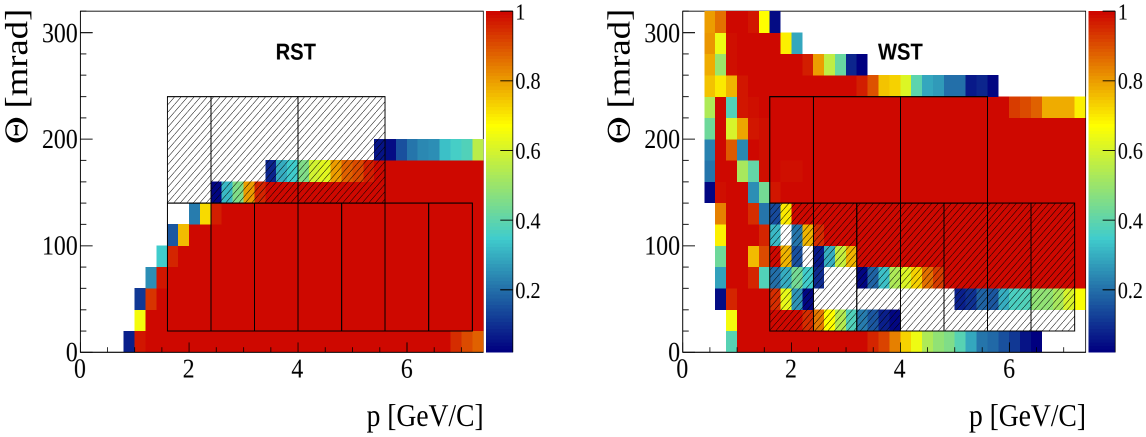

Figure 5.7: Simulated geometrical acceptance for RST (left) and WST (right) with analysis binning super-imposed. Maps are normalized to the number of tracks generated within the selected azimuthal wedges. For a given θ bin, only the topology with maximal acceptance is selected. Hatched areas indicate those which are removed.

5.2.2 Treatment of decays

As has been discussed in Section 4.4, the position of a ToF-F hit is determined only in the x direction and with a precision given by the width of the scintillator slat producing the signal

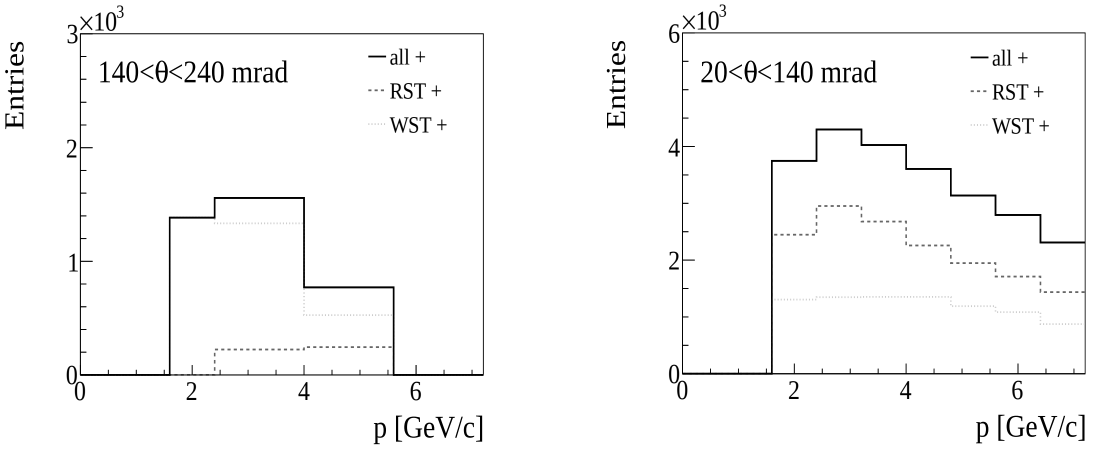

Figure 5.8: RST and WST content of the bins considered for the analysis.

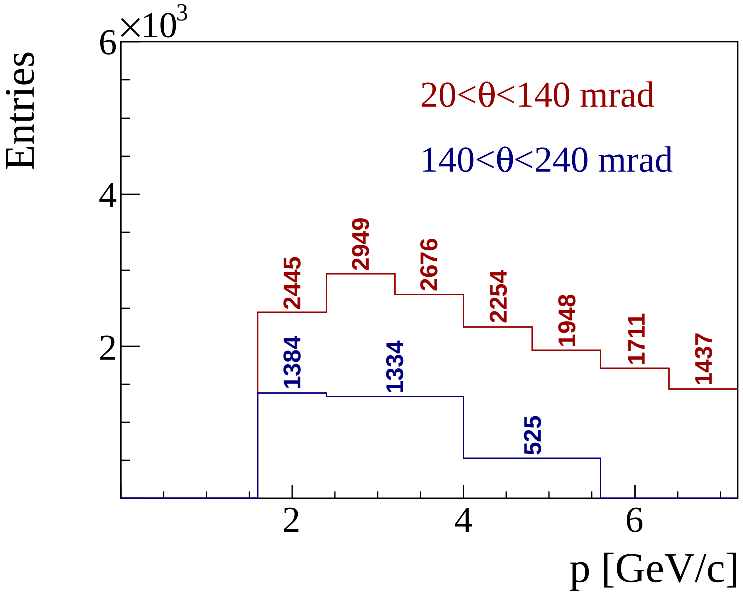

Figure 5.9: Final track content once all selection criteria are applied.

(~ 10 cm). A ToF-F hit is then associated to a track if the trajectory can be extrapolated to the pertaining slat. The relatively short proper decay length of kaons ($c\tau \sim 3.7$ m) compared to the longitudinal extension of the detector (~ 13 m) implies that almost 60% of these particles produced in the target at the lowest laboratory momentum considered, 1.6 GeV/c, decay before reaching the ToF-F array. Thanks to the high Q values of the kaon decay channels (see Appendix C), kink topologies are correctly reconstructed as a primary and a secondary track (i.e. not fitted to the primary vertex) with an efficiency higher than 98%. Figure 5.10 gives the kink angles (angle between the parent and daughter) from a Monte Carlo simulation as a function of the parent momentum for kaon two body decay. The kink angle for pion decay is also

cut		**number**	**% remaining**	**effect**
Event cuts				
all		442434	100%	-
bpd	BPD cut(II)	355227	80.3%	19.7%
Track cuts				
positive tracks	TRK cut(I)	208583	100%	-
number of points in VTPCs	TRK cut(II)	189112	90.7%	9.33%
tof requirement	TRK cut(III)	62545	30%	66.9%
impact parameter	TRK cut(IV)	60881	29.2%	2.66%
azimuthal angle	TRK cut(V)	32602	15.6%	46.4%
last measured point z_{last}	TRK cut(VI)	27620	13.2%	15.3%
selection WST/RST based on acceptance	TRK cut(VII)	18662	8.95%	32.4%

Table 5.1: Impact of the event and track cuts.

shown for comparison. The theoretical curves, computed in Appendix C, corresponding to the maximum allowed angle are super-imposed. At the energies at which we operate, the kink angles are around 10° for kaon and are generally below 1° for pions. Nevertheless, for a 10° kink angle, the secondary particle could produce a hit along the same scintillator bar in which a hit from the primary is expected and a ToF-F hit would thus be associated to a kaon decaying in flight. As a consequence the time of flight measurement could be significantly biased. Such special topologies can be effectively rejected by considering only tracks reconstructed until the downstream edge of the MTPCs (TRK cut(VI)). This is demonstrated in Figure 5.11 where the z coordinate of decay vertices for K^+ decaying between the point of production (-581.4 cm) and the ToF-F ($\sim$ 760 cm) are retrieved from the detector simulation. The black distribution shows the point of decay for K^+ matched to tracks generated with a momentum and angle belonging to the acceptance but not necessarily associated to a ToF-F hit. The super-imposed gray histogram on the other hand, corresponds to those tracks which are associated to the ToF-F. As can be seen without the z_{last} cut a rather large fraction of kaons decaying before the ToF-F are nevertheless associated to a scintillator for the reasons mentioned above. When the track is requested to be reconstructed to the downstream edge of the TPC (Figure 5.11-right) this contamination reduces drastically. Only kaons decaying between $z = 680$ cm and the ToF-F remain in the final selected sample. This small contamination of kaons is accounted for when correcting the spectra for kaon decay (see Section 5.4).

5.3 Particle identification

K^+ are identified by combining the information of the TPC and ToF-F signals (see Section 3.6) to achieve a particle separation that covers the required momentum range. As an example, the distributions of measured m^2 versus dE/dx in the first angular interval, $20 < \theta < 140$ mrad for several momentum bins are shown in Figure 5.12. Accumulations corresponding to protons (p),

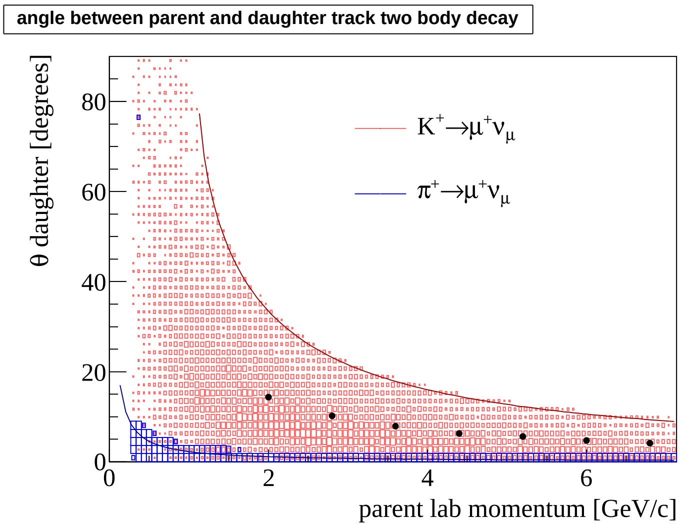

Figure 5.10: Values of the angles between the daughter muon and parent (K^+ or π^+) as a function of the parent lab momentum for Monte Carlo generated events. Theoretical Curves corresponding to the maximum allowed angles are super-imposed. The black markers indicate the mean value of the kaon-muon angle at the center of the bin considered for the analysis.

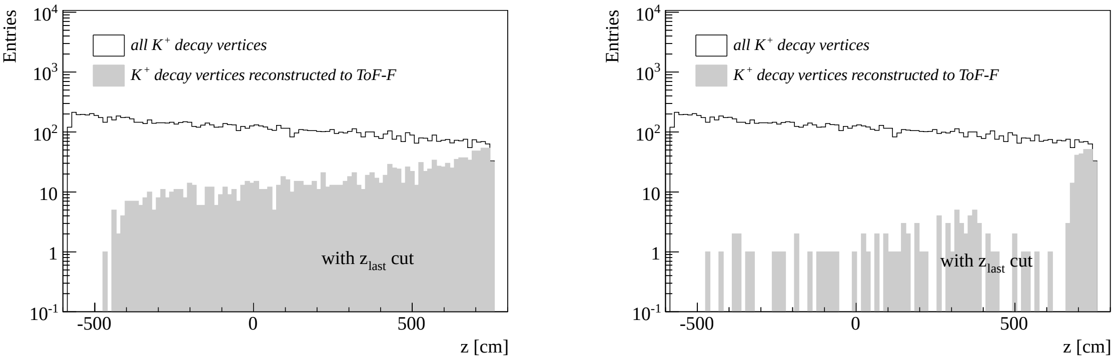

Figure 5.11: z coordinate of the K^+ decay vertices (MC simulation). The gray histogram represents the fraction of tracks which are associated to a ToF-F hit without (left) and (with) the cut on z_{last}.

kaons (K^+), pions (π^+) and positrons (e^+) are clearly observable.

In each $\{p, \theta\}$ bin, we assume that the number of events (x_{dedx}, x_{m2}) in the m^2-dE/dx plane are described by a superposition of four bi-dimensional Gaussians defined by the following p.d.f:

$$f(x_{dedx}, x_{m2}, \alpha) = \sum_{i=e,\pi,K,p} \frac{A_i}{2\pi\sigma^i_{dedx}\sigma^i_{m2}} \exp\left\{\frac{(x_{m2}-\mu^i_{m2})^2}{2\sigma^{2i}_{m2}} + \frac{(x_{dedx}-\mu^i_{dedx})^2}{2\sigma^{2i}_{dedx}}\right\} \quad (5.1)$$

where $\alpha = \{A^i, \mu^i_{dedx}, \sigma^i_{dedx}, \mu^i_{m2}, \sigma^i_{m2}\}$ is a vector containing the normalization factor for particle of type i (A^i), the mean dE/dx and mass squared values $(\mu^i_{m2}, \mu^i_{dedx})$ and the width of the distributions $(\sigma^i_{m2}, \sigma^i_{dedx})$. Altogether the vector has 20 parameters to be determined, 4 yield- 8 width- and 8 mean-parameters. In all analyzed bins, however, the e^+ accumulations in the

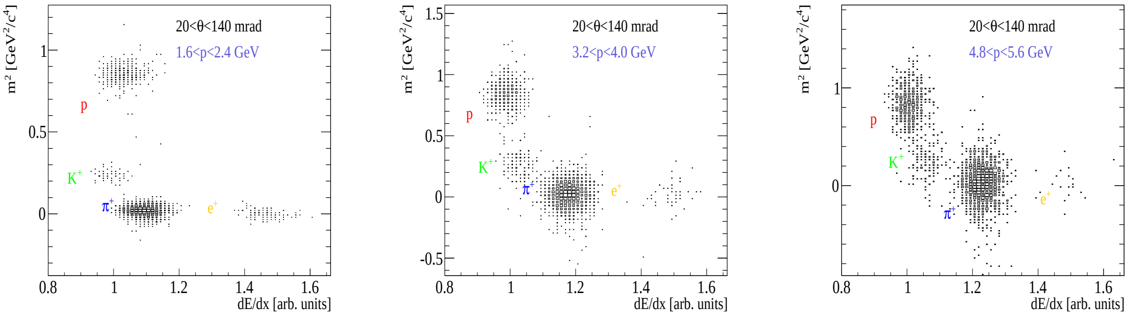

Figure 5.12: Scatter plots of m^2 versus dE/dx measured for the selected tracks in three $\{p, \theta\}$ bins.

m^2-dE/dx plane are fully separated from other particles (see Appendix E) and thus the number of parameters relevant for the kaon yield determination reduces to 15. The parameters are determined by fitting the p.d.f to each m^2-dE/dx distributions using the binned Maximum Likelihood method. The likelihood function $\mathcal{L}$ is evaluated over N m^2-dE/dx bins and is a function of the set of parameters α:

$$\mathcal{L} = \prod_{l=1}^{N} f(x_{dedx}, x_{m2}, \alpha) \tag{5.2}$$

The maximisation is actually performed on the logarithm of the likelihood function $\ln \mathcal{L}$ and is turned into a minimisation procedure by using $-\ln \mathcal{L}$. In order for the minimisation procedure to converge a very accurate initialisation of all the parameters is necessary. Initial values of all the parameters are retrieved from separate one dimensional fits (also with the Maximum Likelihood method) independently to those m^2 or dE/dx distributions for which particle species are well separated. For example, the proton peak can be isolated from the others with m^2 measurements over the whole momentum range of the analysis (i.e up to 7.2 GeV/c, see for instance Figure 4.21) while pion/kaon separation is possible up to around 4 GeV/c. The electron peak from the dE/dx distribution may also be easily fitted in each $\{p, \theta\}$ bin, as well as the pion peak above ~ 4 GeV/c. The results from those fits are parametized in order to predict the values of the parameters over the whole $\{p, \theta\}$ phase-space. The initialization procedure of each parameter is described below.

(i) *width of the m^2 distributions* (σ^i_{m2}): the error on the particle's mass-squared is dominated by the error on the time of flight measurement t:

$$\delta m^2 = \frac{p^2 c^2 t}{l^2} \delta t \tag{5.3}$$

Therefore the resolution on the mass-squared δm^2 deteriorates quadratically with increasing momentum. This is observed in Figure 5.13 where the widths of the proton and pion distributions retrieved from a fit to only the tof measurements are shown. The momentum dependence of the σ^i_{m2} is well fitted by a second order polynomial. σ^i_{m2} is larger for protons than pions, since for the same momentum and path length, the time of flight is larger for heavier particles. The kaon width-parameter cannot be fitted because of the small separation in m^2 of the kaon and pion Gaussians. It is therefore calculated using the fitted width of the pion distribution at the momentum bin center rescaled for the correct mass value. The proton and pion resolution functions are derived via parabolic fits extended over the momentum range where peaks are well separated (e.g. up to 5.6 GeV/c for 20< θ <140 mrad, see Fig. 5.13-left). Initial values for width-parameters are therefore calculated by evaluating the resolution functions at the center of the momentum bin.

(ii) *mean of the* m^2 *distributions* (μ^i_{m2}): is initialized to the particle's mass-squared. A check is performed by fitting the mean-parameters of the m^2 distribution of protons, kaons and pions in the bins in which particle accumulations are well separated (e.g. up to 4 GeV/c for pion/kaon separation and whole momentum range for proton/pion). Figure 5.13 shows a distribution of the fitted mean value of the proton peak in both polar angle bins as an example. As can be seen the values are indeed centered around the expected mass-squared and are independent of momentum or angle which proves the correctness of the ToF-F calibration procedure.

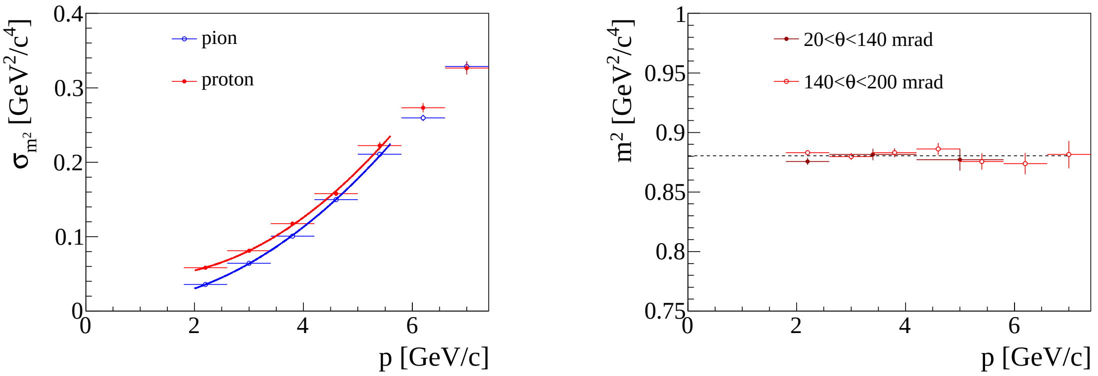

Figure 5.13: **[Left]**:m^2 resolution versus the measured momentum for tracks with 20< θ <140 mrad. Parabolic fits to the best measured points are superimposed. **[Right]**: fitted mean proton mass-squared as a function of momentum for both angular bins. The dotted line indicates the expected m^2.

(iii) *width of the* dE/dx *distributions* (σ^i_{dedx}): the measured width of the different dE/dx peaks is the result of the experimental (detector) resolution and the smearing due to the variation of the dE/dx mean value with the momentum. The experimental resolution decreases as $\propto 1/\sqrt{N_p}$ [121] where N_p is the number of samples (points). As demonstrated in Figure 5.14, the selection of long tracks for the analysis ensures that the number of points is large enough so that the dE/dx resolution is constant at about 3%. Thus, a constant value of $\sigma^{i2}_{exp} = 3\%$ is used to initialize the corresponding parameters of the fit. Selection of long tracks also assures that the simple Gaussian approximation is still applicable because it selects tracks with approximately the same number of points and reduces fluctuations in the dE/dx fit. If, in a given bin, the distribution of number of points were peaked at a lower mean value, or had large variations, the actual distribution of the energy loss would rather be a superposition of Gaussians of different widths. The initial resolution is further scaled by the derivative of the Bethe-Bloch parametrization over the width of the considered momentum bin to take into account the spread of the energy loss distribution due to projections in regions of strong variations (e.g relativistic rise region).

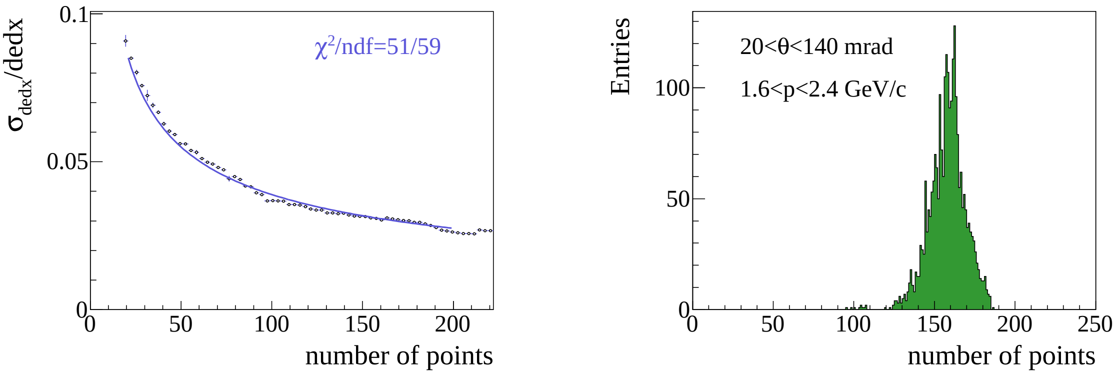

Figure 5.14: **[Left]**: dE/dx resolution as a function of number of points on track. **[Right]**: typical distribution of number of points for a $\{p, \theta\}$ bin of the analysis.

(iv) *mean of the dE/dx distributions* (μ^i_{dedx}): since the mean energy loss depends only on the momentum to mass ratio ($\beta\gamma$), the dE/dx distributions of different particle species with the same momentum are shifted. In the fit only the pion mean energy loss was a free parameter. The kaon and proton mean-parameters were instead calculated using the fitted pion mean and the shifts calculated from the Bethe-Bloch parametrization. The reason for doing so is to avoid the kaon μ^i_{dedx} being systematically biased towards the protons in higher momentum bins where the two peak start to overlap. Using the existing Bethe-Bloch curve as calculated from the calibration procedure is not reliable enough since it represents an overall parametrization of data covering a wide range of track topologies. Dedicated fits in the $m^2 - dE/dx$ plane in regions where the particle species are well separated have shown deviations of up to 4% for the kaon μ^i_{dedx} . A reliable Bethe Bloch parametrization was therefore retrieved from dedicated fits to the analysed data sample. As can be seen in Appendix E and Figure 5.12 the pion accumulations in the $m^2 - dE/dx$ plane can be well determined in all analysed bins. For protons and kaons this is possible in a few lower momentum bins. Thus a precise fit of the dE/dx mean-parameter is possible over the whole $\beta\gamma$ range relevant for the analysis. The results are presented in Figure 5.15. Points with low and intermediate $\beta\gamma$ correspond to protons and kaons while points with high $\beta\gamma$ correspond to pions. Thus, points measured with high precision are the ones with lower and higher $\beta\gamma$ while the intermediate region corresponds to protons and kaons of high momenta for which the accumulations overlap (Figure 5.12).This means that, for intermediate $\beta\gamma$ values, an accurate parametrization of the expected dE/dx can be obtained from a Bethe-Bloch curve fitted only to the high precision measured points, which are in the low- and high-$\beta\gamma$ region, as specified in Figure 5.15. The precision of this procedure, estimated from the residuals with respect to the fit points, is about 0.5%. The Bethe-Bloch function used for the fit is taken from the PDG [144]. It describes the mean rate of energy loss by moderately relativistic charged heavy particles in the region $0.1 \lesssim \beta\gamma \lesssim 1000$ and depends on a variety of parameters the most important ones being the atomic number and mass of the absorber (i.e the TPC gas). The parameters will be noted here by the letters a, b and c. For a complete definition please refer to [144]. The function $\mathcal{F}_{BB}(\beta\gamma)$ used for the fit is described as:

$$\begin{aligned} \mathcal{F}_{BB}(\beta\gamma) &= \frac{a}{\beta^2}\left[\frac{1}{2}\ln(b\beta^2) - \beta^2 - c\right] \\ \text{with } \beta^2 &= \beta^2\gamma^2/(1+\beta^2\gamma^2) \end{aligned} \tag{5.4}$$

a, b and c are left as free parameters to adjust to the measured points. The returned values for this specific fit (shown in Figure 5.15) are $a = 0.136,\ b = 0.543,\ c = -6.750$.

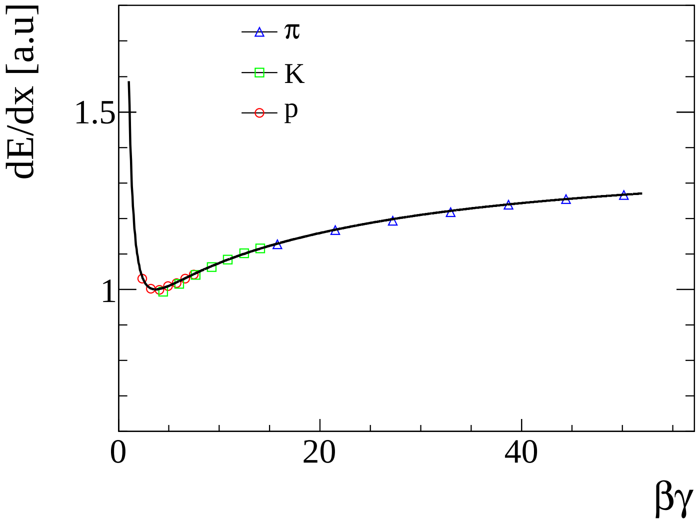

Figure 5.15: Bethe-Bloch function fit to mean dE/dx values (data points). The points used in the fit are from protons and kaons of $\beta\gamma < 6$ and pions of $\beta\gamma > 20$.

(v) *Amplitudes (A^i)*: the p.d.f. being normalized, the yield of a particle of type i is directly given by the A^i parameter of the fit:

$$\iint \frac{A^i}{2\pi\sigma^i_{dedx}\sigma^i_{m2}} \exp\left\{\frac{(x_{m2}-\mu^i_{m2})^2}{2\sigma^{2i}_{m2}} + \frac{(x_{dedx}-\mu^i_{dedx})^2}{2\sigma^{2i}_{dedx}}\right\} \mathrm{d}x_{dedx}\mathrm{d}x_{m2} = A^i \tag{5.5}$$

During minimization, parameters are allowed a 30% variation around their initial value in order to adjust to the data if needed. The range was later varied for different parameters in order to verify the stability of the fit and to estimate systematic errors linked to the fitting procedure (see Section 5.5). Figure 5.16 shows an example of a 2 dimensional fit in a specific bin with the projections of the function along the m^2 and dE/dx axis. The fits for all bins considered in the analysis are further given in Appendix E. Residuals, defined as the bin content minus the value of the p.d.f at the bin center divided by the bin error are also calculated for each projection. For all fits, no significant or systematic shift of those residuals is observed which indicates that the data is well described by the fit function and specifically that the Gaussian assumption is valid (more on that in the next section). The calculated Poisson chi-squared per number of degrees of freedom, χ^2_λ/ndf and it's corresponding p-value were also calculated for each fit as explained in Appendix D. The returned values generally indicate a good level of agreement between the hypothesis and the data.

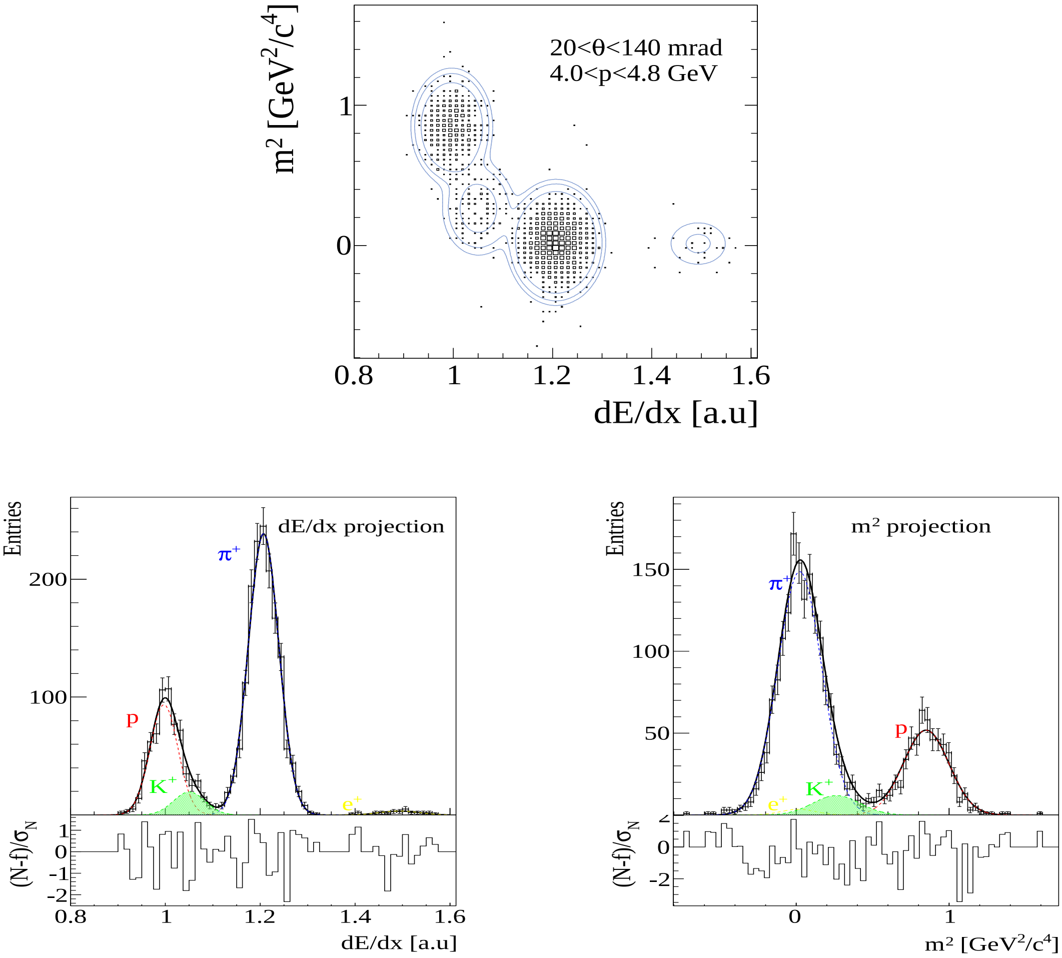

Figure 5.16: Example of a bi-dimensional fit to the $m^2 - dE/dx$ distribution. The function is drawn with the 2, 1.5 and 1 σ contours around the fitted kaon peak. The m^2 and dE/dx projections are also shown superimposed with the results of the fitted functions.

The mean parameters, μ^i_{dedx} and μ^i_{m2} , returned by the fitting procedure are also presented in Figure 5.17 as a function of momentum for the first angular interval. Their respective dE/dx or m^2 versus momentum distributions and the functions parameterizing the input values are also drawn. As can be seen the fitted parameters are very close to their initial value which indicates an accurate initialization. Specifically the deviations of the mean dE/dx for the fitted pion peak (and hence of the proton and kaon since the relative distance is fixed) are always below the percent level which indicates an accurate parametrization of the Bethe Bloch curve.

Finally, the fitted raw yields of all particles are presented in Figure 5.18 and details for the kaons are given in Table 5.2.

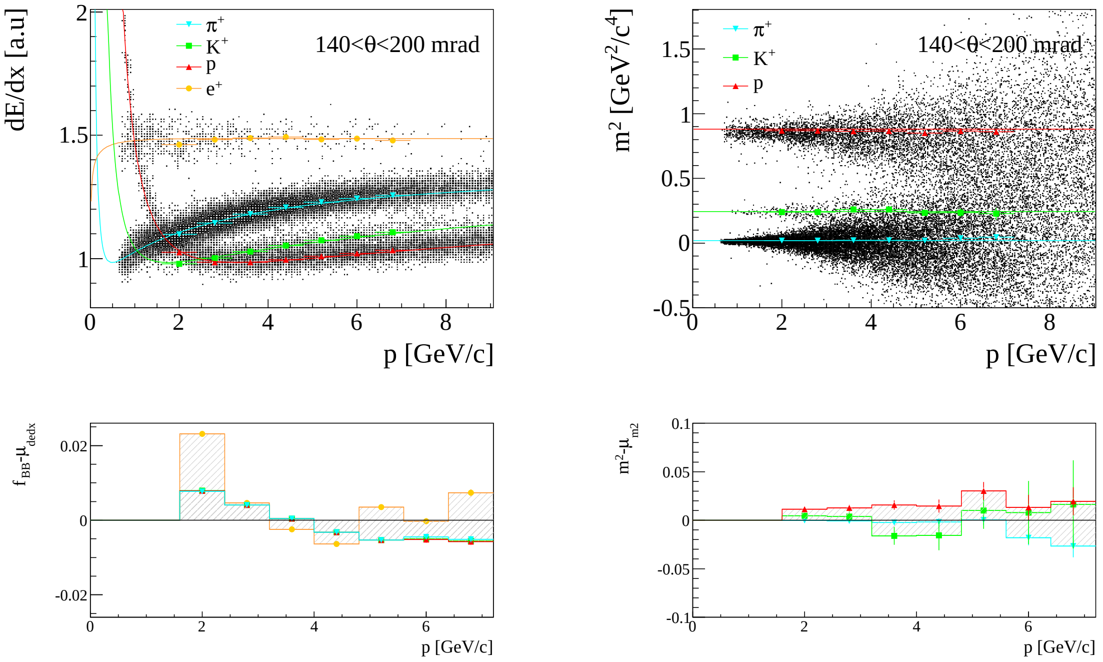

Figure 5.17: **[Top]**: dE/dx and m^2 as a function of momentum with mean parameters returned by the bi-dimensional fit (markers). The functions parameterizing the initial values (Bethe Bloch curve and particle mass-squared) are also super-imposed. **[Bottom]**: difference between initial and fitted values

5.3.1 Estimation of the fit quality

In principle, the mass squared and truncated mean charge distributions are expected to be almost Gaussian and hence accurately described by the hypothesis (Equation 5.3). However, the detector resolutions may systematically affect the data and make it diverge from a purely Gaussian behavior (e.g. typically by producing tails at the edge of the distributions). Within the momentum range of a bin (typically 800 MeV/c) the variation of the mean dE/dx value may also distort the Gaussian shape of the distributions. The intrinsic ToF-F response on the other hand seems to be reasonably Gaussian (see Figure 4.17). Decay in flight could in principle also slightly bias the shape of the distributions, although for the kaons the cut on z_{last}, assures that we select only those which did not decay. To better describe the behaviour of the mass-squared distribution a 2-Gaussian description was tested. One Gaussian with a large variance to describe the base of the distribution and another to fit the narrow peak. Doing so did not lead to any significant improvement neither for the convergence of the fit nor on the comparisons which will be mentioned below. The final number of kaons actually remained largely unchanged. It only introduced more parameters and unnecessary extra complications which are not justified for the level of the 2007 statistics. For the 10 times larger 2009 data set this should however be something to consider.

A strong support for the robustness of the fit, is that the chi-squared and p-values show a good level of agreement between the fitted function and the data (see Appendix E). This is also seen from the residuals which are symmetrically distributed around zero. Additional checks of the fit quality were undertaken and are described below. A slightly non Gaussian response can

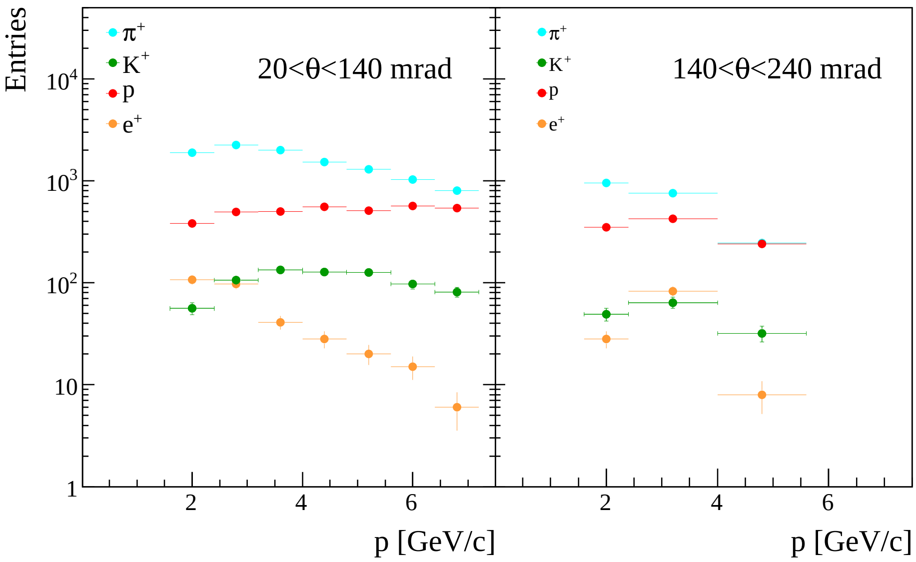

Figure 5.18: Raw particle yields returned by the fit in both angular intervals

be observed on the m^2 projections of the distributions at low momentum (see Appendix E).

Dependence of the fitted kaon yields on the initial parameter values and bounds

A method which allows to estimate the stability of the fit consists in varying both the input parameters and limits and considering the subsequent variation of the returned particle yield. This method serves as an estimate for the systematic uncertainty linked to the PID procedure. In particular, the relative distances of the proton, kaon and pion dE/dx peaks was varied by 4% which is the amount corresponding to the largest of the residuals between the original and re-fitted Bethe-Bloch curve. The constraints on the input parameters were also individually relaxed ant the corresponding parameters were treated as completely free (see Table 5.3). This enables to check whether the allowed variation of 30% around the input value is large enough and if any systematic biases are introduced by parameters reaching the boundaries. The impact on the fitted kaon yields is shown in Figure 5.19 both in terms of raw number of kaons and of deviations from the reference kaon sample, the latter being that of Table 5.2 where all parameters were allowed a ± 30% variation around the input values. The first observation is that, at low momentum, the final yields do not vary significantly, proving the robustness of the fitting procedure. Since peaks are generally well isolated, this can be expected if the initialisation procedure is done carefully. Since the sensitivity to the kaon signal decreases with momentum, the fitted kaon yield naturally has a stronger dependence on the input parameters (and hence on the value of the bounds) as momentum increases. This is especially observed in the last momentum bins of both angular intervals where deviations of around 7% are observed. The parameters which have the strongest influence are the widths of the distributions and the mean mass-squared, relaxing the other parameters on the other hand has little impact on the final yields in all momentum bins. Because the compared samples are fully correlated one can consider these variations to be only due to systematic effects. The observed fluctuations serve as the estimate of the systematic

θ_{low} (mrad)	θ_{high}	p_{low} (GeV/c)	p_{high}	N	N_K
20	140	1.6	2.4	2395	56
		2.4	3.2	2934	106
		3.2	4	2662	134
		4	4.8	2263	127
		4.8	5.6	1964	126
		5.6	6.4	1699	97
		6.4	7.2	1424	81
140	240	1.6	2.4	1399	49
		2.4	4	1340	64
		4	5.6	529	32

Table 5.2: Total number of selected tracks (N) and fitted raw number of kaons (N_K). Each row refers to a different ($p_{low} \leq p < p_{up}, \theta_{low} \leq \theta < \theta_{up}$) bin, where p and θ are the kaon momentum and polar angle in the laboratory frame.

uncertainty linked to the PID (see Figure 5.26).

Reference	all parameters allowed a 30% variation
Fit Var I	varied relative distance by -4%
Fit Var II	relaxed bounds on σ^i_{dedx}
Fit Var III	relaxed bounds on μ^i_{dedx}
Fit Var IV	relaxed bounds on σ^i_{m2}
Fit Var V	relaxed bounds on μ^i_{m2}

Table 5.3: modification of bounds and initial values which were applied to test the robustness of the fit.

Comparison between Integral and count

The accuracy of the fit can also be verified by summing the particles within a specified contour of the kaon peak and comparing the number with the integral of the fit. This comparison was done for the 1, 1.5 and 2σ contours around the fitted kaon peak. The contours are those which are presented in Figure 5.16 and in Appendix E. At low momenta where all accumulations are well separated the comparison is straight forward. For example in the first momentum bin of the first angular interval the counted number of K^+ is 56 for all contours, which is exactly the number returned by the integral of the kaon peak (see Table 5.2). As momentum increases though, particle accumulations overlap and the contamination of other particles in the kaon contour must be subtracted. The contamination, $C(n\sigma)$, is given for a number of sigmas around the fitted kaon peak. It is defined as the ratio of the integral of the kaon peak (f_k) to that of

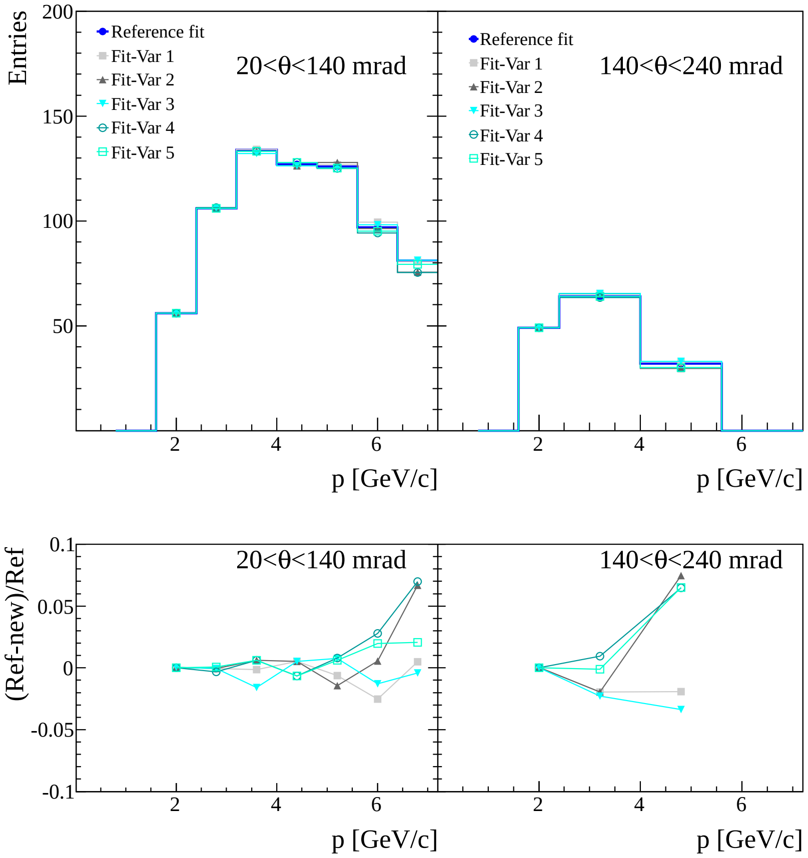

Figure 5.19: Impact on the fitted kaon yields of the modification of bounds and input fit parameter as described in Table 5.3. Relative deviations from the reference sample are shown in the bottom plots.

the total function (f) within the studied contour:

$$C(n\sigma) = 1 - \frac{\iint f_k(x_{dedx}, x_{m2}, \alpha_k)\mathrm{d}x_{m2}\mathrm{d}x_{dedx}}{\iint f(x_{dedx}, x_{m2}, \alpha)\mathrm{d}x_{m2}\mathrm{d}x_{dedx}} \tag{5.6}$$

The contamination is shown as a function of momentum in Figure 5.20 for the 1, 1.5 and 2σ contours. It is close to zero at low momentum and is generally fairly low, except in the last momentum bins where it reaches $\sim 60\%$ at 2 σ mainly due to the strong proton contamination.

The comparison between the particle by particle count, corrected by the corresponding contamination, and the integral of the fit is shown in Figure 5.21 for all contours. As can be seen both are in general good agreement.

In addition to this test, evaluating the fraction of other particle species in the kaon peak provides a quantitative evaluation of the separation power of the combined tof-dE/dx PID. Kaons are of course the particle species with the strongest contamination because of their weak signal and proximity to the protons.

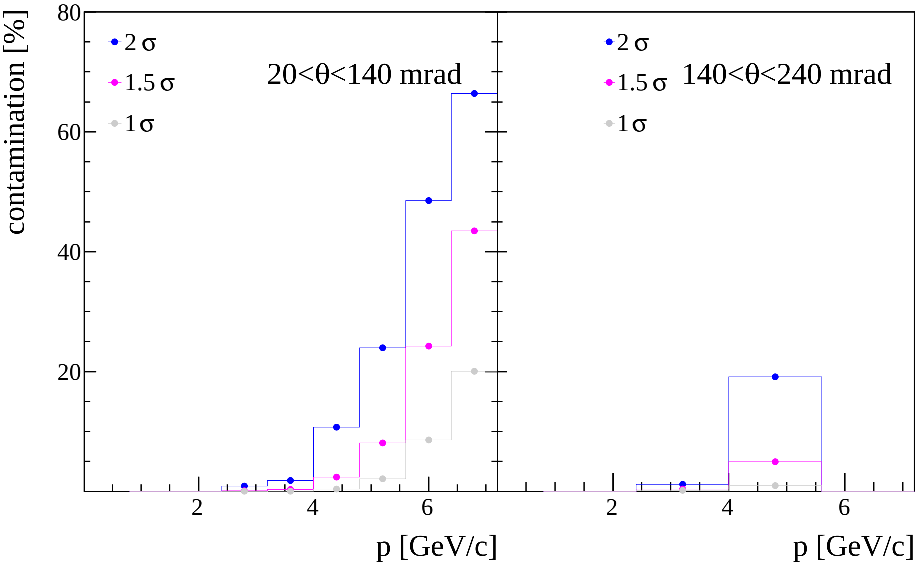

Figure 5.20: Ratio, in percent, of the integrals of the kaon and total function for 3 different contours around the fitted kaon peak. The ratios gives the contamination of other particle species in the kaon sample when they are counted on a particle by particle basis.

Comparison between samples of kaons emitted with $p_y > 0$ and $p_y < 0$

Because of the azimuthal angle cuts, the detector is symmetric along the horizontal plane and hence the same number of kaons should be emitted upward (momentum along the y axis $p_y > 0$) or with $p_y < 0$. As is demonstrated in Figure 5.22 the fitted kaon yields for both sample are in good agreement within the statistical uncertainties. This test also demonstrates that the detector responses (dE/dx and ToF-F resolution, ToF-F efficiency etc...) are identical along the vertical axis.

5.4 Correction factors and efficiencies

The Monte Carlo (MC) simulation described in Section 3.7 was used to calculate corrections for kaon decay, secondary interactions in the target and detector material and track reconstruction efficiency. Instead of applying a global correction factor, each bias was calculated separately with the MC and applied successively to the data. In addition to providing a detailed knowledge of every source of possible corrections, this procedure has the advantage of facilitating the assignment of systematic errors since an uncertainty on each factor may be derived. Systematic errors can be estimated, for example, based on which correction is MC model dependent or which one is purely a consequence of the detector geometry.

The bin-by-bin correction factors and efficiencies for different biases were calculated from 5 Million generated MC events with the VENUS4.12 model. The flat phase-space MC, described in Section 3.7, was also used to derive the geometrical acceptance of the detector and the ToF-F efficiency was estimated from the data. All the considered efficiencies ε are binomial processes with $\varepsilon = k/N$ defined by the probability to obtain k "successes" (k tracks passing the cuts) out

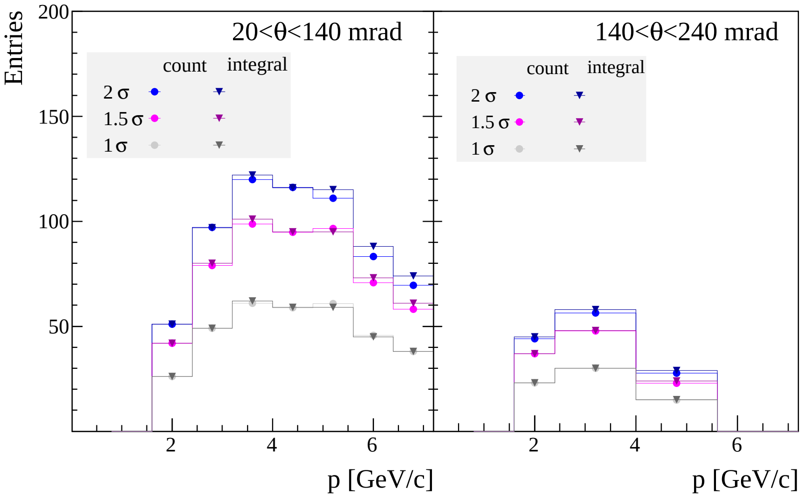

Figure 5.21: Comparison between the integral of the fit and summed number of kaons for three different contours around the kaon peak. For the summed number, the fraction of contaminating particles, as shown in Figure 5.20, are subtracted.

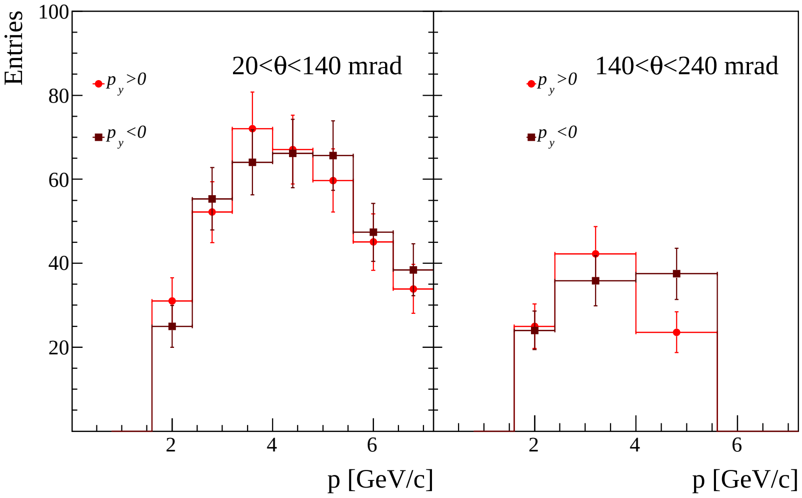

Figure 5.22: Fitted yields of K^+ emitted with positive and negative values of p_y.

of a sample of size N. the corresponding statistical uncertainty on the correction factor, is the standard deviation of the binomial distribution of the number of events k given by:

$$\sigma_k = \sqrt{\varepsilon \frac{(1-\varepsilon)}{N}} \tag{5.7}$$

Limitations to the binomial distribution hypothesis occurs however when the sample size is low. Consider the extreme case where we have a single event $N = 1$, if it passes we find $\varepsilon = 1 \pm 0$ and if it fails we get $\varepsilon = 0 \pm 0$. Clearly the binomial assumption is absurd in this case since the calculation claims perfect uncertainty with only one trial. For a more complete treatment, the errors should be derived using Bayes theorem (see e.g [145, 146]). In the analysis, since the corrections are derived from large simulated MC samples (typically thousands of tracks per bin), the binomial hypothesis along with the approximation of no uncertainty in case of a 100% efficiency does not have any impact on the correction. Actually, for cross-check, corrections were also derived with the Bayes method (`BayesDivide` in ROOT), the difference on both central values and errors was insignificant. The correction factors are presented in Figure 5.23, each of the contribution is detailed below.

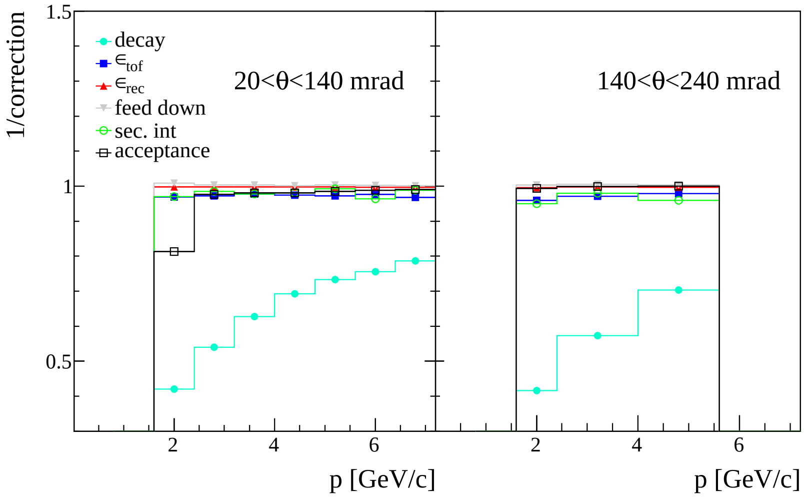

Figure 5.23: breakdown of corrections in both angular intervals of the analysis.

(i) *Geometrical acceptance of the detector:* is computed from the flat phase-space MC described in Section 3.7. As mentioned in Section 5.2.1 the cut on the azimuthal angle in combination with the selection based on track topology assures that only tracks with a close to 100% acceptance are retained. The two cuts remove a large part of the available statistics but assure that the selected sample is well under control, and prevents from making large MC model dependent corrections.

(ii) *ToF-F detection efficiency:* is calculated from the data by requiring that a track traversing the ToF-F wall generates a hit that can be converted into an accurate mass-squared value. Figure 5.24 shows the efficiency as a function of the x coordinate in the ToF-F in both θ bins. In general a track traversing the scintillators will generate a signal in at least one of the two attached PMTs with a 100% probability (light blue line). However, as discussed in Section 4.5.4 not all registered signals give accurate tof measurements because of the double hits produced by overlapping particles. Taking only those for which the signal can be converted into a valid mass-squared reduces the final efficiency to around 97% (darker blue line). The specific x_{tof} intervals in both plots are a consequence of the track topology selection in each bin: for positively charged particles, RST hit the ToF-F at $x_{tof} > 0$ and the selected WST at $x_{tof} < 0$.

(iii) *Reconstruction efficiency:* the track reconstruction procedure is described in Section 3.5. The reconstruction efficiency denotes the capability of the reconstruction algorithm to iden-

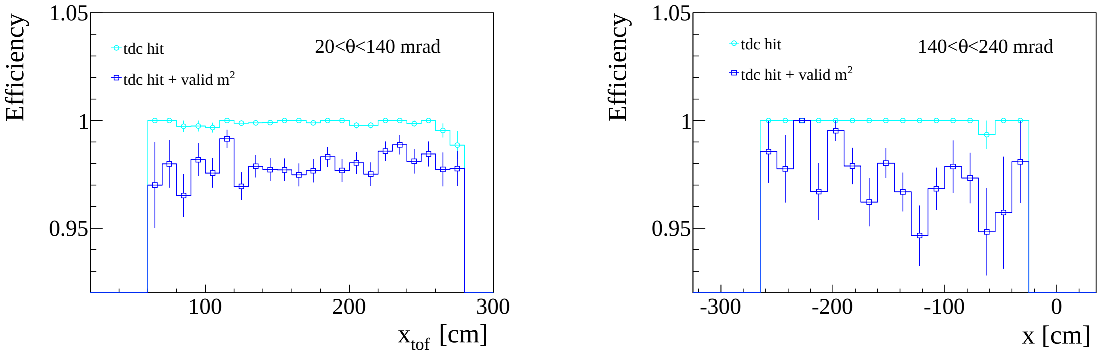

Figure 5.24: ToF-F efficiency as a function of x_{tof} in both angular intervals. The cyan line gives the probability for a track traversing the ToF-F to generate a tdc hit. The dark blue line has the further requirement that the generated hit can be used for a m^2 measurement.

tify the TPC clusters, make RTrack segments, match them between TPCs and fit the tracks to the main vertex. It was estimated from the MC and supplemented by dedicated eye-scans of data with the EventBrowser which is the detector off-line and on-line visualisation tool. The selection of maximal acceptance regions, as described above, combined with the fact that only long track that hit the ToF-F are selected is directly reflected upon the reconstruction efficiency which is close to 100% everywhere.

(iv) *Feed down correction:* the feed down correction concerns kaon tracks fitted to the primary vertex but not produced in the primary interaction. Feed down is only observed from kaons produced by secondary interactions in the target and the effect is below 1% over the whole kinematic range.

(v) *Secondary interactions:* the contribution related to kaon losses due to secondary interactions in the detector material and target is about 2%. Almost all of these losses occur in the target. Interactions in the detector material are almost negligible because of the well defined acceptance, especially the phi-cuts which assure that the tracks do not hit the magnet yokes. Also, during the conception of the spectrometer, material along the particle trajectories was carefully reduced to minimum.

(vi) *Decay in flight:* the decay correction is by far the largest and therefore deserves the most attention. Fortunately kaon decay processes are well understood (the lifetime is known to 0.2 %) and not model dependent. The correction was evaluated from the MC by computing the fraction of kaons produced in the primary interaction which reach the ToF-F wall before decaying. As such, this procedure assumes that the track selection defined in Section 5.2.2, in particular the cut on the z position of the last measured point (z_{last}), is fully efficient in the isolation of a pure sample of stable kaons. Before applying this correction it is therefore necessary to correct the sample of identified kaons for the contamination from those kaons which decayed before reaching the ToF-F but were still associated to a ToF-F hit as shown in Figure 5.11. The corresponding fraction of kaons was estimated in each $\{p, \theta\}$ bin by a dedicated MC simulation. A representation of the level of contamination in each $\{p, \theta\}$

bin is given in Figure 5.25 where the z coordinates of K^+ decay vertices are shown for all tracks belonging to the specified bin and for those associated to the ToF-F (same procedure as for Figure 5.11). The corresponding contamination for $z_{last} > 680$ cm is found to be of about 2-3%.

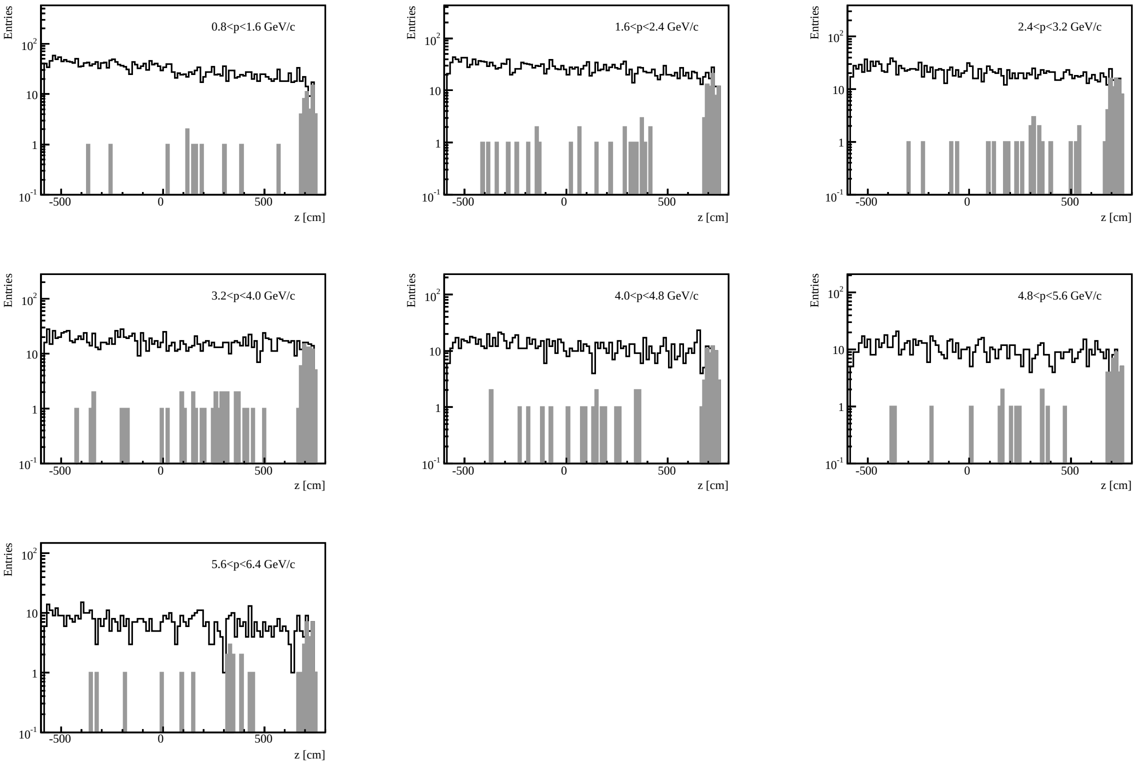

Figure 5.25: z coordinate of the K^+ decay vertices (MC simulation) for all momentum bins of the first angular interval. The gray histogram represents the fraction of the decayed kaons which are associated to a ToF-F hit.

The correction factors are independent from one another and therefore are applied successively to the raw fitted number of K^+ in each $\{p, \theta\}$ bin i:

$$N_{K^+}^{i,cor} = N_{K^+}^{i,raw} \times \frac{1}{\varepsilon_{acc}^{i}} \times \frac{1}{\varepsilon_{Rec.}^{i}} \times \frac{1}{\varepsilon_{Fd}^{i}} \times \frac{1}{\varepsilon_{ToF.}^{i}} \times \frac{1}{\varepsilon_{sec.}^{i}} \times \frac{1}{\varepsilon_{dec}^{i}} \times \frac{2\pi}{\Delta\phi^{i}} \qquad (5.8)$$

The different ε's denote the efficiencies defined above. The fitted number of kaons is also multiplied by a factor which depends on the selected $\Delta\phi$ wedge, to yield a complete 2π azimuthal acceptance. The statistical uncertainties of each correction factor are added in quadrature and contribute to the final statistical error on the corrected yields.

The consistency of the procedure was cross-checked by comparing the multiplication of the different factors with a global Monte Carlo correction:

$$N_{K^+}^{i,cor} = N_{K^+}^{i,raw} \times \frac{1}{\varepsilon_{global}^{i}} \qquad (5.9)$$

where

$$\varepsilon^i_{global} = \frac{N^i \text{ (reconstructed } K^+\text{,MC)}}{N^i \text{ (generated } K^+ \text{ in prim. vertex,MC)}} \tag{5.10}$$

The two methods give identical results which confirms that no correction was forgotten or overestimated in the breakdown.

5.5 Systematic errors

The relative contributions of all considered systematic errors are shown in Figure 5.26 and Table 5.4. The main contribution to the overall systematic error on the yield correction generally arises from the decay correction. Three main contributions to the systematic uncertainty of the decay correction are discussed below.

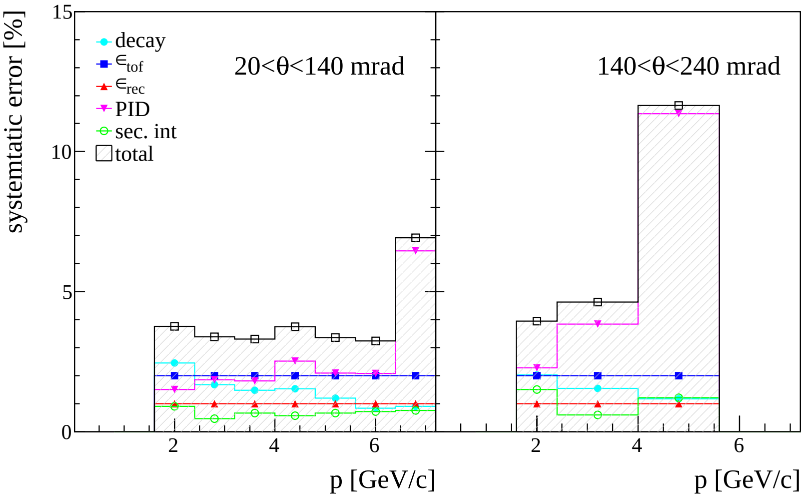

Figure 5.26: Breakdown of systematic errors as a function of momentum in both angular intervals of the analysis.

(i) *The contribution due to kaons decaying in flight.*
As depicted in Figure 5.25, most of the unstable kaons in the selected final sample are decays which take place in the region of space delimited by z_{last} and the ToF-F surface. An alternative way to derive the decay correction is then to calculate the survival probability only until $z = z_{last}$. In this procedure one must correct for the small contamination of kaons decaying between z_{last} and the ToF-F which are not associated to a ToF-F hit. The two methods give results which differ by less than 1%. The systematic error assigned to the bias related to kaon decays was therefore conservatively calculated as 50% of the corresponding contamination defined in Section 5.4-vi.

(ii) *The contribution due to the model dependence of momentum distributions.*
The value of the decay correction depends on the momentum distribution within each $\{p, \theta\}$ bin and therefore on the specific MC model used for the event generation. Significant discrepancies may be observed especially at low momenta where the decay probability (the

θ_{low} (mrad)	θ_{high} (mrad)	p_{low} (GeV/c)	p_{high} (GeV/c)	decay	ε_{tof}	ε_{rec}	sec. int	pid	total
				systematic error [%]					
20	140	1.6	2.4	2.45	2.00	1.00	0.90	1.51	3.75
		2.4	3.2	1.68	2.00	1.00	0.46	1.85	3.38
		3.2	4	1.47	2.00	1.00	0.66	1.81	3.30
		4	4.8	1.53	2.00	1.00	0.57	2.51	3.74
		4.8	5.6	1.19	2.00	1.00	0.66	2.09	3.35
		5.6	6.4	0.83	2.00	1.00	0.71	2.08	3.24
		6.4	7.2	0.90	2.00	1.00	0.75	6.45	6.93
140	240	1.6	2.4	2.02	2.00	1.00	1.50	2.05	3.94
		2.4	4	1.54	2.00	1.00	0.60	3.70	4.63
		4	5.6	1.17	2.00	1.00	1.21	11.31	11.65

Table 5.4: Contribution from the different sources of systematic errors.

correction) is larger and the momentum distribution is steeper. This effect was quantified by using various MC models and comparing the resulting correction factors with those calculated directly from the data. More precisely, the latter factor was derived for the three lowest momentum bins, where unique identification of kaons is possible on a track-by-track basis: the raw yield was corrected by re-weighting each track with its decay probability, calculated for the measured momentum and track length. The resulting deviation of the correction factor was negligible except in the first momentum bin where a maximum difference of about 2% was found. We therefore added this value in quadrature to the systematic uncertainty.

(iii) *The contribution due to the uncertainty in the reconstructed track length.*
Since only well measured tracks which traverse the entire spectrometer are retained, a precision of a few millimeters is achieved on both track length calculation and extrapolation to the ToF-F surface. The accuracy of the extrapolation to the ToF-F is demonstrated in Figure 5.27–left. Such a precision translates into a negligible (order of 0.1 %) error on the decay correction factor. The consistency in track length between data and MC was also verified in each of the bins and a very good agreement between the two was found, this is shown in Figure 5.27–right. The pattern in the distribution is a consequence of the staggered arrangement of the scintillator slats.

Other sources of systematic errors include uncertainties on the ToF-F and reconstruction efficiency and on the contribution from secondary interactions.

Systematic uncertainties on the ToF-F efficiency come from the accuracy of the calibration procedure. The detection itself is 100% efficient which indicates that all channels were operating correctly and that no bias is present in neither the extrapolation or geometrical calibration. The final $\sim$ 97% efficiency is only a consequence of the incorrect tdc measurements being discarded. This is necessary to remove the tails on the m^2 distribution, thus preventing from having distri-

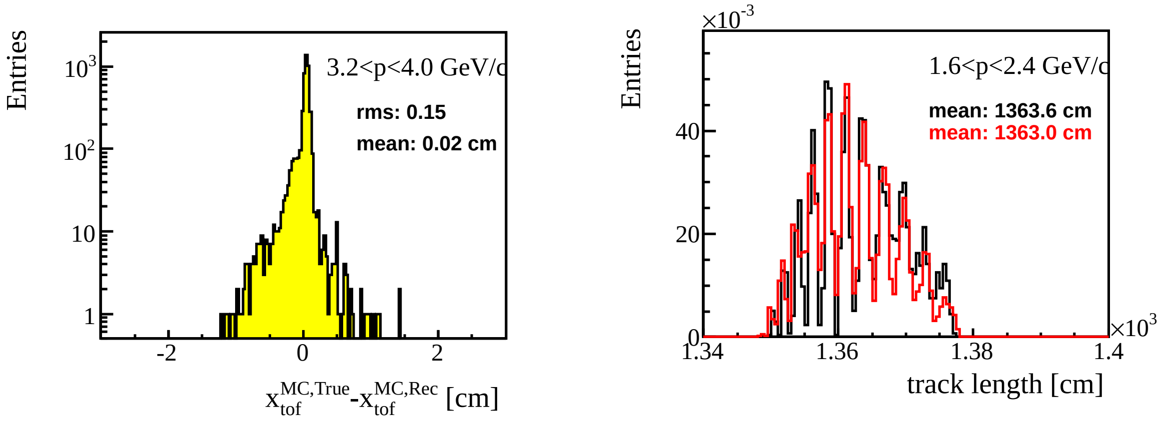

Figure 5.27: **[Left]**: Difference between true and reconstructed MC for extrapolated x to the ToF-F in a specific bin of the analysis. **[Right]**: reconstructed track lengths for data (black) and MC (red).

butions not well defined by the hypothesis of Equation 5.3 which would induce high PID related systematic errors. The ToF-F efficiency is the only correction derived from the data and is clearly dominated by the large statistical fluctuations (see Figure 5.24). As such any detailed study of systematic effects, for example on a scintillator by scintillator basis, is not possible with this 2007 data set. For the analysis we therefore estimated a global 2% error.

An important feature of the analysis was to carefully select regions of high acceptance and reconstruction efficiencies. Thus the reconstruction efficiency is 100% over the selected phase-space and the corresponding systematic is estimated at 1%. Errors were estimated by varying the track selection cuts; any induced biases were small compared to the statistical fluctuations which is anyhow expected considering the high reconstruction efficiency. Potential differences between data and MC on relevant distributions such as azimuthal angle, number of reconstructed TPC clusters and impact parameters (b_x,b_y) were also inspected. As presented in Figure 5.28, both data and MC are generally in good agreement. For the ϕ distribution, in the first angular interval only the flat part around zero is selected (positive RST). The number of TPC points being well described by the simulation is another consequence of the strict acceptance selection: only long tracks which cross a well defined TPC fiducial volume are retained, on the contrary those which are reconstructed on the edges, typically those close to the un-instrumented region around the beam axis, are rejected. A slight deviation of the mean impact parameter along x (b_x) is nevertheless observed at the data level with respect to the MC. The reason why this displacement exists is clearly a matter for more investigation at the reconstruction level, but the difference would only have a significant impact on the analysis if we were to perform sharp b_x selections.

For model dependent corrections such as feed down and secondary interactions a systematic error corresponding to 30% of the correction was assigned. This value is taken from studies that were performed while quantifying the systematic error on the feed down correction for pion yields. Feed down is a significant correction for pions, and especially for π^-, because of Λ and K_s^0 decaying close to the primary vertex. The error was estimated essentially by comparing strange particle production from different MC generators [119]. Since the feed down correction for kaons

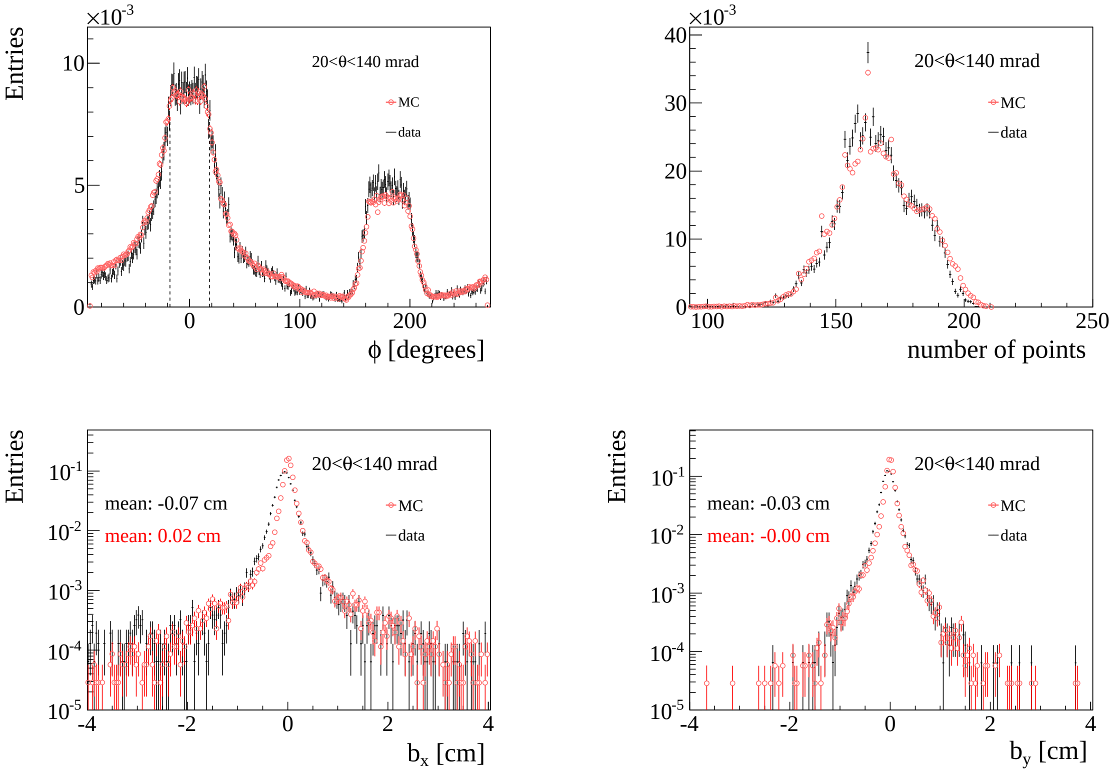

Figure 5.28: Comparison between data (black) and MC (red) for tracks belonging to the first angular interval of the analysis. For the azimuthal angle distribution (top-left), the black lines indicate the selected wedge.

is below the percent level, the corresponding uncertainty is negligibly small. For secondary re-interactions it is generally just below 1%.

Systematic uncertainties related to the procedure used for the PID were quantified by studying the dependence of the fitted kaon yields on the input fit parameters as described in Section 5.3.1. As underlined in the same section, the sensitivity to the kaon signal decreases with the momentum, therefore, the fitted kaon yield depends significantly on the definition of the input parameters. This explains the steep increase of the systematic error in the last momentum bin.

5.6 Normalization of particle yields

For normalization and cross section measurements the NA49 approach is followed. This procedure was used for the determination of the inclusive production of charged pions in proton-proton and proton-carbon collisions at 158 GeV/c beam momentum [110, 122]. The trigger on proton interactions described in Section 3.3 allows to define a "trigger" cross section (σ_{trig}), which is used for the normalization of the differential inclusive K^+ distributions. One must take into account that some of the events selected for the analysis (see Section 5.2) are in fact due to protons interacting in material outside of the carbon target. Therefore σ_{trig} is derived from the probabilities computed for target-in (P_{Tin}) and target-out operations (P_{Tout}). For the number of selected events an interaction probability of (6.022 ± 0.034)% for inserted carbon target and of (0.709 ± 0.007)% for the carbon target removed was computed [119]. These measurements lead to an interaction probability of (5.351 ± 0.035)% in the carbon target, taking into account the reduction of the beam intensity in the material along its trajectory. The corresponding σ_{trig} is (298.1 ± 1.9 ± 7.3) mb, after correcting for the exponential beam attenuation in the target. The systematic error on the trigger cross section was conservatively evaluated by comparing this value with the one obtained without any event selection criteria.

The differential inclusive cross section of K^+ mesons is then calculated as [93]:

$$\frac{d\sigma_K}{dp} = \frac{\sigma_{trig}}{1-\epsilon} \cdot \left(\frac{1}{N^I} \cdot \frac{\Delta n_K^I}{\Delta p} - \frac{\epsilon}{N^R} \cdot \frac{\Delta n_K^R}{\Delta p} \right) , \tag{5.11}$$

where:

(i) N^I and N^R are the numbers of events selected for the analysis with the target inserted and removed, respectively,

(ii) n_K^I and n_K^R are the corrected K^+ yields for the target in and target out data set,

(iii) Δp is the bin size in momentum and

(iv) $\epsilon = \frac{P_{Tout}}{P_{Tin}} = 0.118 \pm 0.001$ is the ratio of the interaction probabilities for removed and inserted target operation.

The total error on the inclusive cross sections resulting from the normalization thus amounts to 2.3%.

The correction for the contribution of particles from out-of-target events (the term $\epsilon/N^R \cdot \Delta n_K^R/\Delta p$) is evaluated by applying the event and track quality cuts from the target-in data to the interactions recorded with the target removed. As shown in Figure 5.29, only a few tens of tracks remain in each $\{p, \theta\}$ bin of the analysis, this can be expected from the fact that only long tracks are selected. Furthermore, most of the particles from out of target interactions are produced at low angle ($\lesssim$ 20 mrad) since they generally come from forward scattering of the proton with material along the beam line. Because of the low statistics of the target-out data set, the distributions cannot be fitted. Instead, the fitted kaon contours were retrieved from the target-in data set and used to evaluate the target-out yields by summing the particles within those contours. In all bins, the kaon yield is consistent with zero which means that, for this analysis, no subtraction from empty target events is needed.

5.7 Results and comparison with models

The K^+ spectra presented in this section refer to positively charged kaons produced in strong and electromagnetic processes in p+C interactions at 31 GeV/c. The differential inclusive K^+ cross sections are presented in Figure 5.30 and Table 5.5 as a function of momentum in the two considered intervals of polar angle. Statistical errors, which are typically of the order of 10%, dominate the systematic uncertainties in all analysed bins.

The K^+ spectra are further compared with the predictions of hadronic event generators. Three models, VENUS4.12 [147, 137], FLUKA2008 [105], and URQMD1.3.1 [148] were selected for

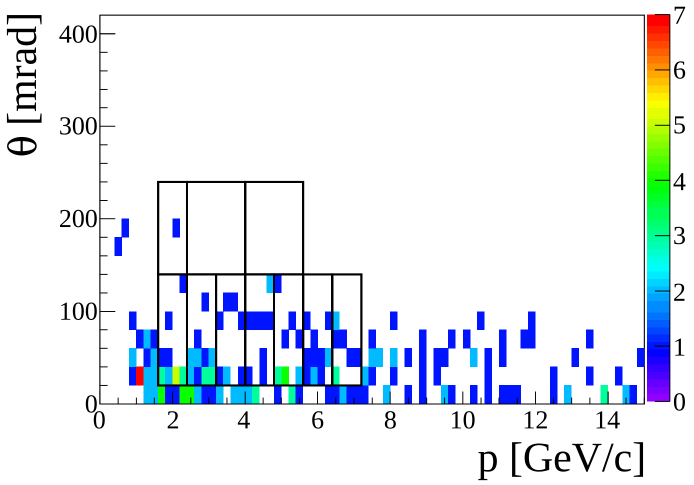

Figure 5.29: momentum-angle distribution of tracks from interactions collected with the target removed (not scaled for the number of events). The binning used for the analysis is superimposed.

θ_{low}	θ_{high}	p_{low}	p_{high}	N	N_K	$d\sigma^{K^+}/dp$	Δ_{stat}	Δ_{sys}
(mrad)		(GeV/c)				(mb/(GeV/c))		
20	140	1.6	2.4	2395	56	1.94	0.26	0.07
		2.4	3.2	2934	106	2.25	0.21	0.08
		3.2	4	2662	134	2.39	0.22	0.08
		4	4.8	2263	127	2.10	0.20	0.08
		4.8	5.6	1964	126	1.94	0.18	0.07
		5.6	6.4	1699	97	1.49	0.17	0.05
		6.4	7.2	1424	81	1.17	0.17	0.08
140	240	1.6	2.4	1399	49	2.89	0.41	0.11
		2.4	4	1340	64	1.32	0.17	0.06
		4	5.6	529	32	0.55	0.12	0.06

Table 5.5: The NA61/SHINE results for the differential K^+ production cross section, $d\sigma/dp$, in the laboratory system, for p+C interactions at 31 GeV/c. Each row refers to a different ($p_{low} \leq p < p_{up}, \theta_{low} \leq \theta < \theta_{up}$) bin, where p and θ are the kaon momentum and polar angle in the laboratory frame. N is the total number of selected tracks and N_K is the fitted raw number of kaons. The central value as well as the statistical (Δ_{stat}) and systematic (Δ_{sys}) errors of the cross section are given. The overall uncertainty (2.5%) due to the normalization procedure is not included.

this purpose. They are part of the CORSIKA [149] framework and are commonly used for the simulation of hadronic interactions at energies below 80 GeV in extensive air showers [150]. VENUS is also the standard model for Monte Carlo simulations of the NA49 and NA61 Collaborations. The results of the comparison between data and models are presented in Figure 5.31. In order to avoid uncertainties related to the different treatment of quasi-elastic interactions, spectra are normalized to the mean K^+ multiplicity in all production interactions (i.e with production of other particles). For the data, the normalization relies on the p+C inclusive production cross

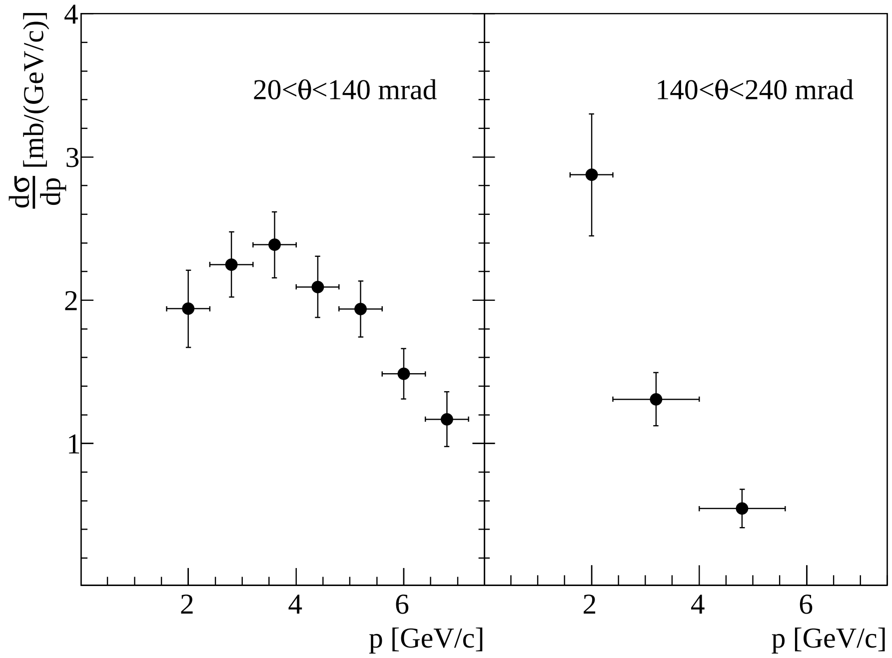

Figure 5.30: Differential cross sections for K^+ production in p+C interactions at 31 GeV$/c$. The spectra are presented as a function of laboratory momentum, p, in two intervals of polar angle, θ. Error bars indicate statistical and systematic uncertainties added in quadrature. The overall uncertainty (2.3%) due to the normalization procedure is not included.

section σ_{prod} which was found to be 229.3±1.9±9.0 mb. The production cross section is calculated from the measured inelastic cross section by subtracting the quasi-elastic contribution. Therefore production processes are defined as those in which only new hadrons are present in the final state. Details of the cross section analysis procedure can be found in [119, 93].

The qualitative behaviour of the data is well reproduced by all models. The quantitative differences can be related to the two main production processes of kaons: pairwise production of a K^+ together with another K meson and production of a K^+ together with a Λ baryon. The latter process dominates kaon production at large momenta and small angles due to the leading particle effect. K^+ at large angles and low momenta stem from pair production of K mesons. Both FLUKA and VENUS provide a reasonable description of the pair-produced kaons. On the other hand, none of the models is in full agreement with the small-angle data. While the VENUS model overestimates the production of K^+ at small angles, FLUKA and URQMD predict a slightly lower kaon production rate.

5.8 Summary

This chapter gave a detailed presentation of measurements of differential production cross sections of positively charged kaons in p+C interactions at 31 GeV$/c$. The results are essential for precise predictions of the high energy tail and intrinsic electron neutrino component of the initial neutrino flux for T2K. Furthermore, they provide important input to improve hadron production models. The data presented in this chapter has been provided to T2K for the calculation of the neutrino

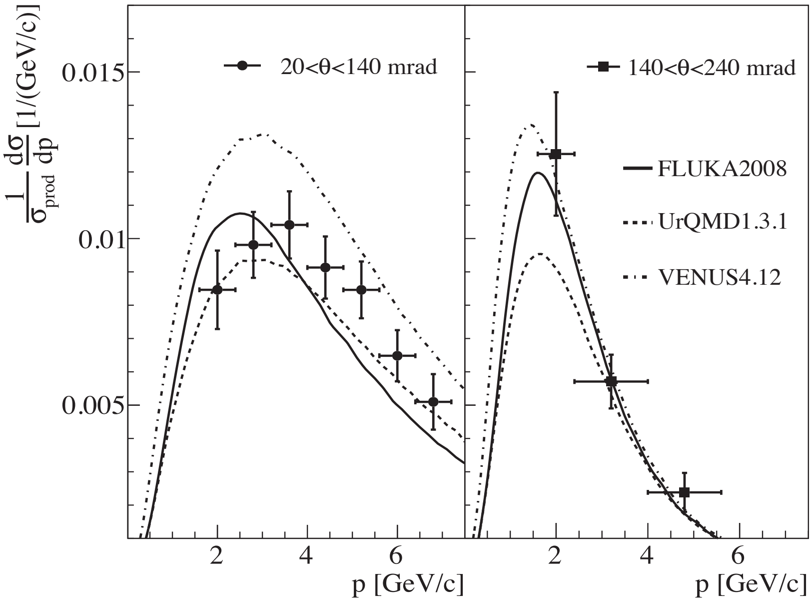

Figure 5.31: Comparison of measured K^+ spectra with model predictions. Distributions are normalized to the mean K^+ multiplicity in all production p+C interactions. The vertical error bars on the data points show the total (stat. and syst. added in quadrature) uncertainty. The horizontal error bars indicate the bin size in momentum.

flux and will be included in the next release of T2K results. The charged pion cross-sections, which are presented in the next chapter, were already used to constrain the neutrino flux in the first T2K ν_e appearance analysis. As we shall see the measurements have significantly reduced the uncertainty on the final oscillation result.

Chapter 6

Charged pion cross-sections and their impact on the first T2K result

The previous section gave a detailed description of the analysis based on the combined PID to extract K^+ production cross-sections. With the same method $\pi^+$and π^-spectra were also obtained from the 2007 data set. Actually the charged pion analysis was done before that of the kaons but for both analyses the global strategy largely remains the same. The PID methods are identical, with the advantage that pions are more abundant and better separated from other particles. For this reason yields were retrieved over a much broader kinematic range and the data was divided into smaller bins. The main differences between the two analyses come from the correction factors and their associated systematic uncertainties: while for the K^+ spectra decay was the largest correction, feed down generally dominates for pions. This chapter briefly describes the analysis techniques, and focuses on the correction factors relevant for pions. A discussion on the systematic errors in NA61/SHINE is also provided. The last section is devoted to an overview of the implementation of the charged pion cross-sections in the T2K beam simulation and summarizes the effect of our results on the T2K systematic uncertainties.

6.1 Data binning and track selection

The kinematic region of interest for positively charged pions whose daughter neutrinos pass through the SK detector is shown in Figure 6.1 with the adopted binning scheme superimposed. The chosen binning takes into account the available statistics of the 2007 data sample, detector acceptance and particle production kinematics. Altogether 9 angular intervals are defined, the momentum bins get coarser as momentum increases to take into account the reduction of the production cross-section. Unlike the kaon analysis, where constraints related to statistics and PID existed, the whole kinematic range of interest is studied. The cutoffs at low momenta ($\lesssim 1$ GeV/c) and high angles are only a consequence of the ToF-F acceptance while the reduced coverage at high momenta is purely due to the available statistics. For the first angular bin (0-20 mrad) the spectra are only calculated up to 7.2 GeV/c momentum, thus excluding tracks passing close to the edges of the TPCs where the reconstruction efficiency is lower and the calculation of the correction for the acceptance is less reliable.

The track selections presented in Table 6.1 are applied to the initial data set. The purpose

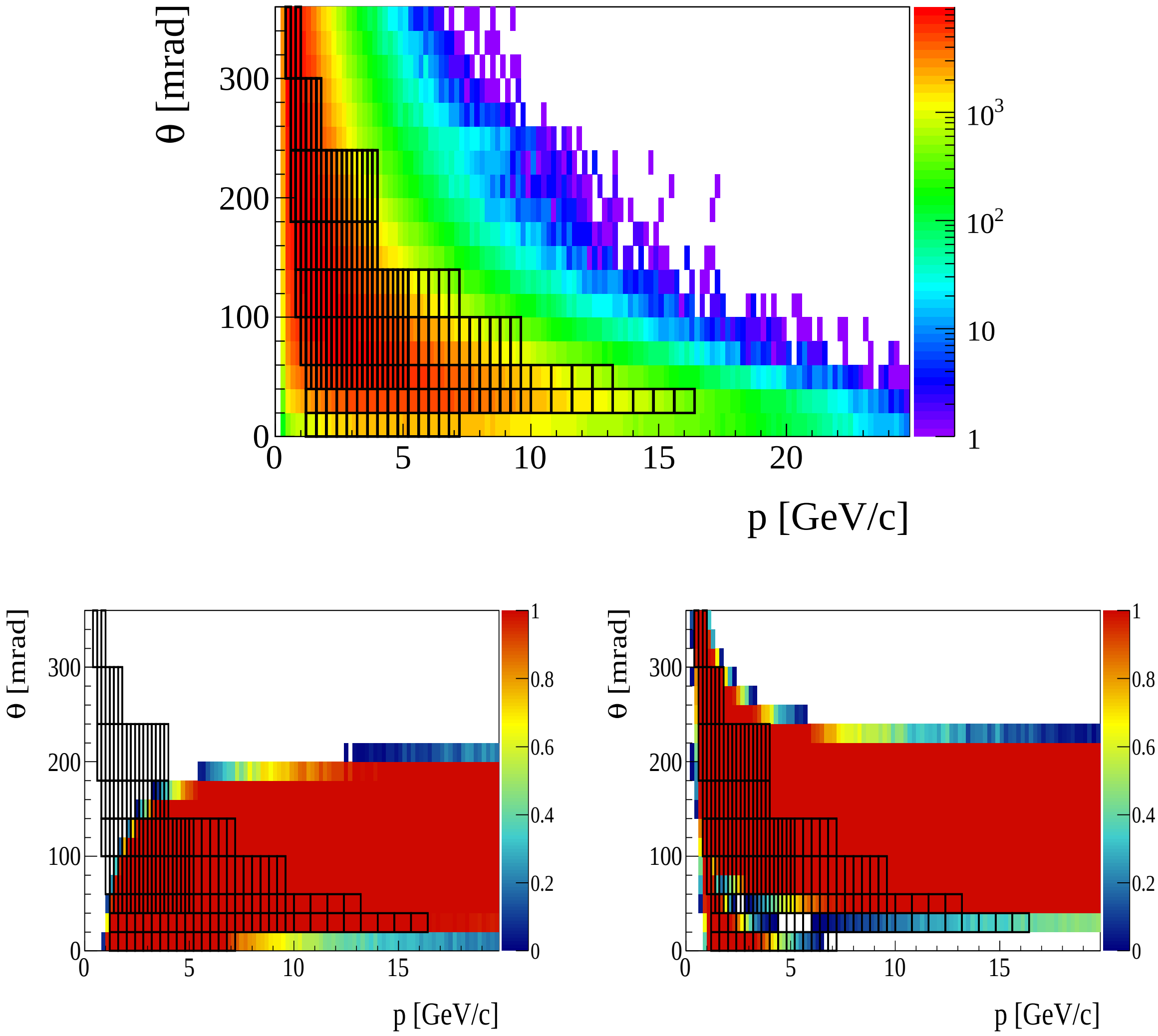

Figure 6.1: **[Top]**: prediction from the T2K beam simulation of the $\{p, \theta\}$ distribution for positively charged pions weighted by the probability that their decay produces a neutrino passing through the SK detector. The binning used in the present analysis is superimposed. **[Bottom]**: Simulated geometrical acceptance for Right-side-tracks (left) and wrong-side-tracks (right) with analysis binning super-imposed.

of each of them has already been discussed in Section 5.2. High acceptance regions were selected by visually inspecting the azimuthal angle distributions in every θ bins of the analysis as shown in Figure 6.2. The values of the selected wedges are summarized in Table 6.2. Similarly to the K^+ analysis, the detection efficiency was further maximised by selecting specific track topologies in each bin. To do so, each right-side-track (RST) or wrong-side-track (WST) sub-sample is treated individually and if the acceptance of a given $\{p, \theta\}$ bin is below 99% the corresponding bin is discarded. The RST and WST acceptances are given in Figure 6.1-bottom. The selection effectively removes a large part of the WST reconstructed close to the uninstrumented region along the beam axis (the low acceptance region below ∼5 GeV/c and ∼100 mrad) and most of the RST above 140 mrad.

No selection on the last reconstructed point z_{last} is required for the pion analysis. While

cut	**number**	**% remaining**	**Difference**
Event cuts			
all	442434		%
bpd	355227	80.3%	19.7%
Track cuts			
all tracks in bin range	550854		%
number of points in VTPCs	460486	83.6%	16.4%
tof requirement	167682	30.4%	63.6%
impact parameter	161194	29.3%	3.87%
azimuthal angle	104078	18.9%	35.4%
selection WST/RST based on acceptance	92643	16.9%	10.1%

Table 6.1: Impact of the event and track cuts.

θ **bin (mrad)**	0–20	20–40	40–60	60–100	100–140	140–180	180–240	240–300	300–360
$\Delta\phi$ **(degrees)**	±40	±40	±33	±17	±16	±10	±10	±8	±8

Table 6.2: value of the selected azimuthal angle wedge in each angular interval.

in the kaon analysis such a cut was necessary to clean up the final sample from contamination due to decay-in-flight, for pions the angle between the parent and daughter is much smaller and therefore requiring a measured point at the downstream end of the MTPCs does not prevent the muon from being associated to the ToF-F. This is illustrated in Figure 6.3 where it can also be seen that, at the energy of the analysis, the kink angle for pion decay is typically below 1°. Because of their similar mass the pion and muon cannot be distinguished within the ToF-F and dE/dx resolution. For the tof measurement, one can consider for example the worst case scenario of a pion decaying just after production and flying as a muon through the entire spectrometer: in this situation the difference in time between a muon and a pion flying a distance of 1350 cm, which is the average track length, is about 100 ps which is just less than the intrinsic resolution of the ToF-F. Therefore distortions to the shape of the m^2 distribution are likely to be very limited or at least negligible with respect to other effects such as detector response or the increase of the m^2 variance within the bin size. Therefore an extrapolated muon originating from pion decay is considered as a pion. It is just a matter of not overestimating the decay correction.

The combined tof-dE/dx particle identification method described in Section 5.3 is used to extract $\pi^+$and π^-yields over the entire phase-space. The p.d.f. used to describe the data is a sum of four bi-dimensional Gaussian consisting of 20 parameters, 4 yields , 8 widths and 8 mean-parameters. As for the K^+ analysis, the relative distance between the kaon and proton mean dE/dx remains fixed. In addition, because of the refined binning and of the weak kaon signal, the other parameters relevant to the kaon peak (both widths and m^2 mean value) are constrained to their input values. It was checked that doing so does not induce any bias to the pion peak. This can be understood from the fact that, in all analysed bins, pions are well isolated from the other particle species and thus the returned pion yields do not depend on the

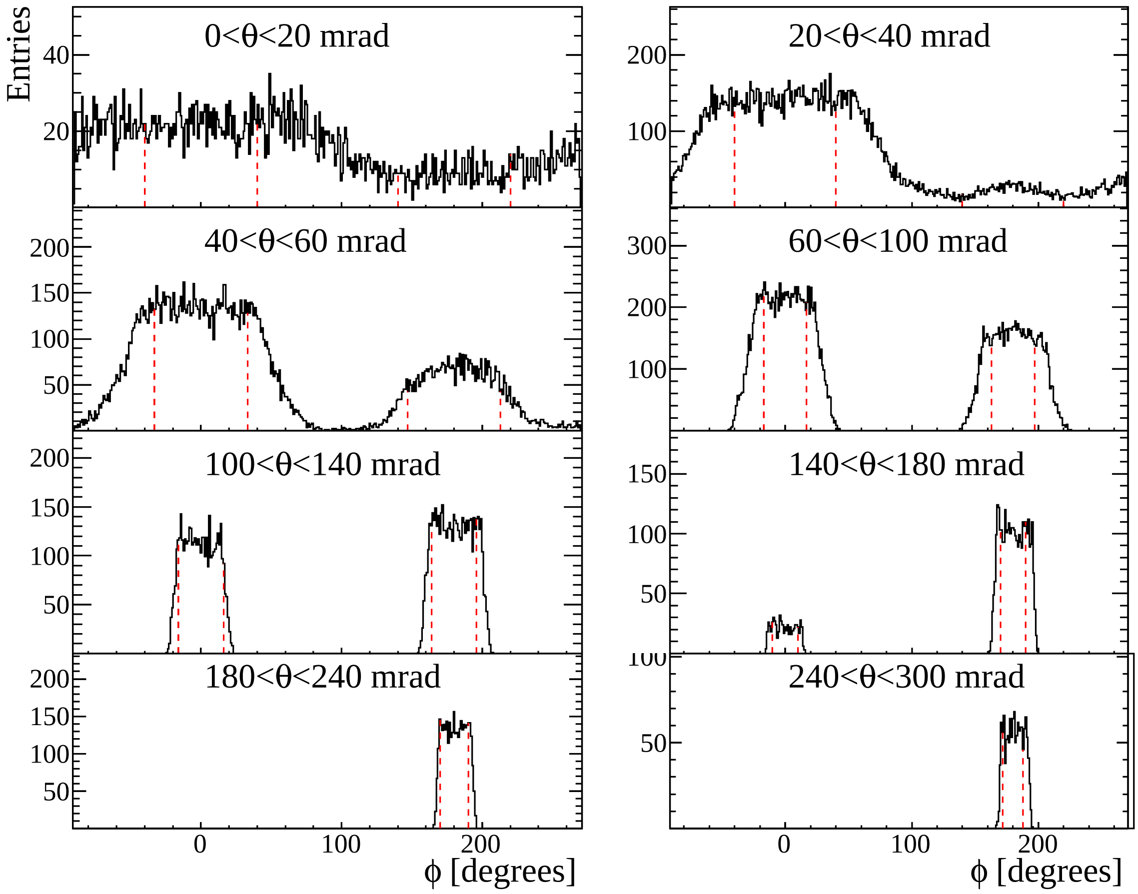

Figure 6.2: Distributions of azimuthal angle for positively charged particles that reach the ToF-F in all angular bins considered for the analysis. The red lines indicate the selected wedges.

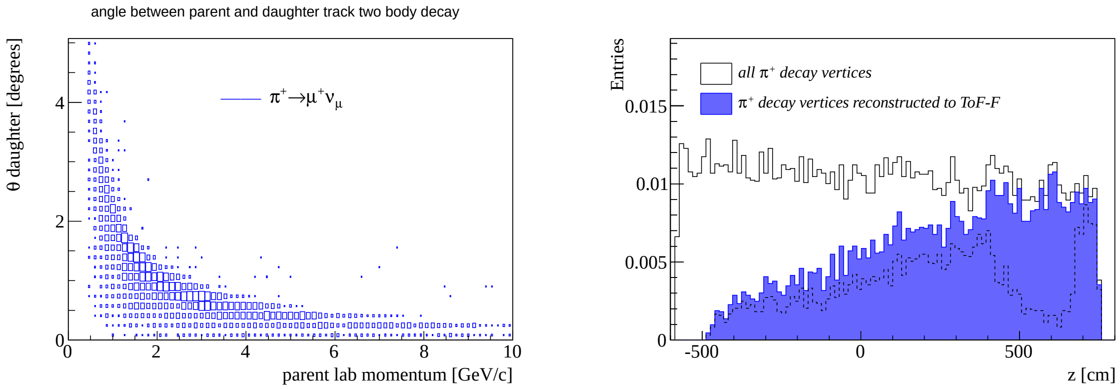

Figure 6.3: **[Left]**: decay angle between the pion and the muon as a function of momentum.**[Right]**: MC simulation of z coordinate of the π^+ decay vertices (solid black line). The fraction of tracks which are associated to a ToF-F hit without (blue histogram) and with (dotted black line) the cut on z_{last} are superimposed.

variables that desrcibe the other peaks. Moreover, as was demonstrated in Section 5.3, the initial parameters were carefully set and the fitted values do not differ significantly from the set ones. An example of bi-dimensional fits in various $\{p, \theta\}$ bins, including one at high momentum, are presented in Figure 6.4. The returned $\pi^+$and π^-yields are presented in Figure 6.5. For the analysis, a minimum of 10 fitted pions are required in each $\{p, \theta\}$ bin.

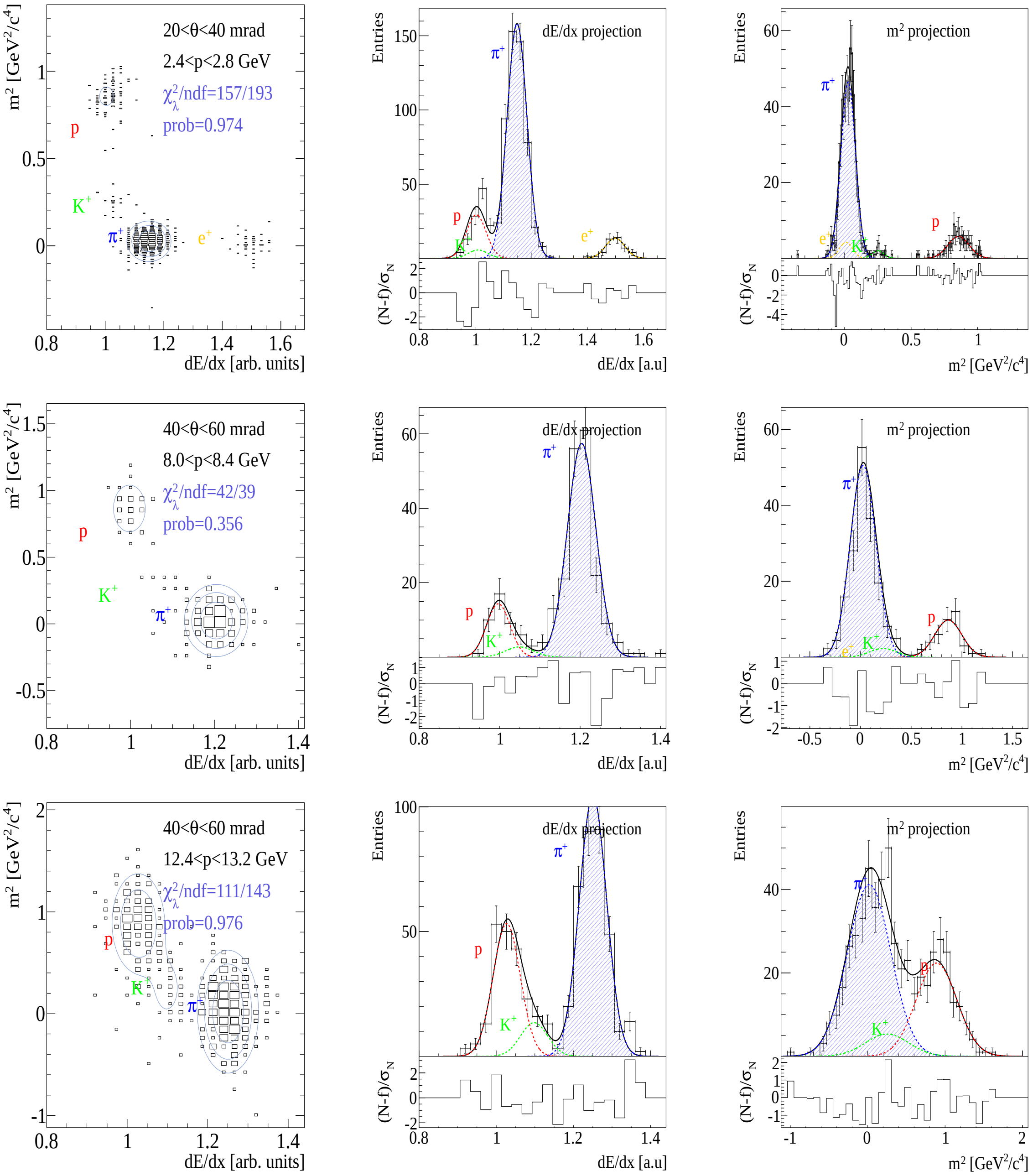

Figure 6.4: Example of bi-dimensional fits to the $m^2 - dE/dx$ distribution. The function is drawn with the 2, 1.5 and 1 σ contours around the fitted pion peak. The m^2 and dE/dx projections are also shown superimposed with the results of the fitted functions. The function describing the π^+peak is shadowed in blue.

The quality of the fits was evaluated with the same methods which are described in Section 5.3. More specifically the returned mean values and widths of the Gaussians were compared to the input values; no significant deviations were found. Since the binning used in the pion analysis extends to higher polar angles, it was also verified that there were no systematic biases on the returned mean and width as θ increases. An example in the polar angle interval $[100, 140]$ is shown in Figure 6.6. The stability of the fit was further checked by varying the input parameters relevant to the pion peak as well as their bounds. The resulting impact on the final pion yields was close to negligible even at high momentum. The distribution of the Poisson chi-squared, χ^2_λ/ndf and p-value (computed in Appendix D) of the fits in all considered bins are shown in Figure 6.7. The χ^2_λ/ndf values are generally relatively close to unity indicating a good agreement between data and hypothesis. The low p-values generally belong to fits performed in $\{p, \theta\}$ bins of low statistics which are located at higher momentum at the edge of the analysis phase-space.

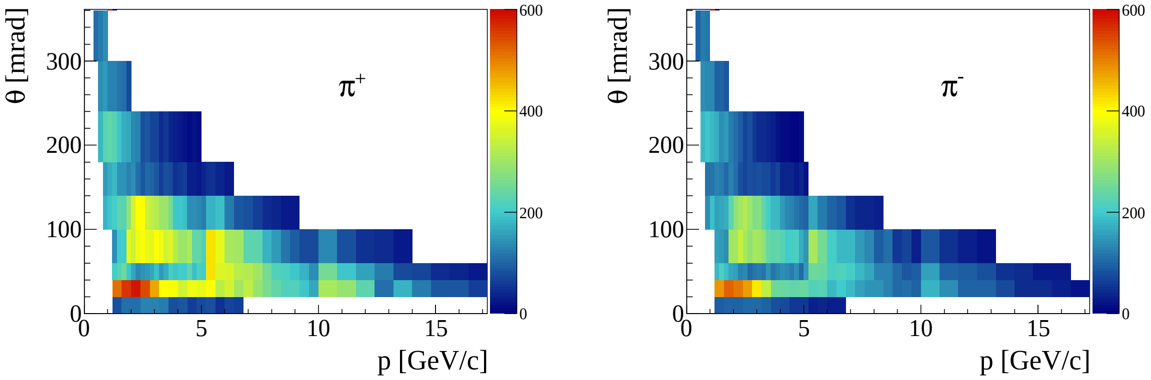

Figure 6.5: Fitted $\pi^+$and π^-yields in all bins.

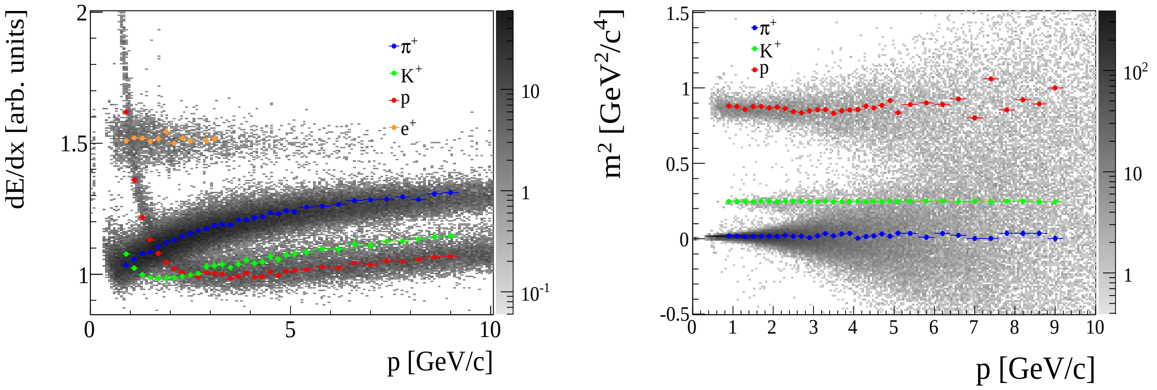

Figure 6.6: dE/dx (left) and m^2 (right) as a function of momentum with mean parameters returned by the bi-dimensional fit in the polar angle interval $[100, 140]$ mrad.

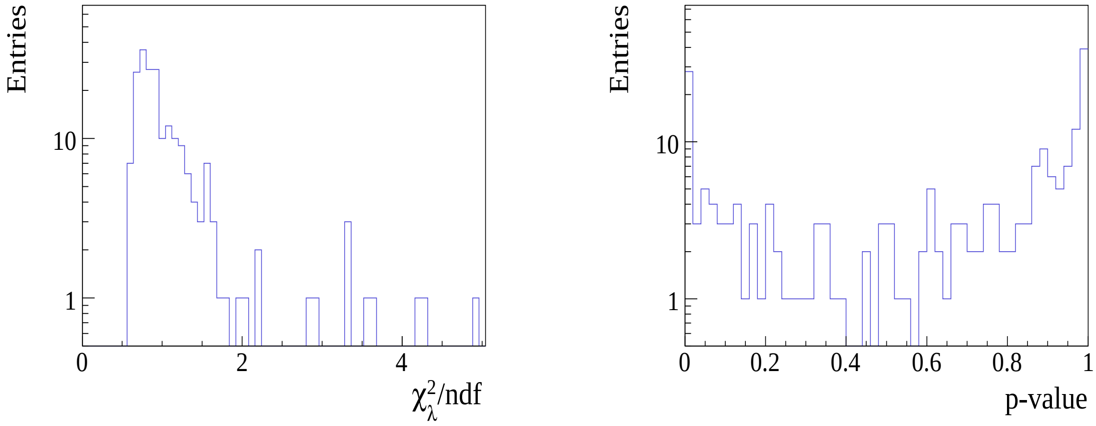

Figure 6.7: distribution of χ^2_λ/ndf and p-values.

6.2 Correction factors and systematic uncertainties

The breakdown of the Monte Carlo correction factors applied to the fitted pion yields are given in Appendix F. An example for the polar angle interval [20,40] mrad is shown in Figure 6.8 for positively and negatively charged pions. The factors include corrections for pions from weak decays (feed down), interactions in the detector material and target, track reconstruction efficiency, detector acceptance and losses due to pion decay. The ToF-F detection efficiency was estimated by requiring that a track traversing the ToF-F wall generates a hit in the ToF-F. The ToF-F inefficiency is almost only due to double hits, as explained in Section 5.4-ii. One immediately notices that, while feed down was negligibly small for K^+, it is a significant correction factor for pions and especially for π^-. This is essentially due to produced Λ hyperons ($\Lambda \to p\pi^-$) and K^0_s ($K^0_s \to \pi^+\pi^-$) decaying close to the target where the daughter pion is reconstructed at the primary vertex. The π^-contamination from Λ decay at low momenta low angle (typically $\theta \lesssim 60$ mrad $p \lesssim 4$ GeV/c) explains the large feed down correction applied to the π^-spectra with respect to the π^+.

The decay correction was computed in order not to reject reconstructed tracks in the ToF-F which are matched to muons from pion decay as explained in the previous section. Figure 6.9 shows an example for a given angular bin of the decay correction if all pions were lost compared to the applied decay correction where extrapolated muons are kept in the final sample. This provides a quantitative estimate of the amount of extrapolated muons present in the final track sample.

Similarly to the K^+ analysis the calculated biases are applied successively to the raw fitted number of pions. For a given $\{p, \theta\}$ bin, i, the corrected yield, $N^{i,cor}_\alpha$, is given by:

$$N^{i,cor}_\alpha = N^{i,raw}_\alpha \times \prod_{j=1}^{N_{cor}} \frac{1}{\varepsilon_j} \times \delta_i \qquad \delta_i = \begin{cases} \frac{2\pi}{2\Delta\phi^i}, & \text{if bin contains WST and RST,} \\ \frac{2\pi}{\Delta\phi^i}, & \text{otherwise.} \end{cases} \tag{6.1}$$

where α stands for π^- or π^+ and ε_j denotes the value of the different correction factors. The spectra are integrated over a 2π azimuthal acceptance with the factor δ_i which varies by a factor

2 whether the bin contains only one track topology or both. Statistical errors on the pion spectra include contributions from the finite statistics of data and from the Monte Carlo simulation used to obtain the correction factors. The Monte Carlo statistics was about 10 times larger than the data statistics and the total statistical errors are dominated by the statistical uncertainty of the data.

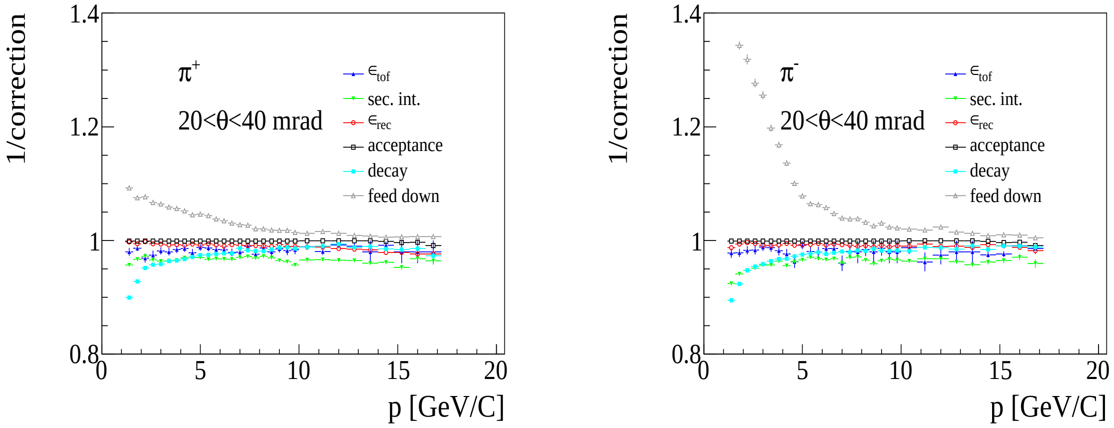

Figure 6.8: Example of momentum dependence of the inverse correction factors, for positively (left) and negatively (right) charged pions in the polar angle interval [20,40] mrad. ϵ_{rec} and ϵ_{ToF} are the efficiencies of the reconstruction and of the ToF-F, respectively. The feed-down correction accounts for pions from weak decays which are reconstructed as primary particles.

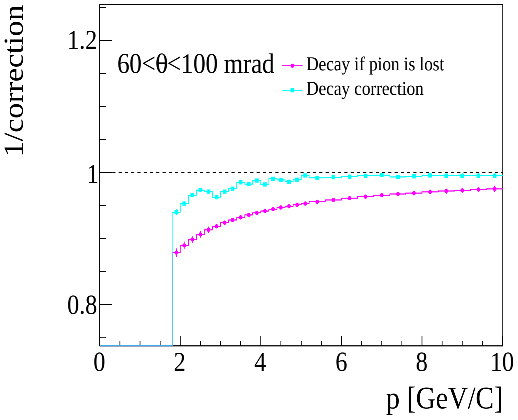

Figure 6.9: Monte Carlo simulation of the decay correction in the angular bin [60,100] mrad: the magenta line corresponds to the fraction of pions that reach the ToF-F before decaying. The cyan line additionally includes secondary muons which are extrapolated to the ToF-F.

The breakdown of the systematic errors are presented in Figure 6.8 for the polar interval [20,40] mrad and in Appendix F for all other intervals. The dominant contributions to the systematic error for both $\pi^+$and π^-spectra come from the uncertainty in the correction for secondary interactions and pion decay in flight as well as for weak decays of strange particles (feed down). The systematic error due to the admixture of pions from the decays of strange particles reconstructed at the primary vertex depends on the knowledge of strange particle production. The error was estimated based on:

(i) comparison of the number of V^0 decays reconstructed in the data and in the VENUS4.12 model with default parameters,

(ii) variation of the strange particles yields in different Monte Carlo generators; for example the K^-/π^- ratio in p+C interactions at 31 GeV/c from FLUKA2008 [105], URQMD1.3.1 [148] and GIBUU1.3.0 [151] (with default value of physics parameters) were compared to the VENUS4.12 [147, 137] generator used in this analysis,

(iii) comparison of the VENUS4.12 predictions with the measured K^-/π^- and K^+/π^+ ratios from p+B_4C interactions at 24 GeV/c at large momenta and small angles [152].

From those comparisons between various models and between models and data we observed that the strange particle production could differ by about 20%, it was therefore decided to apply a conservative 30% uncertainty to the value of the feed down correction. The systematic uncertainty on other model dependent corrections, such as secondary interactions, are also estimated as 30% of the value of the corresponding correction.

At the time the analysis was published in [119] the biases due to secondary interactions and decay were grouped in one common correction which was called "pion-loss correction". The pion loss correction was then treated as model dependent and an uncertainty of 30% of the correction was assigned. For future analysis, the conservative estimate could in principle be reduced if we decoupled the decay correction from the secondary interactions in the treatment of systematics. One can then use the same list of arguments as for the K^+ (Section 5.5) to estimate the systematic error on the decay correction: the model dependence of the decay correction should be negligible because of the smaller bin size and of the longer charged pion lifetime; the uncertainty on the length calculation can also be neglected in this analysis. The systematic error on the decay correction should then only be driven by potential differences between data and MC of the muon contamination in the final sample.

As was the case for the K^+ spectra varying track selection criteria did not lead to the observation of significant biases with respect to the statistical fluctuations. Thus a 1% error on the reconstruction efficiency is estimated. The sample of softer tracks which are bent with a large curvature through the spectrometer, the so-called Wrong-Wrong-Side-Tracks (WWST, see Section 3.5) are assigned a larger (2%) systematic uncertainty. The sensitivity of the correction was found to be larger for that category of tracks when varying the cut on the impact parameter b_x. This is related to the fact that, as seen in Figure 6.11, the b_x distributions are generally wider for WWST.

The systematic uncertainties related to the PID were estimated by comparing the fitted yields with the number of particles summed within 2σ around the fitted pion peak. The resulting deviations were found to be rather small (a few percent) and slightly increased with momentum, reflecting the fact that pions are well separated from other accumulations over the whole considered phase-space. An envelope describing the observed deviations serves as estimate for the PID related systematic uncertainty.

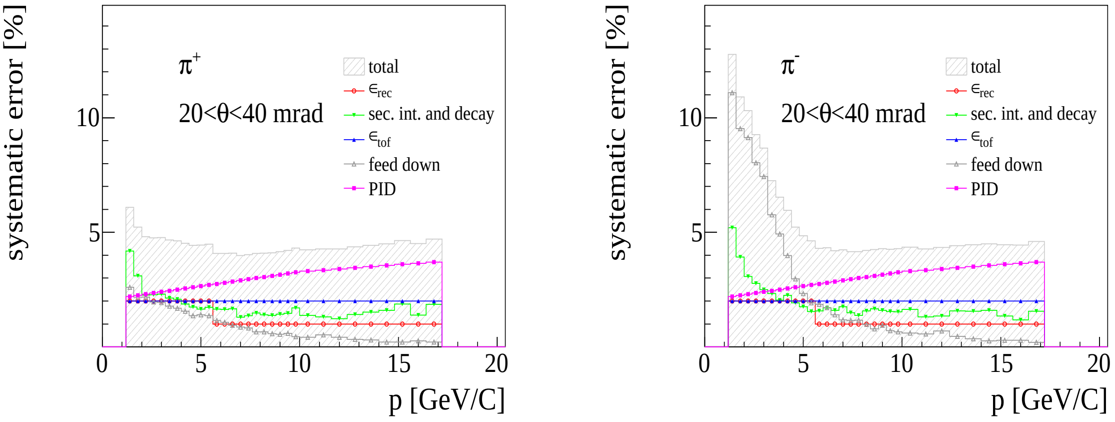

Figure 6.10: Breakdown of systematic errors as a function of momentum for positively (left) and negatively (right) charged pions in the polar angle interval [20,40] mrad.

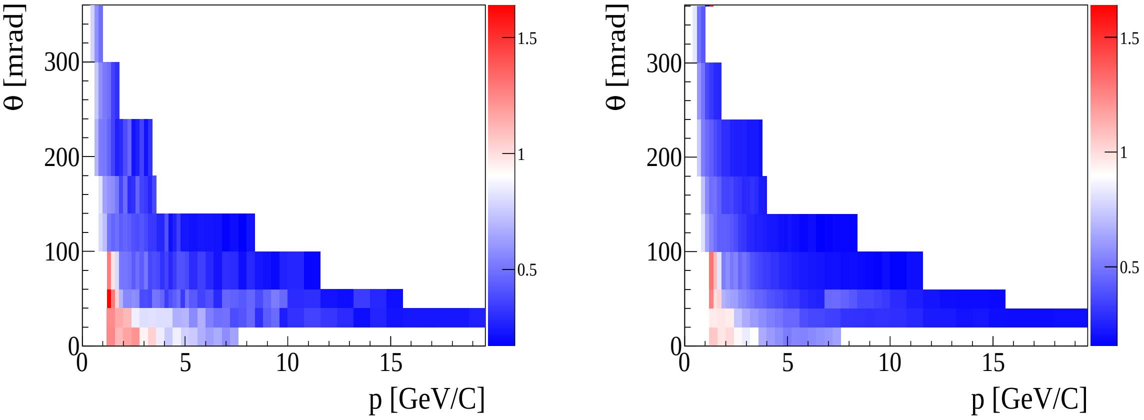

Figure 6.11: RMS of b_x distributions (in cm) for positive tracks in each $\{p, \theta\}$ bin of the analysis for data (left) and Monte Carlo (right)

6.3 Results

The π^+ and π^- spectra presented in this section refer to pions produced in strong and electromagnetic processes in p+C interactions at 31 GeV/c.

The spectra are normalized to the inclusive cross section according to the method presented in Section 5.6. The correction for the contribution of particles from out-of-target events amounts on average to about 7% and 3% in the first two polar angle intervals. It is smaller than about 2% for polar angle bins above 40 mrad. The results are shown in Figures 6.13 and 6.14 for positively and negatively charged pions, respectively. The spectra are compared with the results from two other analyses which are briefly described below.

- The dE/dx analysis at low momentum. tof measurements are not available for low momentum particles since they do not reach the ToF-F detectors (see e.g Figure 6.1). Therefore the analysis of charged pion production at low momentum can only be done by means of particle identification via specific energy loss in the TPCs. A reliable identification of π^+ mesons based only on dE/dx is not possible at momenta above 1 GeV/c where the Bethe-Bloch (BB) curves for pions, kaons and protons cross each other. On the other hand, for π^- mesons, where the contribution of K^- and antiprotons is almost negligible, the dE/dx analysis could be extended in momentum up to 3 GeV/c allowing consistency checks in the region of overlap. The identification procedure was performed in narrow momentum intervals (of 0.1 GeV/c for $p < 1$ GeV/c and 0.2 GeV/c for $1 < p < 3$ GeV/c) to account for the strong dependence of dE/dx on momentum. The spectra were then obtained by means of a global MC correction factor: for a given $\{p, \theta\}$ bin all reconstructed π^+or π^-mesons are divided by the generated primary ones. Details on this analysis can be found in [119, 140].

- The h^- analysis. This analysis is based on the fact that more than 90% of primary negatively charged particles produced in p+C interactions at 31 GeV/c are negatively charged pions. π^- meson spectra can thus be obtained by subtracting the estimated non-pion contribution from the spectra of negatively charged particles and additional particle identification is not required. Note that this method is not applicable to the analysis of π^+ meson spectra due to the much larger and unknown contribution of protons and K^+ mesons to all positively charged particles. A global Monte Carlo factor was used to correct the yields in each $\{p, \theta\}$ bins for the contribution of electrons, primary K^- and $\overline{p}$ as well as secondary particles from weak decays (feed down), secondary interactions and photon conversions in the target and the detector material. Details can be found in [119, 139].

For both alternate analyses, the systematic errors are comparable to those of the analysis presented in this thesis (referred to as the tof-dE/dx analysis). In the case of the h^- analysis systematics at low energy and low angle (typically p$\lesssim$ 2 GeV $\theta \lesssim$ 140 mrad) can be as high as 20% because of the important feed down correction as well as the contamination from electrons in the final track sample. Statistical uncertainties are however generally lower because there is no requirement that the particle hits the ToF-F detector. Also, as can be seen from the results, the spectra from h^- and dE/dx analysis extend up to 420 mrad of polar angle. The analysis presented in this thesis does not cover the θ interval $[360-420]$ mrad because of the limited ToF-F acceptance in this region and the low statistics of the 2007 sample. The agreement between all three analysis is, in general, better than 10%. Note, that data points in the same $\{p, \theta\}$ bin from different analysis methods are statistically correlated as they result from the analysis of the same data set. For the final published spectra consisting of statistically uncorrelated points the measurement with the smallest total error was selected. The table with the final results is given in [119]. Figures 6.15 and 6.16 present the final spectra with comparisons to the predictions of event generators of hadronic interactions. As for the K^+ comparisons, models that have been frequently used for the interpretation of cosmic ray data, i.e. VENUS4.12 [147, 137], FLUKA2008 [105] and URQMD1.3.1 [148] were selected. The VENUS4.12 and FLUKA2008 models follow the data trend in all measured polar angle intervals. The URQMD1.3.1 model qualitatively disagrees with the data only at low momenta ($p < 3$ GeV/c) and polar angles below about 140 mrad. Motivated by this comparison, a correction of a technical shortcoming of the URQMD model was proposed in [153] where it is specified that the drawback of the URQMD1.3.1 model was connected with an inaccurate treatment of low mass string fragmentation. A patch has been proposed to overcome the problem.

Finally, the ratio of K^+ to π^+production cross sections is shown in Figure 6.12. The final π^+spectra central values and errors are recalculated to match the larger binning of the K^+ analysis. The ratios are also compared with the predictions from models: UrQMD1.3.1 is in good agreement with the data, Fluka2008 provides a reasonable description, while Venus4.12 overestimates the production cross section ratio for both small and large angle intervals. Please note that the technical shortcoming of the UrQMD model mentioned above, relates to a phase space region (i.e. $0 < \theta < 20$ mrad and p < 1.5 GeV/c) which is not covered by the kinematic range of the K^+ analysis, therefore the ratios are compared with the original implementation.

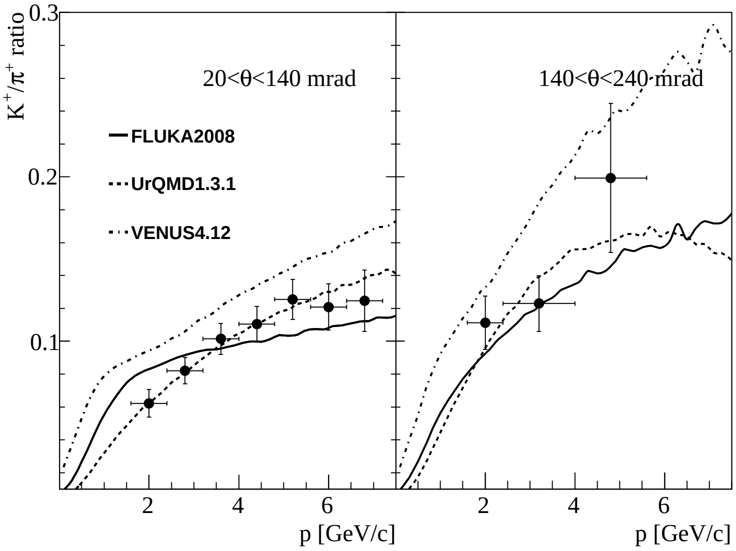

Figure 6.12: Ratio of K^+ to π^+ production cross sections in p+C interactions at 31 GeV/c. The ratios are presented as a function of laboratory momentum, p, in two intervals of polar angle θ. Errors are calculated taking into account only statistical uncertainties. Predictions of hadron production models are superimposed.

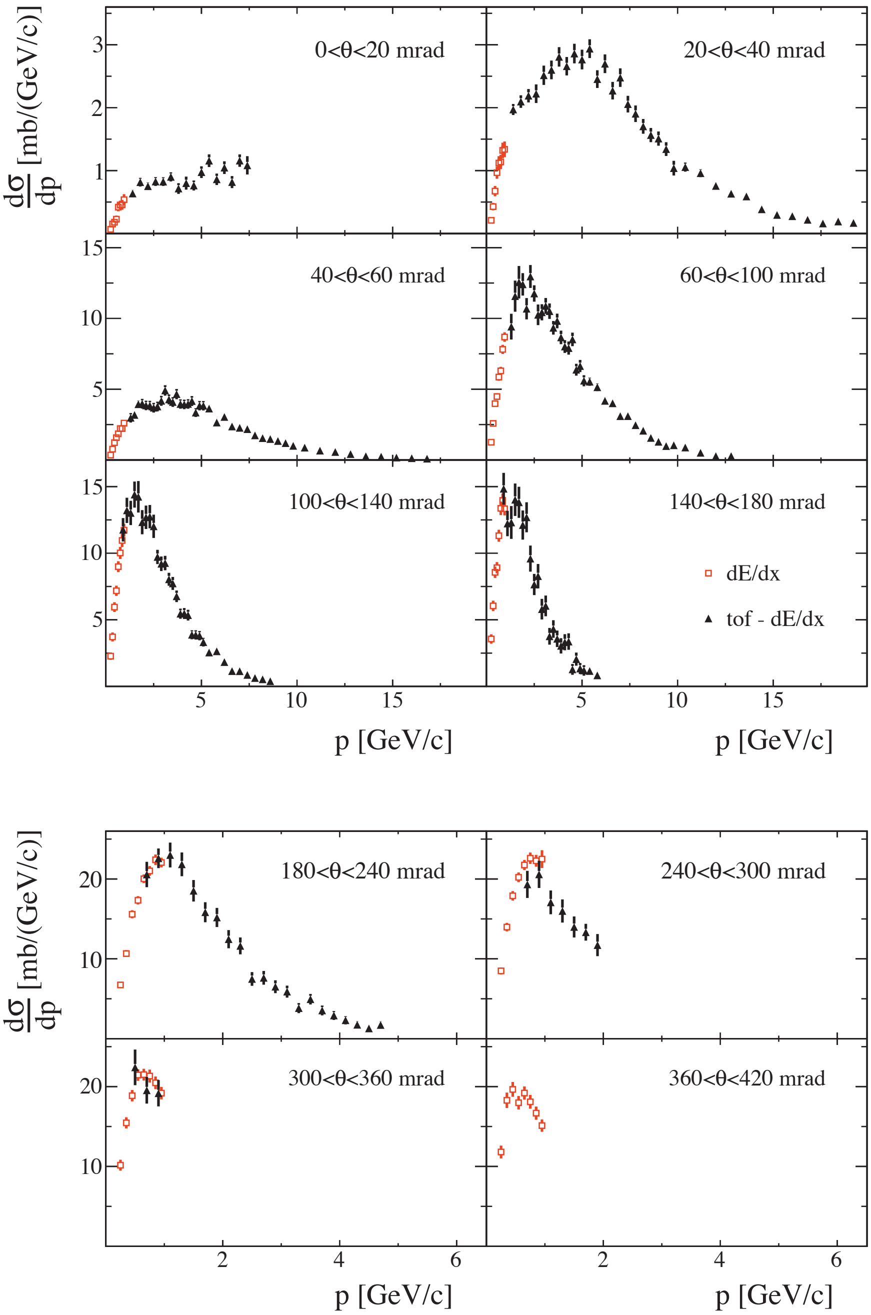

Figure 6.13: Differential cross sections for π^+ meson production in p+C interactions at 31 GeV/c. The spectra are presented as a function of laboratory momentum (p) in different intervals of polar angle (θ). Results obtained using two analysis methods are presented by different symbols: red open squares - dE/dx analysis and black full triangles - tof-dE/dx analysis. Error bars indicate only statistical uncertainties.

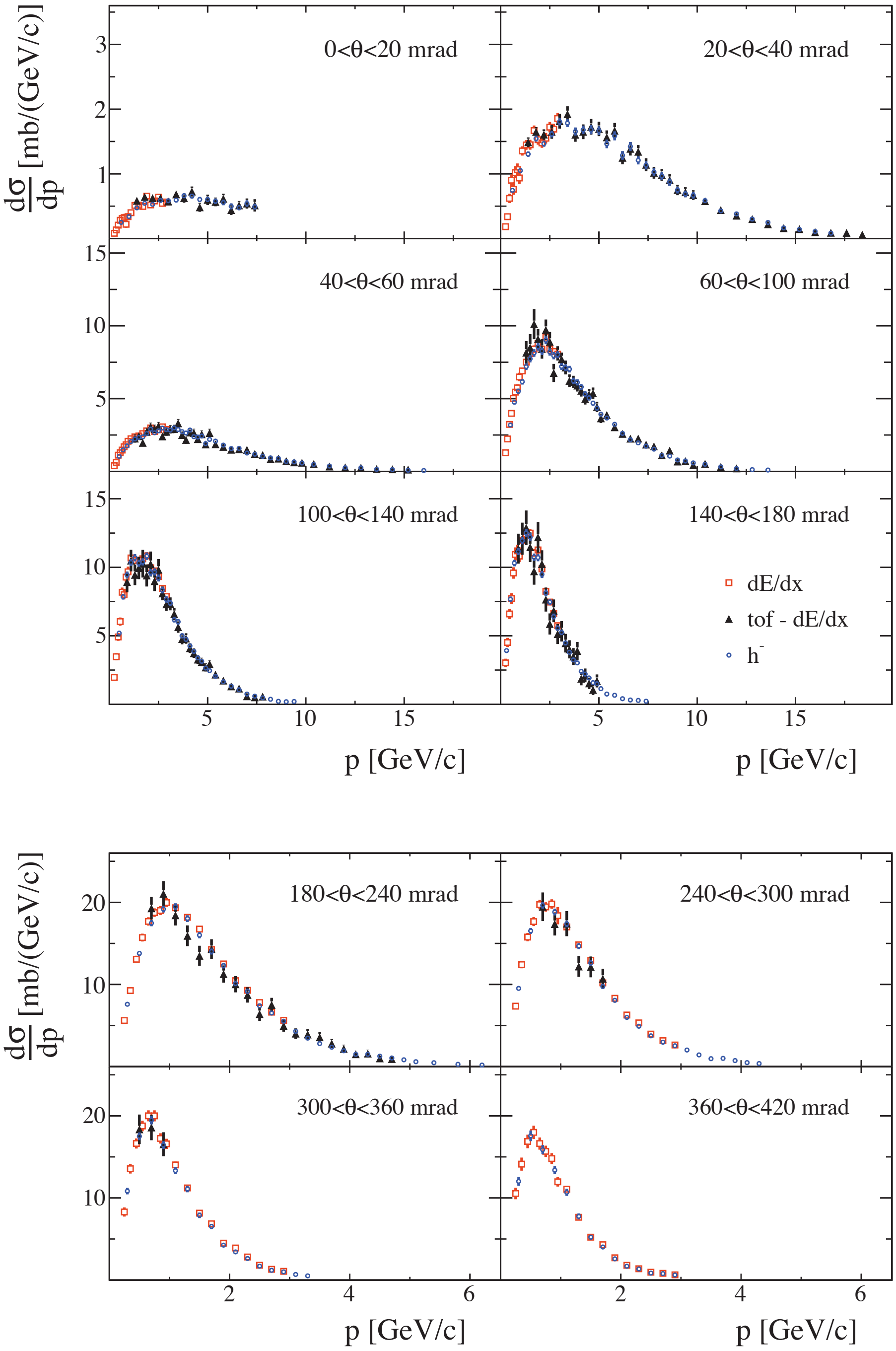

Figure 6.14: Differential cross sections for π^- meson production in p+C interactions at 31 GeV/c. The spectra are presented as a function of laboratory momentum (p) in different intervals of polar angle (θ). Results obtained using three analysis methods are presented by different symbols: blue open circles - h^- analysis, red open squares - dE/dx analysis and black full triangles - tof-dE/dx analysis. Error bars indicate only statistical uncertainties.

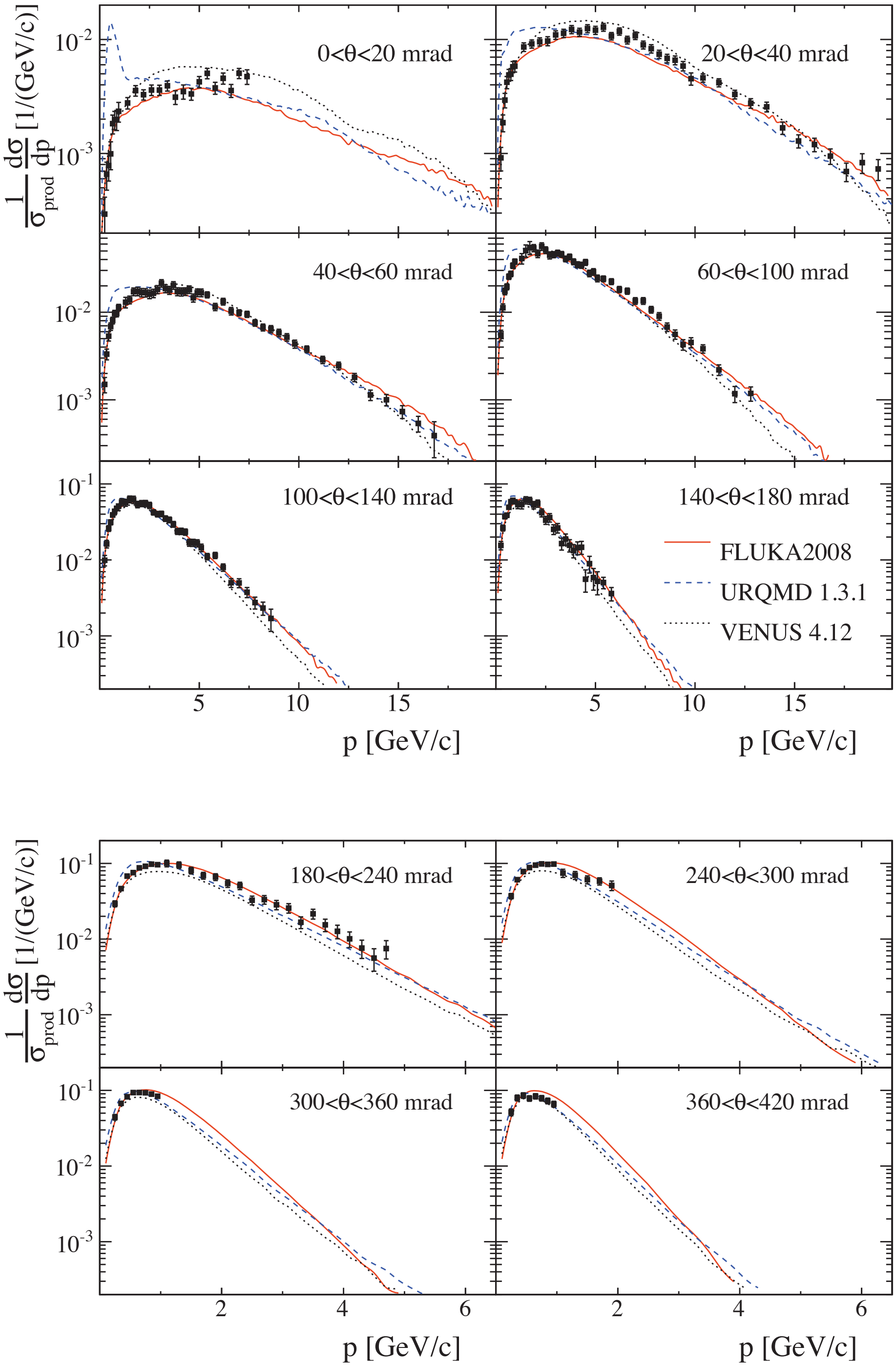

Figure 6.15: Laboratory momentum distributions of π^+ mesons produced in production p+C interactions at 31 GeV/c in different intervals of polar angle (θ). The spectra are normalized to the mean π^+ multiplicity in all production p+C interactions. Error bars indicate statistical and systematic uncertainties added in quadrature. The overall uncertainty (2.3%) due to the normalization procedure is not shown. Predictions of hadron production models, FLUKA2008 (solid line), URQMD1.3.1 (dashed line) and VENUS4.12 (dotted line) are also indicated.

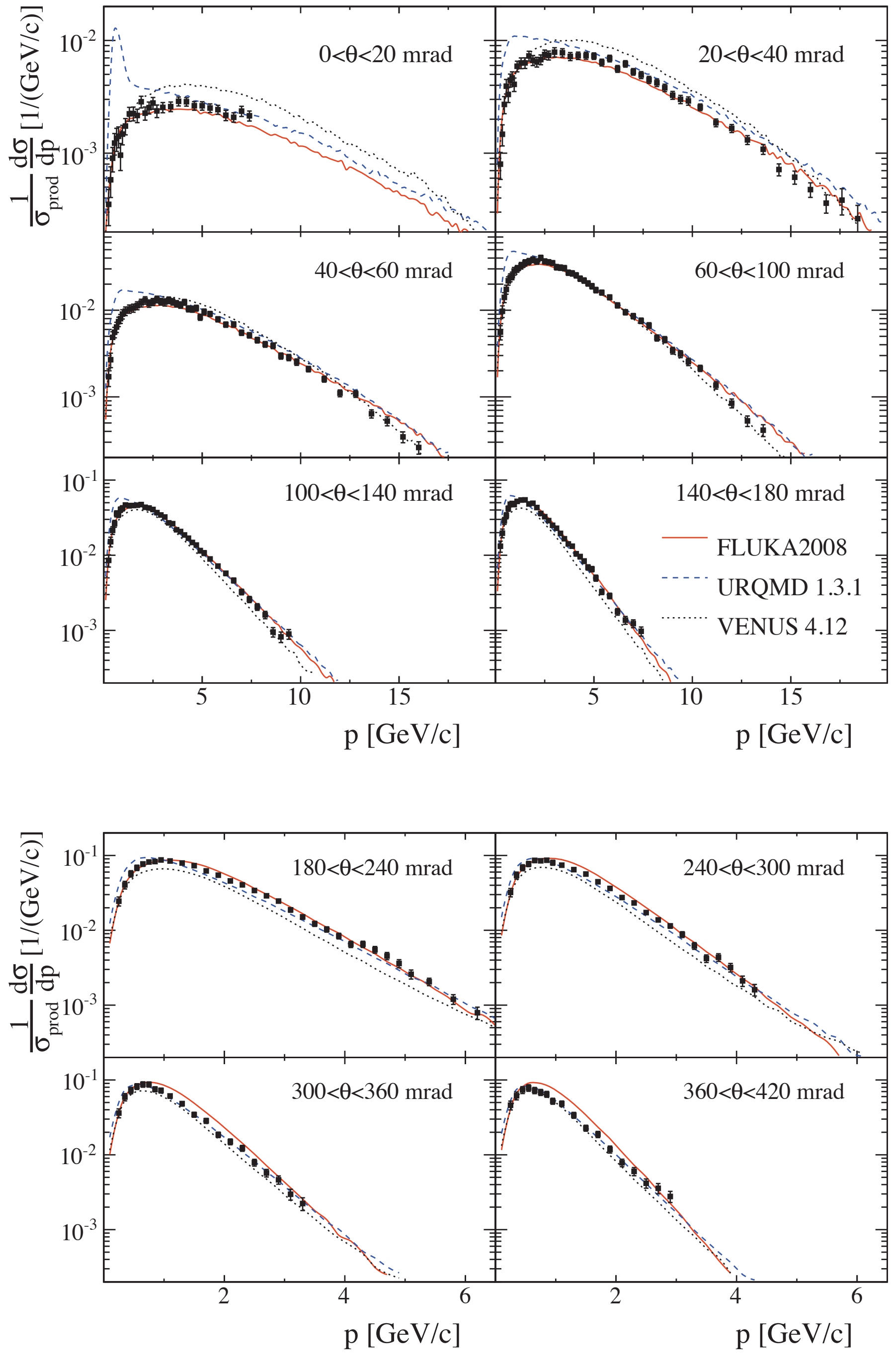

Figure 6.16: Laboratory momentum distributions of π^- mesons produced in production p+C interactions at 31 GeV/c in different intervals of polar angle (θ). The spectra are normalized to the mean π^- multiplicity in all production p+C interactions. Error bars indicate statistical and systematic uncertainties added in quadrature. The overall uncertainty (2.3%) due to the normalization procedure is not shown. Predictions of hadron production models, FLUKA2008 (solid line), URQMD1.3.1 (dashed line) and VENUS4.12 (dotted line) are also indicated.

6.4 Towards high precision measurement: reduction of systematic uncertainties

This section provides a further discussion on the estimate of systematic uncertainties in NA61/SHINE and more specifically to which amount they could be reduced if, for example, we had a lot larger statistics at our disposal such as the 2009 data. For the analysis presented in this thesis, the errors were clearly dominated by the low statistics of the 2007 run (see Appendix G). The statistical error on the results was typically of the order of 10%; in 2009 the sample is roughly 10 times larger and the associated error is thus more likely to be around 3%. Most importantly, while the low statistics of 2007 has privileged conservative estimates of the systematic uncertainties, higher statistics would allow us to improve the estimation and certainly help in reducing the errors. Below I give a summary of the systematic errors which we evaluated and try to think of what could be achieved with higher statistics. In other words what are the limits which are intrinsic to the NA61/SHINE detector itself for such cross-section measurements.

(i) Reconstruction efficiency and acceptance: an important feature of the analysis resides in selecting only areas of high and well defined acceptances. Consequently, what could be the largest of all corrections, and thus the one associated with the highest systematic uncertainty, is reduced to a negligible level. The ToF-F requirement already selects specific areas of phase space with long and well measured tracks. The detection efficiency is then further increased with the ϕ and z_{last} selections. For kaons the cut on z_{last} simplified the estimate of the decay correction and drastically reduced the corresponding systematic uncertainty. I think this selection should be applied regardless of what particle is under study. Since we are using tof measurements for PID, it is reasonable to require that the tracks are reconstructed up to the ToF-F as it prevents from including particles which may have decayed or interacted. Cutting on z_{last} reduces the WST $\{p, \theta\}$ coverage at low momentum (see the difference between the kaon and pion acceptances in Figures 5.1 and 6.1). This difficulty may be overcome by carefully adjusting the binning. With the 2009 data, the larger ToF-F, will also help in partly recovering this area.

(ii) ToF-F efficiency: the detection itself is 100% efficient. In other words a track extrapolated to the ToF-F produces a hit in the expected slat which is seen by at least one of the attached PMTs, indicating that the generated light yield is always above the CFD thresholds. This demonstrates that all the PMT high voltages and corresponding thresholds were correctly set and that the extrapolation procedure is accurate. This is an important point; what must definitely be avoided is to have a completely dead scintillator (i.e both channels not working): since each scintillator has a specific $\{p, \theta\}$ coordinate, the inefficiency of a single malfunctioning bar would directly translate in an important correction factor spanning over a large momentum range of the analysis. This can be understood from Figure 6.17 where the detection efficiency for positive tracks belonging to the pion kinematic range is shown with a scintillator slat artificially switched off.

The 2-3 % inefficiency is only a consequence of the removal of the biased tof measurements which are caused by the double hits. Unless the mass of the particle is known it is not possible to estimate which of the two tdc measurements is correct and which one is biased.

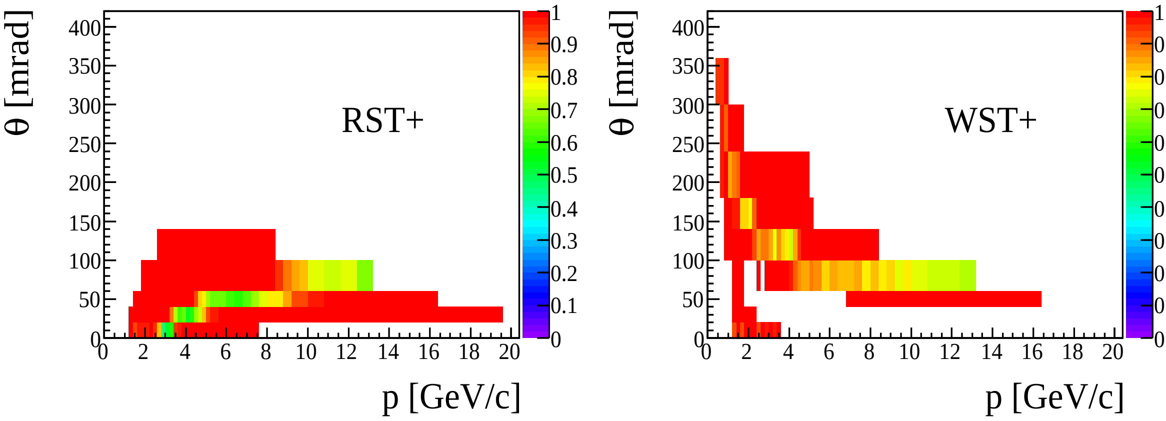

Figure 6.17: Example of ToF-F detection efficiency with a slat artificially removed. For the left plot corresponding to positive RST slat number 20 was removed and for the right one (positive WST) number 40 was taken out.

Therefore to remove the tails from the mass-squared spectra (and consequently reduce the error on the PID) those tracks are discarded and the corresponding loss is treated as a correction factor. Therefore, assigning a 2% systematic error on the ToF efficiency is close to assuming a 100% percent error on the corresponding correction. The conservative estimate is due to the fact that the low 2007 statistics prevents from studying the effect of the cut on a scintillator by scintillator basis. Such a study will however be possible with the 2009 data set. It should then be possible to attribute different systematic uncertainties for each scintillator and it seems reasonable to think that we can reach the level of ∼1% or below. In the future, maybe the implementation of the ToF-F response in the Monte Carlo could also help in further understanding those double hit processes.

(iii) Particle identification: estimations of the quality of the fits were obtained by varying the input parameters and studying the subsequent variations on the particle yields. Comparing the integral of the fitted peaks with the sum of the events in a given contour and computing the contamination also gave good indications. But these estimates are most likely artificially increased by the high statistical fluctuations. At low momenta, the ∼2-3% uncertainty indicates that the yields are rather well described by Gaussian functions. As was specified, when we have a larger data sample it could be worth considering a double Gaussian to better describe the ToF-F response (see Figure 6.18). With higher statistics more precise calibrations can be achieved which would consequently improve the resolution on the final dE/dx and m^2 spectra. Strict track selection criteria are also important to prevent selecting particles which decayed in flight or re-interacted. We may also want to avoid keeping samples which consist of different track lengths with different dE/dx resolutions. All these effects contribute to distort the shape of the distributions. The combined tof-dE/dx method allows to select samples with a close to 100% purity at low momentum, so if the ToF-F and dE/dx calibration are well under control it seems reasonable to believe that at low momentum ($\lesssim$4 GeV/c) we can achieve a systematic error which is close to negligible.

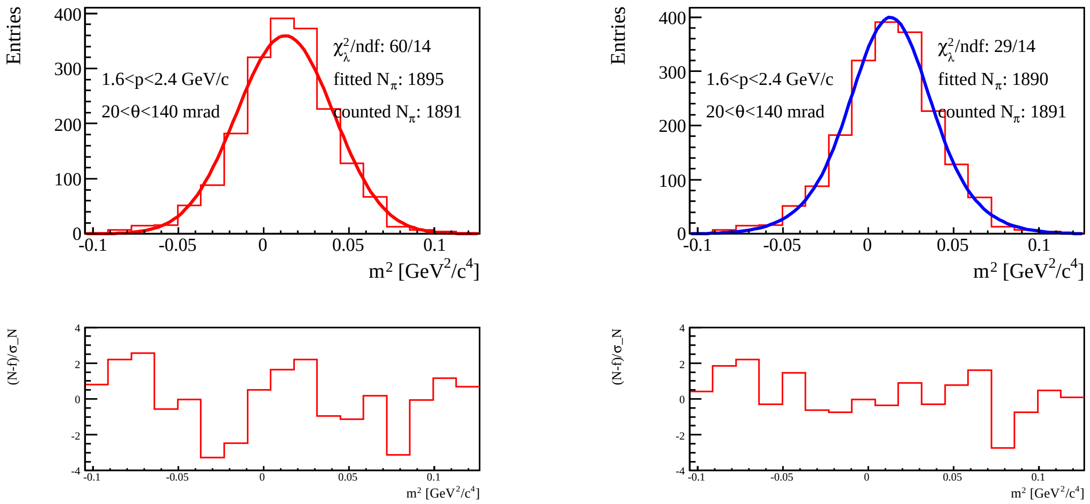

Figure 6.18: Example of fits to the π^+ m^2 peak. The same distribution is fitted with a single Gaussian (left) and a double Gaussian (right) hypothesis. The fitted yields returned by both functions are compared to the sum. Agreement is slightly better for the double Gaussian hypothesis as also seen by the distribution of residuals (bottom).

(iv) Feed down: is the biggest correction for the charged pion cross-sections, and will also be an issue for protons produced by Λ decays. At the moment this correction is 100% model dependent leading to the high quoted systematic uncertainty. Instead the Λ and K^0_s production rate should be directly evaluated from our data by a dedicated V0 analysis. Work has already started in this direction but no results have yet been published or presented outside of the collaboration. The systematic errors associated to the feed down correction will then essentially be driven by the uncertainties of the V0 analysis which will be considerably smaller than the current estimate of 30% of the contamination. Furthermore, the contamination from weak decays may in principle be reduced by applying stricter cuts on the impact parameter. This is demonstrated in Figure 6.19, where the distribution of b_x for MC tracks matched to protons from Λ decay is compared to those from the primary vertex. Clearly the contamination can be reduced with tighter cuts, this would however require a deeper understanding of why the b_x distributions of MC and data differ in some regions.

(v) Other contributions: the correction related to secondary interactions depends on the MC model and on the accuracy of the geometry and material simulation. These are all contributions which have potentially high and difficult to estimate systematic uncertainties. Thus, the best approach consists in minimizing their impact by selecting high detection efficiency regions, thereby preventing the particles from interacting in the magnets or the TPC edges. The only 2-3% contamination left are due to target re-interactions which brings the corresponding systematic error to the percent level assuming 30% error on the MC model.

The decay correction, on the other hand, is not model dependent and mainly depends on the

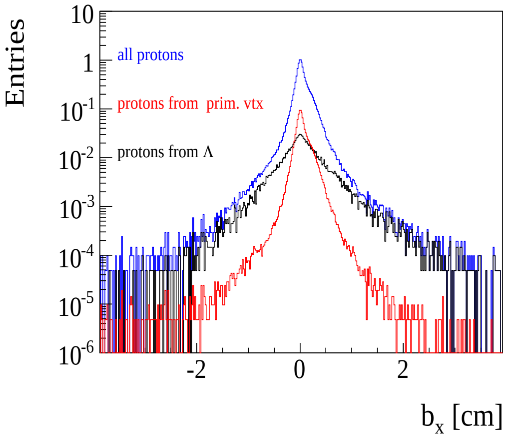

Figure 6.19: b_x distributions of MC tracks matched to protons produced at the primary vertex and those associated to protons from Λ decay.

knowledge of the particle's lifetime and on the precision of the length calculation, both of which yield a ∼ ‰ uncertainty on the value of the correction. The main issue is then trying to estimate what fraction of decayed particles are associated to a tof measurement. The MC simulation is needed for that matter and there will always be an inherent uncertainty due to differences between data and MC. However, as we have seen for the K^+, with careful track selection criteria the related systematic error can be kept to the 1-2% level.

In the analysis that has been described throughout this thesis, one of the main reasons for breaking down the corrections is for an accurate study of the systematic uncertainties. One of the things that has been learnt by doing so is that, in the end, the only significant correction which is model dependent is the feed down. But when derived from a dedicated V0 analysis future results may be essentially free from any model dependent corrections. This is of course an ideal situation for such cross-section measurements.

If we drastically reduce the systematic uncertainties related to feed down along with the PID errors, I think we should be able to reach typical total uncertainties around 3-5% instead of the current 5-10%. Protons, for which no decay correction is needed, could be delivered with a systematic uncertainty that is essentially only due to PID (considering we have accurately measured Λ production). To conclude, the NA61/SHINE detector has proved to be very reliable for those measurements: because it was designed for tracking in high multiplicity collisions the reconstruction algorithm is very efficient and, in addition, the material budget along the particle trajectories is minimal. It is then all a matter of carefully selecting the tracks to reduce the systematic errors. The only limitation of the detector is its low acceptance in the uninstrumented forward region ($p \gtrsim 10$ GeV/c and $\theta \lesssim 15$ mrad). In the 2010 long target campaign the magnetic field was increased for some of the runs in order to bend those high momentum particles back in the acceptance.

6.5 The NA61/SHINE measurements for the T2K ν_e appearance result

In June 2011, after about a year of data taking, T2K reported a strong indication of ν_e appearance from a ν_μ beam [44]. By observing 6 single e-like ring events at Super Kamiokande (SK), while about 1 was expected if θ_{13} =0, T2K disfavors θ_{13} =0 at the 2.5 σ level with a best fit value at $\theta_{13} = 9.8^\circ$ (assuming δ_{CP} =0 and normal mass hierarchy). Later that year, MINOS [45] and Double Chooz [154] also made observations consistent with $\theta_{13} \neq 0$. For these first physics results from T2K, the NA61/SHINE pion measurements reported in this chapter were used to tune the T2K beam Monte Carlo and helped reduce the model dependency on the flux prediction. Consequently the overall systematic error on the published result was reduced. The K^+ cross sections were not yet released at the time the ν_e paper was published but have now been included in the beam MC and are expected to benefit the next T2K results. In this section, I summarize the use of our NA61/SHINE pion results in the T2K beam simulation to constrain the simulated hadron production.

Tuning of pion multiplicities

The pion multiplicity from the beam MC simulation (JNUBEAM), which is provided by FLUKA2008 3.b [105], is first normalized to the model production cross section of 231.3 mb, and compared to the NA61/SHINE pion multiplicity in each $\{p, \theta\}$ bins. For pions generated in the NA61/SHINE phase-space the flux tuning factor is obtained by taking the NA61/SHINE to FLUKA ratio of the mean multiplicity. The ratios are shown in Figure 6.20. The NA61/SHINE systematic error for each $\{p, \theta\}$ bin (typically 5 to 10%, see Appendix G) and the overall NA61 normalization error (2.3%) are also propagated to the uncertainty on the flux. The errors in the bins are treated as fully un-correlated, thus ensuring the largest possible errors on the flux prediction. Bin to bin correlations of the NA61/SHINE systematic errors will be taken into account for future predictions and this conservative estimate will no longer be necessary. Pions contributing to the flux which are generated outside the NA61/SHINE coverage are assigned a 50% error. This value is estimated from the comparison between various MC models.

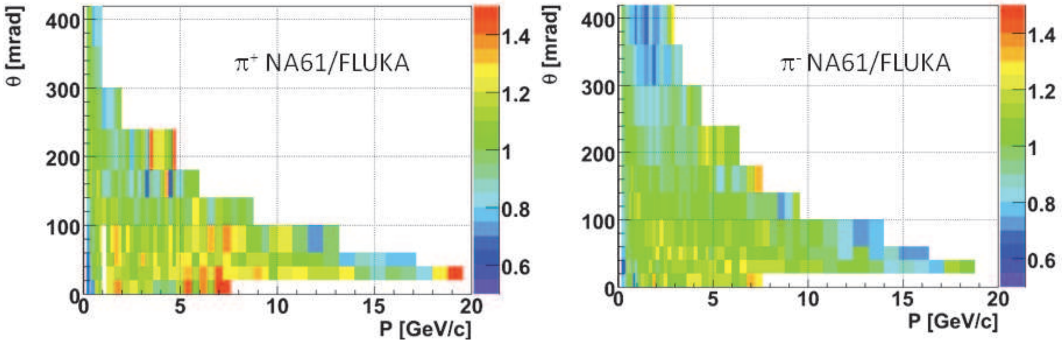

Figure 6.20: NA61/FLUKA ratios of the mean multiplicity for π^+(left) and π^-(right). The figures are from [108].

Tertiary pions (pions produced in the re-interaction of secondary protons) are also re-weighted.

Since they originate from interactions of nucleons with a smaller energy than the NA61/SHINE beam protons, the NA61/SHINE multiplicities are scaled to the required energy according to the approximation of Feynman scaling which suggests that the production cross-sections can be scaled with $\sqrt{s}$ [155]. The NA61/FLUKA weights must first be converted from the $\{p, \theta\}$ to the $\{x_F, p_T\}$ space; they can then be scaled to estimate pion production at different incident proton energies. The tuning of secondary interactions in the horns and target material (mainly Aluminium) is done by scaling the NA61 differential cross sections to different materials (A scaling) according to the method suggested by Bonesini *et al* [156] (summarized in Appendix A of [157]).

Secondary nucleons

As shown in Table 6.3, secondary protons and neutrons contribute to approximately 16% and 5% of the ν_μ flux at SK. The FLUKA $\{x_F, p_T\}$ distribution of secondary protons and neutrons that subsequently produce neutrinos contributing to the SK flux are shown in Figure 6.21. The secondary proton production predicted by FLUKA is compared with the Eichten *et al* [152] and Allaby *et al* [158] data, who measured proton-Be interaction at 24 GeV/c and proton-proton interactions at 19.2 GeV/c respectively. Since they are measured at different energies and for different target materials, the multiplicities are scaled accordingly. The ratio of the secondary proton multiplicity of the data to FLUKA is shown in Figure 6.22, the factors in the phase space not covered by data are determined based on the averaged difference between data and FLUKA in the nearby relevant phase space. The flux is then recalculated by changing the secondary proton and neutron production by those factors; the changes on the flux are used as systematic uncertainty. As can be seen the discrepancies between the data and FLUKA are rather large and especially in the high x_F low p_T region. It is therefore important to also measure the proton production cross-sections in NA61/SHINE. Preliminary proton cross-sections extracted with the same *tof*-dE/dx method as for the charged pions and kaons are shown in Appendix H. Those can be used in the future to improve the prediction of secondary nucleon interactions.

ν species	**Parent particle contribution [%]**				
	$\pi^\pm$	$K^\pm$	p	n	others (Λ, Σ, etc..)
ν_μ	69.5	4.9	15.8	5.2	1.8
ν_e	40.5	27.3	13.6	5.2	1.5

Table 6.3: Contribution of secondary particles to the ν_μ and ν_e fluxes at SK.

Approximately 5% of the parent pions contributing to the F/N ratio come from secondary neutron interaction. For secondary interactions from neutrons it is assumed that the weights are invariant under isospin transformation of the quarks $u \leftrightarrow d$. Therefore the $n + C \rightarrow \pi^\pm + X$ interactions are tuned with the weights derived from the NA61/SHINE $p + C \rightarrow \pi^\mp + X$ cross-sections. The systematic uncertainty on the F/N ratio is then evaluated by adding 20% error to the systematic error of the NA61/SHINE measurements that conservatively allows for isospin symmetry violation in each pion $\{p, \theta\}$ bin.

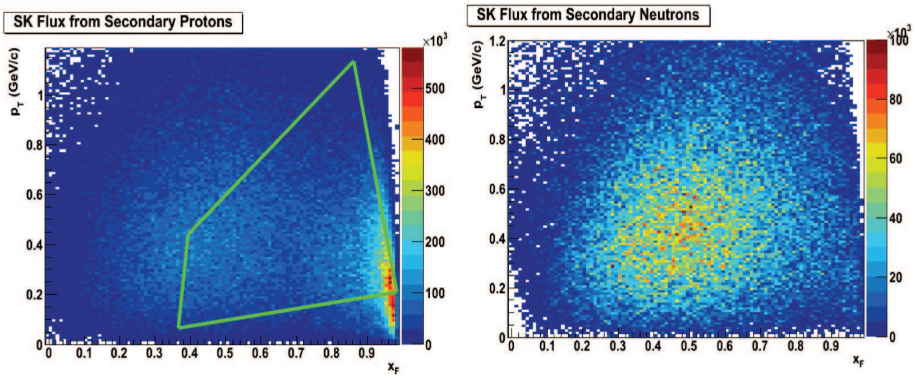

Figure 6.21: Secondary proton (left plot) and neutron (right plot) distribution in $\{x_F, p_T\}$, the subsequent interaction of which contribute neutrinos to the SK flux. The green box superimposed on the left plot shows the phase space covered by the Allaby data. Both figures are from [108].

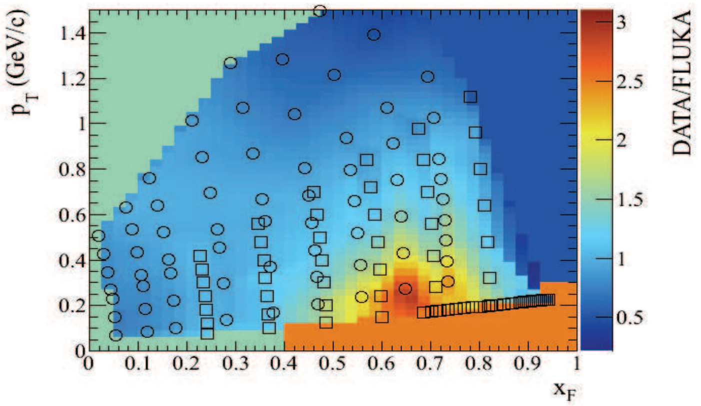

Figure 6.22: Ratio of secondary proton production calculated using the Eichten and Allaby data to FLUKA predictions in $\{x_F, p_T\}$. The ratio is used to evaluate the uncertainty of the flux. Outside the phase space of the data, a factor of 2.5, 1.5 and 0.5 for the regions colored by red, green and blue, respectively, are assigned based on the averaged difference between the data and FLUKA in the nearby relevant phase space. The position of the Eichten data points are shown by circles, and those from Allaby by squares. The figure is from [108].

Kaon multiplicity

The uncertainty on the calculation of charged kaon multiplicity is also evaluated by using the scaled experimental data by Eichten *et al.* from the 24 GeV/c proton interactions (see Figure 6.23). The size of the multiplicity uncertainty in each bin varies from 20% to 50%. For kaons produced outside the region covered by the Eichten data, the multiplicity uncertainty is assumed to be 50% [159].

Other contributions to the flux uncertainty

Other sources of uncertainties which contribute to the error on the neutrino flux are summarized below. They are mainly geometry related effects and are described in more details in [159].

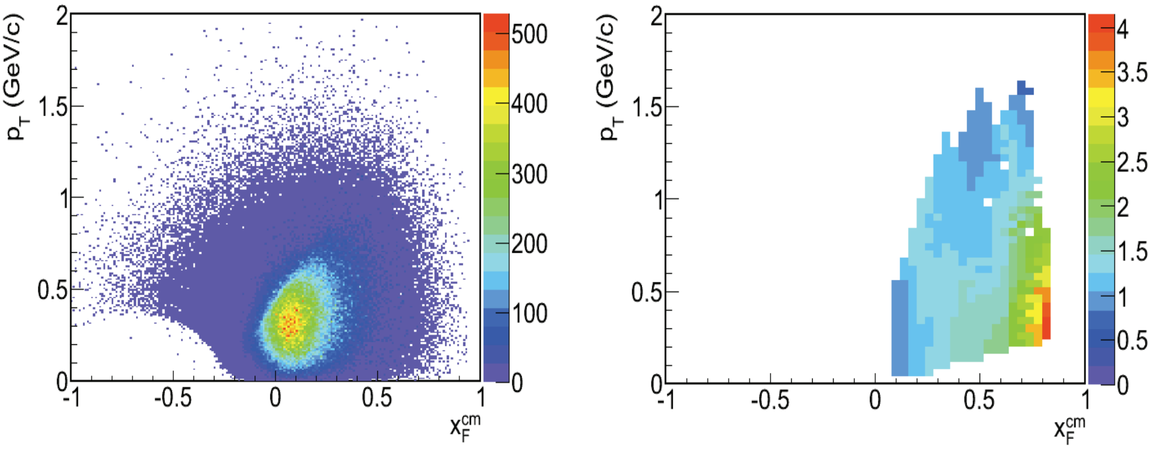

Figure 6.23: $\{x_F, p_T\}$ distribution of secondary K+ (left) whose descendant neutrinos go to SK and ratio of the Eichten data to FLUKA (right). The figures are from [159].

(i) Horn and target alignment: the survey of the focusing horns give an uncertainty of 1.0 mm in y and z (z is the direction of the beam) and 0.3 mm in x. The measured target tilt is 1.3 mrad in the horizontal direction and 0.1 mrad along the vertical axis. The impact of those misalignements were input in JNUBEAM and the corresponding error was propagated to the neutrino flux prediction.

(ii) Neutrino beam direction (off-axis angle): the uncertainty is mainly driven by the systematic error from the INGRID measurements (0.34 mrad in x and 0.38 mrad in y including the INGRID alignment error). This corresponds to 0.44 mrad uncertainty on the off-axis angle. The neutrino flux uncertainty due to the uncertainty of the off-axis angle is evaluated by looking at a variation of the neutrino flux when Super-K and the ND280 off-axis detector in JNUBEAM are moved by the amount corresponding to the off axis angle uncertainty.

(iii) Primary beam optics: the effects of the error on the flux arising from uncertainties associated with the primary proton beam parameters – position, angle, width, and divergence– were also studied. The inputs to JNUBEAM were changed according to the uncertainties given by the alignment and position uncertainties from the proton beam monitors.

(iv) Horn current: a 2% uncertainty on the horn current is input in the simulation. This value is adopted from the specs of the Rogowski coils which monitor the electrical current of the three magnetic horns combined with observation of the stability of the current throughout the data taking period.

Summary and total error on $N_{SK}^{\nu_e,exp}$

The summary of the errors contributing to the ν_μ and ν_e flux are presented in Figure 6.24. The main source of errors on the fluxes come from the uncertainties on pion and kaon multiplicities. For future T2K measurements, those errors will be reduced by the inclusion of the NA61/SHINE K^+ results, and re-calculation of the errors of the pions by taking into account bin to bin correlations of the NA61/SHINE systematic uncertainties. The NA61/SHINE 2009 results will also significantly contribute in the future through their lower statistical errors, reduced systematic uncertainties and increased $\{p, \theta\}$ coverage via the inclusion of the GTPC and the extension of the ToF-F. The large error on secondary nucleon production has a significant impact on both ν_μ and ν_e flux uncertainties. The errors will be reduced once the proton cross-sections are measured in NA61/SHINE.

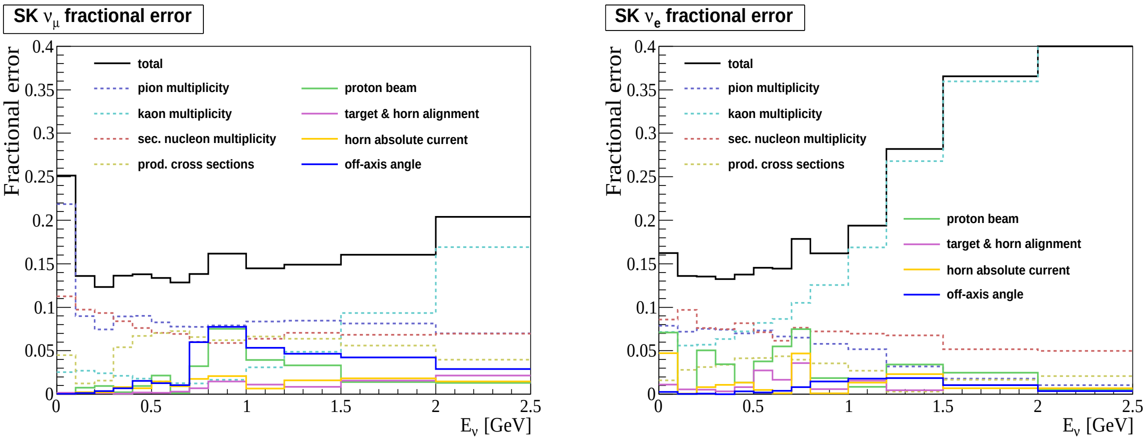

Figure 6.24: Fractional errors on the flux prediction at SK for the ν_μ (left) and ν_e (right) spectra. Kaon multiplicity dominate the high energy parts. These plots were generated with JNUBEAM using the NA61/SHINE pion data. This explains the low π^+ multiplicity error compared to that of the K^+. The figures are from [160].

Table 6.4 summarizes the uncertainties on the far to near ratio $N_{SK}^{\nu_e,exp}/ND$ and on the predicted number of events in SK, $N_{SK}^{\nu_e,exp}$, from various flux uncertainty sources. The total flux uncertainty contributes 14.9% to the far event rate, but the ratio has an 8.5% error due to cancellations. The total error is compared to the one obtained with the pion multiplicities derived from the preliminary NA61/SHINE results [161] for which a 20% systematic error in all $\{p, \theta\}$ bins was estimated. This demonstrates that reducing the systematic error on pion multiplicity from 20% to the one presented in this thesis ($\sim$ 5-10%), significantly improves the overall uncertainty on both the far-to-near ratio and predicted number of events in SK.

The uncertainty on the flux is compared with other sources of errors that contribute to the total systematic uncertainty on the number of expected ν_e events in SK. They are summarized in Table 6.5. The errors depend on the amplitude of the oscillation and thus on θ_{13}; they are shown for $\sin^2 2\theta_{13} = 0.1$ which is close to the best fit value. Neutrino interaction cross sections in the near and far detectors are simulated with the NEUT MC event generator [162] and are constrained with inclusive ν_μ CC measurement in the near detector. The cross sections at the T2K energies are poorly known and thus the errors on $N_{SK}^{\nu_e,exp}$ are mainly driven by the high uncertainties of the MC models, especially the modeling of the intranuclear final state interactions (FSI) and the knowledge of the $\sigma(\nu_e)/\sigma(\nu_\mu)$ ratio. The near detector ν_μ CC selection efficiency uncertainty yields $^{+5.6}_{-5.2}$% and the statistical uncertainty gives 2.7%. The uncertainties on the far detector measurements mainly come from the SK efficiencies and event selections.

The NA61/SHINE pion measurements alone have brought the systematic error on the F/N ratio down to a level that is similar to the other contributions. Once the kaon measurements are used the error will be further reduced. In the future, once we have included the proton

source	$N_{SK}^{\nu_e,exp}/ND$	$N_{SK}^{\nu_e,exp}$
Pion multiplicity	3.04 (9.10)%	6.06 (20)%
Tertiary pion scaling	0.13%	1.27%
Kaon multiplicity	7.3%	4.21%
Prod. cross-sections	2.54%	10.39%
Sec. nucleon multiplicity	0.87%	6.69%
Proton beam	1.39%	0.80%
Off-axis angle	0.56%	2.08%
Target alignment	0.31%	0.05%
Horn alignment	0.15%	0.42%
Horn current	0.63%	1.11%
Total	8.52 (12.10)%	14.9 (24.10)%

Table 6.4: The uncertainties on the number of expected ν_e signal+background events in SK ($N_{SK}^{\nu_e,exp}$) from various flux uncertainty sources using the published NA61/SHINE pion cross sections. The errors are shown in terms of the far to near ratio (left column) and number of events in SK (right column). The values in parenthesis indicate the errors on the pion multiplicity computed with the NA61/SHINE preliminary pion results for which 20% systematic error in all $\{p, \theta\}$ bins was estimated. The values are taken from [108].

cross-sections along with the results from the 2009 high statistics data set, there is little doubt that the goal of 2-3 % error on the F/N ratio (see Section 2.6) can be reached.

source	error
neutrino flux	±8.5%
near detector	$^{+5.6}_{-5.2}\%$
near detector stat.	±2.7%
cross-section	±10.5%
far detector	±9.4%
total ($\delta N_{SK}^{exp}/N_{SK}^{exp}$)	$^{+17.6}_{-17.5}\%$

Table 6.5: Contributions from various sources on the total relative uncertainty of N_{SK}^{exp} for $\sin^2 2\theta_{13} = 0.1$. The values are taken from [44].

Chapter 7

Conclusion

T2K is the first experiment to have provided evidence for $\nu_\mu \rightarrow \nu_e$ oscillation thus pointing to a non-zero value of θ_{13}. After the ν_τ signal at OPERA, T2K is also the only experiment to have observed an appearance signal caused by neutrino oscillation. Though it has been less mentioned in this thesis it has also published a precise measurement of ν_μ disappearance [163]. The obtained values of the atmospheric oscillation parameters are consistent with those reported by MINOS and Super-Kamiokande. Unfortunately, the experiment came to a brutal stop on March 11th 2011 at 14h46 JST when Japan was hit by one of its most powerful earthquake to date. As we are all aware of, the earthquake further triggered the tsunami and the events at the Fukushima power plant that lead to catastrophic human and material losses. Repair work on the experiment has been ongoing for just under a year and we expect to resume data taking in March of this year. The goal of T2K in those coming months is clear: increase the significance of the ν_e appearance measurement by taking more data and further reducing the systematic errors. To do so, further measurements at the near detector of the ν_μ CCQE and beam ν_e spectra are underway to better constrain the cross sections and neutrino flux predictions. From that latter perspective the contribution of NA61/SHINE has already been widely recognised.

The NA61/SHINE experiment started in 2007 and it was quickly evident that a new ToF was necessary for the measurements. We built it in the few months prior to the run and calibrated it shortly after. The information provided by the ToF-F then enabled us to extract the necessary yields with a high precision and consequently provide hadron-production cross-sections with low systematic uncertainties. Both analyses reported in this thesis were published and constitute the two first NA61/SHINE physics papers. The results also helped improve the precision of various Monte Carlo generators. The $tof\text{-}dE/dx$ PID method that was developed has also proved to be the most efficient way of identifying particles and will be the method of choice for future analyses.

Clearly now is the time to move to the analysis of the 2009 data. Work is currently ongoing in this direction and results are expected to be released soon. The goal is to produce pion and kaon but also proton production cross-sections with a lower systematic uncertainty than was reported for the 2007 data. As was stressed in the thesis, neutrinos from secondary protons account for a non negligible part of the flux. Since protons contributing to the flux through re-interactions in the target are mainly produced at high x_F low p_T, the GTPC must be used in the reconstruction to better cover this forward region. However, and this is one of the main limitations of the NA61 spectrometer for the T2K measurements, tracks emitted at low angles and high momenta remain on the verge of the acceptance and cannot be measured with high precision. In fact, it might not be possible to measure the region of biggest difference between the Eichten *et al* results and FLUKA predictions around $x_F \simeq 0.6$ and $p_T \simeq 0.2$ GeV/c (about 20 GeV/c momentum and 10 mrad polar angle) even with the GTPC included, unless we increase the magnetic field as was done for the 2010 long target run. All other regions of phase-space are however fully covered by NA61/SHINE with a high efficiency. The preliminary proton result which are reported in the last appendix of the thesis, even though they do not cover the very forward region, can certainly be used to improve the tuning of the T2K beam Monte Carlo while we wait for the final results from the larger 2009 data set. Finally, the updated results from the replica target analysis should be provided soon and may constitute the ultimate measurements since about $\sim$ 40% of the pions that contribute to the flux come from secondary interactions, including 30% from inside the target. At the moment the secondary interactions are modeled by parametrizations fitted to our published cross-sections. We have seen that this method suffers from high and difficult to estimate systematic uncertainties. Evidently, direct measurements off the replica target will allow much more precision.

With the remaining data that is left to be analysed, including that of the long target, I am confident that NA61/SHINE will further contribute to reduce the T2K systematic uncertainties and thus increase our knowledge of the last unknown neutrino mixing angle θ_{13}. With results or updates from other experiments such as Double-Chooz or Daya-Bay, which are likely to be presented at the Neutrino 2012 conference in June, we could have a $\theta_{13} \neq 0$ exclusion at 3 σ or even a more precise measurement of θ_{13} before the end of the year. Finally the possibility that θ_{13} is large is good news for future experiments such as NOνA as they may be able to measure the angle precisely rather than just setting a limit on it. It also opens the door for the next generation of experiments that will search for the parity violation parameter, δ_{CP}, and the mass-hierarchy.

Appendix A

Off-axis beam kinematics

The idea for an off-axis neutrino beam was first proposed by BNL experiment E889 [164]. In the following we consider that the produced beam of secondary pions is produced without divergence. In this case we can choose the z axis in the pion rest frame to coincide with the direction of the beam in the laboratory system and the problem reduces to a simple two-dimensional case. The 4-vector of the (massless) neutrino in the pion rest is then given by:

$$\mathbf{p}_\nu = (E_\nu^\star, E_\nu^\star \sin\theta^\star, 0, E_\nu^\star \cos\theta^\star) \tag{A.1}$$

Which can be transformed to the lab frame by applying a Lorentz boost:

$$\begin{aligned}\mathbf{p}_\nu^\star &= (E_\nu, E_\nu \sin\theta, 0, E_\nu \cos\theta) && \text{(A.2)}\\ &= (\gamma_\pi E_\nu^\star(1+\beta_\pi \cos\theta^\star), E_\nu^\star \sin\theta^\star, 0, \gamma_\pi E_\nu^\star(\beta_\pi + \cos\theta^\star)) && \text{(A.3)}\end{aligned}$$

where β_π is the pion velocity in the laboratory. From the second component we can deduce a relation for the angle θ between the neutrino and the pion direction in the laboratory frame as a function of the neutrino angle $\theta^\star$ in the pion rest frame:

$$\sin\theta = \frac{E_\nu^\star \sin\theta^\star}{E_\nu} \tag{A.4}$$

Since $\sin\theta^\star$ cannot exceed unity, this relation shows that a given neutrino energy E_ν can only be found up to a maximal laboratory angle:

$$\theta_{max}(E_\nu) = \arcsin\left(\frac{E_\nu}{E_\nu^\star}\right) \tag{A.5}$$

Which means that at a given angle θ from the beam direction, the maximum neutrino energy is:

$$E_\nu^{max}(\theta) = \frac{E_\nu^\star}{\sin\theta} \tag{A.6}$$

The effect of the off-axis beam configuration can be understood from Equation A.6. As can be seen in Figure A.1-left the neutrino energy depends linearly on the pion energy for an on-axis beam. As the neutrino energy approaches the value of E_ν^{max}, a large range of pion energies contributes to a small range of neutrino energies. This is also illustrated in Figure A.1-right, where a numerical simulation of the shape of the neutrino flux for different off-axis angle is shown. Note that to precisely simulate the effect of the shape of the neutrino flux, the Jacobian of the transformation between the pion and neutrino energy distribution $(E_\pi, \cos\theta) \to (E_\nu, \cos\theta)$ must be computed (see for example [106] or [165]).

In conclusion, as the off-axis angle increases, the neutrino energy spectrum becomes narrower and peaked at a lower energy. A broad-band pion beam can therefore be used to generate a narrow-band neutrino spectrum concentrated at the required energy.

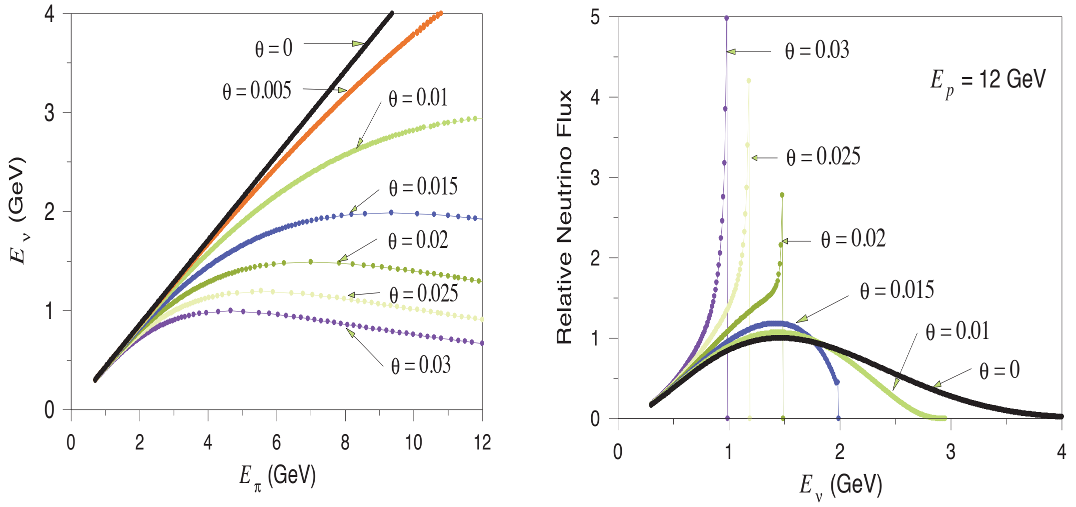

Figure A.1: Example of the off-axis beam properties (for 12 GeV incoming protons): neutrino energy as a function of the pion energy (left) and neutrino flux (right) for different values of the off-axis angle, θ (in degrees). Both plots are from [165].

Appendix B

ToF-F calibration parameters

Table B.1: Parameters from the ToF-F calibration. Each row refers to the channel number of the corresponding scintillator. The mean x coordinate, μ, and width, w, of the scintillators are given. dt corresponds to the TDC sampling of the channel, v to the fitted speed of light in the bar and $t0$ to the global time offset.

scintillator number	channel	μ [cm]	w [cm]	dt [ps]	$\lvert v \rvert$ [cm/ps $\times 10^{-3}$]	t_0 [ps]
1	1	342.86	4.78	24.6	15.7	509.2
1	2			24.6	16.3	-619.8
2	3	333.48	4.71	24.5	16.4	2254.1
2	4			24.5	15.4	-691.6
3	5	324.46	4.36	24.7	15.7	-2192.4
3	6			24.7	16.4	2020.9
4	7	315.51	4.63	24.3	17.8	-1668.2
4	8			24.3	15.0	-1754.3
5	9	306.5	4.42	24.2	16.3	466.5
5	10			24.2	15.1	2875.6
6	11	297.59	4.67	24.4	16.1	-379.3
6	12			24.4	15.7	430.6
7	13	288.68	4.28	24.5	15.5	881.2
7	14			24.5	15.4	-2088.7
8	15	280.25	4.15	25.2	15.2	-561.8
8	16			25.2	15.9	1789.3
9	17	271.39	4.51	25.0	16.7	21146.8
9	18			25.0	16.4	-117.6
10	19	262.02	4.55	24.2	15.8	-1741.8
10	20			24.2	15.8	-769.4
11	21	253	4.49	24.5	15.4	-4259.7
11	22			24.5	15.6	-1219.3
12	23	244.4	4.44	25.4	15.3	-4989.2

Continued on next page

Table B.1: Parameters from the ToF-F calibration. Each row refers to the channel number of the corresponding scintillator. The mean x coordinate, μ, and width, w, of the scintillators are given. dt corresponds to the TDC sampling of the channel, v to the fitted speed of light in the bar and $t0$ to the global time offset.

scintillator number	channel	μ [cm]	w [cm]	dt [ps]	$\|v\|$ [cm/ps $\times 10^{-3}$]	t_0 [ps]
12	24			25.4	16.1	-1360.4
13	25	235.47	4.61	25.4	14.9	-743.8
13	26			25.4	16.0	-1450.9
14	27	226.39	4.76	25.9	15.1	-3508.1
14	28			25.9	15.8	-3401.0
15	29	217.39	4.18	26.3	15.5	-5892.9
15	30			26.3	15.5	-4489.4
16	31	208.73	4.55	25.2	15.3	-2849.0
16	32			25.2	15.3	-2889.3
17	33	199.65	4.57	25.0	15.6	-2540.8
17	34			25.0	15.8	2593.3
18	35	190.74	4.46	25.1	15.9	-2379.8
18	36			25.1	15.8	17.2
19	37	181.84	4.42	24.7	15.6	847.1
19	38			24.7	15.5	-1225.2
20	39	172.8	4.66	24.4	15.7	330.1
20	40			24.4	15.3	-2681.1
21	41	163.82	4.3	25.8	15.4	513.3
21	42			25.8	15.6	-1324.0
22	43	154.96	4.48	23.9	15.5	-390.0
22	44			23.9	15.9	930.6
23	45	146.02	4.52	23.7	15.3	-2253.9
23	46			23.7	15.7	-2170.4
24	47	137.2	4.7	25.1	15.8	-1321.6
24	48			25.1	15.6	386.7
25	49	128.17	4.66	24.7	15.7	-987.4
25	50			24.7	15.4	-1074.0
26	51	119.5	4.39	25.3	15.4	-978.1
26	52			25.3	15.6	-3440.4
27	53	110.58	4.47	25.4	15.6	-2433.7
27	54			25.4	15.8	-703.6
28	55	101.41	4.47	24.3	15.4	-1456.2
28	56			24.3	15.6	-1141.3
29	57	92.57	4.35	24.5	15.4	-2008.1
29	58			24.5	15.7	-2005.6
30	59	83.69	4.48	25.4	15.7	-4641.1
30	60			25.4	15.8	-1280.5

Continued on next page

Table B.1: Parameters from the ToF-F calibration. Each row refers to the channel number of the corresponding scintillator. The mean x coordinate, μ, and width, w, of the scintillators are given. dt corresponds to the TDC sampling of the channel, v to the fitted speed of light in the bar and $t0$ to the global time offset.

scintillator number	channel	μ [cm]	w [cm]	dt [ps]	$\lvert v \rvert$ [cm/ps $\times 10^{-3}$]	t_0 [ps]
31	61	74.81	4.39	24.5	15.5	-717.3
31	62			24.5	15.5	-734.3
32	63	65.87	4.57	24.8	15.5	-1006.0
32	64			24.8	15.8	-3251.4
33	65	57.04	4.21	23.5	15.8	5300.9
33	66			23.5	15.6	4107.9
34	67	47.98	4.52	25.0	15.9	7293.0
34	68			25.0	15.6	6434.4
35	69	39.48	3.98	25.0	15.7	4502.1
35	70			25.0	16.1	5769.5
36	71	30.85	3.92	23.5	15.8	3339.2
36	72			23.5	16.0	2759.2
37	73	24.91	2.32	24.7	16.4	4988.7
37	74			24.7	16.6	4804.5
38	75	13.99	4.83	25.7	16.4	3626.9
38	76			25.7	16.9	5822.9
39	77	4.21	5.39	24.9	18.0	5796.9
39	78			24.9	17.7	2923.0
40	79	-5.67	4.46	24.9	17.6	6308.1
40	80			24.9	18.3	4946.9
41	81	-14.58	4.13	25.0	16.7	1678.3
41	82			25.0	16.7	4133.8
42	83	-24.11	3.72	24.5	16.3	2901.2
42	84			24.5	16.4	2945.6
43	85	-32.09	4.41	25.8	15.7	6027.8
43	86			25.8	16.0	1638.3
44	87	-40.9	4.42	24.9	15.4	4169.7
44	88			24.9	15.9	4248.4
45	89	-49.68	4.51	25.6	15.2	3699.4
45	90			25.6	16.1	372.2
46	91	-58.75	4.41	24.9	15.4	7744.2
46	92			24.9	15.5	4236.3
47	93	-67.63	4.98	24.8	15.5	3296.1
47	94			24.8	15.4	4433.9
48	95	-76.33	4.31	25.4	15.2	5639.1
48	96			25.4	15.3	4070.3
49	97	-85.48	4.39	25.2	15.3	7183.4

Continued on next page

Table B.1: Parameters from the ToF-F calibration. Each row refers to the channel number of the corresponding scintillator. The mean x coordinate, μ, and width, w, of the scintillators are given. dt corresponds to the TDC sampling of the channel, v to the fitted speed of light in the bar and $t0$ to the global time offset.

scintillator number	channel	μ [cm]	w [cm]	dt [ps]	$\|v\|$ [cm/ps $\times 10^{-3}$]	t_0 [ps]
49	98			25.2	15.7	9446.0
50	99	-94.12	4.34	24.7	15.2	5321.5
50	100			24.7	15.7	7480.7
51	101	-102.95	4.61	24.7	15.3	7659.1
51	102			24.7	15.6	7942.3
52	103	-112.16	4.61	25.0	15.6	3221.8
52	104			25.0	15.8	2813.3
53	105	-120.9	4.46	25.2	15.4	6116.0
53	106			25.2	15.3	9347.2
54	107	-129.68	4.21	24.2	15.6	7554.1
54	108			24.2	15.7	6722.0
55	109	-138.36	4.49	26.0	15.3	7790.6
55	110			26.0	16.5	49057.6
56	111	-147.57	4.67	24.8	15.4	5511.2
56	112			24.8	15.8	6505.4
57	113	-156.55	4.37	24.2	15.4	2185.0
57	114			24.2	15.0	3246.5
58	115	-165.27	4.11	24.9	15.3	3580.0
58	116			24.9	15.6	4454.6
59	117	-174	-4.5	25.0	14.8	914.5
59	118			25.0	15.6	2767.3
60	119	-182.75	4.5	25.4	15.7	4167.4
60	120			25.4	15.5	760.7
61	121	-191.88	4.44	25.4	15.1	3637.6
61	122			25.4	15.8	-859.0
62	123	-200.87	4.55	25.1	15.7	3237.7
62	124			25.1	15.4	1042.6
63	125	-210.25	4.81	24.1	15.3	3470.3
63	126			24.1	16.0	1062.1
64	127	-217.58	-0.32	24.1	15.5	2627.4
64	128			24.1	15.5	-1657.8
65	129	-227.77	4.18	25.1	15.1	8766.6
65	130			25.1	15.9	11345.9
66	131	-236.54	4.57	24.6	15.8	8699.0
66	132			24.6	15.3	8839.5
67	133	-246.3	5.22	23.9	15.5	7883.7
67	134			23.9	15.5	8638.0

Continued on next page

Table B.1: Parameters from the ToF-F calibration. Each row refers to the channel number of the corresponding scintillator. The mean x coordinate, μ, and width, w, of the scintillators are given. dt corresponds to the TDC sampling of the channel, v to the fitted speed of light in the bar and $t0$ to the global time offset.

scintillator number	channel	μ [cm]	w [cm]	dt [ps]	$\|v\|$ [cm/ps $\times 10^{-3}$]	t_0 [ps]
68	135	-255.8	4.3	24.5	15.3	5652.1
68	136			24.5	15.9	8264.1
69	137	-262.75	-2.74	25.2	15.2	6177.9
69	138			25.2	15.8	9287.5
70	139	-272.11	4.9	25.7	15.8	-4928.8
70	140			25.7	15.6	7166.8
71	141	-282.05	5.18	24.3	15.2	10648.0
71	142			24.3	15.4	10937.5
72	143	-290.64	3.12	25.1	15.8	2500.2
72	144			25.1	15.4	-10038.3
73	145	-299.37	4.41	24.4	15.0	6866.9
73	146			24.4	15.8	6479.8
74	147	-308.72	4.85	24.8	16.0	3857.3
74	148			24.8	15.5	1927.1
75	149	-317.02	3.51	24.9	15.2	3765.2
75	150			24.9	16.4	512.6
76	151	-325.47	4.68	24.3	16.5	1990.4
76	152			24.3	15.3	-24205.9
77	153	-335.05	4.35	25.5	15.5	4149.4
77	154			25.5	15.6	1749.3
78	155	-343.75	4.57	24.4	14.9	2389.6
78	156			24.4	16.7	2552.3
79	157	-353.44	4.89	24.5	15.1	3038.7
79	158			24.5	16.0	4729.1
80	159	-353.44	4.89	25.7	15.2	2707.5
80	160			25.7	15.4	2815.6

Appendix C

Kink angle for pion and kaon decay

This appendix gives the maximum value of the angle θ between the parent and daughter muon in the laboratory frame (kink angle) for $\pi \rightarrow \nu\mu$ decay (99.9% BR) and $K \rightarrow \nu\mu$ decay (63.5% BR).

Since exactly the same procedure applies for both decays, we first consider the case $\pi \rightarrow \nu\mu$. In the rest frame of the pion (in which quantities will be labeled with the superscript *), the energy momentum conservation can be written as the 4-vector relation:

$$\mathbf{p}_\nu = \mathbf{p}_\pi - \mathbf{p}_\mu \tag{C.1}$$

which squared, gives:

$$m_\nu^2 = m_\pi^2 + m_\mu^2 - 2\mathbf{p}_\pi \cdot \mathbf{p}_\mu \tag{C.2}$$

In the pion rest frame, its 4-vector is:

$$\mathbf{p}_\pi^\star = (m_\pi, 0, 0, 0)) \tag{C.3}$$

and taking the z axis to be the direction of the pion in the lab frame, the 4-vector of the muon in the pion rest frame can be written as:

$$\mathbf{p}_\mu^\star = \left(E_\mu^\star, p_\mu^\star \sin\theta^\star, 0, p_\mu^\star \cos\theta^\star\right) \tag{C.4}$$

The double product from Equation C.2 is therefore:

$$\mathbf{p}_\pi \cdot \mathbf{p}_\mu = m_\pi E_\mu^\star \tag{C.5}$$

Hence from Equation C.2 the energy of the muon in the pion rest frame is (neglecting the neutrino mass):

$$E_\mu^\star = \frac{m_\pi^2 + m_\mu^2}{2m_\pi} \simeq 109.7 \text{ MeV} \tag{C.6}$$

equivalent to momentum

$$p_\mu^\star \simeq 30 \text{ MeV} \quad \text{(pion decay)} \tag{C.7}$$

For the two body kaon decay, by simply replacing the pion mass in Equation C.6 we get the muon momentum in the kaon rest frame:

$$p^{\star}_{\mu} \simeq 236 \text{ MeV} \quad \text{(kaon decay)} \tag{C.8}$$

To get the kink angle we must express the muon 4-vector (C.4) in the laboratory frame using the Lorentz boost:

$$\begin{aligned} \mathbf{p}_{\mu} &= (E_{\mu}, p_{\mu}\sin\theta, 0, p_{\mu}\cos\theta) && \text{(C.9)} \\ &= \left(\gamma_{\pi}E^{\star}_{\mu} + \beta_{\pi}\gamma_{\pi}p^{\star}_{\mu}\cos\theta^{\star}, p^{\star}_{\mu}\sin\theta^{\star}, 0, \beta_{\pi}\gamma_{\pi}E^{\star}_{\mu} + \gamma_{\pi}p^{\star}_{\mu}\cos\theta^{\star}\right) && \text{(C.10)} \end{aligned}$$

The pion and kaon have spin zero, so the decay is isotropic in the pion rest frame. A relation for the angle between the muon and its parent can be obtained from the first and third components of Equation C.10:

$$\tan\theta = \frac{p^{\star}_{\mu}\sin\theta^{\star}}{\beta_{\pi}\gamma_{\pi}E^{\star}_{\mu} + \gamma_{\pi}p^{\star}_{\mu}\cos\theta^{\star}} \tag{C.11}$$

equivalent to a maximum angle of :

$$\tan\theta_{max} = \frac{p^{\star}_{\mu}}{\gamma_{\pi}E^{\star}_{\mu}\sqrt{\beta^2_{\pi} - p^{\star 2}_{\mu}/E^{\star 2}_{\mu}}} \tag{C.12}$$

Hence for a given momentum the angle between the parent and the daughter in the lab will be a lot higher for a kaon than for a pion, because of their different $p^{\star}_{\mu}$ values. This is illustrated in Figure C.1 where the two θ_{max} curves are plotted as function of the parent momentum.

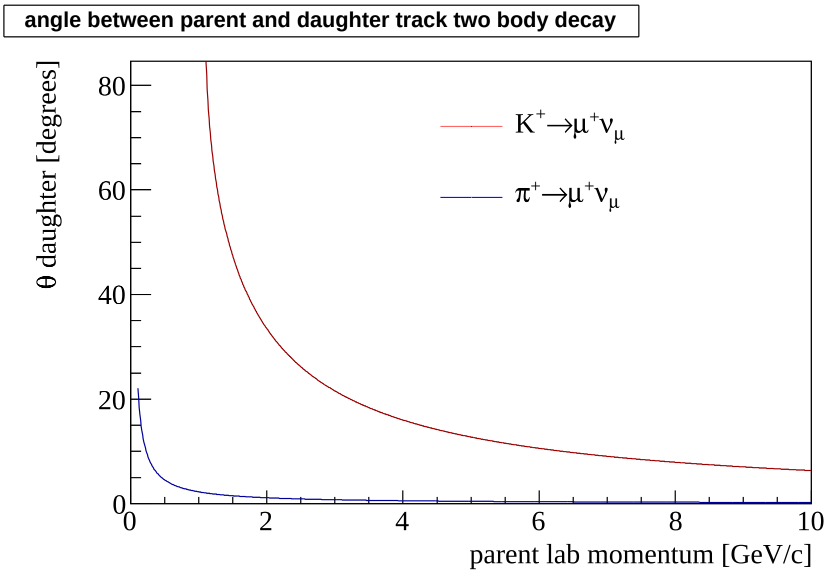

Figure C.1: Maximum lab kink angle for a pion and kaon two body decay as a function of parent momentum.

Appendix D

Goodness of fit for Poisson distributed data

When a fit to binned data is performed, the goodness of fit for bins with large number of entries is traditionally evaluated with the Pearson χ^2:

$$\chi^2_P = \frac{(n_i - y_i)^2}{y_i} \tag{D.1}$$

where y_i are the numbers of events predicted by the fitted hypothesis and n_i the true number of events in bin number i. It assumes that the predicted values y_i (the test statistic) are Gaussian-like distributed in the bins. This is correct if the bins have large number of entries. In our situation however, when the mean number of events in a typical bin is about 10 or smaller, the test statistic is instead Poisson like distributed. The Poisson distribution for n events in a bin, given a mean of y, is:

$$f(y;n) = \frac{y^n e^{-y}}{n!} \tag{D.2}$$

When fitting models to binned data, we select a model which predicts y for each bin (in our case the model is a bi-dimensional Gaussian), and we choose the model which maximizes the likelihood function $L(y;n)$ defined as the product over all N bins of the Poisson distribution:

$$\begin{aligned} L(y;n) &= \textstyle\prod_i^N f(y;n) \\ &= \textstyle\prod_i^N \frac{y_i^{n_i} e^{-y_i}}{n_i!} \end{aligned} \tag{D.3}$$

The product is generally turned into a sum by using the log of the Likelihood function [166]:

$$\begin{aligned} \ln L(y;n) &= \sum_i^N n_i \ln y_i - y_i - \ln n_i! \\ &= \sum_i^N n_i \ln y_i - y_i - \ln \Gamma(n_i + 1) \end{aligned} \tag{D.4}$$

Since it can be tedious to compute $n_i!$, the Γ function ($\Gamma(x) = \int_0^\infty \mathrm{d}y e^{-y} y^{x-1} \mathrm{d}x$ where $n! = \Gamma(n+1)$) is used instead during the fitting procedure.

The goodness of fit test is then performed using the likelihood ratio, λ defined as:

$$\lambda = \frac{L(y;n)}{L(m;n)} \tag{D.5}$$

where m is the true (unknown value) of n that one would get in a given bin if there were no errors and y the value of our hypothesis. The likelihood ratio test theorem states that the Likelihood χ^2 (or Poisson Likelihood) defined as:

$$\begin{aligned} \chi^2_\lambda &= -2\ln(\lambda) \\ &= -2\ln L(y;n) + 2\ln L(m;n) \end{aligned} \tag{D.6}$$

asymptotically obeys a χ^2 distribution [167]. The second term is independent of y and hence, for the fit, it is equivalent to maximise the likelihood function $L(y,n)$ of D.3 or to minimise χ^2_λ. This is why, in addition to give a goodness of fit estimation, χ^2_λ can also be used for the estimation of parameters (i.e for the fitting procedure).

The true values m of D.6 are those that maximize the Poisson likelihood for the observed numbers of events n:

$$\frac{\partial L(m;n)}{\partial m} = \frac{\partial n \ln m - m - \ln n!}{\partial m} = \frac{n}{m} - 1 \tag{D.7}$$

which equals 0 for the condition $m = n$. Thus, replacing m by n in Equation D.6 and using Equation D.4 one gets the following expression for the Poisson likelihood, χ^2_λ (see also appendix of [167]):

$$\chi^2_\lambda = 2\sum_{i=1}^{N} y_i - n_i + n_i \ln\frac{n_i}{y_i} \tag{D.8}$$

This is the quantity used to estimate the level of agreement between the hypothesis at its best fit value y_i and the data n_i. Since χ^2_λ asymptotically follows a χ^2 p.d.f, it can be used to compute a p-value for the fit. The p-value, p, for the hypothesis is given by:

$$p = \int_{\chi^2_\lambda}^{\infty} f(z;ndf)\mathrm{d}z \tag{D.9}$$

where $f(z;ndf)$ is the χ^2 p.d.f for a given number of degrees of freedom (ndf). The later is defined as the number of measurements minus the number of fitted parameters. The p-value denotes the probability that an observed Chi-squared exceeds the input χ^2_λ value by chance, even for a correct model. If our model accurately reproduces the data distribution, the χ^2_λ/ndf should be close to unity and the corresponding p-value should be uniformly distributed between 0 and 1.

Appendix E

Kaon fits

Figure E.1: Bi-dimensional fits to the $m^2 - dE/dx$ distribution of all bins present in the kaon analysis. The functions are drawn with the 2, 1.5 and 1 σ contours around the fitted kaon peak. The m^2 and dE/dx projections are also shown superimposed with the results of the fitted functions.

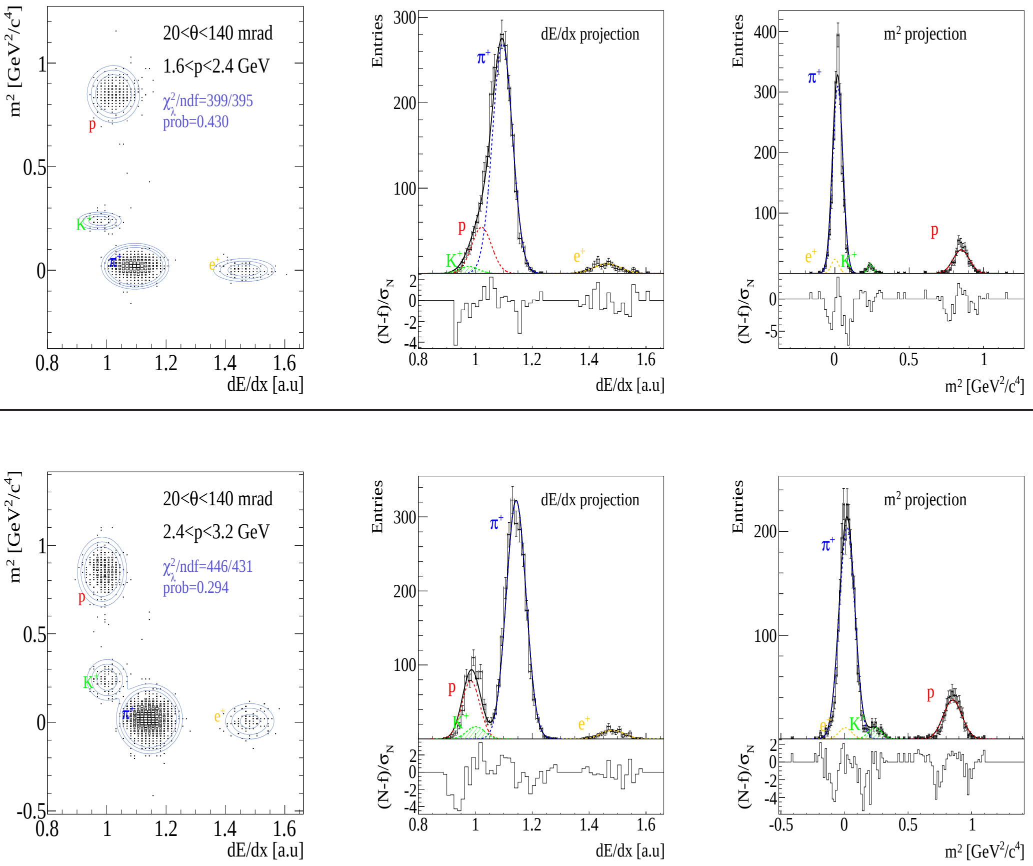

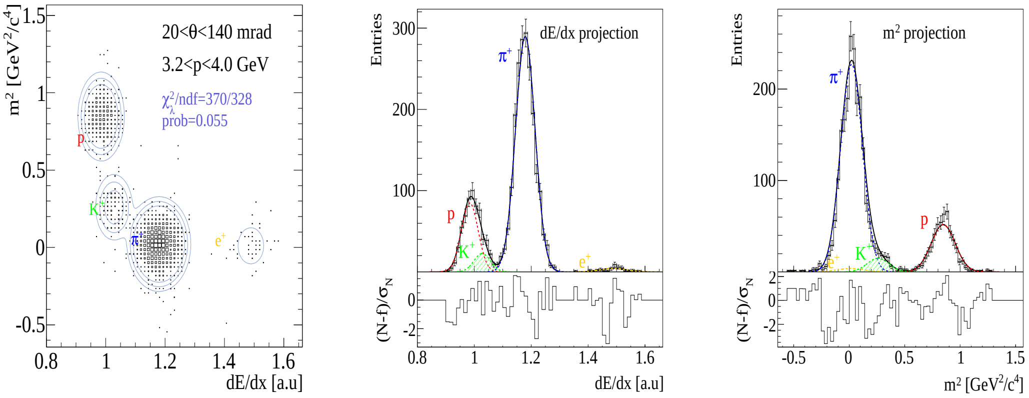
20<θ<140 mrad
3.2<p<4.0 GeV
χ^2_λ/ndf=370/328
prob=0.055
p
K+
π+
e+
m² [GeV²/c⁴]
dE/dx [a.u]
dE/dx projection
Entries
(N-f)/σN
m² projection

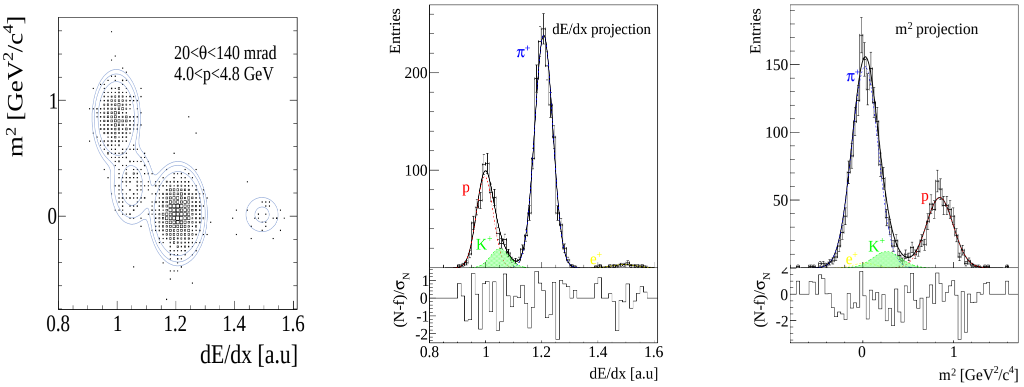
20<θ<140 mrad
4.0<p<4.8 GeV
m² [GeV²/c⁴]
dE/dx [a.u]
dE/dx projection
Entries
(N-f)/σN
m² projection
p
K+
π+
e+

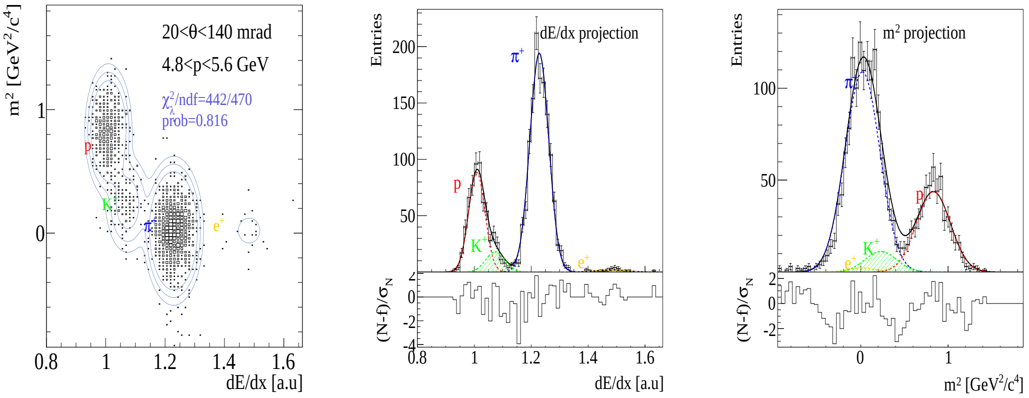
20<θ<140 mrad
4.8<p<5.6 GeV
χ^2_λ/ndf=442/470
prob=0.816
p
K+
π+
e+
m² [GeV²/c⁴]
dE/dx [a.u]
dE/dx projection
Entries
(N-f)/σN
m² projection

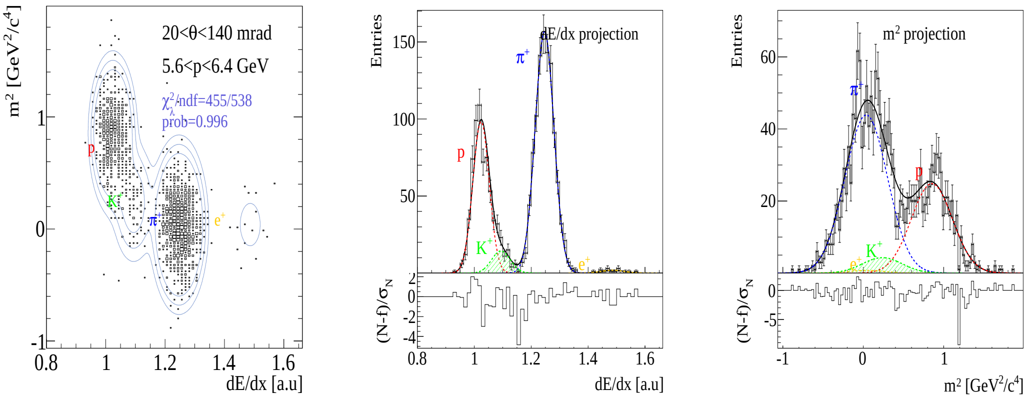
20<θ<140 mrad
5.6<p<6.4 GeV
χ^2_λ/ndf=455/538
prob=0.996
p
K+
π+
e+
m² [GeV²/c⁴]
dE/dx [a.u]
0.8
1
1.2
1.4
1.6
-1
0
1
dE/dx projection
Entries
150
100
50
(N-f)/σN
2
0
-2
-4
m² projection
60
40
20
-5
m² [GeV²/c⁴]

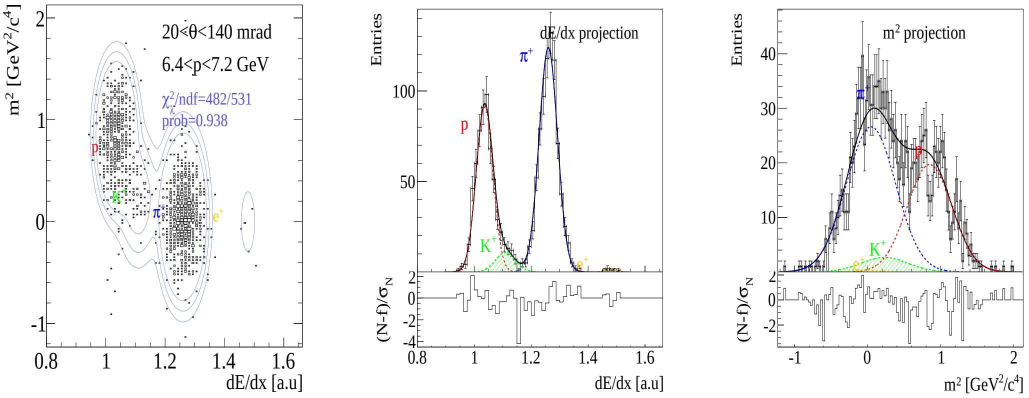
20<θ<140 mrad
6.4<p<7.2 GeV
χ^2_λ/ndf=482/531
prob=0.938
p
K+
π+
e+
m² [GeV²/c⁴]
dE/dx [a.u]
0.8
1
1.2
1.4
1.6
-1
0
1
2
dE/dx projection
Entries
100
50
(N-f)/σN
2
0
-2
-4
m² projection
40
30
20
10
m² [GeV²/c⁴]

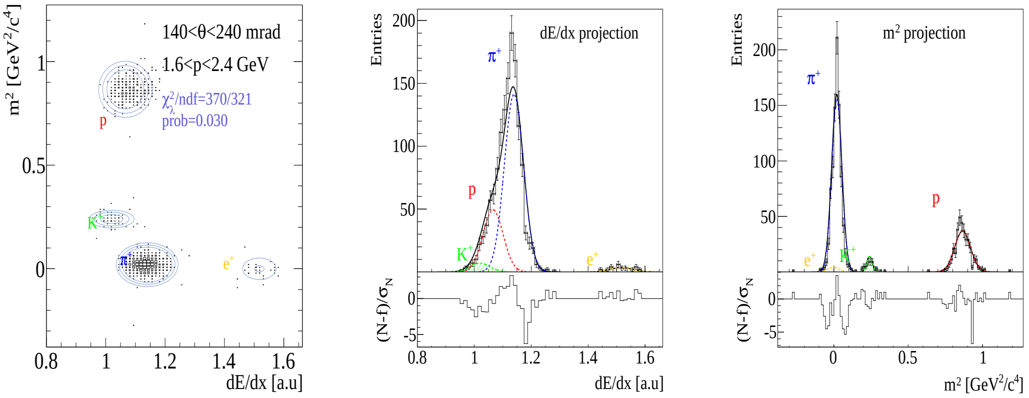
140<θ<240 mrad
1.6<p<2.4 GeV
χ^2_λ/ndf=370/321
prob=0.030
m² [GeV²/c⁴]
dE/dx [a.u]
p
K⁺
π⁺
e⁺
Entries
dE/dx projection
m² projection
(N-f)/σ_N
m² [GeV²/c⁴]

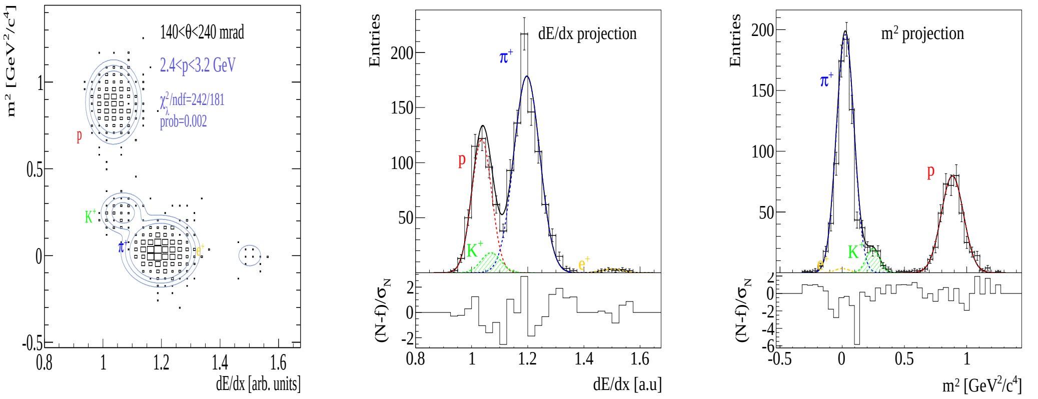
140<θ<240 mrad
2.4<p<3.2 GeV
χ^2_λ/ndf=242/181
prob=0.002
m² [GeV²/c⁴]
dE/dx [arb. units]
p
K⁺
π⁺
e⁺
Entries
dE/dx projection
m² projection
(N-f)/σ_N
dE/dx [a.u]
m² [GeV²/c⁴]

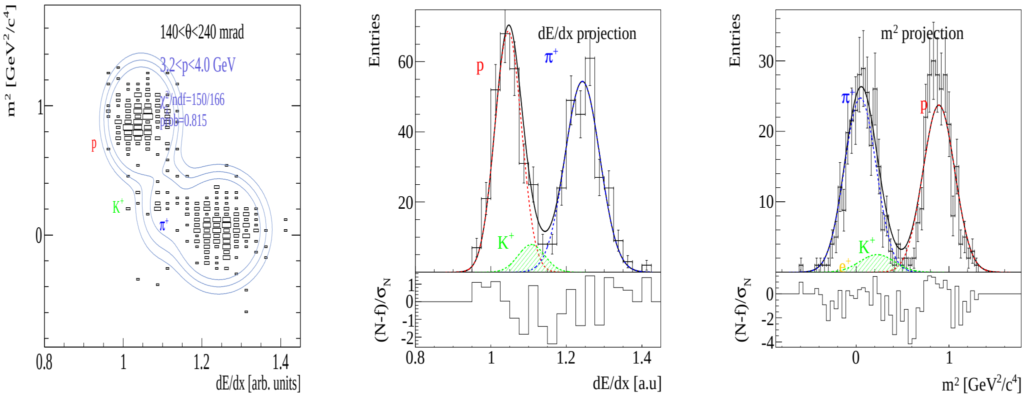
140<θ<240 mrad
3.2<p<4.0 GeV
χ^2_λ/ndf=150/166
prob=0.815
m² [GeV²/c⁴]
dE/dx [arb. units]
p
K⁺
π⁺
e⁺
Entries
dE/dx projection
m² projection
(N-f)/σ_N
dE/dx [a.u]
m² [GeV²/c⁴]

Appendix F

Pion correction factors

Figure F.1: Momentum dependence of the inverse correction factors, for positively charged pions. ϵ_{rec} and ϵ_{ToF} are the efficiencies of the reconstruction and of the ToF-F, respectively. The feed-down correction accounts for pions from weak decays which are reconstructed as primary particles.

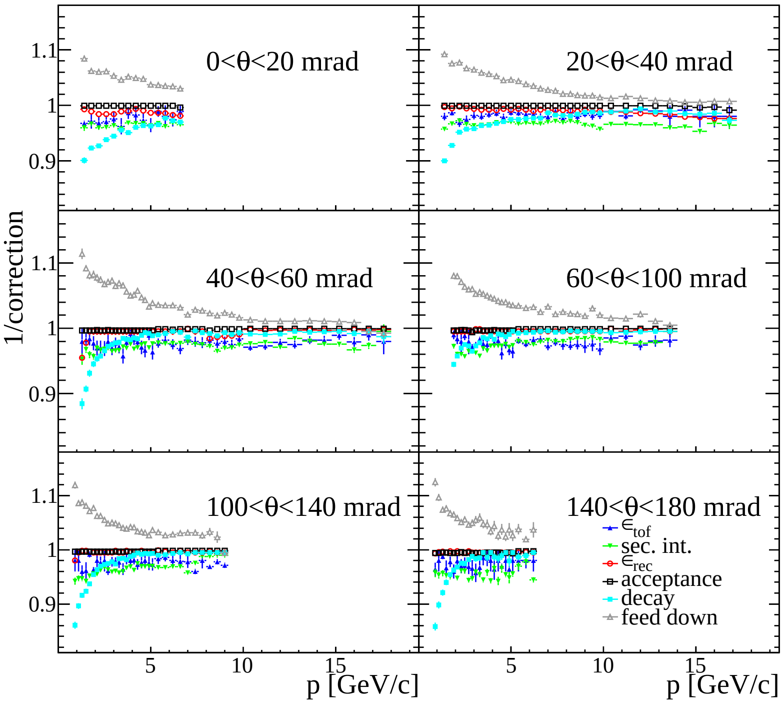

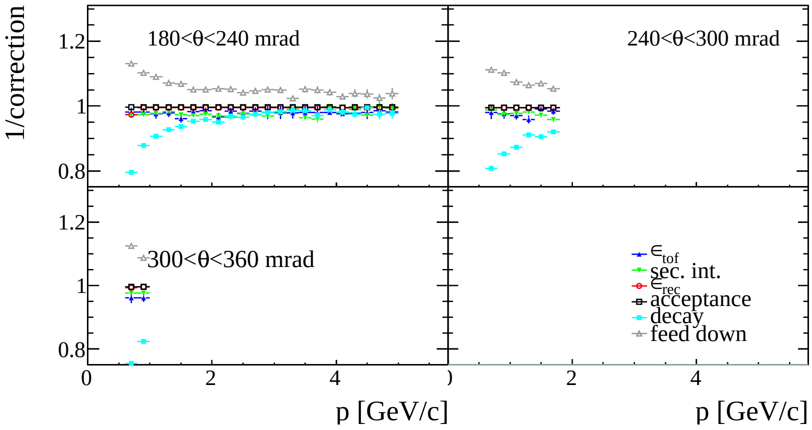

Figure F.2: Momentum dependence of the inverse correction factors, for negatively charged pions. ϵ_{rec} and ϵ_{ToF} are the efficiencies of the reconstruction and of the ToF-F, respectively. The feed-down correction accounts for pions from weak decays which are reconstructed as primary particles.

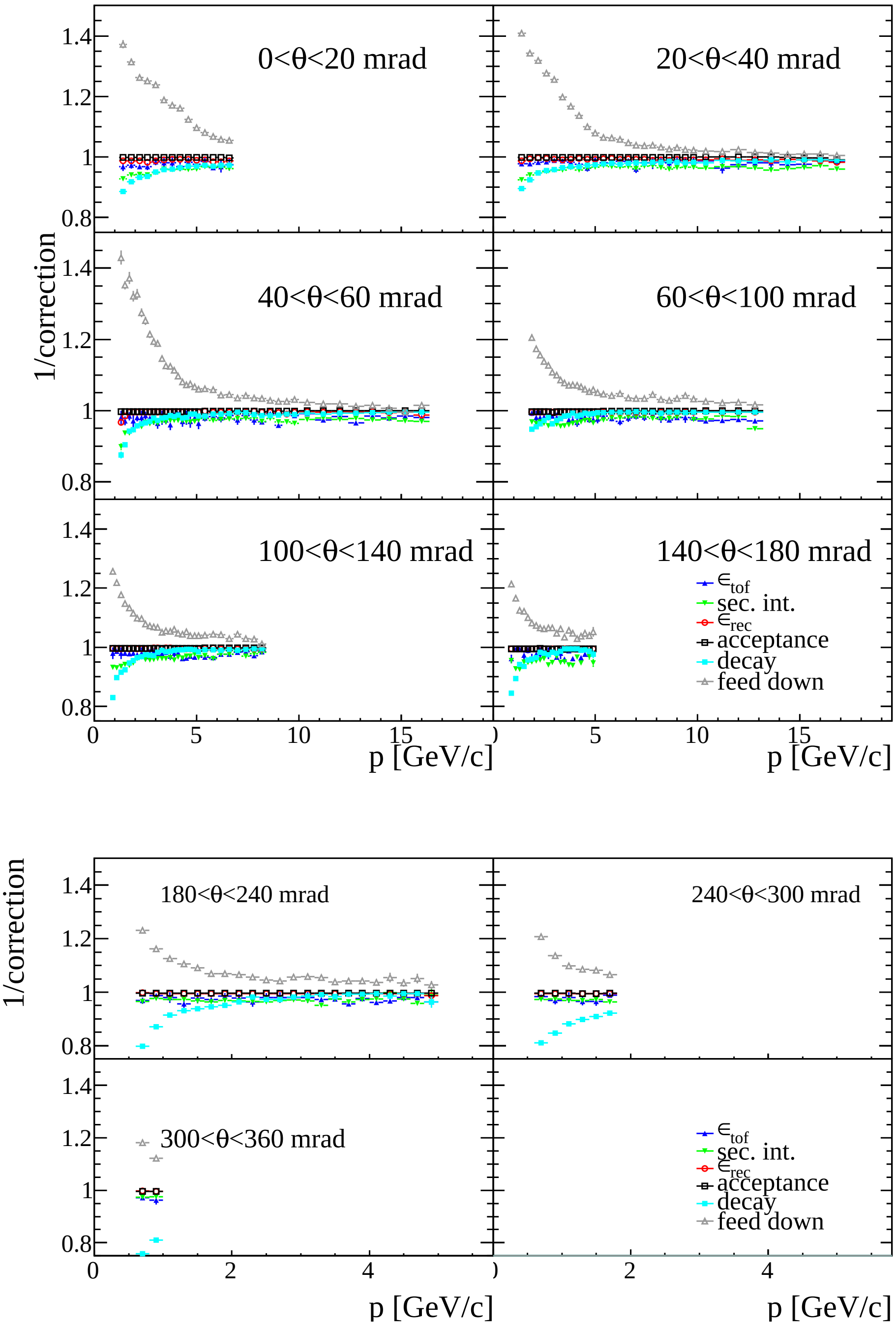

Appendix G

Pion systematic and statistical uncertainties

Figure G.1: Breakdown of systematic errors as a function of momentum for positively charged pions. ϵ_{rec} and ϵ_{ToF} are the efficiencies of the reconstruction and of the ToF-F, respectively. The feed-down correction accounts for pions from weak decays which are reconstructed as primary particles.

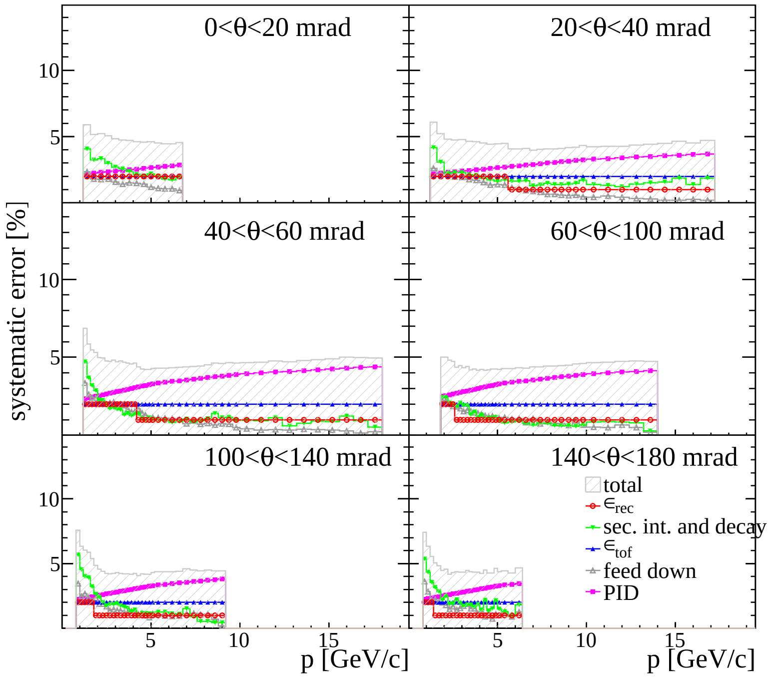

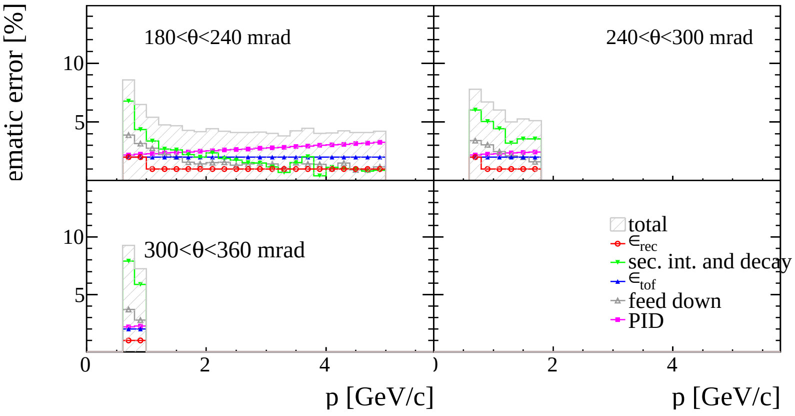

Figure G.2: Breakdown of systematic errors as a function of momentum for negatively charged pions. ϵ_{rec} and ϵ_{ToF} are the efficiencies of the reconstruction and of the ToF-F, respectively. The feed-down correction accounts for pions from weak decays which are reconstructed as primary particles.

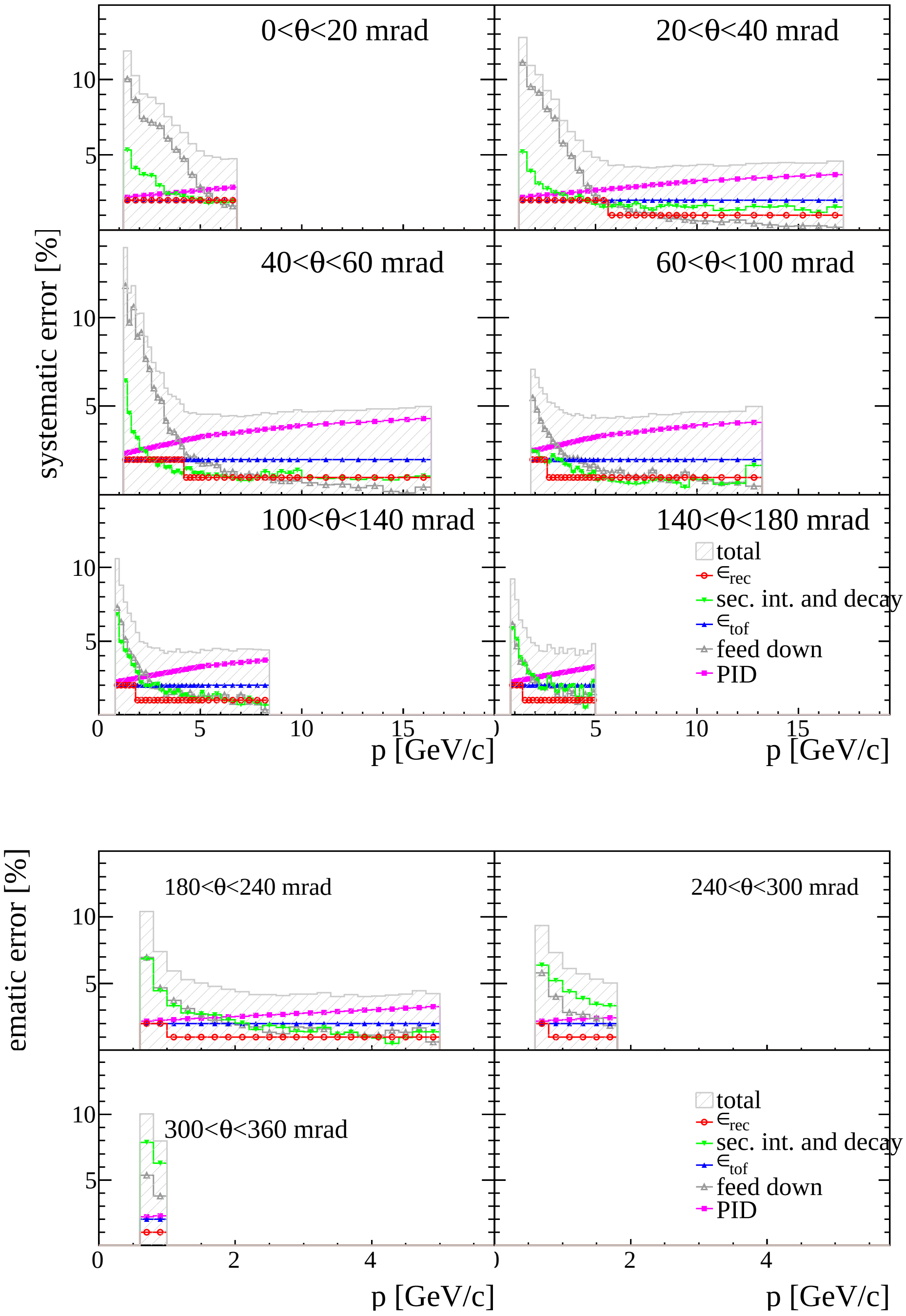

Figure G.3: Relative uncertainties on the π^+cross sections shown in Figure G.1 . Statistical, systematic and total uncertainties are indicated. The overall uncertainty due to the normalization procedure is not shown.

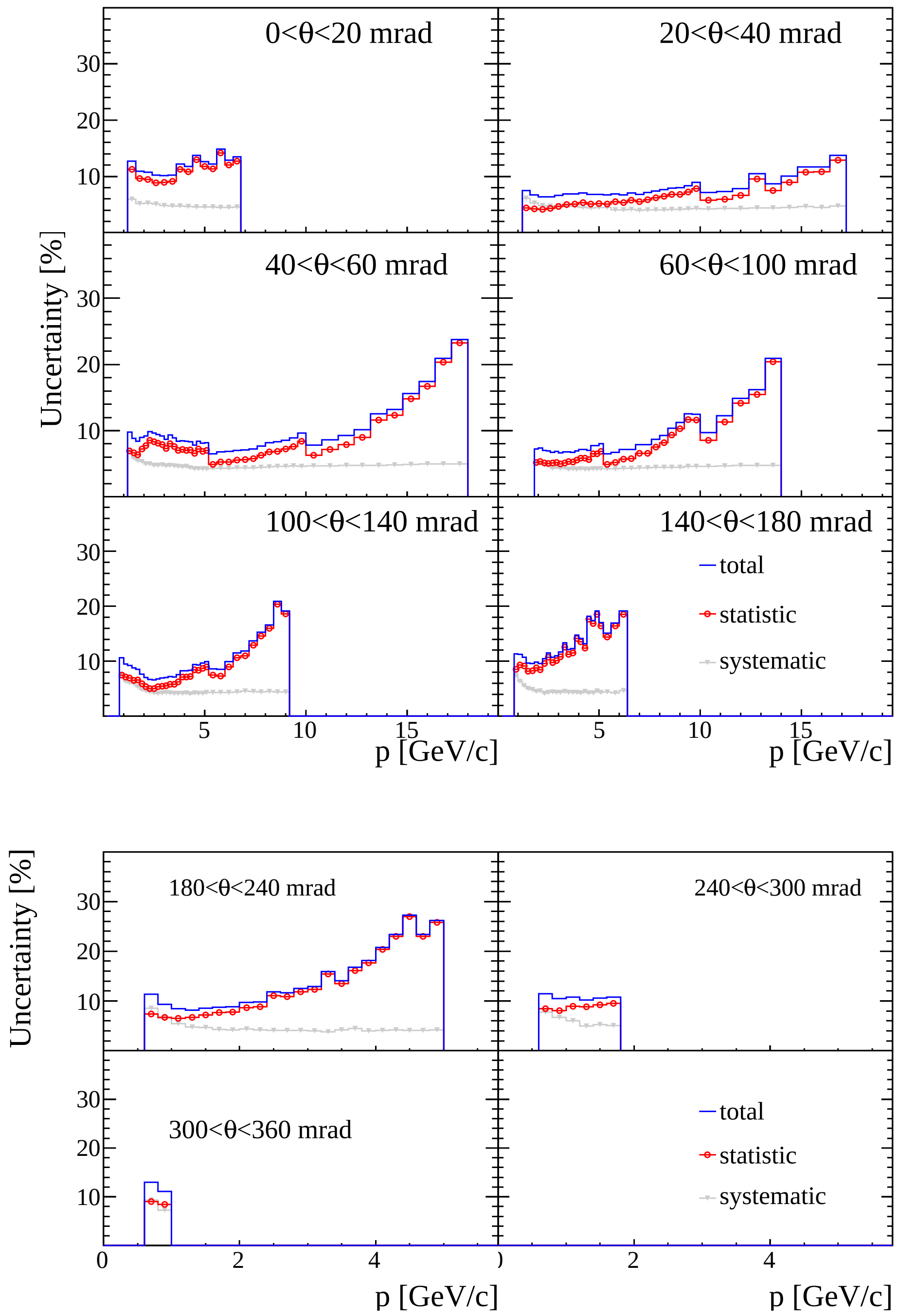

Figure G.4: Relative uncertainties on the π^-cross sections shown in Figure G.2 . Statistical, systematic and total uncertainties are indicated. The overall uncertainty due to the normalization procedure is not shown.

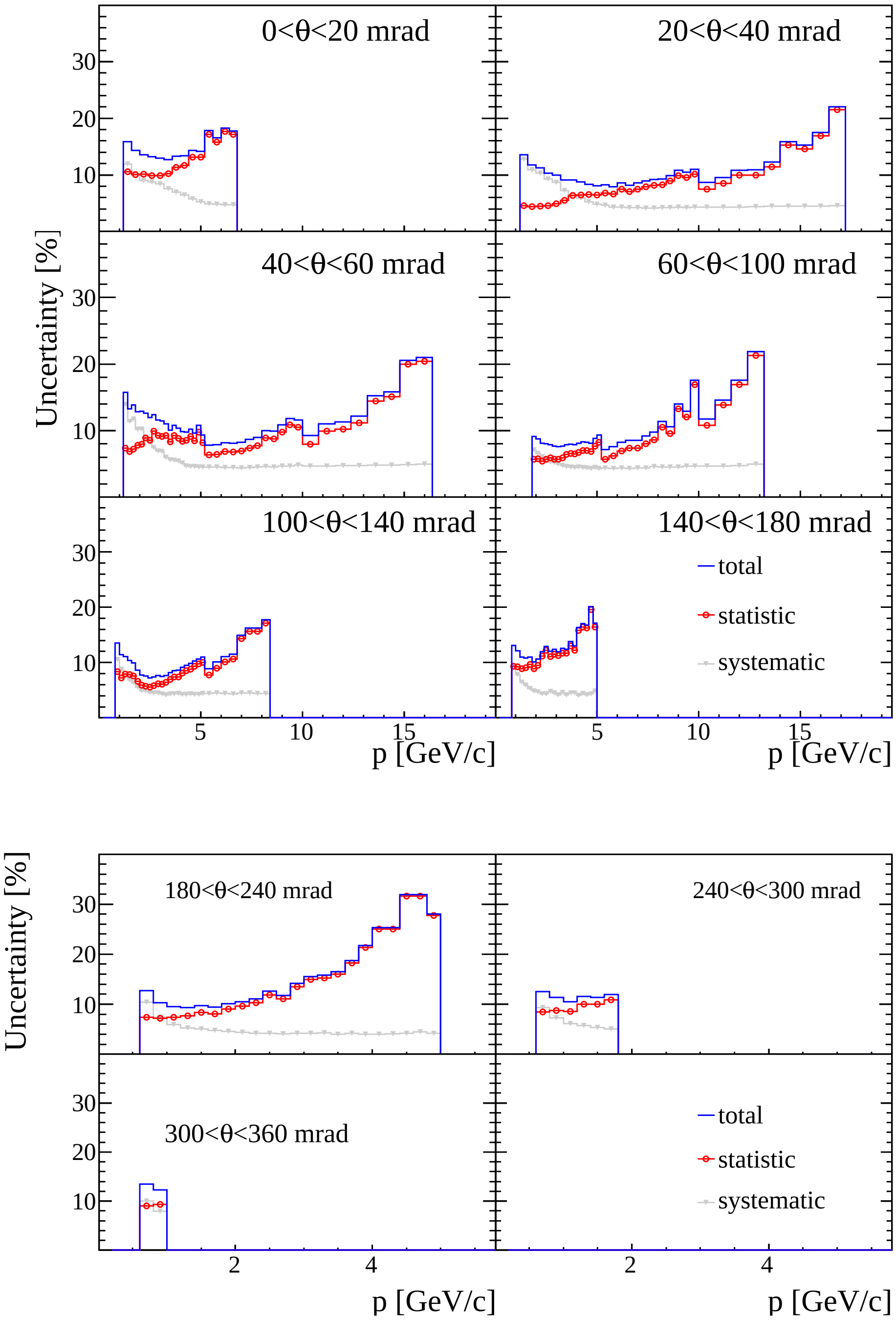

Appendix H

Preliminary proton cross-sections

Figure H.1: Differential cross sections for proton production in p+C interactions at 31 GeV/c. The spectra are presented as a function of laboratory momentum (p) in different intervals of polar angle (θ). Error bars indicate only statistical errors. Those results were obtained at the very end of my thesis with the same methods described for the charged pion and kaon cross-sections.

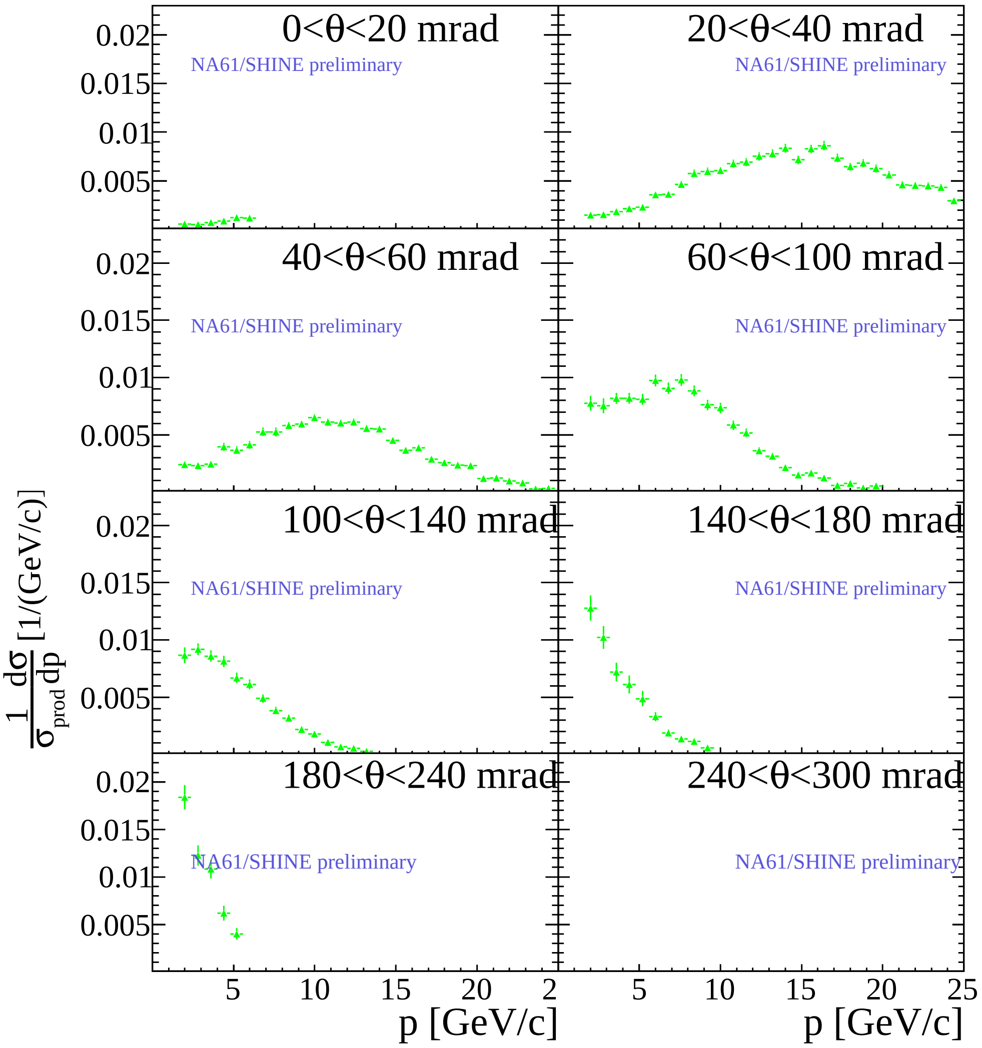

Bibliography

[1] J. Chadwick *V. Deut. Phys. Ges.* **16** (1914) 383.

[2] N. Bohr, "Faraday lecture. chemistry and the quantum theory of atomic constitution," *J. Chem. Soc.* (1932) 349–384. `http://dx.doi.org/10.1039/JR9320000349`.

[3] W. Pauli, "Liebe radioaktive damen und herren ...," 1930. `http://cdsweb.cern.ch/record/83282/files/meitner_0393.pdf`. Pauli Archive, CERN.

[4] B. Pontecorvo *Chalk river Report PD-205* (November 1946) . unpublished.

[5] C. Cowan, F. Reines, F. Harrison, H. Kruse, and A. McGuire, "Detection of the free neutrino: A Confirmation," *Science* **124** (1956) 103–104.

[6] M. Goldhaber, L. Grodzins, and A. W. Sunyar, "Helicity of neutrinos," *Phys. Rev.* **109** (Feb, 1958) 1015–1017. `http://link.aps.org/doi/10.1103/PhysRev.109.1015`.

[7] G. Danby, J.-M. Gaillard, K. Goulianos, L. M. Lederman, N. Mistry, M. Schwartz, and J. Steinberger, "Observation of high-energy neutrino reactions and the existence of two kinds of neutrinos," *Phys. Rev. Lett.* **9** (Jul, 1962) 36–44. `http://link.aps.org/doi/10.1103/PhysRevLett.9.36`.

[8] M. L. Perl *et al.*, "Evidence for anomalous lepton production in $e^+ - e^-$ annihilation," *Phys. Rev. Lett.* **35** (Dec, 1975) 1489–1492. `http://link.aps.org/doi/10.1103/PhysRevLett.35.1489`.

[9] **DONUT** Collaboration, K. Kodama *et al.*, "Observation of tau-neutrino interactions," *Phys. Lett.* **B504** (2001) 218–224, `arXiv:hep-ex/0012035`.

[10] **LEP** Collaboration, G. Alexander *et al.*, "Electroweak parameters of the Z0 resonance and the Standard Model: the LEP Collaborations," *Phys. Lett.* **B276** (1992) 247–253.

[11] Z. Maki, M. Nakagawa, and S. Sakata, "Remarks on the unified model of elementary particles," *Prog.Theor.Phys.* **28** (1962) 870–880.

[12] B. Pontecorvo *J Expt. Theory. Phys.* **33** (1957) .

[13] M. Gell-Mann and A. Pais, "Behavior of neutral particles under charge conjugation," *Phys. Rev.* **97** (Mar, 1955) 1387–1389. `http://link.aps.org/doi/10.1103/PhysRev.97.1387`.

[14] R. Davis, D. S. Harmer, and K. C. Hoffman, “Search for neutrinos from the sun,” *Phys. Rev. Lett.* **20** (May, 1968) 1205–1209. `http://link.aps.org/doi/10.1103/PhysRevLett.20.1205`.

[15] V. N. Gribov and B. Pontecorvo, “Neutrino astronomy and lepton charge,” *Phys. Lett.* **B28** (1969) 493.

[16] **Super-Kamiokande** Collaboration, Y. Fukuda *et al.*, “Evidence for oscillation of atmospheric neutrinos,” *Phys. Rev. Lett.* **81** (1998) 1562–1567, `arXiv:hep-ex/9807003`.

[17] **SNO** Collaboration, Q. R. Ahmad *et al.*, “Measurement of the rate of $\nu e + d \rightarrow p + p + e-$ interactions produced by $b8$ solar neutrinos at the sudbury neutrino observatory,” *Phys. Rev. Lett.* **87** no. 7, (Jul, 2001) 071301.

[18] M. Kobayashi and T. Maskawa, “CP Violation in the Renormalizable Theory of Weak Interaction,” *Prog. Theor. Phys.* **49** (1973) 652–657.

[19] E. Majorana, “Theory of the Symmetry of Electrons and Positrons,” *Nuovo Cim.* **14** (1937) 171–184.

[20] M. Fukugita and T. Yanagida, *Physics of Neutrinos and Applications to Astrophysics*. Springer-Verlag Berlin Heidelberg, 2003.

[21] D. A. Rubbia, “Introduction to neutrino physics,” (2006) 217–223. Cours 3eme cycle suisse romande, ETH Zurich.

[22] V.M. and Lobashev, “The search for the neutrino mass by direct method in the tritium beta-decay and perspectives of study it in the project katrin,” *Nuclear Physics A* **719** no. 0, (2003) C153 – C160. `http://www.sciencedirect.com/science/article/pii/S0375947403009850`.

[23] **KATRIN** Collaboration, J. Wolf, “The KATRIN Neutrino Mass Experiment,” *Nucl.Instrum.Meth.* **A623** (2010) 442–444, `arXiv:0810.3281 [physics.ins-det]`.

[24] **GERDA** Collaboration, K.-T. Knopfle, “Search for neutrinoless double-beta decay of Ge-76 with GERDA,” `arXiv:0809.5207 [hep-ex]`.

[25] N. Ackerman *et al.*, “Observation of Two-Neutrino Double-Beta Decay in Xe-136 with EXO-200,” `arXiv:1108.4193 [nucl-ex]`.

[26] **NEMO** Collaboration, J. Argyriades *et al.*, “Measurement of the Double Beta Decay Half-life of 150-Nd and Search for Neutrinoless Decay Modes with the NEMO-3 Detector,” *Phys. Rev.* **C80** (2009) 032501, `arXiv:0810.0248 [hep-ex]`.

[27] A. D. Dolgov *et al.*, “Oscillations of neutrinos produced and detected in crystals,” *Nucl. Phys.* **B729** no. 79, (2010) , `hep-ph/0505251`.

[28] L. Stodolsky, “When the wavepacket is unnecessary,” *Phys. Rev.* **D58** (1998) , `arXiv:hep-ph/9802387`.

[29] B. Kayser *et al.*, “Theory of neutrino oscillations with entanglement,” *Phys. Rev.* **D82** no. 9, (Nov, 2010) .

[30] O. Lychkovskiy, “Neutrino oscillations: deriving the plane-wave approximation in the wave-packet approach,” arXiv:0901.1198.

[31] E. K. Akhmedov, “Do charged leptons oscillate?,” *JHEP* **09** (2007) 116, arXiv:0706.1216 [hep-ph].

[32] Y. Srivastava, A. Widom, and E. Sassaroli, “Charged lepton and neutrino oscillations,” *Eur. Phys. J.* **C2** (1998) 769–774.

[33] J. H. Christenson, J. W. Cronin, V. L. Fitch, and R. Turlay, “Evidence for the 2π decay of the k_2^0 meson,” *Phys. Rev. Lett.* **13** no. 4, (Jul, 1964) 138–140.

[34] C. S. Wu, E. Ambler, R. W. Hayward, D. D. Hoppes, and R. P. Hudson, “Experimental test of parity conservation in beta decay,” *Phys. Rev.* **105** (Feb, 1957) 1413–1415. http://link.aps.org/doi/10.1103/PhysRev.105.1413.

[35] I. Y. Kobzarev, B. V. Martemyanov, L. B. Okun, and M. G. Shchepkin, “The phenomenology of neutrino oscillation,” *Sov. J. Nucl. Phys.* **32** (1980) 823.

[36] G. P. Zeller, “Low energy neutrino cross sections: Comparison of various Monte Carlo predictions to experimental data,” arXiv:hep-ex/0312061.

[37] D. Casper, “The nuance neutrino physics simulation, and the future,” *Nucl. Phys. Proc. Suppl.* **112** (2002) 161–170, arXiv:hep-ph/0208030.

[38] G. P. Zeller, “Low energy neutrino cross sections from K2K, MiniBooNE, SciBooNE, and MINERvA,” *J. Phys. Conf. Ser.* **136** (2008) 022028.

[39] S. P. Rosen and J. M. Gelb, “Mikheyev-smirnov-wolfenstein enhancement of oscillations as a possible solution to the solar-neutrino problem,” *Phys. Rev.* **D34** no. 4, (1986) .

[40] A. de Gouvea, “TASI lectures on neutrino physics,” arXiv:hep-ph/0411274 [hep-ph].

[41] L. Wolfenstein, “Neutrino oscillations in matter,” *Phys. Rev. D* **17** no. 9, (May, 1978) 2369–2374.

[42] A. Y. Smirnov, “The MSW effect and solar neutrinos,” arXiv:hep-ph/0305106.

[43] G. L. Fogli, E. Lisi, A. Marrone, A. Palazzo, A. M. Rotunno, “Evidence of $\theta_{13} > 0$ from global neutrino data analysis,” (June, 2011) , arXiv:1106.6028v1 [hep-ph].

[44] **T2K** Collaboration, K. Abe *et al.*, “Indication of electron neutrino appearance from an accelerator-produced off-axis muon neutrino beam,” *Phys. Rev. Lett.* **107** no. 4, (Jul, 2011) 041801.

[45] M. Collaboration, P. Adamson, *et al.*, “Improved search for muon-neutrino to electron-neutrino oscillations in MINOS,” arXiv:hep-ex/1108.0015. http://arxiv.org/abs/1108.0015.

[46] **CHOOZ** Collaboration, M. Apollonio *et al.*, “Search for neutrino oscillations on a long base-line at the CHOOZ nuclear power station,” *Eur. Phys. J.* **C27** (2003) 331–374, arXiv:hep-ex/0301017.

[47] F. Boehm *et al.*, “Final results from the palo verde neutrino oscillation experiment,” *Phys. Rev.* **D64** (2001) 112001.

[48] **Daya-Bay** Collaboration, X. Guo *et al.*, "A precision measurement of the neutrino mixing angle theta(13) using reactor antineutrinos at Daya Bay," `arXiv:hep-ex/0701029`.

[49] **Double Chooz** Collaboration, F. Ardellier *et al.*, "Double Chooz: A search for the neutrino mixing angle theta(13)," `arXiv:hep-ex/0606025`.

[50] **RENO** Collaboration, J. K. Ahn *et al.*, "RENO: An Experiment for Neutrino Oscillation Parameter θ_{13} Using Reactor Neutrinos at Yonggwang," `arXiv:1003.1391 [hep-ex]`.

[51] **K2K** Collaboration, M. H. Ahn *et al.*, "Measurement of Neutrino Oscillation by the K2K Experiment," *Phys. Rev.* **D74** (2006) 072003, `arXiv:hep-ex/0606032`.

[52] **T2K** Collaboration, K. Abe *et al.*, "The T2K Experiment," `arXiv:1106.1238 [physics.ins-det]`. accepted for publication in Nucl. Instrum. Methods, article in press.

[53] **MINOS** Collaboration, P. Adamson *et al.*, "Measurement of Neutrino Oscillations with the MINOS Detectors in the NuMi Beam," *Phys. Rev. Lett.* **101** no. 13, (Sep, 2008) 131802.

[54] **NOvA** Collaboration, A. Sousa, "The NOvA experiment: Present and future," *PoS* **ICHEP2010** (2010) 332.

[55] S. J. Parke, "Neutrino oscillation phenomenology," 2008. FERMILAB-PUB-07-767-T.

[56] **MINOS Collaboration** Collaboration, P. Adamson *et al.*, "Search for the disappearance of muon antineutrinos in the NuMI neutrino beam," *Phys.Rev.* **D84** (2011) 071103, `arXiv:1108.1509 [hep-ex]`.

[57] **MINOS Collaboration** Collaboration, P. Adamson *et al.*, "An improved measurement of muon antineutrino disappearance in MINOS," `arXiv:1202.2772 [hep-ex]`.

[58] **OPERA** Collaboration, N. Agafonova *et al.*, "Observation of a first ν_τ candidate in the OPERA experiment in the CNGS beam," *Phys. Lett.* **B691** (2010) 138–145, `arXiv:1006.1623 [hep-ex]`.

[59] **MINOS** Collaboration, D. G. Michael *et al.*, "Observation of muon neutrino disappearance with the MINOS detectors and the NuMI neutrino beam," *Phys. Rev. Lett.* **97** (2006) 191801, `arXiv:hep-ex/0607088`.

[60] **Super-Kamiokande** Collaboration, Y. Ashie *et al.*, "Evidence for an oscillatory signature in atmospheric neutrino oscillation," *Phys. Rev. Lett.* **93** (2004) 101801, `arXiv:hep-ex/0404034`.

[61] **Super-Kamiokande** Collaboration, S. Fukuda *et al.*, "Solar ^{8}B and hep Neutrino Measurements from 1258 Days of Super-Kamiokande Data," *Phys. Rev. Lett.* **86** no. 25, (Jun, 2001) 5651–5655.

[62] Q. R. Ahmad *et al.*, "Direct evidence for neutrino flavor transformation from neutral-current interactions in the sudbury neutrino observatory," *Phys. Rev. Lett.* **89** no. 1, (Jun, 2002) 011301.

[63] **KamLAND** Collaboration, K. Eguchi *et al.*, "First Results from KamLAND: Evidence for Reactor Antineutrino Disappearance," *Phys. Rev. Lett.* **90** no. 2, (Jan, 2003) 021802.

[64] **OPERA** Collaboration, B. Aharmim *et al.*, "An Independent Measurement of the Total Active ^{8}B Solar Neutrino Flux Using an Array of ^{3}He Proportional Counters at the Sudbury Neutrino Observatory," *Phys. Rev. Lett.* **101** (2008) 111301, `arXiv:0806.0989 [nucl-ex]`.

[65] **KamLAND** Collaboration, S. Abe *et al.*, "Precision Measurement of Neutrino Oscillation Parameters with KamLAND," *Phys. Rev. Lett.* **100** no. 22, (Jun, 2008) 221803.

[66] **K2K** Collaboration, S. Yamamoto *et al.*, "Improved search for $\nu\mu \to \nu e$ oscillation in a long-baseline accelerator experiment," *Phys. Rev. Lett.* **96** no. 18, (May, 2006) 181801.

[67] **MINOS** Collaboration, P. Adamson *et al.*, "New constraints on muon-neutrino to electron-neutrino transitions in MINOS," *Phys. Rev. D* **82** no. 5, (Sep, 2010) 051102.

[68] T. A. Mueller *et al.*, "Improved predictions of reactor antineutrino spectra," *Phys. Rev. C* **83** no. 5, (May, 2011) 054615.

[69] O. Mena and S. Parke, "Unified graphical summary of neutrino mixing parameters," *Phys. Rev. D* **69** (2004) 117301.

[70] V. Barger, D. Marfatia, and K. Whisnant, "Breaking eight-fold degeneracies in neutrino CP violation, mixing, and mass hierarchy," *Phys. Rev.* **D65** (2002) 073023, `arXiv:hep-ph/0112119`.

[71] K. Abe *et al.*, "Letter of Intent: The Hyper-Kamiokande Experiment — Detector Design and Physics Potential —," `arXiv:1109.3262 [hep-ex]`.

[72] A. Rubbia, "Underground Neutrino Detectors for Particle and Astroparticle Science: the Giant Liquid Argon Charge Imaging ExpeRiment (GLACIER)," *J. Phys. Conf. Ser.* **171** (2009) 012020, `arXiv:0908.1286 [hep-ph]`.

[73] A. Cervera, F. Dydak, and J. Gomez Cadenas, "A large magnetic detector for the neutrino factory," *Nucl. Instrum. Meth.* **A451** (2000) 123–130.

[74] R. Tschirhart, "Project-X: A new high intensity proton accelerator complex at Fermilab," `arXiv:1109.3500 [hep-ex]`.

[75] V. Barger *et al.*, "Report of the US long baseline neutrino experiment study," `arXiv:0705.4396 [hep-ph]`.

[76] The ISS Physics Working Group, "Physics at a future neutrino factory and super-beam facility," Feb, 2007. `doi:10.1088/0034-4885/72/10/106201`. Technical report.

[77] S. Geer, "Neutrino beams from muon storage rings: Characteristics and physics potential," *Phys. Rev. D* **57** (Jun, 1998) 6989–6997. `http://link.aps.org/doi/10.1103/PhysRevD.57.6989`.

[78] A. Cervera *et al.*, "Golden measurements at a neutrino factory," *Nucl. Phys.* **B579** (2000) 17–55, `arXiv:hep-ph/0002108`.

[79] A. Donini, D. Meloni, and P. Migliozzi, "The silver channel at the Neutrino Factory," *Nucl. Phys.* **B646** (2002) 321–349, `arXiv:hep-ph/0206034`.

[80] D. Autiero *et al.*, "The synergy of the golden and silver channels at the Neutrino Factory," *Eur. Phys. J.* **C33** (2004) 243–260, `arXiv:hep-ph/0305185`.

[81] S. Rigolin, "Physics reach of beta-beams and nu-factories: The problem of degeneracies," *Nucl. Phys. Proc. Suppl.* **155** (2006) 33–37, `arXiv:hep-ph/0509366`.

[82] J. Peltoniemi and J. Sarkamo, "Neutrino oscillations at CERN-Pyhäsalmi baseline," *Nuclear Physics B - Proceedings Supplements* **155** no. 1, (2006) 201 – 202. `http://www.sciencedirect.com/science/article/pii/S0920563206001332`. Proceedings to the 7th International Workshop on Neutrino Factories and Superbeams.

[83] Y. Yamazaki *et al.*, "Accelerator technical design report for J-PARC,". KEK-REPORT-2002-13.

[84] "Recent results from K2K," *Nuclear Physics B - Proceedings Supplements* **145** (2005) 124 – 127.

[85] **NA61/SHINE** Collaboration, N.Antoniou *et al.*, "Study of Hadron Production in Collisions of Protons and Nuclei at the CERN SPS," *CERN-SPSC-2006-034* .

[86] **NA61/SHINE** Collaboration, N.Antoniou *et al.*, "Additional Information Requested in the Proposal Review Process," *CERN-SPSC-2007-004* .

[87] **NA61/SHINE** Collaboration, N.Abgrall *et al.*, "Further Information Requested in the Proposal Review Process," *CERN-SPSC-2007-019* .

[88] **NA61/SHINE** Collaboration, N.Abgrall *et al.*, "Calibration and Analysis of the 2007 Data," *CERN-SPSC-2008-018* .

[89] J-PARC TDR, KEK-Report 2002-13 and JAERI-Tech 2003-044. `http://hadron.kek.jp/~accelerator/TDA/tdr2003/index2.html`.

[90] S. van der Meer. CERN Yellow Report CERN-61-07 (1961).

[91] R. B. Palmer, "Magnetic Fingers,". Presented at Informal Conference on Experimental Neutrino Physics, CERN, Geneva, Switzerland, 20-22 Jan 1965 (C. Franzinetti, (Ed.), CERN-65-32, pp. 141-146).

[92] K. Matsuoka, "Measurement of the Neutrino Beam with the Muon Monitor and the First Result of the T2K Long-Baseline Neutrino Oscillation Experiment,". PhD thesis, Department of Physics, Graduate School of Science Kyoto University (2011).

[93] C. Strabel, "Evaluation of Particle Yields in 30 GeV Proton-Carbon Inelastic Interactions for Estimating the T2K Neutrino Flux,". PhD thesis, ETH Zurich (2011).

[94] N. Abgrall *et al.*, "Time Projection Chambers for the T2K Near Detectors," *Nucl. Instrum. Meth.* **A637** (2011) 25–46, `arXiv:1012.0865 [physics.ins-det]`.

[95] **T2K** Collaboration, T. Lindner, "The fine grained detector for the T2K experiment," *J. Phys. Conf. Ser.* **136** (2008) 042035.

[96] L.Trung, "Event reconstruction and energy calibration using cosmic muons for the T2K π^0 detector,". PhD thesis, Stony Brook University, (2009).

[97] Y. Giomataris, P. Rebourgeard, J. P. Robert, and G. Charpak, "MICROMEGAS: A high-granularity position-sensitive gaseous detector for high particle-flux environments," *Nucl. Instrum. Meth.* **A376** (1996) 29–35.

[98] M. Ziembicki *et al.*, "The SMRD subdetector at the T2K near detector station," *Acta Phys. Polon.* **B41** (2010) 1579–1584.

[99] **Super-Kamiokande** Collaboration, M. Shiozawa *et al.*, "Search for Proton Decay via $p \to e + \pi^0$ in a Large Water Cherenkov Detector," *Phys. Rev. Lett.* **81** (1998) 3319–3323, `arXiv:hep-ex/9806014`.

[100] **Super-Kamiokande** Collaboration, Y. Hayato *et al.*, "Search for proton decay through $p \to \bar{\nu} K^+$ in a large water Cherenkov detector," *Phys. Rev. Lett.* **83** (1999) 1529–1533, `arXiv:hep-ex/9904020`.

[101] **Super-Kamiokande** Collaboration, H. Nishino *et al.*, "Search for Proton Decay via $p \to e^+\pi^0$ and $p \to \mu^+\pi^0$ in a Large Water Cherenkov Detector," *Phys. Rev. Lett.* **102** (2009) 141801, `arXiv:0903.0676 [hep-ex]`.

[102] **T2K** Collaboration, Y. Itow *et al.*, "The JHF-Kamioka neutrino project," `arXiv:hep-ex/0106019`.

[103] R. Brun, F. Bruyant, M. Maire, A. C. McPherson, and P. Zanarini, "GEANT3,". CERN-DD-EE-84-1.

[104] `http://www.staff.uni-mainz.de/zeitnitz/Gcalor/gcalor.html`.

[105] G. Battistoni *et al.*, "The FLUKA code: Description and benchmarking," *AIP Conf. Proc.* **896** (2007) 31–49.

[106] N. Abgrall, "Constraining neutrino flux predictions with hadron production data: the NA61/SHINE measurements for the T2K experiment.,". PhD thesis, University of Geneva (2011). Also private discussions.

[107] N. Abgrall, B. Popov and J.-M. Levy, "Predictions of neutrino fluxes for T2K: NA61 analysis and data taking strategy,". NA61/T2K Internal note 2009-01 draft 2.1 (2010).

[108] N. Abgrall and beam working group, "Neutrino flux prediction,". `http://www.t2k.org/docs/technotes/054`. T2K Technical note 054 (2011).

[109] **HARP** Collaboration, M. G. Catanesi *et al.*, "Measurement of the production cross-section of positive pions in p Al collisions at 12.9-GeV/c," *Nucl. Phys.* **B732** (2006) 1–45, `arXiv:hep-ex/0510039`.

[110] **NA49** Collaboration, C. Alt *et al.*, "Inclusive production of charged pions in p + C collisions at 158-GeV/c beam momentum," *Eur. Phys. J.* **C49** (2007) 897–917, `arXiv:hep-ex/0606028`.

[111] S. E. Kopp, "Accelerator neutrino beams," *Phys. Rept.* **439** (2007) 101–159, `arXiv:physics/0609129`.

[112] **HARP** Collaboration, M. G. Catanesi *et al.*, "The HARP detector at the CERN PS," *Nucl. Instrum. Meth.* **A571** (2007) 527–561.

[113] **HARP** Collaboration, M. G. Catanesi *et al.*, “Measurement of the production cross-section of positive pions in the collision of 8.9 GeV/c protons on beryllium,” *Eur. Phys. J.* **C52** (2007) 29–53, `arXiv:hep-ex/0702024`.

[114] **HARP and NA61** Collaboration, B. A. Popov, “HARP and NA61 (SHINE) hadron production experiments,” *AIP Conf. Proc.* **1189** (2009) 97–104.

[115] C. L. Wang, “Pion, Kaon, and Antiproton Production Between 10 and 70 BeV,” *Phys. Rev. Lett.* **25** no. 15, (Oct, 1970) 1068–1072.

[116] R. Raja, “The main injector particle production experiment (MIPP) at Fermilab,” *Nucl. Instrum. Meth.* **A553** (2005) 225–230, `arXiv:hep-ex/0501005`.

[117] **Pierre Auger** Collaboration, J. Abraham *et al.*, “Properties and performance of the prototype instrument for the Pierre Auger Observatory,” *Nucl. Instrum. Meth.* **A523** (2004) .

[118] **KASCADE** Collaboration, T. Antoni *et al.*, “The Cosmic ray experiment KASCADE,” *Nucl. Instrum. Meth.* **A513** (2003) 490–510.

[119] **NA61/SHINE** Collaboration, N. Abgrall *et al.*, “Measurements of Cross Sections and Charged Pion Spectra in Proton-Carbon Interactions at 31 GeV/c,” *Phys. Rev.* **C84** (2011) 034604.

[120] **NA61/SHINE Collaboration** Collaboration, N. Abgrall *et al.*, “Measurement of production properties of positively charged kaons in proton-carbon interactions at 31 gev/c,” *Phys. Rev. C* **85** (Mar, 2012) 035210.

[121] **NA49** Collaboration, S. Afanasev *et al.*, “The NA49 large acceptance hadron detector,” *Nucl.Instrum.Meth.* **A430** (1999) 210–244.

[122] **NA49** Collaboration, C. Alt *et al.*, “Inclusive production of charged pions in p p collisions at 158-GeV/c beam momentum,” *Eur. Phys. J.* **C45** (2006) 343–381, `arXiv:hep-ex/0510009`.

[123] **NA49** Collaboration, W. Rauch *et al.*, “The NA49 Data Acquisition System,”.

[124] L. P. C.Bovet, R. Maleyran *et al.* `http://sba.web.cern.ch/sba/Documentations/docs/cedar.pdf`. CERN Yellow Report CERN-82-13.

[125] W. W. T. Lohse *Adv.Ser.Direct.High Energy Phys.* **9** (1992) 81–155.

[126] unpublished notes and private discussions with Alex Korzenev.

[127] K. Levenberg, “A method for the solution of certain problems in least squares.,” *Quart. Appl. Math.* **2** (1944) 164–168.

[128] C. Strabel, “Energieabhaengigkeit der K^0_s-Produktion in zentralen Pb+Pb Reaktionen,”. Master thesis, Goethe University Frankfurt (2006).

[129] **NA49** Collaboration, C. Alt *et al.*, “High p_T spectra of identified particles produced in Pb+Pb collisions at 158-GeV/nucleon beam energy,” *Nucl. Phys. A* **774** (2006) 473, `arXiv:nucl-ex/0510054`.

[130] R. Zybert and P. Buncic, “DSPACK: Object manager for high energy physics,”. Prepared for International Conference on Computing in High Energy Physics (CHEP 95), Rio de Janeiro, Brazil, 18-22 Sep 1995.

[131] http://na49info.web.cern.ch/na49info/na49/Software/DSPACK/dspack-overvie%w/chapter2.2

[132] D. Irmscher, “Philosophy and parts of the global tracking chain,” *NA49 Note number* **131** (1997) . https://edms.cern.ch/file/815824/1/global_tracking.pdf.

[133] http://castor.web.cern.ch/.

[134] http://na61.web.cern.ch/na61/pages/root61/.

[135] **NA49** Collaboration, B. Lasiuk, “Particle identification in the NA49 TPCs,” *Nucl. Instrum. Meth.* **A409** (1998) 402–406.

[136] R. M. Sternheimer and R. F. Peierls, “General expression for the density effect for the ionization loss of charged particles,” *Phys. Rev. B* **3** (Jun, 1971) 3681–3692. http://link.aps.org/doi/10.1103/PhysRevB.3.3681.

[137] K and Werner, “Strings, pomerons and the venus model of hadronic interactions at ultrarelativistic energies,” *Physics Reports* **232** no. 2-5, (1993) 87 – 299. http://www.sciencedirect.com/science/article/pii/037015739390078R.

[138] **NA61/SHINE** Collaboration, S. Murphy, “Preliminary results of charged pions cross-section in proton carbon interaction at 30 GeV measured with the NA61/SHINE detector,” *XLVth Rencontres de Moriond, Electroweak interactions and unified theories* (2010) , arXiv:1005.3689 [hep-ex].

[139] T. Palczewski. Ph.D. Thesis in preparation, National Center for Nuclear Research, Warsaw Poland (2012).

[140] M. Posiadala. Ph.D. Thesis in preparation, University of Warsaw, Warsaw Poland (2012).

[141] http://www.phys.ufl.edu/courses/phy4803L/group_I/muon/bicron_bc400-416.pdf.

[142] G. Palla *et al.*, “The grid-geometry time-of-flight detector used in the NA49 experiment at the CERN SPS,” *Nucl. Instrum. Meth.* **A451** (2000) 406–413.

[143] R. E. Kalman, “A New Approach to Linear Filtering and Prediction Problems,” *Transactions of the ASME - Journal of Basic Engineering* no. 82 (Series D), (1960) 35–45. http://www.cs.unc.edu/welch/kalman/media/pdf/Kalman1960.pdf.

[144] http://pdg.lbl.gov/2011/reviews/rpp2011-rev-passage-particles-matter.pdf.

[145] M. Paterno, “Calculating efficiencies and their uncertainties,” 2003. http://home.fnal.gov/~paterno/images/effic.pdf.

[146] F. James, *Statistical Methods in Experimental Physics*. World Scientific, 2006.

[147] K. Werner, “Space-time structure and rescattering in ultrarelativistic nuclear collisions,” *Nucl.Phys.* **A525** (1991) 501–506.

[148] S. A. Bass *et al.*, "Microscopic models for ultrarelativistic heavy ion collisions," *Prog. Part. Nucl. Phys.* **41** (1998) 255–369, `arXiv:nucl-th/9803035`.

[149] D. Heck *et al.* Report Forschungszentrum Karlsruhe FZKA-6019, (1998).

[150] H.-J. Drescher, M. Bleicher, S. Soff, and H. Stoecker, "Model dependence of lateral distribution functions of high energy cosmic ray air showers," *Astropart. Phys.* **21** (2004) 87–94, `astro-ph/0307453`.

[151] K. Gallmeister and U. Mosel, "Production of charged pions off nuclei with 3...30 GeV incident protons and pions," *Nucl. Phys.* **A826** (2009) 151–160, `arXiv:0901.1770 [hep-ex]`.

[152] T. Eichten *et al.*, "Particle production in proton interactions in nuclei at 24 GeV/c," *Nucl. Phys.* **B44** (1972) 333–343.

[153] V. Uzhinsky, "How to Improve UrQMD Model to Describe NA61/SHINE Experimental Data," *arXiv 1107.0374* (2011) .

[154] **DOUBLE-CHOOZ Collaboration** Collaboration, Y. Abe *et al.*, "Indication for the disappearance of reactor electron antineutrinos in the Double Chooz experiment," `arXiv:1112.6353 [hep-ex]`.

[155] R. P. Feynman, "Very high-energy collisions of hadrons," *Phys. Rev. Lett.* **23** (Dec, 1969) 1415–1417. `http://link.aps.org/doi/10.1103/PhysRevLett.23.1415`.

[156] M. Bonesini, A. Marchionni, F. Pietropaolo, and T. Tabarelli de Fatis, "On particle production for high energy neutrino beams," *Eur. Phys. J.* **C20** (2001) 13–27, `arXiv:hep-ph/0101163`.

[157] V. Galymov and beam working group, "Flux Prediction and Uncertainties for the 2011 Oscillation 1 Analysis,". `http://www.t2k.org/docs/technotes/099`. T2K Technical note 099 (2011).

[158] J. V. Allaby *et al. CERN Report* **70-12** (1970) .

[159] V. Galymov and beam working group, "Neutrino flux uncertainty for 10a data analysis,". `http://www.t2k.org/docs/technotes/054`. T2K Technical note 039 (2011).

[160] N. Abgrall *et al.*, "Pilot analysis of the NA61/SHINE 2007 long target data,". to be submitted to Nucl. Instrum. Meth.

[161] Sebastien Murphy on behalf of the NA61/SHINE collaboration, "Results of charged pions cross-section in proton carbon interaction at 31 GeV/c measured with the NA61/SHINE detector," *12th international Workshop on Neutrino Factories, SuperBeams and Beta Beams* (2011) , `arXiv:1105.6241 [hep-ex]`.

[162] Y. Hayato, "Neut," *Nuclear Physics B - Proceedings Supplements* **112** (2002) 171 – 176. `http://www.sciencedirect.com/science/article/pii/S0920563202017590`.

[163] **T2K** Collaboration, K. Abe *et al.*, "First Muon-Neutrino Disappearance Study with an Off-Axis Beam," `arXiv:1201.1386 [hep-ex]`. submitted to Phys. Rev. Lett.

[164] D. Beavis *et al.*, “P889: Long baseline neutrino oscillation experiment at the ags,”. Report No. BNL-52459, April, 1995.

[165] K. T. McDonald, “An Off-axis neutrino beam,” `arXiv:hep-ex/0111033 [hep-ex]`.

[166] H. Nelson, “Goodness of fit for poisson distributed data.” `www-cdf.fnal.gov/physics/statistics/notes/cdf5718_loglikeratv2.ps.gz`.

[167] S. Baker and R. D. Cousins, “Clarification of the use of chi-square and likelihood functions in fits to histograms,” *Nuclear Instruments and Methods in Physics Research* **221** no. 2, (1984) 437 – 442. `http://www.sciencedirect.com/science/article/pii/0167508784900164`.

List of Figures